Quantifying the Effect of Plasma Processes on the Global Stability of Solar Prominences

Jack Michael Jenkins

A dissertation submitted in partial fulfillment

of the requirements for the degree of

Doctor of Philosophy

of

University College London.

Department of Space and Climate Physics

University College London

March 3, 2020

I, Jack Michael Jenkins, confirm that the work presented in this thesis is my own. Where information has been derived from other sources, I confirm that this has been indicated in the work.

Eileen & Michael

To whom my gratitude cannot be expressed in words.

...but here's 59,112 words anyway.

Abstract

Solar prominences are structures formed of cool, chromospheric plasma magnetically suspended in the solar corona for up to several solar rotations. Prominences are observed to migrate through quasi-equilibria until their host magnetic field loses equilibrium with its surroundings. It has traditionally been assumed that this observed plasma evolution is a consequence of evolution in the magnetic field alone. However, recent results indicate that this interpretation is incomplete. This thesis uses a combination of observations and modelling to quantify the different contributions of plasma and magnetic field to the stability of solar prominences.

Firstly, the effect of prominence plasma on its host magnetic field was determined using an observational case study. The optical thickness of the prominence was used to estimate column density and mass in the lead up to its eruption. An estimate of the ratio of plasma and magnetic forces indicates plasma processes can heavily influence the equilibrium.

The study of mass was then expanded to a more general study using an analytical model. The full equilibrium governing a general prominence was quantified and used to show that the effect of plasma on the structure is two-fold. Firstly, including plasma in the equilibrium stabilises the prominence, when comparing with the massless case, additional magnetic forces are therefore required to overcome the modified equilibrium. Secondly, removing plasma from a prominence in equilibrium can enable the magnetic field to become unstable and cause an eruption of the prominence.

Finally, the fine-scale evolution of plasma within a prominence was studied using a combination of high-resolution observations and state-of-the-art models.

The results suggest that the force-balance varies over the length of the prominence, hence these structures cannot be considered solely magnetically dominated.

This work suggests that the relationship between prominence plasma and magnetic field on both global- and fine-scales contributes more to the stability of prominences than previously believed.

Impact Statement

'Space Weather' refers to the initiation, evolution, and influence of solar storms on the Earth and near-Earth environment. According to the National Risk Register[1], the risks that space weather pose to the Earth are of national importance. As such, a large contigent of the UK Solar & Plasma Physics communities strive to better understand and predict the associated phenomena.

Coronal mass ejections (CME), one of the possible manifestations of this space weather, are a complex mix of plasma and magnetic field. Initiated at the Sun, they can travel at up to a few thousands of kilometers per second through interplanetary space, potentially interacting with the near-Earth environment and causing a wide range of damaging effects. The work carried out in this thesis focusses on the pre-eruptive stage of these CMEs, providing additional understanding of the possible initiation processes and associated timescales involved.

Historically, CME initiations are studied with particular interest given to the evolution of their magnetic field. The work that I have carried out in this thesis demonstrates that the role of their internal mass, prominence plasma, is of non-negligible importance to this initiation. By additionally considering this mass, these structures that can take, on average, three days to traverse the Sun – Earth gap can either have their initiation triggered early, or delayed by up to two days. Such a large error demonstrates that the models currently employed for predictive purposes are incomplete; the mass of the interior prominence is a vital component that must, going forward, be incorporated if we ever wish to accurately predict their associated eruptions.

[1] UK National Risk Register 2017

Acknowledgements

I cannot continue without first acknowledging the people that started this ball rolling. To Kevin, for introducing me to Star Trek I owe all I have achieved to you and your interest in Sci-Fi, one that I of course now share. To Aled, for always making me question things and for the odd science-based feedback loop we seem to share. To Hoppy and Doran for the years of academic friendship, and let's not forget that card game. To Balasz for seeing past those abysmal A-level grades to the eager student behind them. To Huw, for believing in that persistent, and quite possibly annoying, undergraduate student enough to give him a shot at that summer internship, before introducing me to Jason and Jackie at RAL and the invaluable experience that afforded me. To Lucie, for giving me the inspiration to apply to MSSL, and in turn to Lidia, Ian, and Daisuke for granting me the STFC funding to undertake this mammoth task, and finally to Alex, Magnus, Steph, Francesco, and Jamie for making me feel at home in G01 upon my arrival.

To Dave, I have never met a more dedicated and meticulous person and I consider myself fortunate to have availed myself of your experience and expertise over the last three years. Without you, I would have missed those hidden science questions, bored audiences with my rambling presentations, and dumbfounded anyone attempting to read my written word. Thank you for taking the time.

To Lidia, you are the most knowledgeable and kind-hearted person I have ever met. Always ready to inspire with questions, teach with clarity, and challenge with rigour. I cannot hope to attain half of the scientific prowess you have achieved, but in your name I shall try. You are my idol.

To Deb, for the chats in 208 that went on for what seemed like, and on more than one occasion were, hours. For fueling my coffee addiction with an introduction to the world of George Clooney's Nespresso. For providing a friendly face whenever my code didn't work, whenever academia was giving me a series of right-hooks, whenever life was throwing curve-ball after curve-ball, whenever I needed to rant about something; anything; everything, whenever. For providing access to doggos, laughter, and a friendship that I hope endures a lifetime. Thankyou for being you.

And to the rest of MSSL's Solar Physics Group, G01 students and staff alike, thank you for creating an environment in which each and every member is valued and respected. I may not have a sample from which I can draw an effective comparison, but it is clear that the collection of people here is a special one and I hope to continue working with each of you.

To Gherardo and Christian, you have added more scientific content and understanding to this thesis than any other persons, so much so that it's hard to imagine what physics I actually understood before learning from you both. To Pascal and Guillaume for dismantling me, putting me back together, and allowing me to challenge and change your minds in return - prominence mass is important afterall!

To Lindsey Stirling, Martin O'Donnell & Michael Savatori, Nickelback, Pentatonix, Pendulum, Taylor Swift, 'Jess', and last but not least Carly Rae Jepsen. None of you know me, and none of you will likely ever read this, but thank you for keeping me focused, and giving me the beat I needed to push myself through. Similarly, a huge thankyou must go to the developers of Halo (and all versions therein), Overwatch, Gmod, Civ V, X3, and KOTOR (1&2) without whom this poor PhD student wouldn't have had a downtime.

Outside of the academic bubble there are of course the many family and friends who have done so much in so many ways that are too enumerable to count - I think I also have a page limit here so... - I see you, and I thank you.

Finally, to Social Services for trying to condemn a 5 year old's life to mediocrity.

Take a seat.

List of Publications

1. **J. M. Jenkins**, C. Beck, D. M. Long, L. van Driel-Gesztelyi, D. P. Choudhary. Plasma and structural properties of a prominence footpoint observed with the IBIS spectrometer. *Astrophys. J.*, In prep.

2. S. Wang, **J. M. Jenkins**, V. M. Pillet, C. Beck, D. M. Long, D. P. Choudhary, and James McAteer, Magnetic Structures of the Erupting Filament Observed on May 29 - 30, 2017, *Astrophys. J.*, Accepted.

3. P. Schwartz, S. Gunar, **J. M. Jenkins**, D. M. Long, P. Heinzel, D. P. Choudhary. 2D non-LTE modelling of a filament observed in the H_alpha line with the DST/IBIS spectropolarimeter. *Astron. Astrophys.*, 631:A146, Nov 2019. doi: 10.1051/0004-6361/201935358.

4. David M. Long, **Jack M. Jenkins**, Gherardo Valori. Multi-wavelength observations of 4 homologous global coronal waves. *Astrophys. J.*, 882(2):90, Sep 2019. doi: 10.3847/1538-4357/ab338d.

5. **Jack M. Jenkins**, Matthew Hopwood, Pascal Démoulin, Gherardo Valori, Guillaume Aulanier, David M. Long, and Lidia van Driel-Gesztelyi. Modeling the Effect of Mass-draining on Prominence Eruptions. *Astrophys. J.*, 873(1):49, Mar 2019. doi: 10.3847/1538-4357/ab037a.

6. David M. Long, Louise K. Harra, Sarah A. Matthews, Harry P. Warren, Kyoung-Sun Lee, George A. Doschek, Hirohisa Hara, and **Jack M. Jenkins**. Plasma Evolution within an Erupting Coronal Cavity. *Astrophys. J.*, 855(2):74, Mar 2018. doi: 10.3847/1538-4357/aaad68

7. **J. M. Jenkins**, D. M. Long, L. van Driel-Gesztelyi, and J. Carlyle. Understanding the Role of Mass-Unloading in a Filament Eruption. *Solar Phys.*, 293:7, January 2018. doi: 10.1007/s11207-017-1224-y.

Contents

List of Figures

List of Tables

Chapter 1

Introduction

The Sun has been a source of much curiosity over the course of human history. As a provider of a significant amount of heat and light incident on the Earth's surface, it has been crucial to the survival of the human race, perhaps even the origin. It has often been speculated that the disappearance of the Sun in the sky is the will of a divine being (*e.g.*, Amun-Ra - Egyptians; Helios - Greeks; Amaterasu - Japanese), punishing humans for their trespasses and reminding them of their reliance on this bright orb in the sky. In the modern day, we realise that the Sun is merely a collection of the most abundant elements in the universe, undergoing fusion due to the forces of gravity at the core, in turn creating the light and heat that the human race requires to survive. Yet, one must not consequently presume this ascribes the Sun as "understood".

Observations of the Sun have revealed that it is capable of doing much more than just supplying heat and light. Amongst its plethora of dynamics, solar eruptions are perhaps the most spectacular events to occur within the solar system, injecting the heliosphere with billions of tonnes of bright solar material and magnetic field travelling at up to thousands of kilometres per second. From once per week to multiple times per day, the occurrence of solar eruptions of ranging magnitudes is commonplace. The frequent interaction of these solar storms with the near-Earth environment induces effects within the Earth's magnetosphere, such as the spectacular displays of the Northern/Southern Lights. However, with the evolution of the human civilisation to beyond the surface of the Earth, we have discovered more

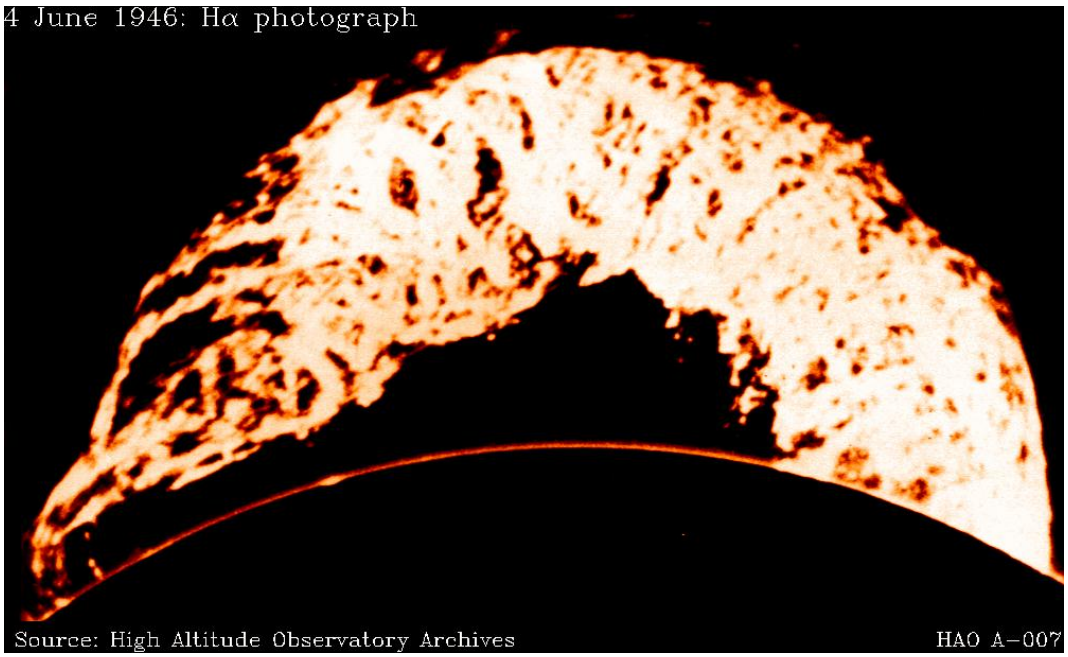

Figure 1.1: The "Granddaddy", a particularly large prominence imaged during its eruption on 4 June 1946. The occulted limb of the Sun is indicated at the bottom of the image as the faint semi-circular ring, giving scale to the erupting prominence. Image courtesy *www2.hao.ucar.edu*.

disruptive consequences to these storms and the hazards that they present to our modern way of life.

A large endeavour has been undertaken in recent decades in a bid to understand these eruptions, from initiation at the Sun, to their evolution in the solar wind, and finally to their arrival here at the Earth. Early observations of the Sun revealed that solar prominences, like that shown in Figure 1.1, were an eruption precursor and it is these structures that this thesis concerns itself with. However, before engaging in a comprehensive overview of solar prominences, this thesis begins with a brief overview of the Sun itself.

1.1 The Solar Interior

The Sun, a G2V type main sequence star of $\approx$ 4.5 billion years of age, lies at the centre of our solar system, and completes one full spin on its axis every 25 – 35 days (equator to pole, respectively). Having a mass of $\approx 1.98 \times 10^{30}$ kg, the resulting pressure due to gravity towards the centre of the Sun is suggestive of a core temperature and density of order 15 MK and 1.6×10^5 kg m^{-3}, respectively (Eddy and Ise, 1979). Of the possible fusion products (*e.g.*, helium nucleii, neutrinos, positrons) the (gamma) photons then begin their long journey to the solar surface through the remainder of the solar interior.

The upper boundary of the solar core is loosely defined as the depth where the temperature and density drops sufficiently such that fusion no longer occurs, believed to be at a radius of ≈ 0.25 R$_\odot$. After this point the photons enter the optically-thin radiative zone, so named as the temperature and density gradient in this region of the solar interior is steep enough that energy is more efficiently transported to shallower depths through photons than thermal convection or conduction. At a radius of ≈ 0.7 R$_\odot$, the temperature of the photon's surroundings decreases sufficiently for the formation of neutral atoms, forcing the photon's environment from optically-thin to opaque and the energy transport regime to change from radiative to conductive/convective. There is also a change in the rotational behaviour of the Sun at this radius, from solid body ($< 0.7\ R_\odot$) to differentially rotated ($> 0.7\ R_\odot$) (cf. Howe, 2009). This transitional and highly sheared layer is referred to as the tachocline, and it is at this depth that the magnetic field of the Sun (generated by the fact the Sun is a giant ball of constantly moving charged ions) is believed to be coherently amplified; this is further discussed in Section 1.4.

The change to a conductive energy transport regime at the tachocline means that the material above this layer is heated from the bottom, causing it to expand and rise when its density becomes less than its surroundings, before then cooling enough so that it can sink back to be heated once more. Such a temperature gradient sets up a convective instability, and the immense convective cells produced are able to efficiently carry the energy, incident on the underside of the cells, to shal-

lower depths. The upper boundary of the convective zone is therefore defined as the turnover point of these convective cells - where the density is sufficiently low. These convective cells also assist in the transportation of the magnetic field amplified at the base of the convective zone up to the solar atmosphere (see Section 1.4 for a full discussion). The decrease in density at the top of the convective zone causes the environment surrounding the trapped photons to become optically-thin for a second time, and the photons are able to freely escape into space. This boundary is called the photosphere and is the defined surface of the Sun *i.e.*, the layer below which the Sun is opaque.

Because the material below the photosphere is opaque, we are only able to infer the properties of the solar interior through either theory, or indirect methods such as helioseismology. The optically thin property of the solar atmosphere means direct observations can be taken of any associated phenomena. Furthermore, these structures and their associated dynamics may be diagnosed. This will be discussed in the following section.

1.2 The Solar Atmosphere

The solar atmosphere encompasses everything from the photosphere, defined as the deepest layer of the Sun that we may observe using direct methods, through to the heliosphere, defined as the outermost region of the Sun influenced by the solar wind. The physical properties of the *low* solar atmosphere, the domain of relevance for this thesis, span many orders of magnitude over a relatively short range of heights (Gabriel and Mason, 1982). The conditions, and evolution therein, of the solar material and magnetic field present here are responsible for the many interesting and dynamic phenomena frequently observed throughout the entire solar atmosphere. Most importantly, the Sun and its dynamic atmosphere may be resolved to a very high degree, unlike other stars, providing the scientific community with the unique opportunity of using the solar atmosphere as a resolvable astrophysical laboratory. It is here that solar physicists choose to test their many theories of plasma physics; see Section 1.3 for a discussion on solar plasma.

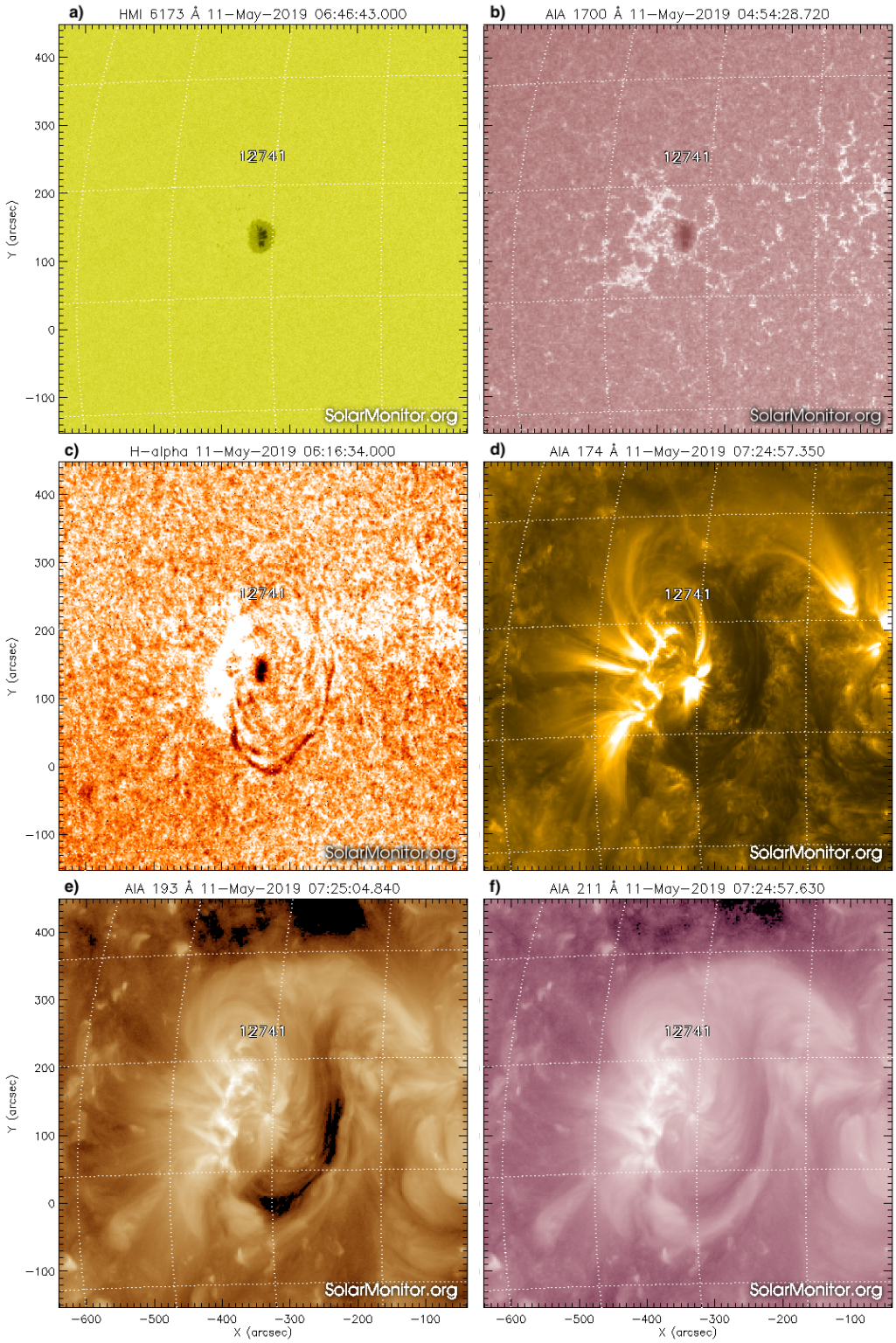

Figure 1.2: Images taken of the Sun in various passbands corresponding to different regions of the solar atmosphere. Panel a was taken by SDO/HMI, panels b,d,e,f were taken by SDO/AIA, and panel c was taken by an instrument observing the hydrogen-α line at Kanzelhöhe Observatory. Images courtesy *www.solarmonitor.org*.

The various sections that follow contain multiple references to spectral lines and their properties at given points within the solar atmosphere; a brief overview of spectral lines and their formation within the solar atmosphere is available in Section 3.1.

1.2.1 The Photosphere

The photosphere, commonly termed the surface of the Sun, is a thin layer ($\approx$ 100 km, Cox, 2000) of the solar atmosphere that ranges in temperature from $\approx$ 6400 K at its base to the so-called "temperature minimum" of $\approx$ 4400 K at the top. Spectral imaging of the Sun reveals that the solar emission is close to that of a blackbody of $\approx$ 5800 K; see Section 3.1. Although an opaque surface, with a density of $\approx 2 \times 10^{-4}$ kg m^{-3}, the photosphere is significantly less dense than water, for example.

The primary feature to be noted when observing the photosphere with high-resolution imaging is the granulation. As previously mentioned, the photosphere sits atop the convective zone of the solar interior and thus the granulation pattern is due to the overturning of material that has risen to the photosphere from below. These structures are typically on the order of $\approx$ 1.1 Mm ($\approx 1.5''$) in diameter. Similarly, but on a much larger scale of $\approx$ 30 Mm ($\approx 41''$), supergranular cells can also be observed. The top two panels of Figure 1.2 are a pair of images taken using continuum (6173 Å) and 1700 Å filters by the *Helioseismic Magnetic Imager* (HMI; Scherrer et al., 2012) and *Atmospheric Imaging Assembly* (AIA; Lemen et al., 2012) instruments on board the *Solar Dynamics Observatory* (SDO; Pesnell et al., 2012) spacecraft; see Chapter 3.2 for in-depth descriptions of these instruments. The images show a snapshot of the photosphere where a sunspot, the dark central blob, is flanked on all sides by (super) granulation. Here, the supergranular cells can be seen in the top-right panel as they are outlined by the bright network - the signature of magnetic elements grouped at granular boundaries (Spruit, 1976; Solanki, 1993). Sunspots, however, are not a ubiquitous feature and are rather a signature of the occasional breaching of the photosphere by particularly strong and concentrated bunchings of magnetic field from the interior; see Section 1.4 for more details. The

magnetic tension of such strong magnetic field is capable of inhibiting the local sub-surface convection resulting in limited energy being transported to the surface in these locations, hence sunspots appear dark in comparison to their weaker-field surroundings (*e.g.*, Cattaneo et al., 2003).

Routine, daily observations of the photosphere are carried out using many ground- and space-based solar observatories such as SDO/AIA and the *Global Oscillations Network Group* (GONG)[1]. The photosphere is best imaged in white-light wavelengths such as G-band, Titanium-Oxide (TiO: 7057 Å), and blue continuum (4700 Å).

1.2.2 The Chromosphere

The chromosphere is the $\approx$ 2000 km thick region of the solar atmosphere that lies above the photosphere. The temperature of the chromosphere increases from the aforementioned "temperature minimum" of $\approx$ 4400 K to $\approx$ 20,000 K as its density drops from $\approx 2 \times 10^{-4}$ kg m^{-3} to $\approx 1.6 \times 10^{-11}$ kg m^{-3} (Kontar et al., 2008).

Named after the Greek word for colour (*khrōma*), the reference comes from early solar eclipse observations in which red flame-like structures were seen to protrude from the limb of the occulting Moon. The chromosphere emits largely in the red side of the optical and in the infrared (IR) and is commonly observed using the H-α spectral line at 6562.8 Å. An example of an observation taken of an active region using the H-α telescope at the Kanzelhöhe Observatory is shown in the middle-left panel of Figure 1.2. The mottled pattern shown here corresponds to the fibrils and spicules that are ubiquitous in observations taken of the chromosphere (*e.g.*, Hansteen et al., 2006; de Pontieu et al., 2007). These fibrils and spicules are also well imaged in high-resolution by the *Dutch Open Telescope* (DOT; Rutten et al., 1997) in the right panel of Figure 1.3, in addition to a few prominences in the left panel; the dark, elongated, and collimated structures with varying degrees of curvature.

Prominences are collections of $\approx 10^4$ K material suspended above the chromosphere at coronal heights (Labrosse et al., 2010). As a result they absorb and

[1] http://halpha.nso.edu/index.html

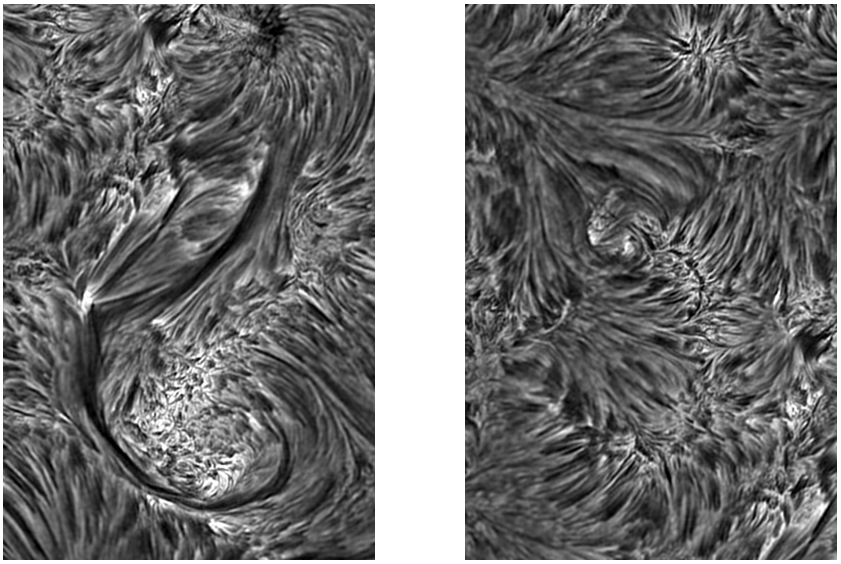

Figure 1.3: An example observation of prominences using a H-α filter and taken at the *Dutch Open Telescope* (DOT). They are seen in the left panel as the darker, more elongated, and collimated structures of varying degrees of curvature. Prominences are not to be confused with the fibrils and spicules ubiquitous to the chromosphere and imaged in both panels, but isolated in the right panel. Image courtesy *www.staff.science.uu.nl*.

scatter the incident light from the chromosphere below and appear dark in comparison with the solar disk. It is important to quickly note that, historically, these dark structures have been referred to as filaments whereas the word prominence tends to refer to the same structure but as viewed at the limb. Here, projected against the darkness of space, prominences appear in emission and are bright in comparison to their background, rather than the filaments that appear dark. Indeed, it is the elevated nature of prominences that early observers saw as flame-like protrusions from the solar surface during eclipses. Despite the tendency to use the words prominence and filament interchangeably, the word filament provides no information as to their elevated nature. Henceforth, these structures will be consistently referred to as prominences unless otherwise explicitly indicated. A complete description of prominences is available in Chapter 2.

1.2.3 The Transition Region

Above the chromosphere lies a very thin layer (a few hundred kilometres) of the solar atmosphere wherein the temperature dramatically increases from approximately $10^4 - 10^6$ K. The exact reason for this sudden, large, and somewhat un-intuitive in-

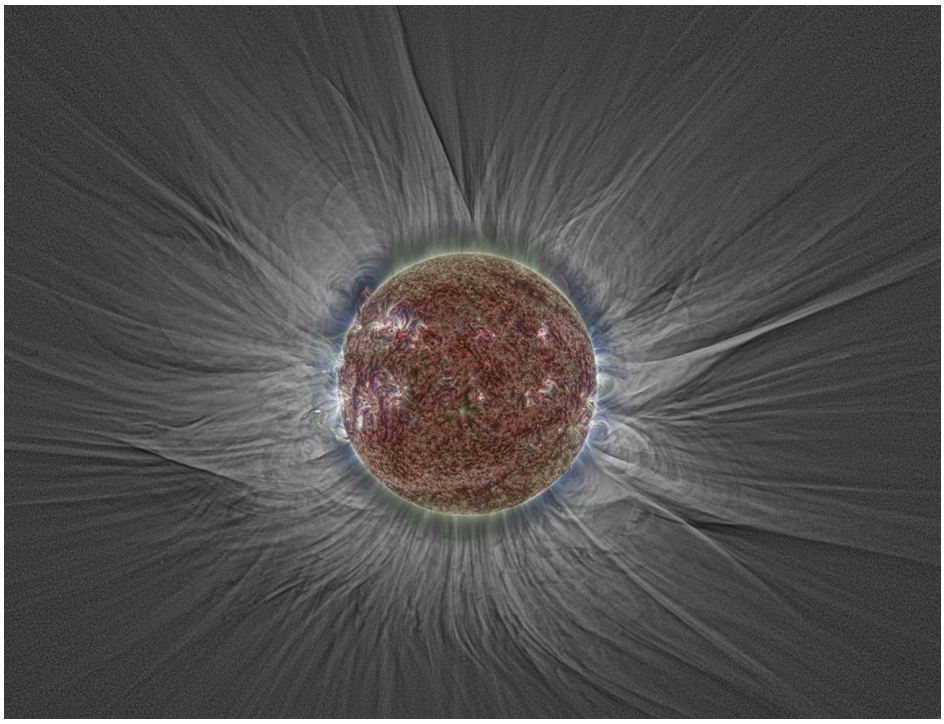

Figure 1.4: A composite image of the 20 March 2015 eclipse produced by combining the 171, 193, and 211 Å passbands of SDO/AIA with a white-light eclipse observation taken in Longyearbyen, Svalbard. The SDO/AIA and eclipse images were processed using the multiscale Gaussian normalisation (MGN: Morgan and Druckmüller, 2014) and phase correction (PC: Druckmüller, 2009) techniques, respectively, prior to combination. Taken from Yeates et al. (2018).

crease is currently an outstanding question in solar physics, although it has received much attention over recent years with the advent of new instrumentation *e.g.*, SDO (see the reviews by Klimchuk, 2006 and De Moortel and Browning, 2015). The middle-right panel of Figure 1.2 shows an image taken by SDO/AIA using a passband filter centred on 171 Å; a passband that samples the emission sourced at transition region temperatures.

1.2.4 The Corona

The corona is the region of the solar atmosphere above the transition region. Here, the temperature is on the order of 10^6 - 10^7 K, presumably as a result of the same process(es) occurring in the transition region below. Due to the extreme temperature of this region, most of the elements present have been heavily ionised resulting in a significant amount of free electrons, hence the density of the corona is best charac-

terised through the electron (n_e) population equal to approximately 10^9 cm^{-3}. The corona's high temperature and low density then slowly decreases with increasing height before transitioning into the heliosphere.

Home to the majority of the stable prominences, the *lower* corona is typically observed using full-disk, extreme ultraviolet (EUV) imagers such as AIA on board SDO. The *upper* corona has historically been observed during solar eclipses, with the moon obscuring the entire solar disk the corona can be easily observed with the naked eye[2]. Prominences observed using this method are typically either particularly elevated *e.g.*, polar crown prominences (see Chapter 2.1) or are in the process of erupting. An example observation taken of the Sun during the solar eclipse of March 2015 is shown in Figure 1.4 in which the dark disc of the moon has been replaced with a full-disk solar image from SDO/AIA.

In the presence of the coronal magnetic field, the heavily ionised elements and free electrons of the corona are bound to, and gyrate around, the field lines. Hence, the density structure of the corona is dominated by the topology of the solar magnetic field; refer to Section 1.3.1 for a description of the magnetisation of solar material. Two of the most commonly observed structures in these white-light (visible) observations of the solar corona are those of helmet streamers and coronal holes; both are demonstrated in the eclipse observation shown in Figure 1.4. The helmet streamers, shaped like the pointed-end of a teardrop, appear to reside above the brighter regions on the solar surface, referred to as active regions (see, van Driel-Gesztelyi and Green, 2015, for a comprehensive review of active regions). The bright nature of these regions is a consequence of the strong magnetic field (several hundred to a few thousand Gauss) associated with the sunspots that lie underneath in the photosphere. The evolution of such strong magnetic fields supplies a significant amount of energy to the dense material trapped within the coronal loops associated with the active region, and hence these regions appear bright in the corona (see, Reale, 2014, for a detailed review of coronal loops). Coronal holes are regions of open magnetic field *i.e.*, magnetic field that has connectivity in both the photosphere

[2]Using specialist equipment; please do not look directly at the Sun.

and the heliosphere such that the magnetic field topology appears largely radial (see, Cranmer, 2009, for a detailed description of the coronal hole phenomenon). These structures are most easily seen in the bottom portion of Figure 1.4 and upper portion of Figure 1.2e.

Unlike the previously described layers of the solar atmosphere, there is no formal upper bound to the height of the corona due to the widely varying dimensions of the structures that exist within it. At some point the corona transitions into the solar wind that travels at supersonic speeds and continues out to the edge of the heliosphere. The edge of the heliosphere, and indeed the solar system, is defined at the point where the pressure of the solar wind equals that of the interstellar medium (Treumann and Jaroschek, 2008). Although post-eruption solar prominences could presumably be measured at such distances from the Sun, this thesis is concerned with prominences at their stable, pre-eruptive state typically observed in the lower solar corona.

1.3 The Plasma of the Sun

The observed properties of the solar corona in addition to those theorised for the solar interior indicate that solar material can exist at temperatures in excess of 1 MK (*e.g.*, Grotrian, 1939; Eddy and Ise, 1979). Although such high temperatures are immediately indicative of the solar material being a plasma, there are two formal criteria for a volume of charged particles to be considered so, in addition to the following initial assumption,

> *The volume of charged particles contains sufficient electrons such that the charge of the ions may be shielded i.e., Debye spheres may be established.*

The two formal criteria are explored in the following sections along with the application to solar material.

§— **Quasi-neutrality**

Any given volume of solar material is comprised of constantly moving charged ions and electrons. Electrons, having mass $\approx$ 2000 times less than ions, travel much

faster than their relatively heavy ion counterparts. Electrons therefore form clouds around these charged ions such that the detected charge of the ion decreases by 1/e at a distance (inversely) proportional to the (density) temperature of the volume. These clouds, called Debye spheres, have a characteristic radius referred to as the Debye length, defined as,

$$\lambda_{\mathrm{D}} = \sqrt{\frac{\epsilon_0 k_{\mathrm{B}} T}{e^2 n_0}}, \tag{1.1}$$

where ϵ_0 is the permittivity of free space, k_{B} is the Boltzmann constant, T is the plasma temperature, e is the elemental charge of an electron, and n_0 is the material number density. Hence, the Debye length describes the required distance from the ion such that its charge is completely shielded by the associated electron cloud. If the characteristic length scales of the environment are larger than the Debye length of the material within the environment, the material may be considered quasi-neutral ($\nabla.E \simeq 0$). For solar material, using the values of T and n_0 from Sections 1.1 and 1.2, it is found that the Debye length ranges from $\approx 10^{-11} - 10^{-3}$ m from the solar core to the solar corona, respectively. Therefore, in prominences that have an average temperature of $\approx 10^4$ K and number density of $\approx 10^{16}$ m^{-3}, $\lambda_{\mathrm{D}} \approx 10^{-5}$ m. The physical scales required to describe solar phenomena *e.g.*, the solar core of diameter $\approx 0.5\ R_\odot$ and active regions/prominences of lengths up to $\approx 10^8$ m, are significantly larger than the corresponding Debye lengths. Hence, solar material at all locations within the solar interior/atmosphere, including prominence material, can be considered quasi-neutral.

§— **Plasma Frequency $>$ Neutral Collision Frequency**

The frequency of electrostatic electron oscillations within a plasma is given by,

$$\omega_{\mathrm{p}} = \sqrt{\frac{n_0 e^2}{\epsilon_0 m_{\mathrm{e}}}}, \tag{1.2}$$

where m_{e} is the electron mass. The neutral collision frequency is defined as,

$$\nu_{\mathrm{n}} = n_0 \sigma_{\mathrm{c}}, \tag{1.3}$$

where σ_c is the collisional cross-section, equal to πd_0^2 for simple binary collisions. If we assume that the background corona is mainly populated by neutral hydrogen with a theoretical atomic radius ($d_0/2$) of 5.3×10^{-11} m (Clementi et al., 1967), we find for the corona $\omega_{p,c} \approx 10^9$ rad s^{-1} and $\nu_{n,c} \approx 10^{-5}$ s^{-1}. For prominences, we find $\omega_{p,p} = \sqrt{10}\omega_{p,c}$ and $\nu_{n,p} = 10\nu_{n,c}$. Indeed, in the case of both the corona and prominences, $\omega_p \gg \nu_n$. Therefore, it is clear that the material of the solar corona, and that of prominences, may be considered as a plasma.

1.3.1 Prominence Plasma

Stable, pre-eruptive prominences are structures suspended within the million degree corona and comprised of relatively cool solar plasma; see Chapter 2 for a complete topological description. An immediate question is how this prominence plasma comes to be suspended above the solar surface. If the prominence plasma is supported in hydrostatic equilibrium by its intrinsic pressure then we would expect to see prominence material existing at heights up to its gravitational scale height H, expressed as,

$$H = \frac{RT}{\mu g}, \tag{1.4}$$

where R, T, and μ are the specific gas constant, temperature, and molecular mass of the plasma, respectively, and g is the acceleration due to gravity. Assuming typical values for a prominence plasma comprised primarily of hydrogen ($R_H = 8248$ J kg^{-1} K^{-1}, $T = 10^4$ K, $\mu = 1.00783$ g mol^{-1}, $g = 274$ m s^{-2}), $H \approx 300$ km which is significantly less than the heights at which prominences are typically observed ($10^4 - 10^5$ km, Démoulin, 1998). Therefore, the suspension of prominences above the solar surface to the observed heights cannot be due to pressure.

However, if prominence plasma is sufficiently magnetised, it could be supported by the Lorentz force of the coronal magnetic field; see Section 1.5 for explicit details. Plasma in the presence of a magnetic field may be considered highly magnetised if the path of the plasma is strongly influenced by the orientation of the field *i.e.*, the gyroradius r_g of the plasma must be smaller than its characteristic

length-scale (mean free path λ_{mfp} in this case). In the opposite case, where the gyroradius is greater than the mean free path length, the plasma can be considered highly collisional. The gyroradius of a plasma, defined as,

$$r_{\mathrm{g}} = \frac{m v_{\perp}}{qB}, \tag{1.5}$$

describes the distance of the gyrating ion of charge q (taken as $|e|$) from the axis of the guiding magnetic field of strength B, where m is the mass of the ion at the centre of the Debye sphere, $v_{\perp}$ is the velocity of the ion around the magnetic field *i.e.*, perpendicular to the field orientation assuming $v_{\perp} = \sqrt{\frac{3k_{\mathrm{B}}T}{m_{\mathrm{i}}}}$.

The classical expression for the collisional mean free path is $\lambda_{\mathrm{mfp}} = (\sqrt{2} n_0 \sigma_{\mathrm{c}})^{-1}$, assuming a Maxwellian distribution of particle velocities. Then, following the derivation of Chiuderi and Velli (2015), λ_{mfp} for two charged ions is given by,

$$\lambda_{\mathrm{mfp}} = \frac{\pi}{\sqrt{2} n_0} \left(\frac{6\epsilon_0 k_{\mathrm{B}} T}{Z_1 Z_2 e^2} \right)^2, \tag{1.6}$$

where Z_1 and Z_2 are the charge numbers of the respective ions (here assuming isolated protons so that $Z_1 = Z_2 = 1$).

For typical coronal values ($v \approx 10^5$ m s^{-1}, $B \approx 10^{-3}$ T, $T \approx 10^6$ K, $n_0 \approx 10^{15}$ m^{-3}), $r_{\mathrm{g,c}} \approx 10^0$ m and $\lambda_{\mathrm{mfp,c}} \approx 10^6$ m. For typical prominence values ($v \approx 10^4$ m s^{-1}, $B \approx 10^{-2}$ T, $T \approx 10^4$ K, $n_0 \approx 10^{16}$ m^{-3}), $r_{\mathrm{g,p}} \approx 10^{-2}$ m and $\lambda_{\mathrm{mfp,p}} \approx 10^1$ m. In both coronal and prominence cases $r_{\mathrm{g,(c/p)}} < \lambda_{\mathrm{mfp,(c/p)}}$, indicating that the plasma comprising the corona and prominences is highly magnetised. Hence, the global effect of magnetic fields on the stability of prominences needs to be addressed, see Section 1.5.1 for details.

1.4 The Solar Magnetic Field

When talking about the solar (coronal) magnetic field, it is important to quickly address how it is both generated and transported to the corona. Magnetic fields are generated by moving charges; in the Sun's case the entire solar interior is a ball of constantly moving charged particles (plasma, according to Section 1.3). As such,

the largest magnetic fields are generated/amplified at locations containing both large current densities and large gradients in the bulk plasma velocity; such a shear occurs at the aforementioned tachocline at a depth of $\approx 0.3\ R_{\odot}$ (recall the review by Howe, 2009). A bundle of these generated magnetic field lines tends to create an elongated region of flux that is separated by the external (unmagnetised) plasma. This is referred to as a flux tube. For a flux tube in equilibrium at the base of the convective zone, the total pressure inside the flux tube (magnetic and plasma) is equal to the total pressure outside (plasma alone), with the result that the plasma pressure is lower inside the flux tube. Assuming the flux tube is in local thermodynamic equilibrium (LTE), the less dense flux tube will rise through the decreasingly dense solar interior and expand to maintain pressure balance with its surroundings until just under the photosphere where it ceases to be buoyant but instead laterally spreads out, *i.e.*, flattens (cf. Magara, 2001).

For the majority of flux tubes generated at the tachocline, the magnetic flux (also pressure) is weak enough such that only small portions of the tube may break through the photosphere in small, isolated episodes of flux emergence (cf. Parker Instability; Parker, 1966; Cheung and Isobe, 2014). Such isolated episodes of emergence may be additionally facilitated by the convective motion of the photospheric granulation, as described by Pariat et al. (2004). For flux tubes that are particularly magnetically-dense, a large quantity of these small concentrations may merge together, manifesting themselves as pairs of circular sunspots as shown in Figure 1.2 (see *e.g.*, Rempel et al., 2009b; Leake et al., 2013, and references therein). As previously mentioned, the observational signature of dark sunspots is due to the inhibition of convection below the surface. Nevertheless, convection and associated granulation continue to occur at the sunspot periphery. Such granulation is capable of isolating small portions of the flux associated with the sunspot and migrating its footpoints away and into the quiet-Sun, resulting in the slow but persistent erosion of flux from the sunspot (cf. simulations by Rempel et al., 2009b,a). Hence, in line with observations, sunspots decrease in size after their initial emergence (see

van Driel-Gesztelyi and Green, 2015, for a comprehensive review of sunspot (active region) evolution).

As with granulation, the aforementioned migration mechanism is ubiquitous to the solar surface; the footpoints of the coronal magnetic field can be migrated great distances. Therefore, although emergence of magnetic field through the solar surface tends to be localised with respect to the total solar surface area, outwardly- and inwardly-directed magnetic fields are present across the entire solar surface (van Driel-Gesztelyi and Green, 2015). Convective motions associated with granulation are also responsible for bringing together oppositely oriented magnetic field at the solar surface, forcing the cancellation of magnetic elements and general topology changes in the coronal magnetic field (*e.g.*, Moore et al., 2001). This concept will become important in the theory of prominence formation presented in Section 2.2.

1.5 Magnetohydrodynamics (MHD)

Continuing the discussion from Section 1.3.1, it was shown that the solar coronal magnetic field is sufficiently strong to magnetise prominence plasma. However, this alone does not explain how prominence plasma remains suspended at coronal heights. To understand the balance between plasma and magnetic forces within the solar environment, and how prominences remain suspended, we must introduce the magnetohydrodynamic (MHD) equations.

Ideal MHD describes the dynamics of highly magnetised, non-relativistic plasma like that of the Sun, assuming a single-fluid approximation, using a set of closed equations,

$$\frac{\partial \rho}{\partial t} + \nabla \cdot (\rho \mathbf{v}) = 0, \qquad \text{Mass Continuity Eqn.} \qquad (1.7)$$

$$\frac{\partial p}{\partial t} + \mathbf{v} \cdot \nabla p + \gamma p \nabla \cdot \mathbf{v} = 0, \qquad \text{Energy Eqn.} \qquad (1.8)$$

$$\rho \left(\frac{\partial \mathbf{v}}{\partial t} + \mathbf{v} \cdot \nabla \mathbf{v} \right) = -\nabla p + (\mathbf{J} \times \mathbf{B}) + \mathbf{F}, \qquad \text{Momentum Eqn.} \qquad (1.9)$$

$$\frac{\partial \mathbf{B}}{\partial t} = \nabla \times (\mathbf{v} \times \mathbf{B}), \qquad \text{Induction Eqn.} \qquad (1.10)$$

where ρ, p, γ, $\mathbf{v}$, $\mathbf{J} = \nabla \times \mathbf{B}$, and $\mathbf{B}$ are the bulk fluid mass density, scalar pressure, ratio of specific heats, velocity, current density, and magnetic field, respectively. The bold font is used here, and henceforth, to indicate vector quantities of three components (x,y,z). $\mathbf{F}$ refers to any additional forces acting on the system *e.g.*, gravity. In addition, the magnetic field must satisfy the condition $\nabla \cdot \mathbf{B} = 0$.

Non-ideal MHD refers to ideal MHD with the addition of finite resistivity. As this thesis does not consider ohmic dissipation and thermal conduction *i.e.*, terms included in the non-ideal form of Eq. (1.8), we need only consider the non-ideal form of the induction equation,

$$\frac{\partial \mathbf{B}}{\partial t} = \nabla \times (\mathbf{v} \times \mathbf{B}) + \eta \nabla^2 \mathbf{B}, \tag{1.11}$$

where η is the diffusivity of the system, related to resistivity ρ_e as $\eta = \frac{\rho_e}{\mu_0}$.

1.5.1 Magnetic Support of Prominence Plasma

By evaluating the ideal MHD equations in static equilibrium we may assume the hydrostatic conditions,

$$\mathbf{v} = 0, \ \frac{\partial}{\partial t} = 0. \tag{1.12}$$

As such, and recalling Ampères law,

$$\mathbf{J} = \frac{1}{\mu_0}(\nabla \times \mathbf{B}), \tag{1.13}$$

we may rewrite the momentum equation (Eq. 1.9) as,

$$0 = -\nabla p + \frac{1}{\mu_0}(\nabla \times \mathbf{B}) \times \mathbf{B} + \mathbf{F}. \tag{1.14}$$

Then, using the vector identity $(\nabla \times \mathbf{B}) \times \mathbf{B} = (\mathbf{B} \cdot \nabla)\mathbf{B} - \frac{1}{2}\nabla(\mathbf{B} \cdot \mathbf{B})$ we find,

$$\underbrace{-\nabla\left(p + \frac{B^2}{2\mu_0}\right)}_{\text{Total Pressure}} + \underbrace{\frac{1}{\mu_0}(\mathbf{B} \cdot \nabla)\mathbf{B}}_{\text{Magnetic Tension}} = \underbrace{\mathbf{F}}_{\substack{\text{Additional Forces} \\ (e.g., \text{ gravity})}}, \tag{1.15}$$

where the first part can be considered the gradient of the total pressure (plasma + magnetic), the second part equals magnetic tension, and **F** which may include gravitational forces. Hence, this form of the MHD momentum equation for a system in hydrostatic equilibrium clearly states the balance of forces acting on prominence plasma is maintained by a combination of pressure and tension forces, and the gravitational force. However, Eq. 1.15 does not address the relative importance of each term. Instead, by introducing a characteristic length scale (λ), we find from Eq. 1.13 that the magnetic pressure gradient may be expressed as $\mathbf{J} \times \mathbf{B} \approx \frac{B^2}{2\mu_0 \lambda_B}$, and the equivalent for the thermal pressure gradient as $\nabla p \approx \frac{p}{\lambda_p}$. Taking the ratio between these quantities we find,

$$\beta = \frac{\text{Plasma Pressure}}{\text{Magnetic Pressure}} = \frac{2\mu_0 p}{B^2} \frac{\lambda_B}{\lambda_p}, \tag{1.16}$$

and results in an estimate to which force is dominating in a given region of space *i.e.*, if Plasma β (or β for short) < 1, magnetic pressure dominates over plasma pressure, and vice versa. For simplicity, the length scales of the two pressures have been assumed equal, however if they are separated by an order of magnitude then this should of course be considered. For the solar atmosphere, Gary (2001) produced the now standard 1D estimate to the height stratification of β through a strong field region such as an active region. The results from their model, along with measurements from various space-borne instruments, are shown in Figure 1.5. For the solar corona, the region of the atmosphere in which prominences are observed to exist, the value of β is shown to be significantly less than one, and so we may conclude that magnetic pressure dominates over plasma pressure in the solar corona. Although this has already been shown in Section 1.3.1, here we see that the full Lorentz force dominates the pressure-gradient force and must therefore provide the necessary force to suspend the plasma of a prominence. The magnetic tension then ensures that the plasma remains suspended, as explored by Kippenhahn and Schlüter (1957).

Ideal MHD provides a neat way of representing the global interaction between the plasma and magnetic fields of the universe. However, by definition ideal MHD

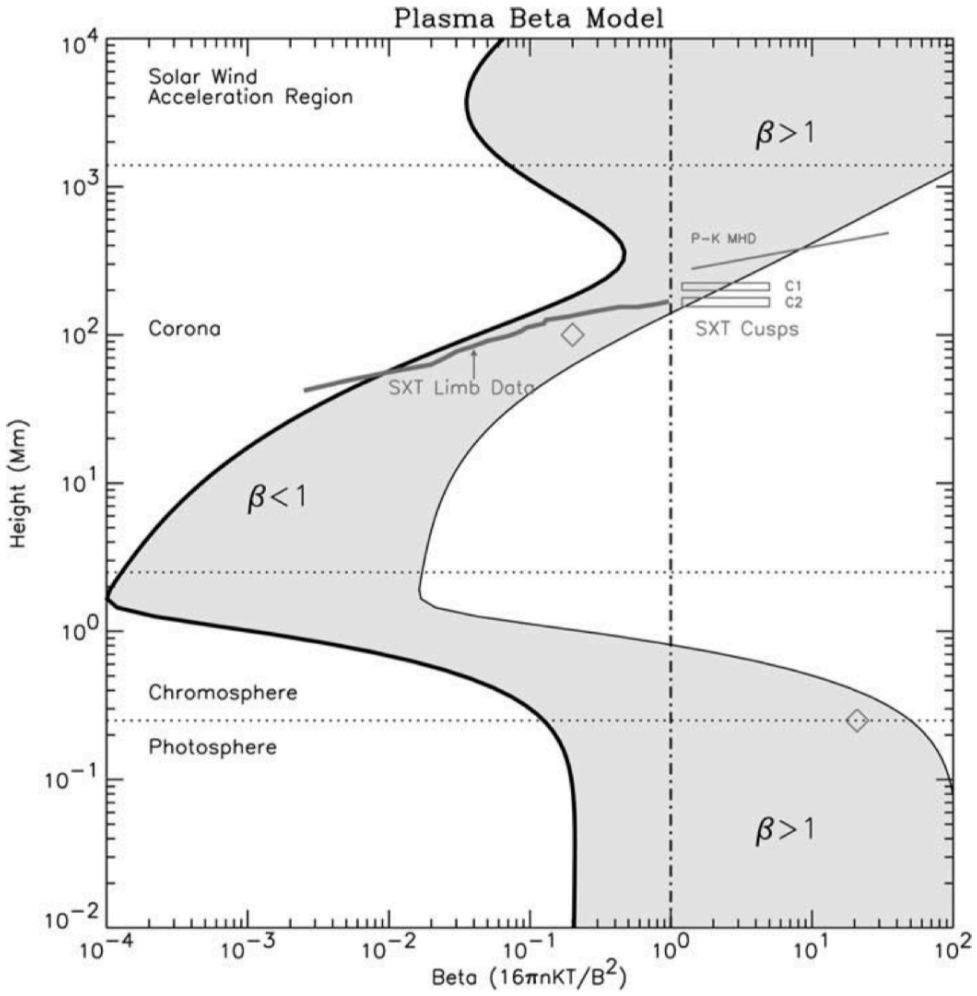

Figure 1.5: The 1D height stratification of β above a strong field region similar to an active region. β is seen to transition from > 1 in the solar interior, to $\ll 1$ in the solar corona, before returning to > 1 in the solar wind. Taken from Gary (2001).

does not take resistivity into account despite its, albeit finite, presence in reality. Hence, it is not immediately clear that the Lorentz force, although dominating in the solar corona, is capable of isolating the plasma and preventing it from diffusing into the surrounding corona. Recalling Eq. 1.11, the second part describes the diffusion of magnetic field through plasma whilst the first describes advection (induction) in the same sense. Taking the ratio of advection to diffusion, we find,

$$\mathcal{R}_{\mathrm{m}} = \frac{\text{Advection}}{\text{Diffusion}} = \frac{\nabla \times (\mathbf{v} \times \mathbf{B})}{\eta \nabla^2 \mathbf{B}} \tag{1.17}$$

where $\mathcal{R}_{\rm m}$ is the dimensionless magnetic Reynolds number. Introducing characteristic velocity v and length l scales for a given system, we find,

$$\mathcal{R}_{\rm m} \approx vl\mu_0\sigma \tag{1.18}$$

where $\sigma = \frac{1}{\mu_0\eta}$ is the conductivity of the system. For astrophysical systems, the length scales are understandably large. In combination with the corona's large conductivity, $\mathcal{R}_{\rm m} \gg 1$. Hence, magnetic fields of the solar corona are "frozen-in" to the plasma. This is also addressed in Alfvén's Theorem in which the author deduces under such conditions that plasma may travel along field lines but may not move across (perpendicularly) between them (Alfvén, 1942). For plasma to diffuse through magnetic field, $\mathcal{R}_{\rm m} =$ finite, a condition only satisfied in the corona at points of magnetic reconnection - a topic that is outside the scope of this thesis.

It has been established in the preceding sections that: stable solar prominences are collections of cool chromospheric material held in equilibrium within the solar corona by a combination of pressure (magnetic & thermal), magnetic tension, and gravitational forces; the support mechanism for this plasma is the total Lorentz force, albeit tension dominated, and the prominence plasma suspended at coronal heights is tied to the associated field lines that are providing the support. Therefore, the global appearance of prominences as clouds of material suspended above the solar surface for extended periods of time has been explained. Finer-scale details, and variations therein, are explored in the following chapter.

Chapter 2

Prominences

The first recorded observation of a solar prominence is detailed by Vyssotsky (1949) to have occured in 1185. Since the 1850's this phenomenon has received a great deal of scientific study, yet despite the collective research spanning the more than 150 years that have followed, these structures still represent a great deal of mystery and intrigue.

A comprehensive overview of our current understanding of the solar prominence phenomenon can be found in the many available textbooks and reviews on the topic (*e.g.*, Tandberg-Hanssen, 1995; Labrosse et al., 2010; Mackay et al., 2010; Vial and Engvold, 2015), while specific reviews of prominence observational characteristics and magnetic modelling can be found in Parenti (2014) and Gibson (2018). In addition, specific reviews of spectral observations and modelling can be found in Heinzel (2007) and Gunár et al. (2014). This section will highlight the relevant prominence theory required for this thesis.

2.1 General Characteristics

Although prominences are not ubiquitous solar features, such as spicules and fibrils, their tendency to form, evolve, and erupt/decay over the course of multiple solar rotations results in an increased possibility of observing one with a solar telescope at any given time. The top panel of Figure 2.1 is an image taken of the full solar disk in the H-α line by the *New Solar Telescope* (NST; Goode and Cao, 2012), now called the *Goode Solar Telescope* (GST), at the *Big Bear Solar Observatory* (BBSO), in

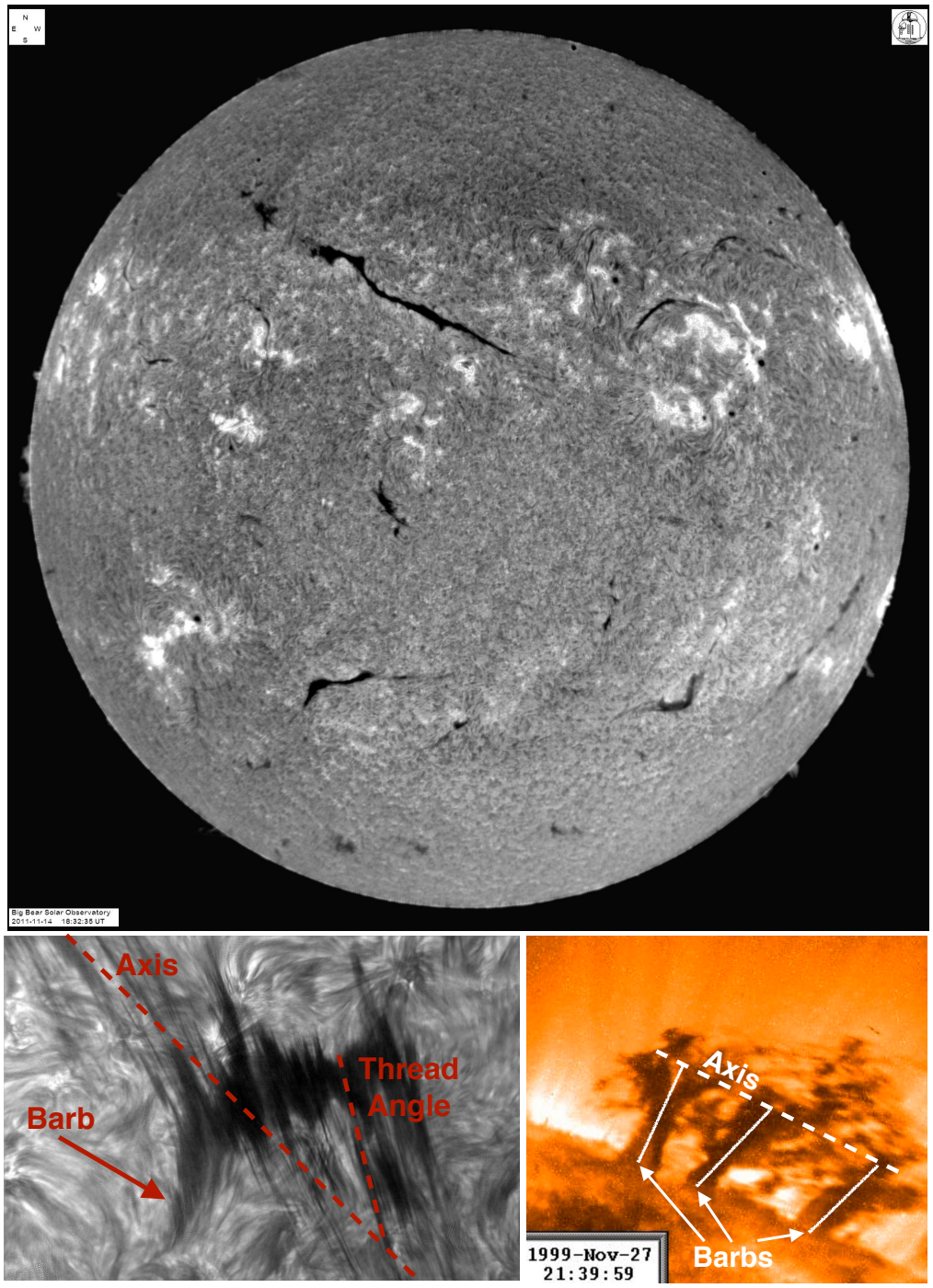

Figure 2.1: Full-disk and high-resolution images of solar prominences. The top image is of the solar disk as seen in H-α on 11 November 2011 by the New Solar Telescope (NST) at the BBSO. The bottom-left image is of a solar prominence as seen in H-α by the Swedish Solar Telescope (SST) on 22 August 2004. The bottom-right image is of a solar prominence as seen using a 171 Å filter on the TRACE spacecraft. Top panel image courtesy *www.bbso.njit.edu*. Bottom-left panel image courtesy O. Engvold at *wwwmpa.mpa-garching.mpg.de*. Bottom-right panel image adapted from Panasenco et al. (2014).

which multiple prominences both across the solar disk (the dark, elongated features) and protruding from the limb (the bright hills distorting the circumference) are shown.

Prominences are clouds of relatively cool plasma with a core temperature of the order 10^4 K (Labrosse et al., 2010; Mackay et al., 2010). At such temperatures, prominences are best observed in the spectral lines that have formation heights from the mid-chromosphere to the transition region such as, *e.g.*, Fe IX/X EUV at 171 Å, H-α optical at 6562.8 Å, and Ca II IR at 8542 Å, see Chapter 3.1 for an overviw of spectral lines . When looking top-down on the structure in H-α, the cool plasma appears dark as it absorbs and scatters the light that is incident from below out of the line of sight (LOS). When looking from the side in H-α *i.e.*, with the structure protruding above the limb, the cool plasma structure appears bright as it scatters light emitted from below into the LOS; the bottom of the structure is illuminated by the solar chromosphere below.

Observationally, prominences are typically comprised of a spine – the major axis of the elongated structure, barbs – the small extensions away from this spine that, when observed from the side, hint at some form of lower-altitude connection (see the bottom-left and bottom-right panel of Figure 2.1 and *e.g.*, Aulanier and Démoulin, 1998), and two extreme ends sometimes referred to as footpoints. The long prominence in the north-eastern quadrant of the top panel is a good example of how extended these structures can be. However, in some cases the observations suggest collections of many smaller prominences with no clear spine to relate them, *e.g.*, the bottom-left panel of Figure 2.1 showing a portion of a prominence as observed using a H-α filter at the *Swedish 1-m Solar Telescope* (SST; Scharmer et al., 2002). This can incorrectly lead an observer to the conclusion that these structures are completely separate (cf. Gunár and Mackay, 2015; Kuckein et al., 2016).

Prominences can be roughly separated into three different categories, namely active, quiescent, and intermediate, with the distinction lying in where they are found in relation to the strength of their surrounding magnetic field. Active prominences are those originating within active regions; surrounded by magnetic fields of

order $\gtrsim 10^2$ G, such prominences tend to be quite short in length (10s of Mm), close to the surface (few Mm), and have short lifetimes (hours to days). Quiescent prominences refer to those originating in the quiet-Sun; surrounded by magnetic fields of order $\sim 10^{0-1}$ G, quiescent prominences tend to be quite long in length (up to hundreds of Mm), extend to very large heights (tens of Mm, cf. polar-crown), and remain stable for up to several months (solar rotations). Intermediate prominences exist between these extremes, typically forming on the periphery of, between, or with one end rooted within active regions (Malherbe, 1989; Labrosse et al., 2010; Mackay et al., 2010; Parenti, 2014). Despite the large range of environments in which prominences are observed to exist, they are theorised to share similar if not identical formation mechanisms.

2.2 Prominence Formation

Prominences are observed to form over a period of days to weeks (as reviewed in Démoulin, 1998). They are also observed to form above polarity inversion lines (PILs), the imaginary line drawn between regions of opposite magnetic polarity on the photosphere; see Section 4.3.1 and Figure 4.3. It was therefore quickly deduced that prominences were related in some way to the magnetic field of the Sun (Babcock and Babcock, 1955). As previously discussed in Section 1.5.1, the value of β changes from being larger than one in the photosphere to much less than one in the corona (Gary, 2001). Hence, and as we have previously explored, the prominence must be supported in the corona by the magnetic field (Kippenhahn and Schlüter, 1957; Anzer, 1969).

The magnetic field of the solar corona emerges in an already-sheared state (Leka et al., 1996), *i.e.*, the magnetic field contains currents and therefore energy above potential - its lowest possible energy state. The granulation of the photosphere then proceeds to constantly buffet and migrate the footpoints of these emerged magnetic loops. This process, in addition to the differential rotation, naturally creates highly-sheared regions of opposite polarity, delineated by this imaginary PIL. Following the work of Kippenhahn and Schlüter (1957), authors such as

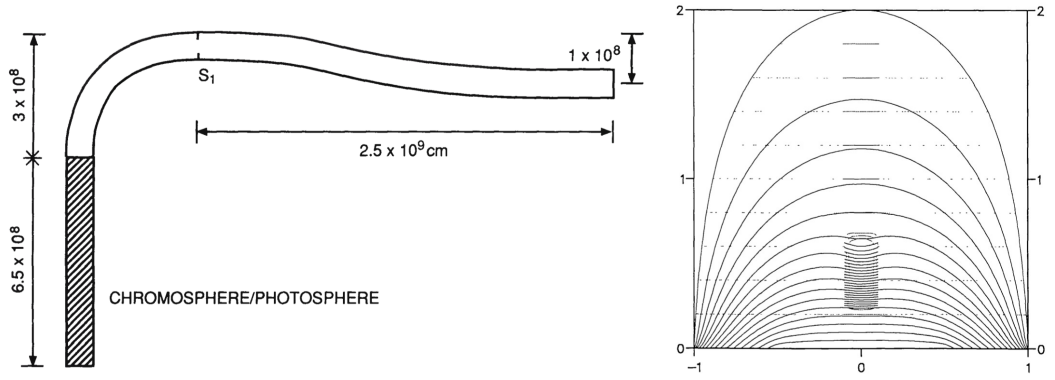

Figure 2.2: Sheared arcade models for prominence formation. *Left*; The initial topology of the half magnetic flux tube rooted in the chromosphere/photosphere and containing a pre-existing magnetic dip, used in the numerical simulation of Antiochos and Klimchuk (1991). *Right*; Results of a numerical simulation by Fiedler and Hood (1992) in which the magnetic field topology has been modified by plasma. Such dips are formed at the apex of the loops due to the condensation of material that was first evaporated from the chromosphere through the thermal instability.

Oran et al. (1982), Klimchuk et al. (1987), Antiochos and Klimchuk (1991), Fiedler and Hood (1992), and Fiedler and Hood (1993) established that magnetic topologies of a sheared loop with a (pre-) existing dip could be filled with plasma as summarised in Figure 2.2. An ensemble of these sheared field lines may then resemble the elongated structures observed as prominences. van Ballegooijen and Martens (1989) proposed an additional step whereby helical field is formed in which topological dips need not be preset, but are instead inherent; see Figure 2.3. Collections of these helical fields along the PIL produce a rope-like structure of magnetic field, or rather a *magnetic flux rope* (see also *e.g.*, Titov and Démoulin, 1999; Amari et al., 2003). Exact topology aside, as rigorously explored by authors such as Kippenhahn and Schlüter (1957) and Anzer (1969), the required property of the magnetic field is dips that are capable of suspending chromospheric material. In addition, Démoulin (1998) noted that, according to observations, prominences form on the order of days and weeks whereas heavy plasma is capable of deforming the topology of magnetic field lines on the order of hours. Hence, observations suggest that the prominence's formation process is magnetically driven rather than a response and deformation of field topology due to the weight of the plasma.

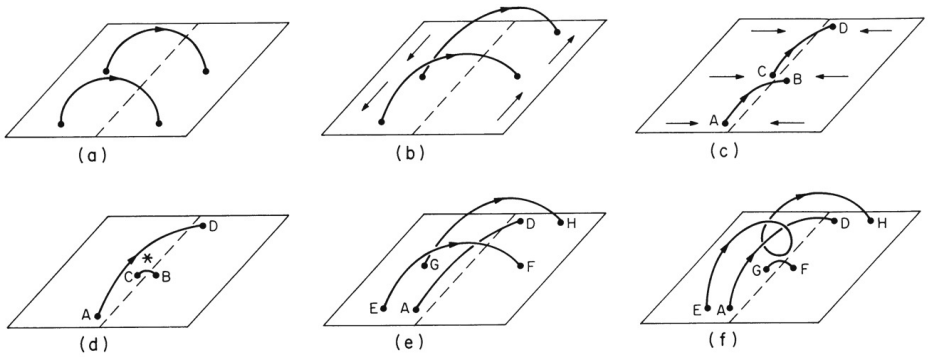

Figure 2.3: Cartoon model of flux rope formation by van Ballegooijen and Martens (1989). *Panel a*; Regions of positive and negative polarity (indicated by the orientation of the field loops) separated by the imaginary polarity inversion line. *Panels (b & c)*; The ongoing shearing and converging process supplied by the photospheric granulation and differential rotation that brings field lines together for reconnection (d). Continuation of such processes produces flux rope (f), here the prominence material naturally collects in the inherent magnetic dips of the topology.

So, if prominences form in regions of magnetic field that have the pre-existing topology capable of holding chromospheric plasma, the next question is of course how does the chromospheric plasma come to reside at coronal heights? It has long been understood that the material supply cannot come from a coronal condensation processes. For example, Saito and Tandberg-Hanssen (1973) discussed and compared the relative masses of an observed prominence with the mass of the total corona, highlighting that the solar corona simply does not contain enough mass. If the plasma cannot come from above then the plasma source has to be from below, from the chromosphere.

The three main processes that have been proposed to explain the material supply of prominences are injection, levitation, and evaporation/condensation. A comprehensive description of these processes are offered in Mackay et al. (2010) and so only an overview is presented here; see Figure 2.4. The injection model (*e.g.*, Wang, 1999; Chae, 2003) describes plasma that is propelled to coronal heights due to some form of reconnection event in close proximity to the footpoints of the prominence magnetic field (top-left of Figure 2.4). The injected material then collects in the dips of the magnetic field. The levitation mechanism (*e.g.*, van Ballegooijen and Martens, 1989; Litvinenko and Wheatland, 2005) refers to plasma trapped on field

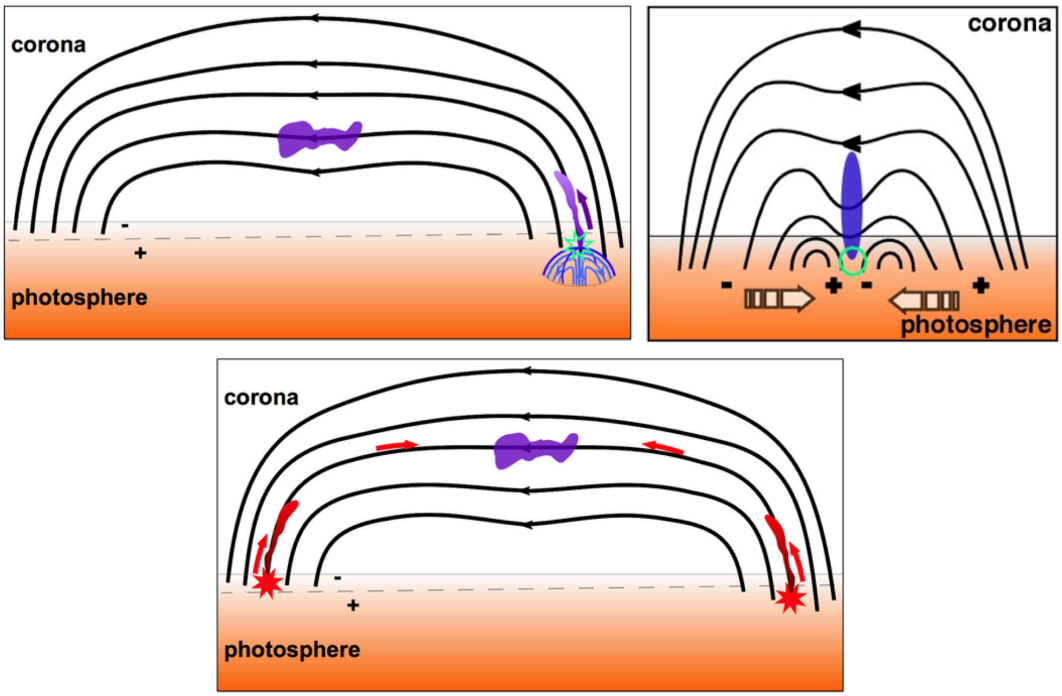

Figure 2.4: Cartoons representing the three main supply mechanisms for prominence material. *Top-left*; the injection mechanism. *Top-right*; the levitation mechanism. *Bottom*; The thermal instability mechanism. Figure adapted from Mackay et al. (2010)

lines that have recently reconnected in the chromosphere and been lifted to coronal heights (top-right of Figure 2.4). As shown in the figure, this mechanism requires a velocity component within the photosphere to force the low-altitude reconnection although as previously mentioned, the ubiquitous process of convection could supply this. The evaporation/condensation mechanism (*e.g.*, Field, 1965; Xia et al., 2012) describes the occurrence of sudden heating at the footpoint(s) of the prominence magnetic field. This sudden heating causes the plasma to expand and travel up the field to coronal heights where it catastrophically cools back to chromospheric temperatures in the dips of the magnetic field (bottom of Figure 2.4, see also the reviews by Klimchuk (2019) and Antolin (2019), private communication). All of these mechanisms successfully describe how the plasma of a prominence can be supplied to the dips of the related magnetic field. However, the ability for the levitation model to successfully liberate plasma from the chromosphere, a domain where β can be greater than one, is unclear and requires more attention; see Chapter 7 for more information.

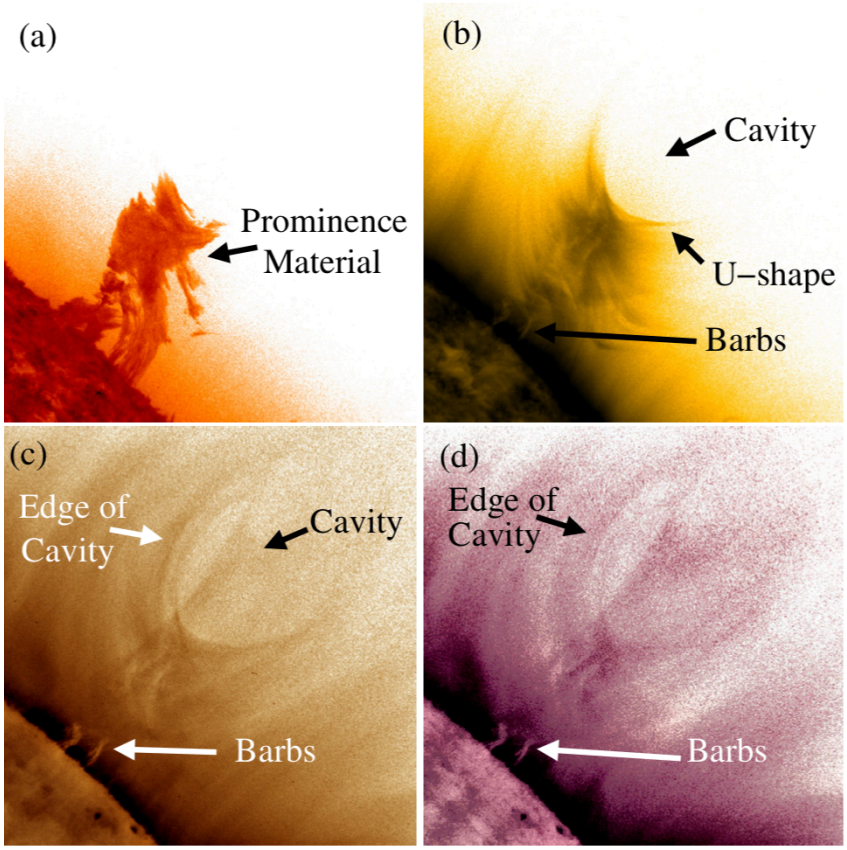

Figure 2.5: A prominence cavity as viewed in EUV by SDO/AIA with a reverse colour table. *Panel a*; 304 Å. *Panel b*; 171 Å. *Panel c*; 193 Å. *Panel d*; 211 Å. Image taken from Régnier et al. (2011).

Importantly, the end result of all of these proposed formation mechanisms is the suspension of chromospheric plasma at coronal heights courtesy of the magnetic field topology. Although the models for the exact magnetic field topology *i.e.*, sheared field (twist $<$ one full turn) vs. magnetic flux rope (twist $>$ one full turn) compete to explain observations with almost equal representation, the magnetic flux rope interpretation is supported significantly by observations of coronal cavities (*e.g.*, Gibson et al., 2006; Gibson and Fan, 2006; Forland et al., 2013; Gibson, 2018). As shown in Figure 2.5, the lack of emission from plasma within coronal cavities appears to outline a circular region with the cool plasma (panel a) residing in the underside (panel b). Recall that the corona is a $\beta < 1$ domain and as such the density structure is largely defined by the coronal field. Hence, this particular observation is interpreted by Régnier et al. (2011) as the LOS becoming closely

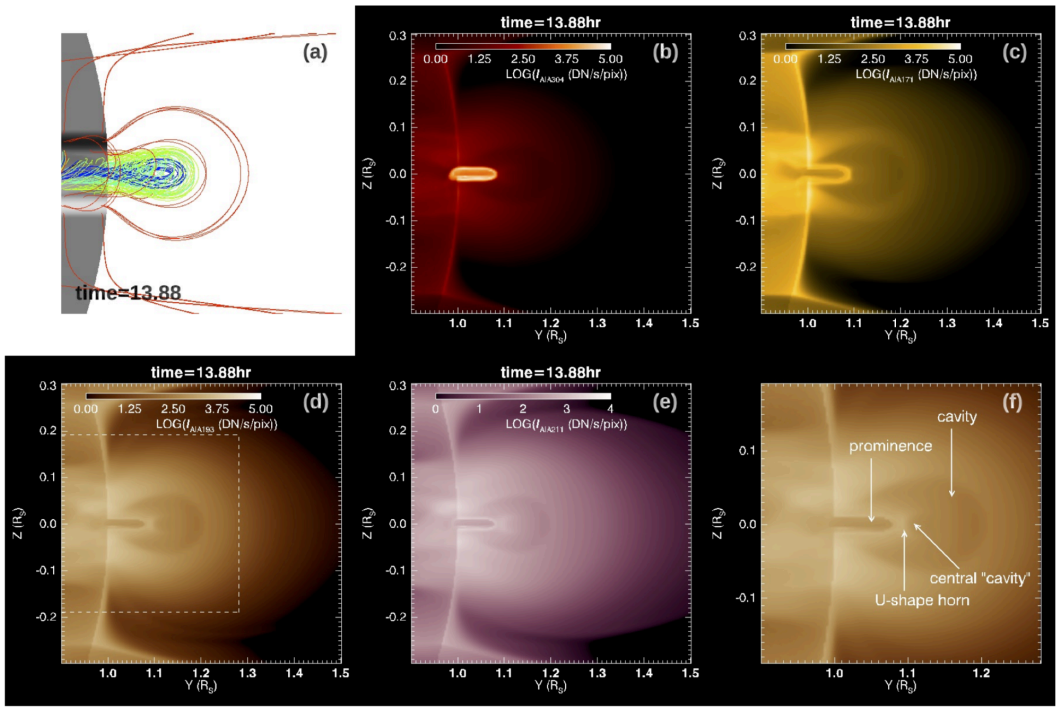

Figure 2.6: Synthetic multi-wavelength observations of a prominence embedded within a coronal cavity. *Panel a*; The magnetic flux rope model viewed along its axis. *Panels b, c, d, e*; The model shown in (a) but synthesised as would be viewed in the 304, 171, 193, and 211 Å passbands of AIA, respectively. Key features of the synthesis are labelled in (f). Figure taken from Fan and Liu (2019).

aligned with the axis of the flux rope such that the circular shape in EUV observations represents the integrated cross-section of the flux rope (as was initially argued by Gibson et al., 2006). The cool plasma residing in the underside of this cross-section then corresponds to the prominence material collecting in the dips of the flux rope topology. This has also been well argued by, in particular but certainly not exclusively, Fan and Liu (2019) in which the authors use their simulation of a flux rope in the solar atmosphere to generate synthetic observations in four of the AIA passbands; shown here in Figure 2.6. Similar results have also been shown by authors such as Xia and Keppens (2016) and Fan (2017, 2018). The strength of the cavity – flux rope assumption is particularly well highlighted by comparing such synthetic observations to the *real* observations of Régnier et al. (2011) in Figure 2.5.

Physical Parameter	Labrosse et al. (2010) & Mackay et al. (2010)	Leroy and Priest (1989) & Engvold et al. (1990)
$T(K)$	4300 – 10000	$\leq$ 200,000
$V_{\rm mt}$ (km s^{-1})	N/A	3 – 20
$n_{\rm e}$ (cm^{-3})	$10^9 - 10^{11}$	$10^9 - 10^{11}$
P (dyn cm^{-2})	$\approx$ 0.02 – 1	$\approx$ 0.02 – 1
$N(H^+)/N(H^0)$	N/A	0.2 – 0.9
V (km s^{-1})	$\approx$ 5	$\leq$ 70
B-Strength (G)	3 – 15	20 – 80
B-Azimuth (°)	40	20 – 30

Table 2.1: Typically observed prominence core plasma and magnetic field properties, where T is the temperature, $V_{\rm mt}$ is the microturbulent velocity, $n_{\rm e}$ is the electron density, P is the gas pressure, $N(H^+)/N(H^0)$ is the ratio of hydrogen ionisation, V is the bulk flow velocity, B-Strength is the magnitude of the field suspending the plasma, and B-Azimuth is the acute angle the field vectors make with the prominence long-axis. N/A indicates values that have not been updated. Information taken from Labrosse et al. (2010) and Mackay et al. (2010).

2.3 Stable Prominence Properties

After a prominence initially forms, it enters a somewhat *stable* period in which there is limited/slow evolution in terms of height. This is most obvious for quiescent prominences that can exist in this stable state for up to several solar rotations. It is this portion of a prominence's life cycle that has received the most attention as in the absence of significant flows or magnetic activity, their spectral lines are most easily interpreted. The typically observed properties of the plasma and magnetic field of solar prominences have been discussed in detail in Labrosse et al. (2010) and Mackay et al. (2010). Their summary of results from Engvold et al. (1990) are summarised as part of Table 2.1 alongside updated results from more recent studies.

The *stable* behaviour of prominences in this period of their existence is due to the slow evolution of their host magnetic field. The properties of the host magnetic field are derived by studying the Zeeman and Hanle effects (López Ariste and Casini, 2002) on the polarisation of light originating in prominences (*e.g.*, Leroy and Priest, 1989; Heinzel et al., 2005; Asensio Ramos et al., 2008, and explained in more detail in Section 3.1.1.1). Sunspots, the regions of the solar photosphere that

have been penetrated by particularly strong magnetic field, exhibit particularly large splittings in their observed spectral lines. Conversely, due to the weak nature of the magnetic fields involved, at least in comparison with those of sunspots, the degree of Zeeman splitting observed in prominences is extremely small. Fortunately, the Hanle effect is more sensitive to weak magnetic field than the Zeeman effect and is therefore a more suited method for diagnosing prominence plasma. Although unable to directly polarise light, the Hanlé effect is able to affect light that has already been polarised by the Zeeman effect (see Section 3.1.1.1 for more details). As a result, the orientation of the magnetic field in prominences is known to be approximately horizontal to the surface in the middle of prominences (*e.g.*, Casini et al., 2003; Levens et al., 2016a,b, 2017), consistent with the theory that the plasma is suspended in magnetic dips (*e.g.*, Leroy and Priest, 1989). Prominence B-field magnitude and azimuth measurements are summarised in Table 2.1.

Despite having the ability to measure the orientation of a prominence's magnetic field, in addition to the assumption that plasma resides in the dips of this magnetic field, the exact internal plasma structure of solar prominences remains not well understood. Before the advent of high-resolution observations, prominences were often described as cloud-like monolithic structures (*e.g.*, Pettit, 1943; Schmieder et al., 1984). As a result, early theoretical attempts to model prominences assumed a cloud/slab-like topology with a thickness of a few thousand kilometres (*e.g.*, Beckers, 1964; Mein et al., 1996; Heinzel et al., 1999). Modern observations have suggested that prominences can be better described as collections of individual threads, believed to have a width of order of a flux tube *i.e.*, 100 – 150 km (Lin et al., 2005). Although now in agreement with the theoretical picture of a prominence provided by the magnetic field measurements, current observations still suffer from the inability to fully resolve the plasma at these scales as single pixels sample on the order of 70 $\times$ 70 km (see the top-left and right panels of Figure 2.7). This is complicated by the fact that the threads are not necessarily a stationary feature but rather they can be displaced in position by hundreds of kilometres on the order of minutes. Gunár et al. (2008) reduced this to a static case and treated a theoretical prominence

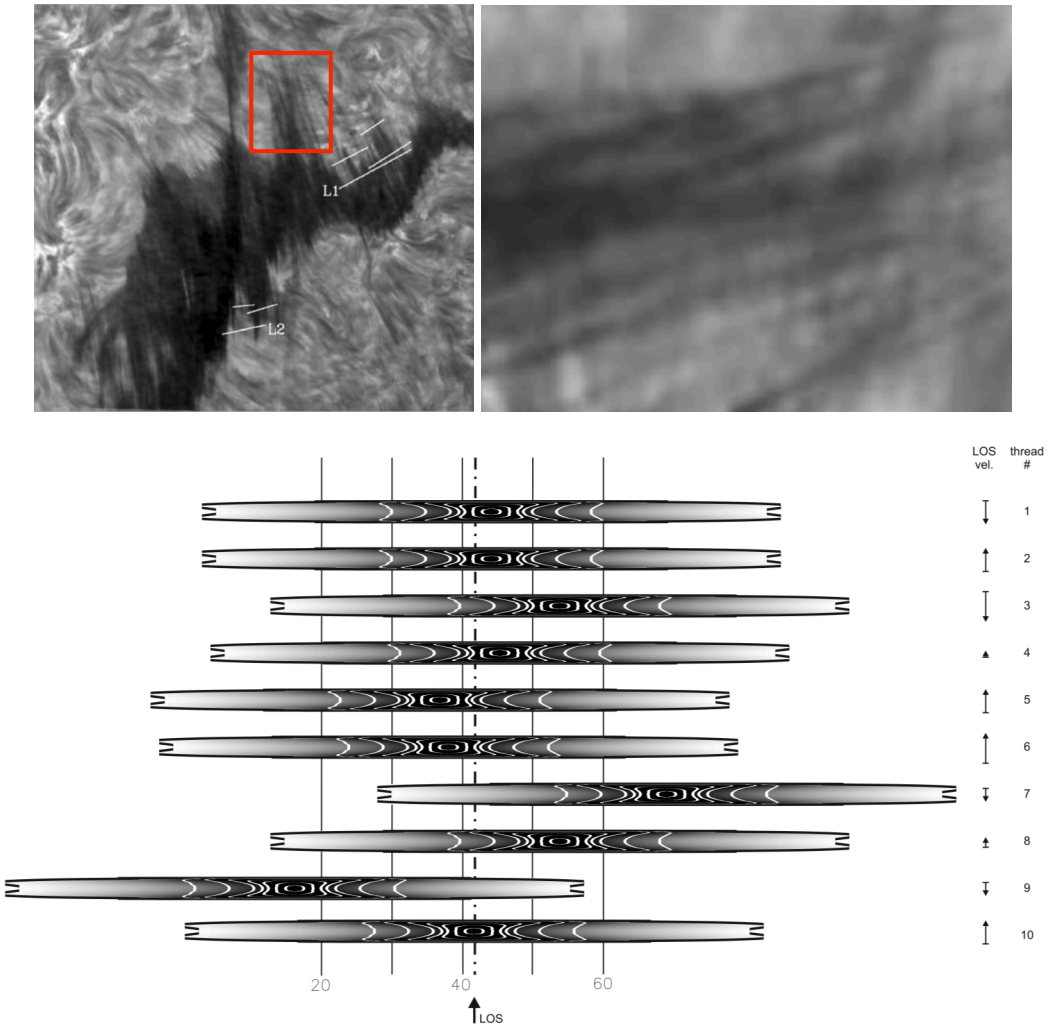

Figure 2.7: The thin and numerous threads of solar prominences. *Top-left*; An observation of a prominence showing the thin, thread-like nature of a prominence as seen from above, taken by Lin et al. (2005) on 26 August 2003. *Top-right*; a zoom in and 90° rotation of the red box of (a) showing a portion of the prominence where the threads are particularly well isolated. *Bottom*; The set-up of the multi-thread model of Gunár et al. (2008). The observed signal along the LOS is then the superposition of 10 identical threads (w.r.t internal density structure cf. contours within each thread) that are displaced in the plane-of-sky and are assigned a LOS velocity with a random magnitude and direction as indicated on the right of the panel.

as a bunch of 10 unresolved threads with varying contributions to the LOS; see the bottom panel of Figure 2.7. The authors showed that even by removing the dynamic nature while maintaining a corresponding but random (instantaneous) velocity, the number and position of the threads along the LOS plays an equally important role in the shape of the observed spectral line. Hence, the varying superposition of many threads along the LOS, perhaps up to several dozen (*e.g.*, Wiik et al., 1993, 1999), makes this an interesting observational challenge.

The temperature of the plasma within prominences appears to remain fairly stable in spite of this extended period of existence within the MK solar corona. The exact reason for this remains an outstanding question in solar prominence research. However, this unusual behaviour is thought to be related to the formation of a so-called *prominence-corona-transition-region* (PCTR) around the prominence, shown by *e.g.*, Gunár et al. (2007) to most likely be a sheath that envelopes the individual threads of a prominence (Vial et al., 2012). This PCTR is believed to mimic the behaviour of the transition region of the solar atmosphere in some way, albeit much thinner, whereby the number density transitions from $10^8 - 10^6$ cm^{-3}, and temperature increases from $10^4 - 10^6$ K from the inner to outer edge (Labrosse et al., 2010).

Prominences (both active and quiescent) frequently display large-scale/counter-streaming/buoyant flows and oscillations (*e.g.*, Lin et al., 2003; Luna and Karpen, 2012; Hillier, 2018). The distinction between the active and quiescent dynamics is then in the amplitude/magnitude of their associated dynamics. Due to their scale, quiescent prominences that experience some form of large perturbation *e.g.,* a nearby eruption, tend to display dynamics that have larger spatial amplitudes and smaller velocity magnitudes as they are comprised of weaker magnetic field (supplying a weaker restoring force to any form of perturbation experienced). In contrast, active prominences tend to display larger velocity magnitudes and smaller spatial amplitudes as both the free energy available to drive perturbations and the magnetic field strength (damping) is proportionally larger (see, Labrosse et al., 2010; Mackay et al., 2010, and references therein).

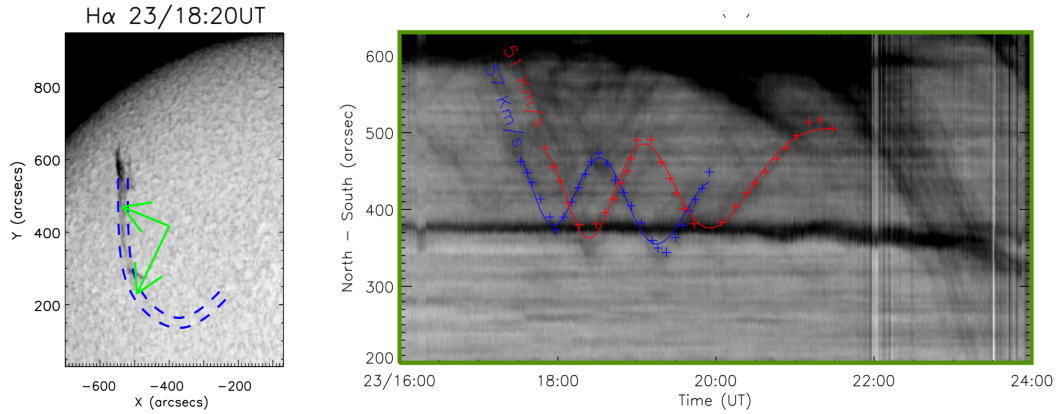

Figure 2.8: An example of a large-scale flow within a prominence, as observed by Bi et al. (2014). *Left*; The prominence as observed by GONG on 23 February 2012. *Right*; the variation in pixel intensity along the track bound between the dashed-blue lines in the left panel. The large-scale flow of material is indicated here as the dark streaks extending from $\approx 600-200$ arcsec. The oscillations of the plasma observed prior to the large-scale flow are indicated by the blue and red, fitted crosses.

Large-scale flows within prominences are typically identified as any significantly correlated and long-lived motions of prominence plasma (*e.g.*, Deng et al., 2002; Seaton et al., 2011; Bi et al., 2014, see Figure 2.8). Counter-streaming flows are frequently observed within prominences and are interpreted as either the general flowing of plasma along multiple independent threads and superimposed over each other (*e.g.*, Ahn et al., 2010; Diercke et al., 2018), or an ongoing plasma-supply process that may be realised on more-vertically-aligned field lines as Doppler motions (*e.g.*, Zirker et al., 1998; Litvinenko and Martin, 1999; Wang, 1999, see Figure 2.9). However, these Doppler signatures have also been interpreted as buoyant flows driven by, for example, the Rayleigh-Taylor instability (RTI) (*e.g.*, Berger et al., 2011; Hillier, 2018), or small-scale oscillations of the host magnetic field (cf. Lin et al., 2007). The potentially ambiguous nature of prominence dynamics signatures lies in our current inability to resolve down to the finest scales required[1], as was previously described to be the case for general prominence structure. Large-scale oscillations of prominences are somewhat easier to distinguish as they are observed as large-scale coherent variations in Doppler velocity. These motions are

[1]The upcoming Daniel K. Inouye Solar Telescope (DKIST) will have the ability to resolve down to a few tens of kms and should be invaluable in addressing these degenerate observations

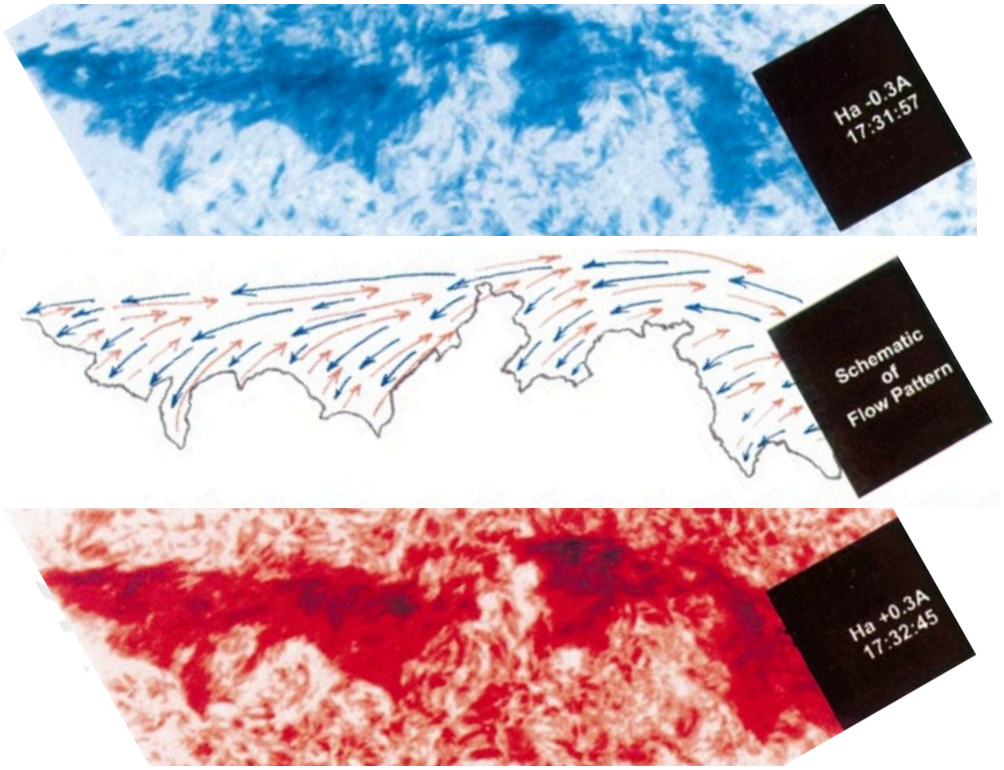

Figure 2.9: An example of counter-streaming flows within a prominence, as observed by Zirker et al. (1998) on 16 April 1993. *Upper panel*; the observations of the prominence in the blue wing (-0.3 Å) of H-α. *Lower panel*; the observations of the prominence in the red wing (+0.3 Å) of H-α. *Middle panel*; what the authors refer to as the"schematic of flow pattern" as a result of both blue- and red-shifted motions recorded co-spatially.

interpreted as being caused by variations in the position of the magnetic field supporting the plasma in response to, *e.g.*, a nearby flare or eruption (*e.g.*, Ramsey and Smith, 1966; Jing et al., 2003).

Prominences do not remain in a stable state indefinitely. The formation processes covered in Section 2.2 do not cease after the appearance of the prominence material above the surface. The continuation of these processes can result in a growth and/or a change in the shape of a prominence over an extended period of time. For example, Kuckein et al. (2016) reported on an observation of a prominence approximately $817''$ in length as shown in panel a of Figure 2.1. Prominences of such dimensions can take a long time to form by extension of one or both ends, or are the result of a combination of multiple prominences that are a part of the same filament channel or PIL. Such a structure with significant extent must incorporate and encounter a wide range of magnetic flux and plasma density across its length.

As the Sun is a dynamic body, it is perhaps unsurprising that such a delicate balance can be lost suddenly, and in some cases very violently.

2.4 Prominence Global Evolution and Destabilisation

As will be further explored in Chapter 5 of this thesis, the magnetostatic stability of a solar prominence can be reduced to an equilibrium of three primary forces. The upward *hoop* force supplied by the flux rope itself, the downward forces of magnetic tension supplied by the background and overlying coronal field, and gravity acting on the prominence plasma itself (for more information, see Figure 5.1). The evolution of this system can then occur when one or more of these forces begins to dominate over the others. For the majority of a prominence's existence, this process occurs slowly and can be represented as a migration of equilibrium conditions through a series of neighbouring quasi-equilibria *i.e.*, evolution happens slower than the information transport time. However, the *complete* destabilisation of the system can occur upon *complete* loss-of-equilibrium *i.e.*, the system may begin to feed back into itself resulting in an evolution that is both sudden and accelerating. The multiple varieties of prominence evolution/eruption are discussed in this section.

2.4.1 Upward (Hoop) Force

The upward-directed force of a flux rope is a result of its curvature, whereby the magnetic pressure acting on its minor radius is greater than the magnetic pressure acting on its major radius. This is well represented graphically in Figure 2.10, in which a flux rope is presented as a slinky toy although in reality a flux rope is a combination of many slinky toys whereby each slinky represents a single field line of a flux rope. Nevertheless, the magnetic pressure is well demonstrated as the difference in separation between the inner and outer portions of the same flux surface. The more flux involved in a flux rope, the greater this inner pressure would be. Therefore, in order to increase the upward force of a flux rope, either additional

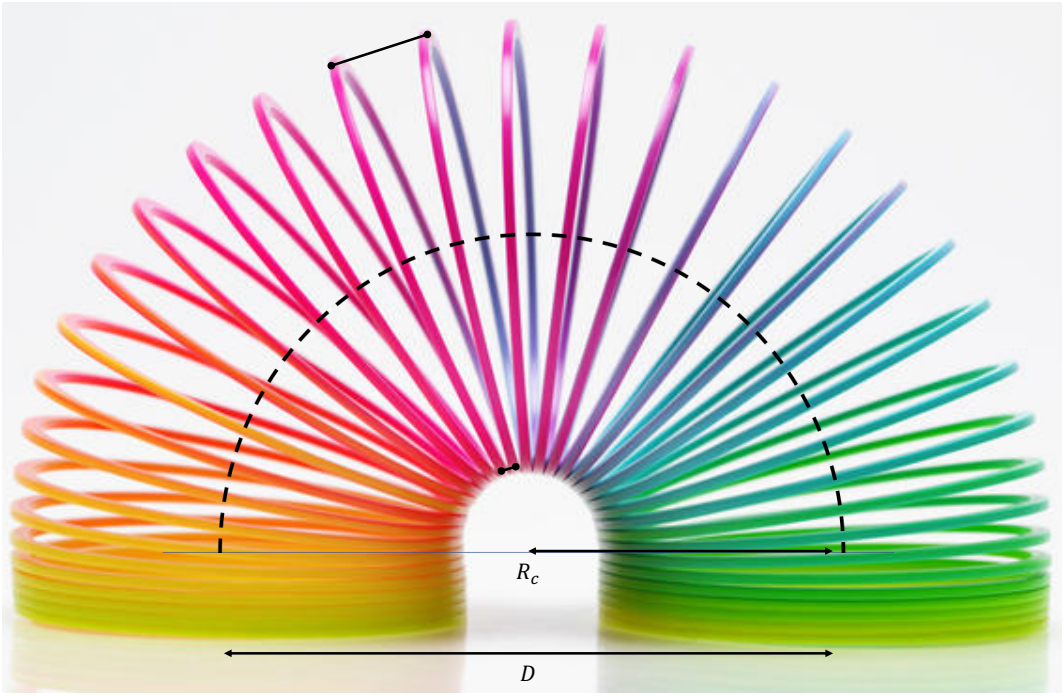

Figure 2.10: A simple flux rope (slinky) diagram with the solar surface at the bottom of the image. The flux rope is represented as a slinky with a radius of curvature of R_c and a footpoint separation D. The axis of the flux rope is indicated by the dashed black line. The two lines drawn at the edges of the flux rope (top and middle of figure) demonstrate how the magnetic pressure is greater underneath the flux rope than above. Background image courtesy *www.nbcphiladelphia.com*

flux has to be injected into the flux rope or the number of turns in the magnetic field per unit length (twist) along the axis of a flux rope has to be increased.

An increase in the twist of a flux rope can occur by introducing more flux into the system per unit length through *e.g.*, reconnection between field internal to a flux rope and highly-sheared external field. An increase in twist may also be achieved by rotating the footpoints of a flux rope through some form of photospheric motion *i.e.*, like twisting a piece of string at its ends (cf. sunspot rotation, Brown et al., 2003). Török and Kliem (2003) noted that if the field lines comprising a flux rope have, on average, greater than 1.75 turns from end-to-end then the system will become unstable to an ideal kink instability. In comparing theory to observations, Török and Kliem (2005) suggested that as helicity (a measure of total twist within a volume, Scheeler et al., 2017) is conserved, the kink instability transfers twist into writhe, resulting in the increase in the height of the flux rope's axis (a theory later

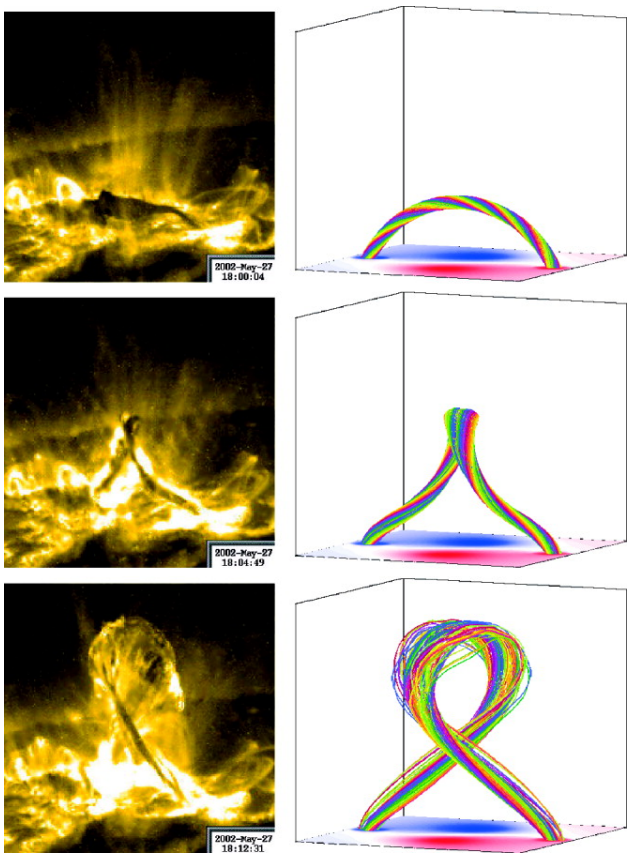

Figure 2.11: Comparison between the observations of Jing et al. (2003) (left) and the simulations of Török and Kliem (2005) (right), showing the evolution (top – bottom) of a flux rope and associated prominence as a result of the host flux rope becoming kink-unstable. Image from Török and Kliem (2005).

confirmed by Török et al., 2010). Although described as an instability, as explored by Török and Kliem (2005) the initiation of the kink instability does not guarantee the ejection/eruption of an associated flux rope (+ prominence). As a result, this instability differs from the aforementioned complete loss-of-equilibrium. When a flux rope is subject to the kink-instability an equilibrium state may be regained if, at the cessation of the height increase, the gradient in the magnitude of the background field is too shallow. In other words, the background field at the height of a flux rope post-kinking, may be too strong and the rate of the decay of this field magnitude too slow. This results in the flux rope remaining restrained so that the kink instability has simply served to increase the height and change the topology of a flux rope. This height increase and associated writhing typically acts over the course of

minutes – hours, significantly increasing the inclination of the prominence hosting field over this short period of time. As a result, the field suspending the prominence material will suddenly have a much larger component of gravity acting along its length. Hence, such a failed/confined eruption often results in the unloading of the prominence material from a flux rope if one was initially present, as was observed by Jing et al. (2003); see Figure 2.11.

Alternatively, if additional flux is instead added into a flux rope through a process such as that proposed by van Ballegooijen and Martens (1989), the magnetic pressure (and therefore upward force) of the flux rope would increase without, necessarily, the corresponding increase in twist. If the downward-directed forces do not increase to the same degree then a flux rope would rise through the solar atmosphere until a new equilibrium is found. In the absence of any additional, potentially more dynamic, phenomena, this transition through neighbouring quasi-equilibria is believed to be the primary mechanism responsible for prominence evolution, as evidenced by their typically slow increase in height over time (see also the review by Parenti, 2014).

Independent of any specifically assumed solar magnetic model (*e.g.*, (non) potential, bipolar/quadrupolar, etc.), the magnitude of the background coronal field decreases with height. At some point, the gradient in the magnitude of the restraining field with height, referred to as the decay index, will be such that any further increase in a flux rope's magnetic pressure can no longer be counteracted by the restraining field. A flux rope rising through this threshold would experience an increase in its internal (minor-radius) pressure whilst simultaneously encountering an increasingly weak restraining field; the resulting acceleration would be *runaway*. At this point, referred to as the *critical* decay index, such a flux rope is catastrophically unstable leading to a complete loss-of-equilibrium *i.e.*, the flux rope would be ejected into space carrying the prominence with it. A flux rope that encounters such an instability is referred to as being *torus unstable*.

Kliem and Török (2006) studied this torus instability criterion and established that for a perfectly toroidal, thin flux rope to experience loss-of-equilibrium, the

decay index n of the background potential field, defined by Bateman (1978) as,

$$n = -\frac{h}{B(h)}\frac{\delta B(h)}{\delta h}, \tag{2.1}$$

where $B(h)$ is a given model for the background field, and h is the height of the flux rope's axis, must be $n > 3/2$ to first order. For a perfectly straight, thin flux rope believed to be indicative of a long quiescent prominence, the critical decay index was established to be $n = 1$ (Démoulin and Aulanier, 2010).

It was previously stated that the kink instability is not a necessary cause of a solar eruption *i.e.*, it *triggers* the initiation of an eruption that may then be *driven* by the torus instability under suitable conditions (Török and Kliem, 2005; Kliem and Török, 2006; Aulanier et al., 2010; Green et al., 2018). However, it is important to quickly note that some recent works have started to question the assumption that the initiation of an eruption due to the torus instability is a foregone conclusion, *i.e.*, that if a flux rope becomes *torus-unstable* it is guaranteed to erupt successfully (*e.g.*, Myers et al., 2015; Amari et al., 2018). Specifically, these authors have pointed out that if the restraining field is treated correctly (by using a (non-potential) background field that contains currents, see Myers et al. (2015) for explicit details) it may inhibit the successful eruption of a torus-unstable flux rope by directly removing flux during the eruption. Flux ropes that experience a kink and/or torus instability but are unsuccessful in leaving the solar atmosphere are typically referred to as either "confined" or "failed" (see Zhou et al., 2019, and references therein).

2.4.2 Downward Magnetic Force

The downward-directed magnetic force acting on a flux rope is supplied by the tension of the surrounding background field of the corona. As explored in the previous section, prominences are observed to slowly rise through the solar corona, a dynamic that can be facilitated by the slow increase in the hoop force of the host flux rope. Furthermore, this slow evolution may also be facilitated by a weakening in the strength of the overlying field, realised as an increase in the distance between the footpoints of the overlying field. As was the assumption for the model of van

Ballegooijen and Martens (1989), granulation is capable of migrating the footpoints of magnetic arcades. Hence, if the footpoints of the overlying field are systematically migrated away from each other, the magnitude of the magnetic tension force acting downwards will decrease. However, as the motion of footpoints due to the buffeting by granulation tends to be towards PILs rather than away, it is unlikely that such a mechanism alone could separate the footpoints of the overlying arcade to a non-negligible degree.

Granulation is essentially the emergence of plasma from below the photosphere that bubbles up and spreads laterally, pushing the field as it goes (recall that the field is frozen into the plasma in the photosphere where $\beta > 1$). Consider, instead, the emergence of magnetic field through the solar photosphere that can occur on granular to supergranular scales (e.g., Feynman and Martin, 1995; Moreno-Insertis et al., 2018). Magnetic flux emergence is a result of bundles of flux tubes rising through the interior, breaching the photosphere, and expanding into the corona (recall Section 1.4 and see the recent review by Cheung and Isobe, 2014).

Newly emerged flux may interact with the already-present magnetic field of the corona, in 2D the resulting dynamics then depend explicitly on the relative orientations. The four main positions and 2D orientations of small-scale emerging flux relative to a pre-existing flux rope and associated overlying/background field are shown in column (i) of Figure 2.12. Rows (a) & (b) represent external emergence (outside of the field overlying the flux rope), whereas (c) & (d) represent internal emergence. The photosphere and chromosphere are represented as the horizontal black and grey lines, respectively. The flux rope and corresponding prominence are presented as the series of solid-red concentric rings and a dark-blue ellipse, respectively. The overlying/background field are represented as the set of three solid-black arcades overlying the flux rope. In each case (a-d), the emergence is represented by the separate set of solid-black arcades to the right of the flux rope. The orientation of the magnetic arcades are indicated by their polarities (+/-) noted at their footpoints. Columns (i-iii) then represent the evolution of each configuration in time,

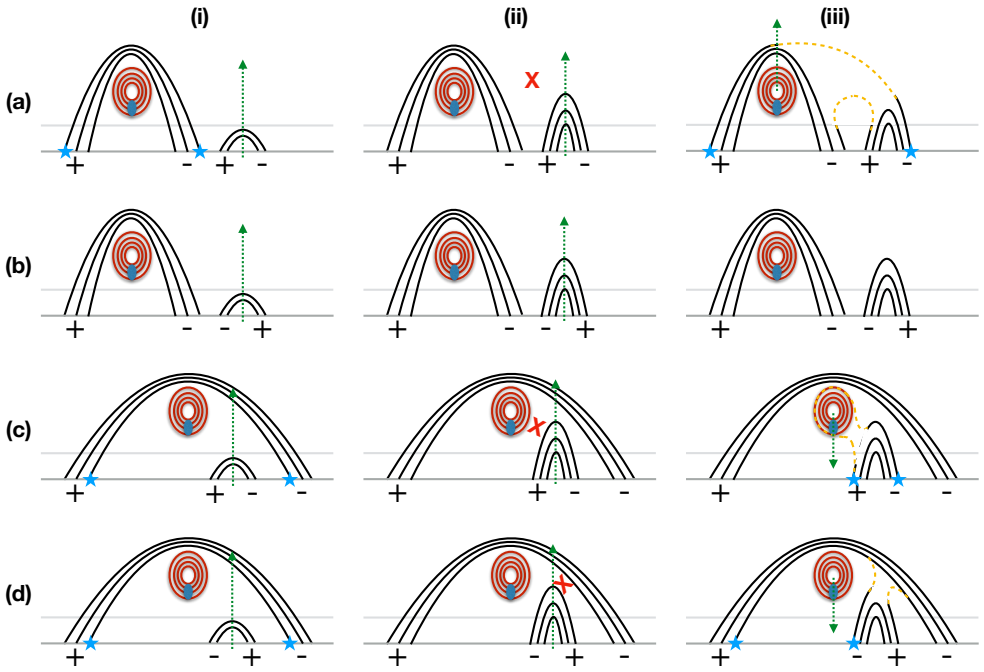

Figure 2.12: The possible combinations (a-d) of 2D interactions between newly emerging flux and a pre-existing flux rope & overlying field. Rows (a) & (b) represent external emergence, (c) & (d) represent internal emergence. Photosphere and chromosphere are represented as the horizontal black and grey lines, respectively. Flux rope & prominence are represented as the set of red concentric rings with a blue ellipse at the bottom, respectively. Background & overlying field represented as the set of three solid-black arcades arching over the flux rope. Emerging flux occurs in each case to the right of the flux rope, also indicated by solid-black arcades. Photospheric polarities of overlying and emerging fields are indicated at their footpoints (+/-). Columns (i-iii) represent evolution in time, from (i) to (iii). The dashed-green arrows in (i) and (ii) represent the direction of emergence of new flux. The red cross represents the x point for reconnection between oppositely oriented field. The dashed-yellow lines represent the new topology after reconnection at x point. The blue stars in (i) and (iii) are for illustrative purposes only, indicating in each case whether the footpoint separation has increased or decreased during the emergence and reconnection. The dashed-green arrows in (iii) indicate the direction that the axis of the flux rope migrates as a result of each configuration.

from (i) to (iii). The dashed-green arrows in (i) and (ii) represent the direction of emergence of new flux. The red cross represents the approximate position of the x point for reconnection between oppositely oriented field. The dashed-yellow lines represent the new topology as a result of the 2D reconnection at the indicated x point. The blue stars in (i) and (iii) are for illustrative purposes only, indicating in each case (a-d) whether the footpoint separation has increased or decreased during the emergence and reconnection.

Configuration (a) results in a decrease in the magnitude of the field overlying a flux rope and associated prominence, (b) results in no interaction between the emergence and pre-existing field, (c) results in an interaction between the emergence and the flux rope itself, increasing the tension force acting on the flux rope, similarly so for (d) but as a consequence of an interaction with the overlying field.

The interactions summarised in Figure 2.12 are presented in 2D, yet they remain, nonetheless, largely valid when formulated in 3D. Reconnection outside of the flux rope–prominence–background field system can result in a reduction in the magnitude of the background field if the orientation of the emerged bipole is favourable for reconnection with the overlying field. If the orientation is not exactly-favourable *i.e.*, slightly misaligned as would be expected in a 3D system, there may still be a component of the magnetic field, associated with the bipole and/or overlying field, that *would* be favourable for reconnection (interchange reconnection; Cheung and Isobe, 2014). Hence, if a small bipole emerges outside, but close by, the field overlying a flux rope–prominence system, it is likely that the magnitude of the overlying magnetic tension would be reduced (potentially leading to an eruption, *e.g.*, Dacie et al., 2018). If a small bipole emerges underneath, it is likely that a flux rope–prominence system would experience an increase in the tension force of the background field (cf. Kusano et al., 2012).

The result of these interactions between newly emerged flux and the flux rope–prominence–background field system is that the axis of the flux rope moves depending on the restructuring of the background field. For each case (a-d) in Figure 2.12, the resulting evolution of the flux rope axis is shown in column (iii) by the dashed-

green arrows. If the magnitude of the tension force decreases then the flux rope axis increases in height to a degree directly proportional to the decrease in the flux density of the restraining overlying field. As previously stated, such an evolution is typically observed as the slow increase in the height of a prominence. The same is true for the opposite evolution in the tension force, although such an evolution in prominence height - towards lower heights - is yet to be observed. This is likely due to either the observed dynamics being dominated by a combination of processes that result in the increase of the height of the flux rope–prominence, or our current observational capabilities being insufficient to record and/or correlate an increase in the overlying tension force and the decrease in prominence height. This is further complicated by the dynamic nature of the prominence plasma and the problems differentiating between local and global plasma motions - coupled further with the possibility that these motions are themselves influencing the behaviour of the host magnetic field.

2.4.3 Downward Gravitational Forces

Early observations of solar filaments noted that their eruption was frequently preceded by the disappearance of the on-disk absorption signature; the so-called 'disparition brusques' (*e.g.*, Olivieri, 1948). As early observations were subject to lengthy times between exposures, it occurred to observers that the sudden lack of an absorption signature between frames could be caused by the complete evacuation of filament mass. The sudden reduction in gravitational forces acting on a magnetic structure that had built up a sufficient amount of free energy would then expand towards a more potential state, believed at the time to be manifested as an eruption (*e.g.*, Hyder, 1967). Kuperus and Raadu (1974) explored this interpretation theoretically and concluded that the sudden eruption of filaments *could* be explained by the complete removal of all mass. However, such observations were taken using a single narrowband filter centred on the core of the H-α absorption line. Therefore, as a filament erupts with a velocity component towards the observer the spectral line will blueshift out of the narrow filter, resulting in the filament seeming to disappear. Although the 'disparition brusques' could now be explained, the theory that the re-

moval of mass was capable of causing an eruption was maintained. For example, over three decades later authors such as Low (1996), and the review by Klimchuk (2001), continued to explore the 'mass-loading' theory, maintaining it as a possible mechanism for the eruption of prominences.

Around the same time however, Forbes (2000) studied the energy budget of solar eruptions and noted that the energy density of the solar magnetic field was several orders of magnitude higher than gravity. This work, in addition to the plasma-β study of Gary (2001), led the solar physics community to the assumption that the corona, and the evolution/eruption of structures therein, could be largely described by the properties of the magnetic field alone. If the influence of plasma on the magnetic field is assumed to be largely negligible, the system can then be reduced to one where the Lorentz force dominates the coronal equilibrium; such a condition is typically referred to as the low-β approximation (*e.g.*, Ruan et al., 2008). More commonly, the effect of plasma is actually completely neglected (*e.g.*, zero-β; Titov and Démoulin, 1999) and from Section 1.5.1 we find that this leads to the Lorentz force $\mathbf{J} \times \mathbf{B} = 0$, referred to as the *force-free* approximation. Under this assumption, the criteria for (in)stability of coronal flux ropes in the absence of mass has since been explored in great detail (*e.g.*, Török and Kliem, 2003, 2005; Kliem and Török, 2006; Fan and Gibson, 2007; Démoulin and Aulanier, 2010; Kliem et al., 2014, also Section 2.4.1).

Despite the general assumption of "force-free" flux ropes, several authors have explored the possibility and validity of prominences that contain plasma with non-zero plasma β. In the absence of suitable observations, such studies are typically isolated to theoretical endeavours (*e.g.*, Anzer and Heinzel, 1998; Heinzel and Anzer, 1999; Gunár and Mackay, 2015). To date, Hillier et al. (2012a) is the only study that attempts to deduce the values of plasma β through observations. Using the behaviour of prominence plumes, the authors measure β values of between $0.47 \pm 0.079 - 1.13 \pm 0.08$. Perhaps unsurprisingly, these values are significantly higher than those ascribed to the corona by Gary (2001), and subsequently used in the numerical models of flux rope evolution/eruption. However, it is important to

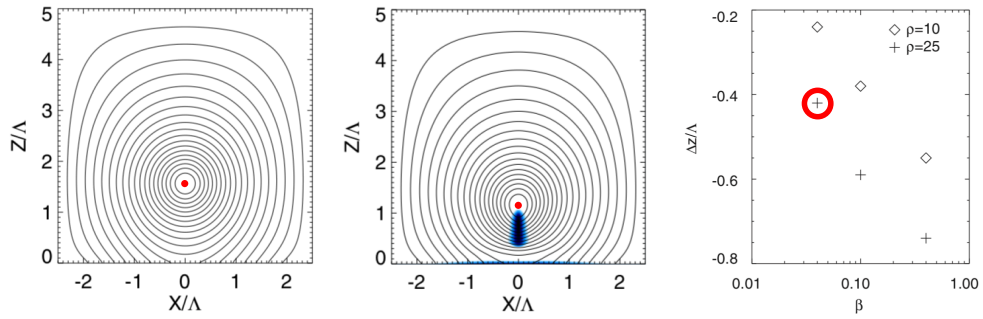

Figure 2.13: The decrease in equilibrium height of a flux rope as a result of including mass. *Left*; Contours of magnetic field strength in an x-z plane, modelling a magnetic flux rope in equilibrium. Approximate position of the flux rope axis/o-point indicated by the red dot. *Middle*; The same flux rope now containing prominence material with the density and forced plasma-β values circled in the right panel ($\rho' = 25$, $\beta = 0.04$). *Right*; The change in height of the o-point of the flux rope as a result of the inclusion of the range of mass densities and plasma-β indicated in the top-right. Figure adapted from Hillier and van Ballegooijen (2013).

highlight that in both of the works carried out by Forbes (2000) and Gary (2001) the underlying assumption was that conditions within the corona and above active regions are representative of the entire Sun. Active region magnetic fields are significantly stronger, by several orders of magnitude, than the field found in the quiet-Sun; although the force-free assumption may hold for such active conditions, the direct applicability to the quiet-Sun is non-trivial. Then, assuming that the mass of active region and quiet-Sun prominences are equal, the balance of magnetic vs. gravitational forces may be equally non-trivial when considering quiescent prominences.

To further explore this theoretically, Petrie et al. (2007) and Blokland and Keppens (2011) presented a 2D magnetohydrostatic (MHS) model in which they quantified the effect of gravity, realised as a small perturbation to the magnetically-dominated equilibrium, on the height of the axis of a modelled flux rope. Termed the *Shafranov shift*, the authors showed that as gravity is increased the axis of a flux rope would be increasingly pulled to lower altitudes. A similar result was later presented by Hillier and van Ballegooijen (2013), however the authors instead removed the limiting assumption that gravity was merely a small perturbation imparting a

negligible effect on the equilibrium. Hence, Hillier and van Ballegooijen (2013) noted some inconsistencies between the Shafranov shift of Blokland and Keppens (2011) and the shift in the flux rope axis measured using their more relaxed numerical approach. The specific conditions explored by the authors are summarised in Figure 2.13. Furthermore, considering the highest density and strongest magnetic field (lowest β) case circled in the right panel ($\rho' = 25$, $\beta = 0.04$, where $\rho_{\text{prominence}} = \rho' \rho_{\text{corona}}$), this yielded a change in height of $\approx 0.4H$. Although not explicitly stated in their work, for their 1 MK corona (setting the gravitational scale height H at 55 Mm) this equates to an $\approx 30\%$ shift in the axis' height from the initial mass-less equilibrium.

Although Petrie et al. (2007), Blokland and Keppens (2011), and Hillier and van Ballegooijen (2013) have each shown that the hydrostatic equilibrium of a mass-less flux rope can be perturbed by the inclusion of mass, each study notes that their formulation does not permit the study of the effect of mass on the stability of the system. Indeed, this can be well understood by noting that the typically used metric for stability, the decay index (Eq. 2.1), is mass-independent.

2.5 Thesis Outline

For several decades, it has been assumed that the magnetic forces acting on a solar flux rope are the primary forces responsible for their (in)stability. However, recent work has begun to suggest that this assumption is limited and the mass of a prominence, or more specifically the additional force due to gravity, can impart an effect on the equilibrium conditions of a flux rope. This interpretation raises several explicit questions,

1. Can the effect of gravity on prominence eruptions be inferred/deduced observationally?

2. Can the effect of gravity on the *stability* of a prominence be explored theoretically?

3. What do state-of-the-art models tell us about the internal structuring of this mass and its ability to impart a non-negligible force on small-scales?

It is these questions that this thesis aims to explore.

An overview of the instruments used to obtain the observations used in this thesis, in addition to the standard processing methods, is presented in Chapter 3. Question 1 is tackled in Chapter 4 through a dual-spacecraft case study of a prominence eruption that occurred on 11 December 2011. Here opacity – density estimation methods are used to deduce the evolution in total prominence mass. Question 2 is addressed in Chapter 5 by constructing a simple model of minimum equilibrium, and evaluating stability criteria following the formulation outlined by Démoulin and Aulanier (2010). Chapter 6 then explores Question 3 using observations from a ground-based campaign carried out in May 2017, specifically through a combination of inferred plasma/magnetic parameters and reconstructed thermal profiles. Chapter 7 closes with the main conclusions of this thesis, and remarks on the possible future work to be carried out following such conclusions.

Chapter 3

Observing the Sun

In the modern world, solar physicists have a plethora of observatories available to study the Sun for extended periods of time. Historically, observations of the Sun have been carried out using ground-based instrumentation/observatories. However, observations at EUV and shorter wavelengths, corresponding to emission from the transition region and coronal layers of the Sun, are absorbed by the Earth's atmosphere and are therefore only observable using space-based instrumentation. Since the advent of the space era, more and more instrumentation is being flown in space but such missions suffer from many operational limitations such as, cost, technical limits (weight, size, telemetry data rate), and (since the loss of the Solar Maximum Mission - SMM) fixed instrumentation (no repairs, replacements, or upgrades). Although ground-based instrumentation/observatories do not necessarily suffer the same limitations, space-based observatories also have many operational benefits in addition to the wavelength range such as, continuous observations, no image distortion induced by atmospheric turbulence, and more-stable pointing (no wind). Despite the inherent benefits and drawbacks of both space- and ground-based instrumentation, neither are capable of completely replacing the other and indeed, both offer the other complementary data sets.

With multiple space- and ground-based observatories in operation, each having a different goal in mind to guide their design, solar physicists are becoming ever more able to describe and connect the phenomena observed on and below the surface, to their effect on the upper atmosphere, and each layer in between. To

achieve this, observations of a wide range of diagnostics are utilised including narrowband/broadband intensity images, dopplergrams, magnetograms, etc.

This chapter includes a general description of the formation of spectral lines with a focus on the solar atmosphere, specifically solar prominences. The chapter then continues by detailing the instrumentation used in this thesis with an overview presented of each instrument, their technical specifications, pipeline processing, and observations and diagnostics. The chapter then ends with a comparative summary of these instruments.

3.1 Spectral Lines

3.1.1 Formation

The emission of radiation is generally due to the energy exchange between an electron and a photon. This electron is described as 'bound' if bound to an atom and 'free' if not. Hence, if an interaction is described as bound-bound, the electron was bound to an atom prior to the interaction with a photon and remains bound after. This is similarly true for free-free emission and any variations therein.

Considering, for a moment, bound-bound emission, recall from elementary atomic physics that the energies of electrons bound to an atom are given by discrete energy levels. Therefore, any variation in the energy of the electrons within these bound states will absorb/emit photons of discrete energies following the relation,

$$E = \frac{hc}{\lambda}, \tag{3.1}$$

where E is the amount of energy involved in the transition, h is the Planck constant, c is the speed of light, and λ is the wavelength of the emitted/absorbed photon. If an electron within an atom was to spontaneously de-excite/relax then the energy of the emitted photon must be exactly that of the energy lost by the associated electron *i.e.*, the emitted light is of a discrete wavelength.

Bound-free, free-bound, and free-free interactions, however, do not adhere to such discrete energy limitations and so the related emission/absorption pro-

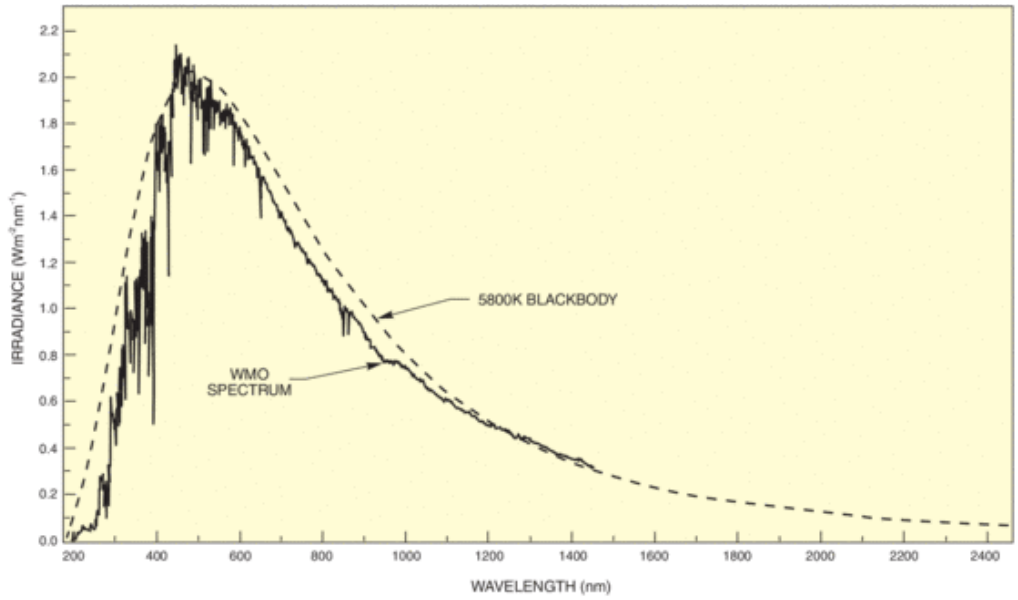

Figure 3.1: The comparison between the 200 – 2500 nm (2000 – 25,000 Å) solar spectrum, as measured by the World Meteorological Organisation[1](WMO), and theoretical emission of a blackbody at 5800 K. Image courtesy *www.newport.com*

cesses can produce associated photons of essentially *any* energy (*e.g.*, thermal bremsstrahlung). The resulting spectrum is therefore not discrete, but instead continuous. Indeed, the majority of light emitted from the Sun is in the form of a continuous spectrum of light; sourced from the solar photosphere this continuous spectrum is referred to as the solar continuum. Planck discovered that the exact shape of this continuum *i.e.*, the intensity of emission B_λ vs. wavelength λ, is dependent on the (effective) surface temperature of the emitting source. If assumed to be in LTE, the relationship is given by,

$$B_\lambda \propto \lambda^{-5}\left[\exp\left(\frac{hc}{\lambda k_B T}\right)-1\right]^{-1}, \tag{3.2}$$

where T is the effective temperature of the emitting source. Figure 3.1 details the theoretical blackbody curve of Eq. 3.2 assuming $T = 5800$ K in comparison with the WMO-measured, disk-integrated[2] solar spectrum between 2000 and 25,000 Å.

[1] https://public.wmo.int/en

[2] Although we are able to resolve individual structures across the solar disk, we are also capable of combining the intensity of photons at a single wavelength measured across the full-disk into a single value *i.e.*, treating the Sun as a point source - like a star.

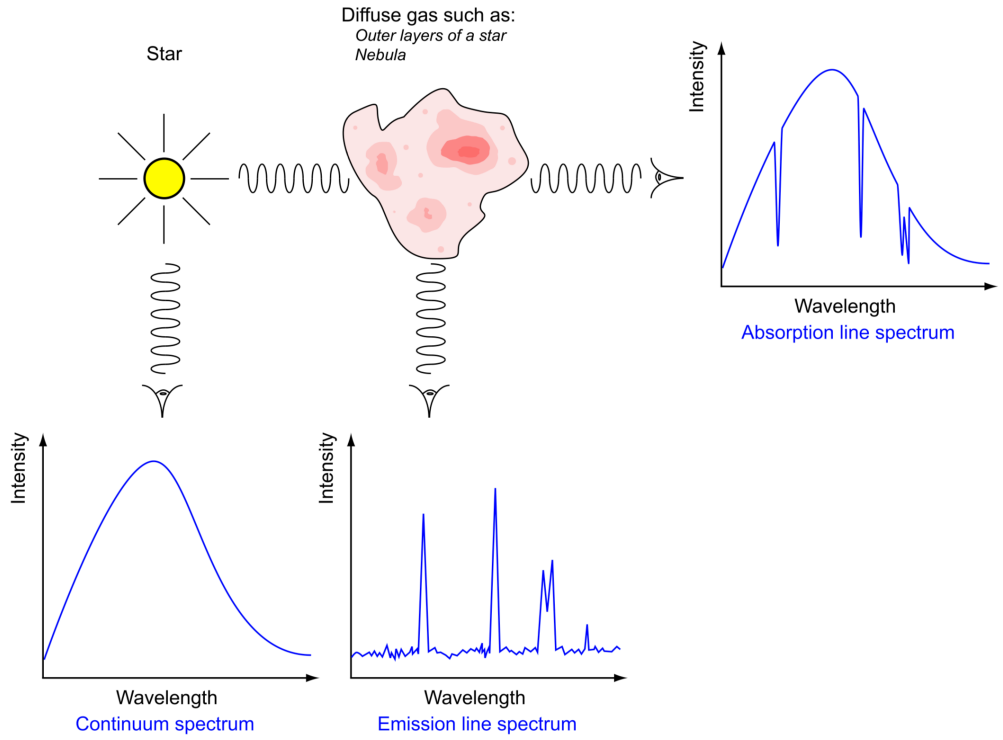

Figure 3.2: A cartoon depicting the relationship between the continuum, emission, and absorption spectrum of stellar objects. *Continuum spectrum*; the result of free-free emission within the solar photosphere. *Absorption spectrum*; the result of a cloud of gas, between source and observer, absorbing photons at wavelengths dependent on the constituents of the gas cloud (elements & ionisations therein); absorption spectrum are the continuum spectrum minus intensity at specific wavelengths. *Emission spectrum*; emission of photons at wavelengths corresponding to the gas cloud constituents; the example above demonstrates how absorption and emission spectra may contain similar information that differs depending on the LOS. Image courtesy *www.astro.su.se*

Although it is known that the photosphere is not in true LTE (*i.e.*, $\mathrm{MAX}(T_{\mathrm{Phot}}(h)) \neq \mathrm{MIN}(T_{\mathrm{Phot}}(h))$, where $T_{\mathrm{Phot}}(h)$ is the temperature stratification of the photosphere with height) this alone does not account for the variation between the theoretical blackbody and the actual measured radiation curve that can be clearly seen in Figure 3.1. If the observed variations in intensity cannot be ascribed to the source alone, they must instead be caused by the medium between the source and the observer *i.e.*, the solar atmosphere.

Unlike the photosphere, the electron density of the solar atmosphere is too tenuous to be completely dominated by free-free processes. Instead, bound-bound processes dominate due to the abundance of photons at all wavelengths incident

from the photosphere below. Hence, and as summarised in Figure 3.2, observations through the solar atmosphere with the backdrop of the solar surface will produce an absorption spectrum based on the constituents (elements + ionisations therein) of the solar atmosphere. If observed in an isolated manner, such as above the limb, then the solar atmosphere emits at the exact wavelengths where absorption signatures are seen in the absorption spectrum. However, the intensity of this emission spectrum will always be significantly weaker than the corresponding absorption spectrum as the re-emission process, in response to the initial absorption, can emit in any given direction.

Note that, as previously stated, the absorption and/or emission of photons covered by the bound-bound process produces absorption/emission signatures at discrete wavelengths corresponding to the discrete energy levels of any given atom. Therefore, one would expect to detect these discrete wavelengths as Dirac δ-functions at wavelengths corresponding to the energy levels within the materials that comprise the solar atmosphere. However, due to the quantum uncertainty principle the exact energy of the emission cannot be known. Furthermore, and indeed more noticeably, when considering a system that is not static, the random thermal motion of the absorbing/emitting atoms introduce random Doppler shifts to the emitted/absorbed light. From the central limit theorem we find that the sum of these processes is a Gaussian *i.e.*, 1D projection of a Maxwellian distribution, hence the thermal motion of particles acts to broaden these δ-functions into Gaussians. The exact thermal width $\Delta\lambda_{\text{th}}$ of these spectral lines is then dependent on the temperature T, rest wavelength λ_0, and mass m of the source material according to the relation,

$$\Delta\lambda_{\text{th}} = \frac{\lambda_0}{c}\sqrt{\frac{2k_{\text{B}}T}{m}}. \tag{3.3}$$

Additional broadening can occur due to non-thermal motions (turbulence, waves) and instrumental broadening (filters have finite widths, this is discussed later in this section). For conceptual purposes we may assume the plasma is thin and so re-absorption processes are negligible. This allows us to refer to the Gaussian ab-

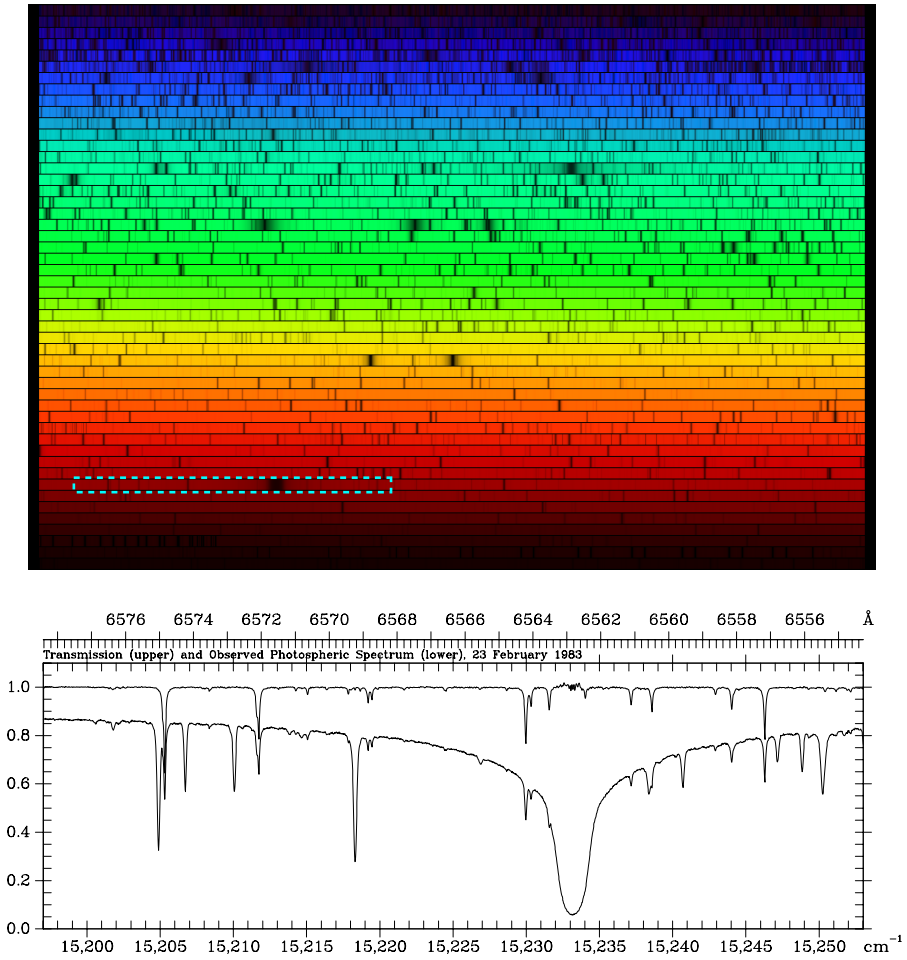

Figure 3.3: *Top*; The solar absorption spectrum between 4000 – 7000 Å (top-right – bottom-left), as measured by the Fourier Transform Spectrometer at the McMath-Pierce Solar Facility, National Solar Observatory, near Tucson, Arizona. Here the spectrum has been split into 50 rows of 60 Å. *Bottom*; Zoom-in view of the region bound by the dashed-cyan box of the top panel showing the H-alpha absorption line of 6562.8 Å. Top image courtesy *www.solarsystem.nasa.gov*. Bottom image courtesy *www.nso.edu*.

sorption and emission characteristics interchangeably *i.e.*, we assume the emission *and* absorption processes are occurring within an *optically thin* plasma.

The top panel of Figure 3.3 is the solar spectrum between 4000 and 7000 Å as measured by the Fourier Transform Spectrometer (FTS; Kurucz et al., 1984) instrument that was mounted at the McMath-Pierce Solar Facility near Tucson, Arizona. Presented as 50 rows of 60 Å increasing from top-right to bottom-left, the many absorption lines of the solar atmosphere are identifiable as dark, vertical lines that vary in width/wavelength-extent. The bottom panel is a zoom-in of the region iso-

lated by the dashed-cyan box in the top panel, showing the strongest absorption line of the solar chromosphere, H-α at 6562.8 Å; it is clear that such spectral lines are not δ-functions.

As in Figure 3.1, the visible spectrum shown in Figure 3.3 is full-disk-integrated. The shape of the measured solar spectrum varies negligibly under such conditions, dependent only on the position of measurement (on the Earth) or the time of day alone. However, when considering emission/absorption from individual structures within the solar atmosphere, the exact shape of the given spectra may vary. For example, consider a blob of emitting solar material moving with a bulk velocity, the emission from this blob would be Doppler shifted according to its motion relative to the observer. As such, the Maxwellian distribution would be maintained but the central peak of the associated Gaussian emission would shift in wavelength. Similarly, if the observed structure is comprised of a number of distinct clouds each moving with a different velocity, the overall shape of the profile would completely deform (see Figure 3.6). As mentioned, the velocity of the emitting/absorbing source/sink is directly proportional to the shift in the wavelength of the incident light. From the classical relationship between a wave's speed v and its associated wavelength λ and frequency ν, $v = \lambda\nu$, we find,

$$\frac{v_{\mathrm{D}}}{c} = \frac{\Delta\lambda}{\lambda_0}, \tag{3.4}$$

where v_{D} is the Doppler velocity of the observed material, c is the speed of light, and $\Delta\lambda$ is the wavelength shift of the emission/absorption signature from the known, or measured, rest wavelength λ_0.

3.1.1.1 Spectral Lines In the Presence of a Magnetic Field

Light emitted from elements that are sensitive to their surrounding magnetic field is predominantly subject to the Zeeman effect. On the atomic level, the presence of the magnetic field slightly perturbs the spin-orbit coupling that defines the energy levels in which the electrons of the atom reside. This perturbation results in the simultaneous splitting of many of the atom's energy levels. In the simplest case a

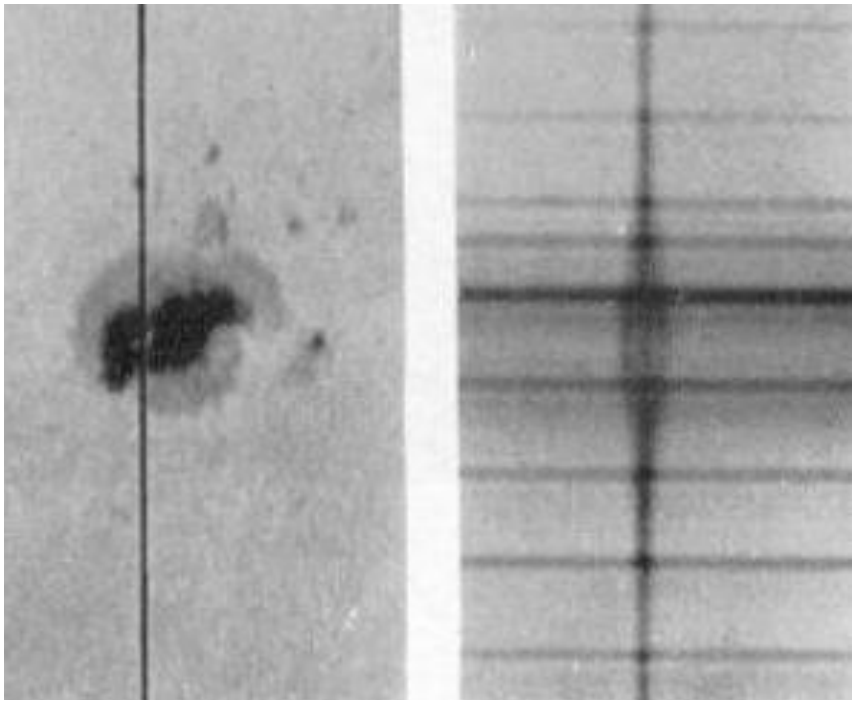

Figure 3.4: Early image of a sunspot in which the Zeeman splitting of the Fe I 6173 Å line is observed. *Left*; the Sunspot imaged on 9 March 1916 with the slit position indicated with the vertical black line. *Right*; The corresponding spectrum along the slit position on the left, showing the increased splitting within the sunspot compared to the quiet region of the solar surface. Figure originally from Hale et al. (1919). Enhanced image courtesy *www.hao.ucar.edu*.

single level gains two additional levels, that were previously degenerate, wherein one has a slightly higher energy and the other a slowly lower. As such, the emission of photons from such a set-up will produce spectra with additional peaks/troughs that are indicative of the energy of this splitting. As the splitting is directly proportional to the strength of the field in which the atom is located, it is possible to directly observe the effect of the magnetic field on the spectral lines (Figure 3.4) and subsequently measure it.

The light emitted/absorbed from an atom with split energy levels is described to be circularly polarised, wherein the higher energy one is left-hand polarised and the other right-hand polarised. The light emitted from the unperturbed energy level is then linearly polarised. The combination of the circularly-polarised and linearly-polarised light allows the characterisation of both the strength, and the directionality of the associated magnetic field. Measurements of the circular polarisation details

give the orientation of the magnetic field vector into or out of the plane, whereas the linear polarisation measures the directionality within the plane of the sky. To better represent these magnetic properties, the I, Q, U, and V Stokes parameters are invoked, wherein I is the overall (unpolarised) intensity of the spectral line, Q and U are the linear polarisation (measured 45° apart), and V is the circular polarisation. In order to measure the complete magnetic field vector, the complete Stokes vector $S = [I, Q, U, V]$ is required.

The Zeeman effect is not the only process capable of modifying the polarisation of light. The Hanle effect and optical pumping are two of such processes commonly measured to effect the linear polarisation signal of solar radiation. Specifically, both the Hanle and optical pumping (not discussed within this thesis) effects introduce a larger-than-expected directional linear polarisation signal in both the Q and U components, caused by the anisotropic incident radiation from below. The primary (observed) distinction between these processes and that of the Zeeman effect then lies in the strength of the atom's ambient field. The Zeeman effect dominates in strong field regions, whereas the Hanle and optical pumping effects dominate in weaker fields. The careful handling of all three processes provides tools capable of probing the magnetic field of the Sun at all scales (*e.g.*, Asensio Ramos et al., 2008; Socas-Navarro et al., 2015, where descriptions of additional processes may be found).

3.1.2 Observation

In order to study a specific section of the solar spectrum, one has to first remove the wavelengths from the incident light that are not of interest. This is carried out using filter optics - the role of which, in the most general sense, is to reflect or block the wavelengths of light that are either not within a specific range, or above/below a given wavelength. Once a region of the solar spectrum has been isolated, the type of studies to be carried out fall, largely, into the two categories of broadband or narrowband. The difference therein is defined based on the relative dimensions (in wavelength) of a given filter to the spectral line that it has been constructed to observe.

Broadband observations, as the name suggests, are captured using filters that have broad widths (in wavelength) and span a significant portion of, if not completely cover, the spectral line(s) of interest. Narrowband observations are essentially the opposite, the associated filters have widths that are typically much less than the widths of the targeted spectral lines. Furthermore, broadband observations use either single filters placed within the light-beam, or a selection with widths incrementally-decreasing from the source to the detector. Whereas narrowband observations require the use of diffraction (slit spectrometers *e.g.*, the *EUV Imaging Spectrometer* (EIS; Culhane et al., 2007) in space), or interference (Fabry-Pérot interferometers *e.g.*, the *Interferometric Bidimensional Spectropolarimeter* (IBIS; Cavallini, 2006) on the ground) to create filters with effective widths small enough to sample a given spectral line multiple times. For observations of light at EUV wavelengths and smaller, it becomes impractical to use Fabry-Pérot interferometers and so all spectroscopic observations at such wavelengths have to be done with slit-spectrometers.

Broadband observations are also beneficial for capturing a lot of light in a short amount of time (exposures). In addition, broadband observations allow multiple spectral lines to be observed simultaneously, provided the spectral lines are close enough together (in wavelength). These properties of broadband filters mean such filters are ideal for fast context imagery *i.e.*, observations relatively insensitive to Doppler shifts; recall the 'Disparition Brusques' and how such observations were taken using filters that actually were not broad *enough* to be insensitive to Doppler motions. Broadband filters are typically used to observe structures like the photospheric granulation (continuum), however AIA also uses broadband filters to observe the solar EUV emission as described in Section 3.2.1.1.

Once again the opposite is true for narrowband observations. The summed intensity from the limited range of transmitted wavelengths can require longer exposure times to build up a sufficient signal. However, the thin dimensions of the narrowband filters allows multiple exposures to be taken at different positions within the line of interest, allowing an observer to study how the line changes shape over

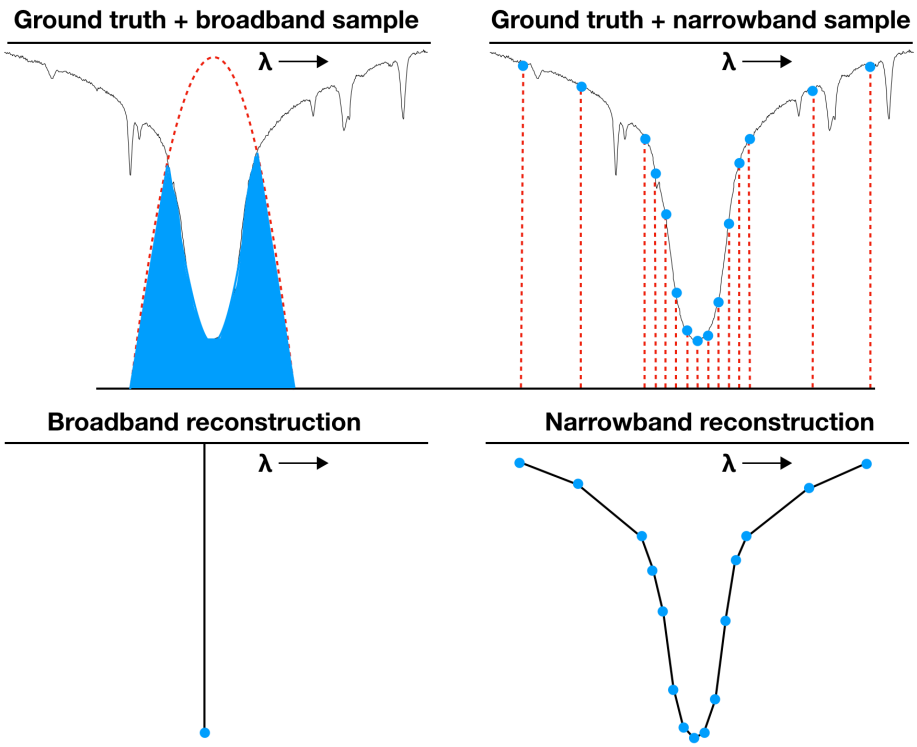

Figure 3.5: *Top row*; FTS-observed spectral line of H-α (solid-black) with the position and width of the filter(s) overlaid in dashed-red. The left and right columns correspond to broadband and narrowband as indicated, intensities measured by the filters are indicated with the shaded region and blue dots, respectively. *Bottom row*; a representation of what an observer can deduce, from broadband and narrowband observations; the former provides a single intensity value whereas the latter may provide enough intensity values to reconstruct the shape of the H-α profile.

time *i.e.*, observations that are sensitive to variations in the source material such as Doppler motions and temperature variations. A combination of longer exposure times per filter position and multiple filter positions means that narrowband observations can typically take an order of magnitude longer to complete in comparison to the broadband counterparts.

The outcome of such broadband and narrowband observing methods is summarised in Figure 3.5. A broadband observation produces a single intensity measurement as to the depth/height (compared to the continuum) of the spectral line(s), H-α in this example, from the integrated intensity across the filter width. This measured intensity can be assumed to have been centred at the wavelength set by the filter itself, regardless of whether multiple spectral lines are included. For example, the 193 Å passband of SDO/AIA has an approximate full width at half maximum

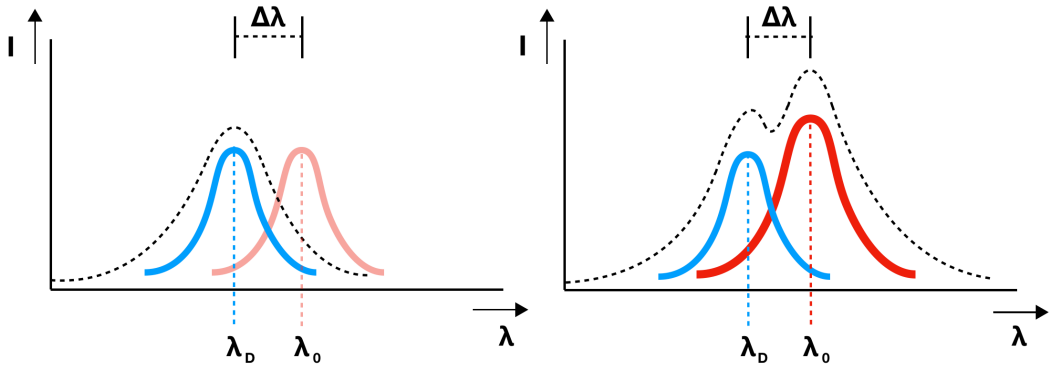

Figure 3.6: *Left*; The observed spectral profile (dashed-black) is fitted with a Gaussian (blue:λ_D). The observed spectral profile is completely shifted to shorter wavelengths relative to the *expected* profile position (red:λ_0), hence the observed light has been blue-shifted. *Right*; The observed spectral line (dashed-black) contains a second component, requiring the summation of two Gaussians (blue:λ_D + red:λ_0). As only a component of the spectral line has been shifted, the measured light source contains material both at rest and at a velocity towards the observer.

(FWHM) of 6.3 Å centred on 193.1 Å (based on the passband functions of AIA shown in Figure 8 of Boerner et al. (2012), see also the discussions of Williams et al., 2013). In contrast, a narrowband observation samples the spectral line at multiple positions, each measuring a different intensity and allowing the reconstruction of the spectral line to an accuracy dependent on the position and number of filter positions.

The emission/absorption of light is commonly compared to the shape of a Gaussian. Modelling such profiles using functional forms of a Gaussian (one or more) enables the physical properties (temperature, velocity) of the emitting/absorbing material to be measured,

$$f(\lambda) = I_0 e^{-\frac{mc^2(\lambda_0-\lambda)^2}{2k_B T\lambda_0^2}} + I_{\text{cont.}}, \tag{3.5}$$

where $I_{\text{cont.}}$ is the continuum emission intensity and I_0 is the peak emission/absorption intensity relative to the continuum (presented graphically in Figure 3.6), and m is the mass of the emitting/absorbing material. Here, the FWHM of

the Gaussian is related to the temperature of the observed material as,

$$\text{FWHM} = 2\sqrt{2\ln 2}\cdot\sigma = \frac{2\lambda_0}{c}\sqrt{\frac{2k_\text{B}T}{m}\ln 2}, \tag{3.6}$$

$$\Rightarrow T = \frac{\sigma^2 c^2 m}{\lambda_0^2 k_\text{B}}, \tag{3.7}$$

where σ is the standard deviation of the fitted Gaussian. The Gaussian's shifted centroid position provides the Doppler velocity using Eq. 3.4.

3.1.2.1 Observations of Optically Thick Spectral Lines - A brief note

This section has thus far treated absorption and emission spectra in the same sense using Gaussians imposed on a continuous spectrum, a perfectly valid approximation for regions of the solar atmosphere that adhere to an optical thickness $\text{Log}(\tau) < 1$ (the optically-thin regime). However, under certain conditions there are numerous processes that may occur between the source and observer that further complicate the actual measured shape of the absorption/emission spectra, and prominences are phenomena wherein such processes occur. The optical thickness τ of prominences in absorption lines can be greater than one resulting in complete absorption along the LOS and hence the purely Gaussian-shaped absorption profile that we have assumed above is no longer an accurate description. The plasma species responsible for such complete absorption are, of course, also capable of re-emission. In the case of complete redistribution (CRD), the energy of the absorbed light is evenly re-distributed across all frequencies. For partial redistribution (PRD), the frequencies of the emitted light are far narrower and centred on the frequency of the initially incident light. In either case, this further complicates the shape and interpretation of the resulting and measured profile. Spectral lines that behave in this way are referred to as being *optically thick*.

The difficulties associated with interpreting the optically thick spectral lines within prominences are typically addressed using *inversions* and their associated models (*e.g.*, Beckers, 1964; Mein et al., 1996; Molowny-Horas et al., 1999; Heinzel

and Anzer, 2001, and summarised particularly well by Tziotziou (2007)). The simplest subset of these inversions are referred to as 'cloud models' wherein a 'cloud' of material (the prominence) is assumed suspended above and completely isolated from a background light source. The properties of this cloud are then dependent on the thickness of the cloud. Hence, the measured intensity at a given wavelength is a function of the initial intensity incident on the underside of the cloud and the combined removal and addition of intensity due to the absorption and emission processes within the cloud. This process is described by the formal solution to the radiative transfer equation (RTE),

$$I(\lambda,\mu) = \underbrace{I_0(\lambda,\mu)\mathrm{e}^{-\frac{\tau(\lambda)}{\mu}}}_{\text{Absorption}} + \underbrace{\int_0^{\tau(\lambda)} S(t)\mathrm{e}^{-\frac{t(\lambda)}{\mu}}\,\mathrm{d}t/\mu,}_{\text{Emission}} \tag{3.8}$$

where, for a given wavelength and observing angle ($\mu = cos(\theta)$, where θ is the angle the LOS makes with the normal to the surface of the observed cloud), $I(\lambda)$ is the measured intensity, $I_0(\lambda)$ is the initial intensity incident on the bottom of the cloud, $S(t)$ is the local source function as a function of the local optical thickness $t(\lambda)$, and $\tau(\lambda)$ the total optical thickness of the cloud. As indicated, the first part of the right hand side of Eq. (3.8) refers to the decrease in the incident intensity as a response to absorption within the cloud, the second part refers to the emission (specifically, the emission and self-absorption) of light from within the cloud itself.

The local optical thickness is then defined as the local absorption coefficient $\chi(\lambda)$ at position x' within the cloud. Integrating along the LOS then provides the total optical thickness of the cloud,

$$\tau(\lambda) = \int_x^{x_0} \chi(\lambda)\mathrm{d}x', \tag{3.9}$$

where x_0 is the surface of the cloud closest to the observer and x is the surface of the cloud at the furthest point from the observer along the LOS.

Finally, the source function is defined as the ratio of absorption to emission coefficients within the cloud $\chi(\lambda)/\eta(\lambda)$ (hence the description of the second part

of Eq. (3.8)). In general, the source function of the cloud varies with optical thickness and may be assumed to be the Planck function of Eq. (3.2) if and only if the cloud is in LTE. However, this would be an improper approach for prominences as their density is far too low for LTE to apply (*e.g.*, Section 6.5 of Labrosse et al., 2010). In addition, and as explored by Hirayama (1963), the prominence plasma is not isotropically illuminated meaning the source function is preferentially modified by the irradiance from below. Furthermore, although represented above as the simple ratio between emission and absorption coefficients, these quantities themselves are functions dependent on the equations of statistical equilibrium *i.e.*, the atomic level population of the plasma species assumed to be present within the cloud, and the surrounding radiation field. As such, the source function is in fact a non-local thermodynamic equilibrium (NLTE) function that must be handled numerically. (A more complete description of the delicate nature of handling optically-thick observations is presented in Labrosse et al., 2010, and Vial and Engvold (2015)).

3.2 Instrumentation

3.2.1 Space-based Instrumentation

3.2.1.1 The Solar Dynamics Observatory (SDO)

The SDO is a result of the collaboration between Stanford University, Lockheed Martin Solar Astrophysics Laboratory, and University of Colorado. SDO was launched on 11 February 2010 on the Atlas V 401 rocket by the National Aeronautics and Space Administration (NASA) into an inclined geosynchronous orbit (28.5°) at a height of 35,789 kilometres above New Mexico, United States of America. Such an orbit ensures that images may be taken for long periods of time without encountering an eclipse due to either the Earth or the Moon. SDO was launched as part of the Living With a Star programme designed to gain a better understanding of the Sun-Earth connection and the Sun's direct impact on the Earth and near-Earth environment. SDO provides near-simultaneous observations in multiple wavelengths from multiple instruments, allowing insights into the relationship between the many layers of the solar atmosphere. The instruments on board SDO

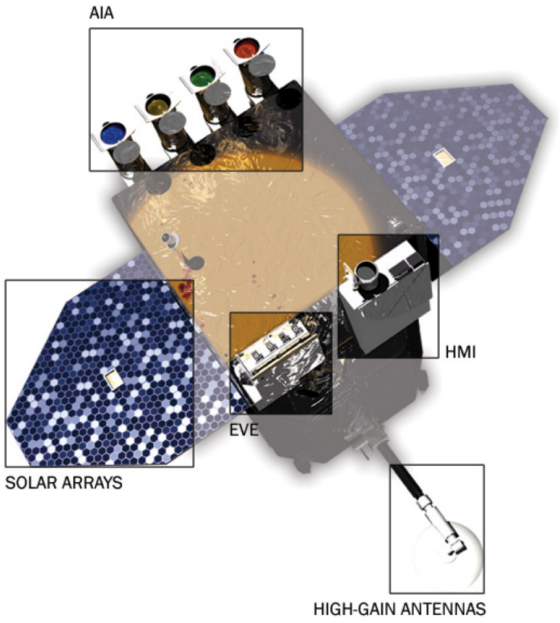

Figure 3.7: Schematic of the Solar Dynamics Observatory spacecraft. AIA is the Atmospheric Imaging Assembly, EVE is the Extreme Ultraviolet Variability Experiment, and HMI is the Helioseismic Magnetic Imager. Taken from Pesnell et al. (2012).

are shown in Figure 3.7 and comprise the AIA, the HMI, and the *Extreme Ultraviolet Variability Experiment* (EVE; Woods et al., 2012).

The Atmospheric Imaging Assembly (AIA)

AIA images the full-disk of the Sun in 10 broadband passbands, seven EUV + three UV–visible as summarised in Table 3.1. The source of the emission recorded in the seven EUV passbands is the solar atmosphere, specifically the transition region and corona, with the three UV–visible passbands recording emission close to the photospheric height. As shown in Table 3.1, six of the EUV passbands are dominated by emission from different ionisation states of iron (Fe). The ability to observe the response of the different ionisation states of Fe provides insights into how energy is deposited into the coronal plasma, and how it is released. To achieve this, AIA makes use of unprecedented (for a space-based EUV imager) spatial sampling ($0.6''\text{pix}^{-1}$) and temporal cadence ($\leq$ 12 s) to image 41 $\times$ 41 arcmin along the charge-coupled device (CCD) axis and 46 $\times$ 46 arcmin along the CCD diagonal,

Wavelength (Å)	Primary Ion(s)	Region of Atmosphere	Char. log(T)
94	Fe XVIII	Flaring regions (Partial readout possible)	6.8
131	Fe VIII, XX, XXIII	Flaring regions (Partial readout possible)	5.6, 7.0, 7.2
171	Fe IX	Quiet corona, upper transition region	5.8
193	Fe XII, XXIV	Corona and hot flare plasma	6.1, 7.3
211	Fe XIV	Active region corona	6.3
304	He II	Chromosphere, transition region	4.7
335	Fe XVI	Active region corona	6.4
1600	C IV + cont	Transition region, upper photosphere	5.0
1700	Continuum	Temperature minimum, photosphere	3.7
4500	Continuum	Photosphere	3.7

Table 3.1: Wavelengths observed by the AIA instrument on SDO. 'Char.' is a shortening of 'Characteristic'. 'Partial readout possible' refers to the availability of observing modes in which cropped CCD output can increase temporal cadence, useful for observing flares for example. Reproduced from Lemen et al. (2012).

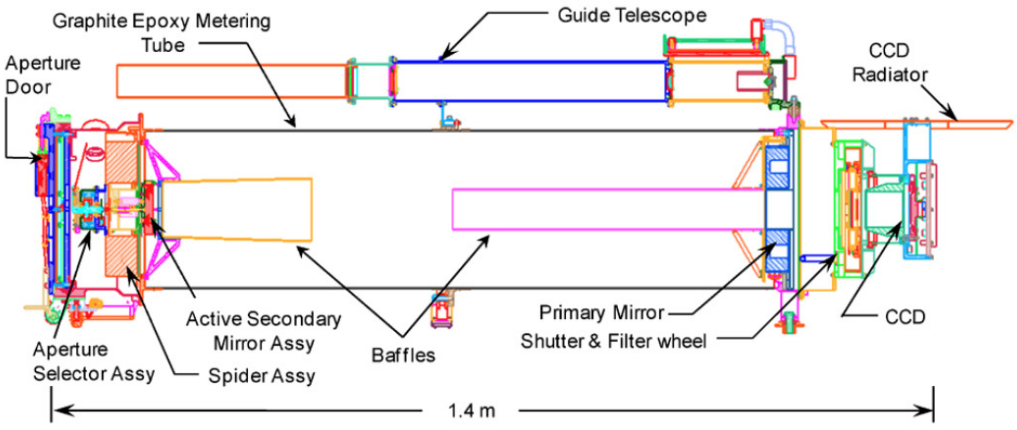

Figure 3.8: Cross section of one of the Cassegrain telescopes that comprise the AIA instrument on SDO, and its guider telescope. Each of the four Cassegrain telescopes has an accompanying guider telescope to stabilise the image on the CCD through deformation of the active secondary mirror assembly. Taken from Lemen et al. (2012)

covering the entire solar disk and part of the lower corona. AIA also has the capability to increase the temporal cadence to 2 s for dedicated observations of energetic transient phenomena such as flares.

The AIA instrument is comprised of four f/20 Cassegrain telescopes, each with an effective focal length of 4.125 m, designed to observe the Sun's (E)UV–visible emission in the range of 94 Å to 4500 Å across the full disk. Figure 3.8 details the cross section of one of the four Cassegrain telescopes and its guider telescope. The four main telescopes are each encased in a graphite epoxy metering tube and are all comprised of an aperture door (in place during launch to protect the internal optics), an aperture selector assembly, a spider assembly, an active secondary mirror assembly, light baffles, the 20 cm primary mirror, the shutter and filter wheel, the 4096×4096 pixel, thinned, back-illuminated CCD, and the CCD radiator. In addition, each of the four telescopes have a guide telescope mounted above the main aperture. Despite the mountings of each main telescope being fixed to ensure they all point in the same direction at all times, the inclusion of a guider telescope and an active, tip-tilt secondary mirror assembly ensures that the image of the Sun is always centred on the CCD to account for jitter in the main telescope pointing.

None of the data recorded by the instruments on board SDO are stored or processed within the systems of the spacecraft. Instead all of the data are immediately downlinked to one of two sites in White Sands, New Mexico. In order for the downlinked observations captured by SDO/AIA to be suitable for scientific study by the scientific community, the data have to, first, be processed to remove certain features that could otherwise lead to incorrect analysis. To carry out the necessary processing, the data are transferred to Stanford Universities Joint SDO Operations Center (JSOC) science-data processing (SDP) facility where the data are stored as level-0 under lossless Rice compression. The conversion from level-0 to level-1 is completed in five steps,

1. Removal of overscan rows (if present)

2. Dark field removal (digital camera offset, CCD read noise, dark current)

3. Flat field correction (gain, vignetting, shadowing)

4. Correction of pixel values (bad pixels, SEP or cosmic ray spikes)

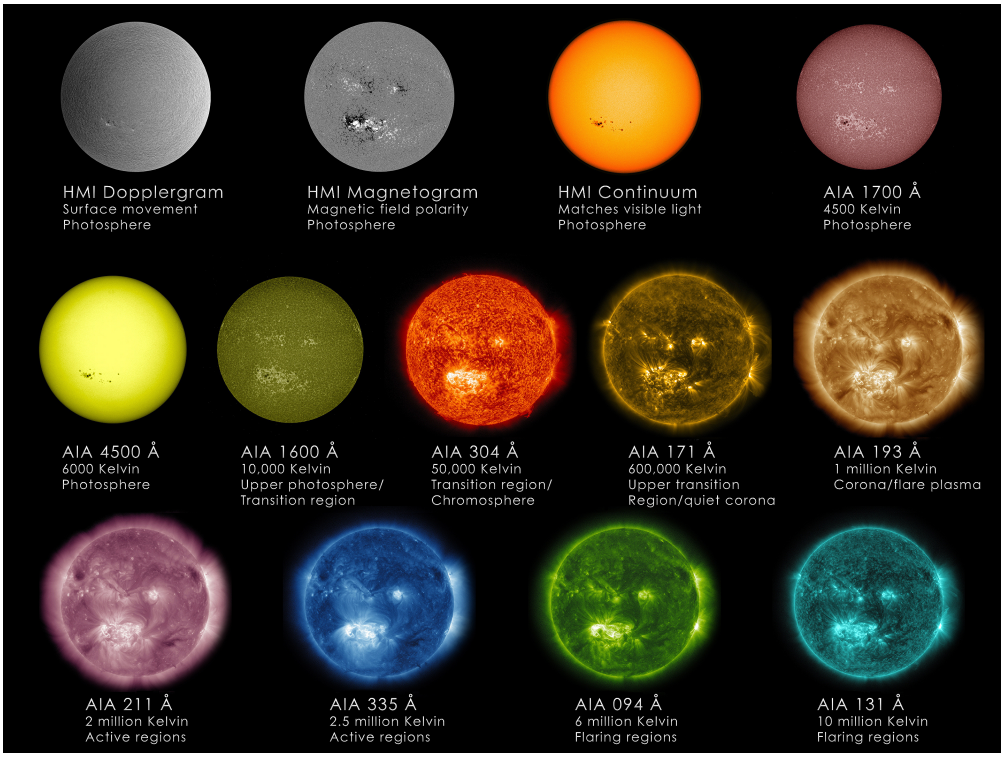

Figure 3.9: Sample set of observations taken by SDO AIA and HMI. From the top left, the first three are observations taken by the HMI instrument on board SDO and the remaining 10 are taken by the AIA instrument. Each passband has been false-coloured to a standard for user-friendliness. (Picture courtesy *www.nasa.gov*)

5. Image is flipped so that solar north is at the top of the image and header information is updated

The level-1 data are then backed-up and also transferred to various repositories across the globe to be as freely available as possible. Level-1 data are then converted into level-1.5 data by the user through the application of the aia_prep.pro function within the Interactive Data Language (IDL) SolarSoftWare (SSW; Freeland and Handy, 1998) package. This routine applies three corrections in a single step: co-aligning the images from the four different telescopes to account for the minor offset between each, correction for the variations in the plate-scale size due to the small differences in focal length of each telescope, and finally the correction to the bore-sight pointing offsets. After the conversion from level-1 to level-1.5 data, the observations are suitable for scientific study.

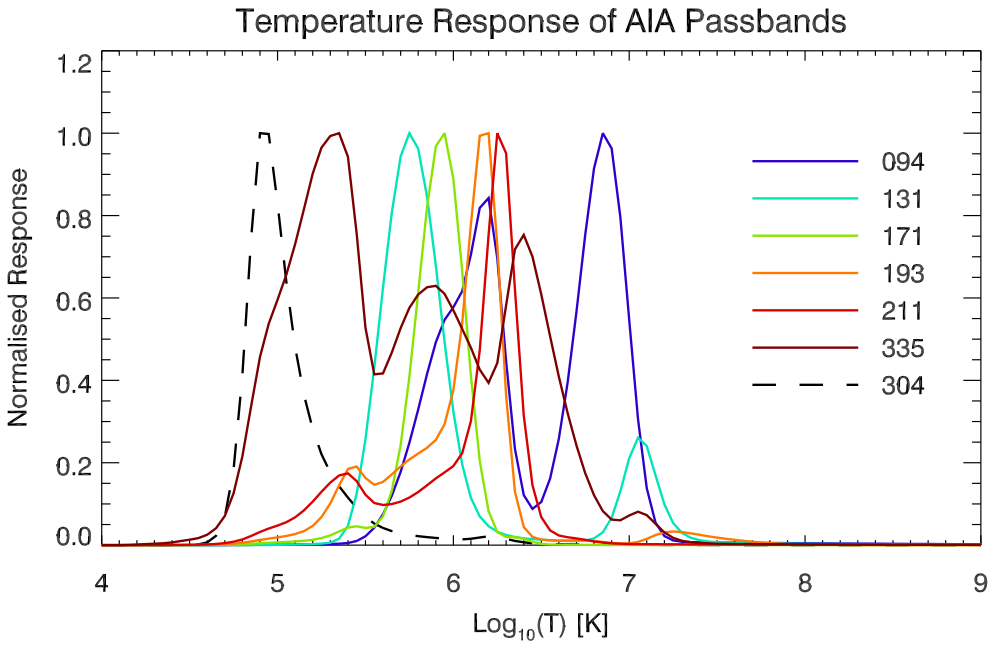

Figure 3.10: Temperature response curves of the seven EUV passbands imaged by AIA, calculated using the SolarSoft routine get_aia_response.pro and using the CHIANTI model for the assumed solar emissivity. Solid lines represent the passbands in which the contribution to the emission intensity is dominated by the ionisation states of Fe, as summarised in Table 3.1. The dashed line of 304 Å has a majority contribution from He II.

The primary product of AIA is a 2D intensity image in discrete broadband passbands of the full solar disk as viewed along the Sun-Earth line; see Figure 3.9. The intensity of EUV emission/absorption measured by AIA is dependent in each case on the temperature and density of both the emissive source and the material that the emitted light encounters along the LOS. The temperature response curves of the six Fe dominated EUV passbands of AIA shown in Figure 3.10 highlight the unique capability of SDO/AIA to observe the intensity of the solar atmosphere at a large range of temperatures. The density sensitivity means that prominences are well observed at EUV wavelengths using AIA, provided their density is sufficient to produce an absorption signature.

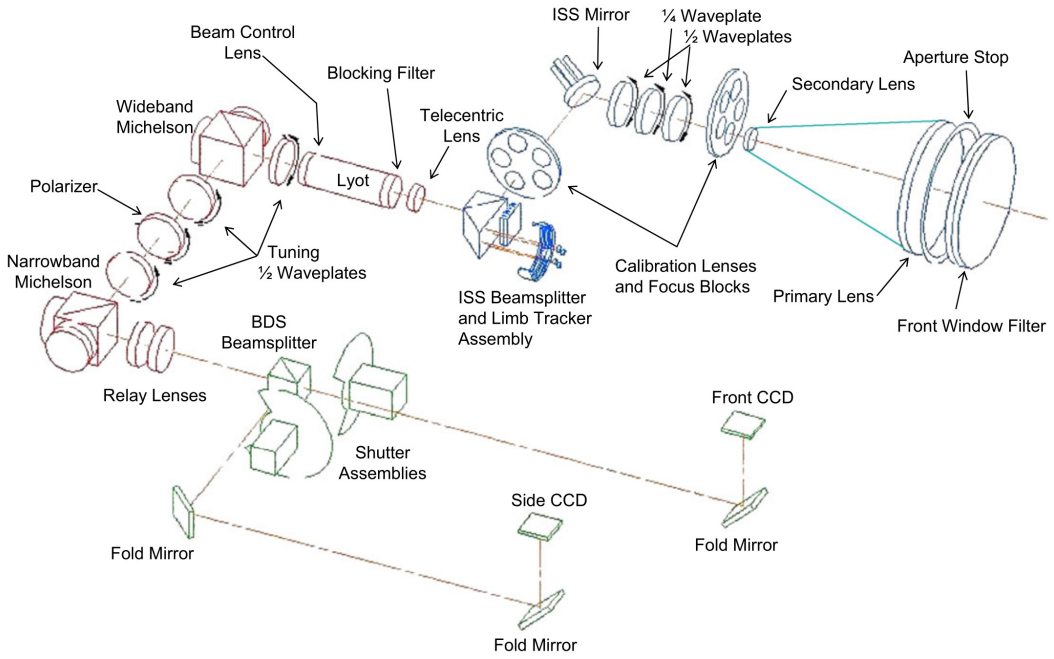

Figure 3.11: The optical layout of HMI. Taken from Schou et al. (2012)

The Helioseismic and Magnetic Imager (HMI)

The HMI is a solar filtergraph capable of spectropolarimetry, designed to measure the intensity variation across the Fe I 6173 Å absorption line instantaneously across the entire solar disk. The design of HMI is heavily based on the highly successful *Michelson Doppler Imager* (MDI; Scherrer et al., 1995) but with improvements in spatial and temporal resolution, the addition of a second CCD and therefore the ability to observe I+QUV and I-QUV simultaneously, and the removal of onboard processing to reduce the load on the spacecraft systems. Like the AIA, HMI makes use of unprecedented (for a space-based filtergraph) spatial sampling ($0.505''$ pix^{-1}) and temporal cadence (3.75 s) to image a similar field of view (FOV) as AIA, but onto two 4096^2 CCDs.

The optical layout of the HMI instrument, with an effective focal length of 4.95 m, is shown in Figure 3.11. The filter system within HMI consists of the 50 Å bandpass filter front window, an 8 Å FWHM bandpass blocking filter, a Lyot Filter with a single tunable element (a rotating half-wave plate) and a 612 mÅ FWHM of the non-tunable part, and two tunable Michelson Interferometers - one wide band

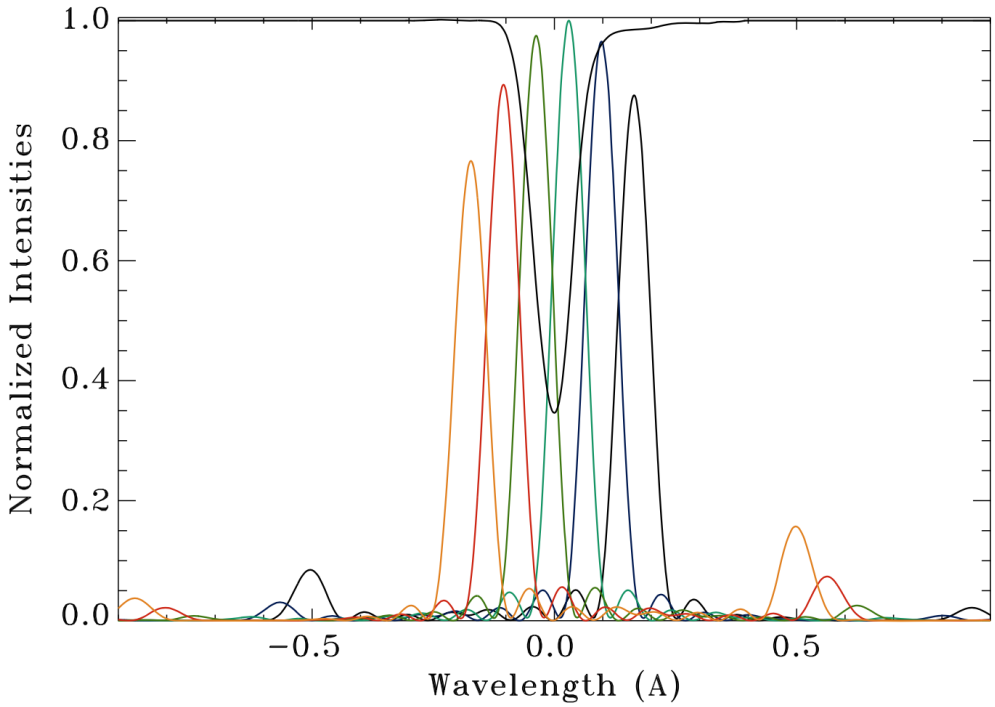

Figure 3.12: The six (tuned) filter positions of the HMI instrument, indicated by the coloured Gaussians, equidistantly-sampling the Fe I 6173 Å solar absorption line (solid black line at the top of the figure). Taken from Schou et al. (2012)

(FWHM 172 mÅ) and one narrow band (FWHM 86 mÅ). The result of this system is a narrow-band bandpass of 76 mÅ FWHM with maximum tunable range of 690 mÅ; the six tuning positions chosen and observed within this range are detailed in Figure 3.12.

As with the data from the AIA instrument, none of the data observed using HMI are stored on board the spacecraft. For the line-of-sight observables pipeline, the first step in the processing of the data from the level-0 to level-1 products is identical for HMI as with AIA *i.e.*, removal of overscan rows, dark field removal, flat field correction, correction for bad pixels, and header updates. After this, the computation of the LOS components are as follows,

1. Discrete estimates of the first and second Fourier coefficients of the Fe I line are calculated from the six wavelengths of Figure 3.12, for each I$\pm$V polarization.

2. The first Fourier coefficient is used to calculate the LOS velocity

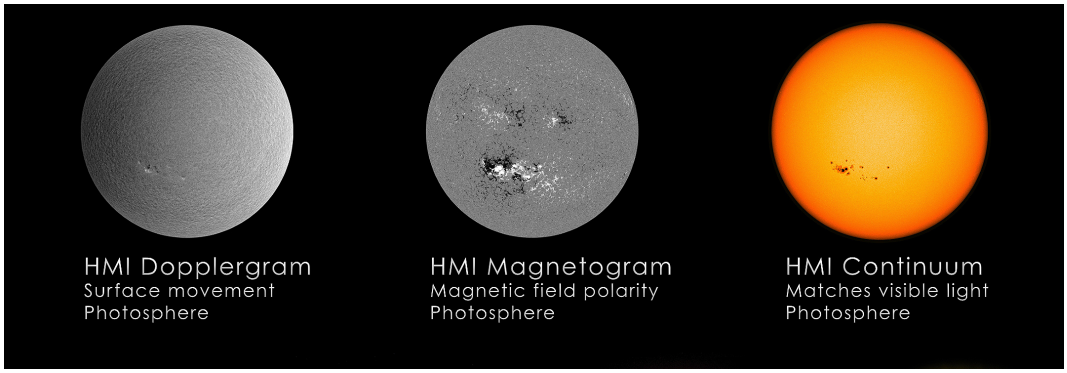

Figure 3.13: A zoom in of the first three panels of Figure 3.9 showing the three main products of HMI. *Left*; Dopplergram, *Middle*; Magnetogram, *Right*; Continuum intensity image. (Picture courtesy *www.nasa.gov*)

3. Corrections to the estimation of the LOS velocity are made due to:

    - Assumptions made in the estimation of Fourier coefficients *i.e.*, HMI filter profiles are not delta functions.
    - Sun-SDO radial velocity correction (due to orbital motion of SDO around the Earth)

4. Calculation of LOS magnetic field measurement (proportional to the difference between corrected I-V and I+V Doppler velocities.)

As with AIA, the use of the aia_prep.pro function within IDL SSW applies the final corrections and prepares the data for scientific use.

The primary observable of HMI is the variation in the intensity of six wavelength points that cover the Fe I absorption line, the shortest of which samples the continuum level. The resulting diagnostics are full-disk maps of the LOS velocity and continuum emission of the solar photosphere, examples of which are shown in the left and right panels of Figure 3.13, respectively. The primary focus of the HMI is to study the variation in the surface oscillations using the LOS Doppler diagnostic and infer the conditions in the interior of the Sun. However, this topic lies outside of the scope of this thesis. Fortunately, the polarisation of the Fe I 6173 Å absorption line is susceptible to the Zeeman effect and so HMI can also be used to create LOS magnetic polarity maps of the photosphere, as shown in the middle panel of

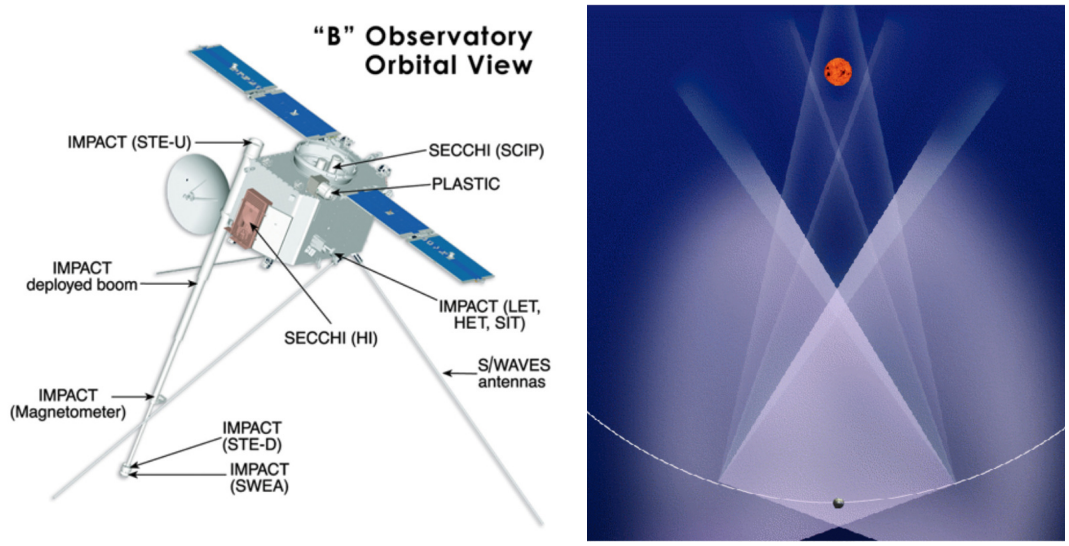

Figure 3.14: *Left*; Schematic of the Solar Terrestrial Relations Observatory Behind spacecraft taken from Kaiser et al. (2008). The remote sensing packages consist of SECCHI(SCIP) and SECCHI(HI). The first is the Sun Earth Connection Coronal and Heliospheric Investigation (Sun Centered Imaging Package) containing three telescopes, EUVI, COR1, and COR2. EUVI is the Extreme Ultraviolet Imager, COR1 and COR2 are the Coronagraphs. SECCHI(HI) are the Heliospheric Imagers (HI-1 and HI-2). *Right*; The overlapping FOVs of instruments from both STEREO-A and -B. Image courtesy *www.secchi.nrl.navy.mil*.

Figure 3.13. Here, positive (negative) polarity is indicated in white (black) corresponding to magnetic field aligned along the LOS toward (away from) the observer.

3.2.1.2 The Solar Terrestrial Relations Observatory (STEREO)

The STEREO mission consists of two identical (to within manufacturing limitations) spacecraft in heliocentric orbits. Launched in 2006 on a Delta 7925 rocket, and after several manoeuvres involving gravity assists from the Moon, STEREO-A (-B) assumed its orbit just inside (outside) that of the Earth with an orbital period of 347 (387) days. This is where the two spacecraft get their names, A-Ahead of the Earth in its orbit and B-Behind. As time passes, the position of the spacecraft around the Sun relative to the Earth changes on the order of $\sim$ 22 degrees per year due to the different orbits. As the mission goes on and the separation between the two spacecraft and the Earth increases, the limitations on telemetry increase. The mission aims and planning were required to take this into account and the cadence of the remote sensing observations were to be lowered as the separation increased.

Wavelength (Å)	Primary Ion(s)	Char. log(T)
171	Fe IX, Fe X	5.8
195	Fe XII	6.1
284	Fe XV	6.3
304	He II, Si XI	4.7

Table 3.2: Wavelengths observed by the EUVI instrument on STEREO. 'Char.' is a shortening of 'Characteristic'. Information taken from Howard et al. (2008).

The initial aim of the mission was to study the low coronal signatures of solar eruptions with a gradual transition to the study of the evolution of coronal mass ejections (CMEs) in the interplanetary medium (IPM).

In order to be able to fulfil these objectives, a suite of instruments suited to both low coronal and IPM observations was required. The two groups of remote sensing instruments are the *Sun Earth Connection Coronal and Heliospheric Investigation* (SECCHI; Howard et al., 2008) Sun Centered Imaging Package (SCIP) and SECCHI Heliospheric Investigation (HI), see Figure 3.14. SECCHI(SCIP) is comprised of three instruments, a full-disk EUV imager (*Extreme Ultraviolet Imager* EUVI; Wuelser et al., 2004, Full-disk–1.7 $R_\odot$) and two white-light (COR)onagraphs with slightly overlapping FOVs (COR1: 1.4-4 $R_\odot$, COR2: 2.5-15 $R_\odot$). SECCHI(HI) is comprised of two white-light heliospheric imagers observing the heliosphere (not pointed at the Sun) between 15-215 $R_\odot$ (HI1:15-80 $R_\odot$, HI2: 80-215 $R_\odot$). The HI package is not used in this thesis.

The Extreme Ultraviolet Imager (EUVI)

The EUVI images the full-disk of the Sun in four broadband EUV passbands, summarised in Table 3.2. The emission measured in the four EUV passbands originates from the solar atmosphere, specifically from the transition region to the corona. EUVI makes use of a $1.6''$ pix^{-1} spatial sampling to image 55 $\times$ 55 arcmin along the CCD axis and 77 $\times$ 77 arcmin along the CCD diagonal, covering the entire solar disk and part of the lower corona. The temporal cadence of the observations varies throughout the orbit depending on phase of the study; the fastest cadence to date

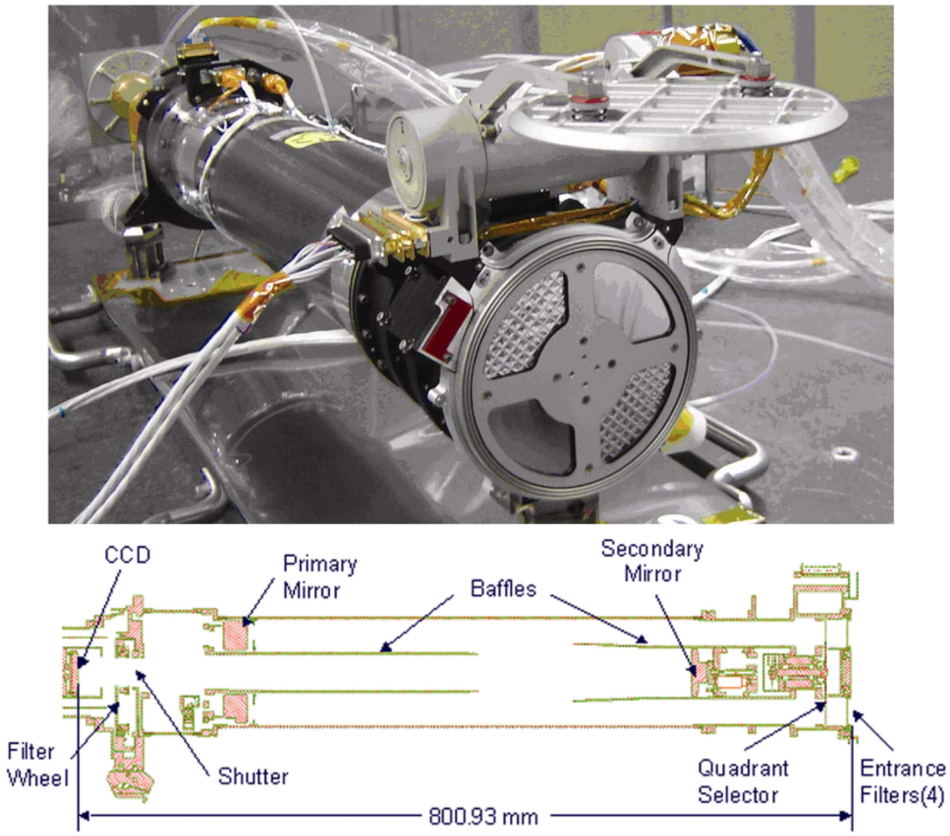

Figure 3.15: *Top*; Photo of the EUVI instrument imaged from the front entrance window. *Bottom*; cross-section of the EUVI instrument, taken from Howard et al. (2008).

has been 75 seconds for the 171 Å passband and the lowest has been 120 minutes for the 171 and 284 Å passbands.

The EUVI is part of the SECCHI(SCIP) group of instruments and is based on the successful design of the *Extreme Ultraviolet Imaging Telescope* (EIT; Delaboudinière et al., 1995). EUVI is a normal-incident Ritchey-Chrétien telescope with an effective focal length of 1.75 m, designed to observe the Sun's EUV emission in the range of 171 to 304 Å across the full disk. Figure 3.15 details the cross section of the telescope. The telescope is encased in a graphite/cyanate ester metering tube and is comprised of an aperture door (in place during launch to protect the internal optics), a quadrant selector, a primary mirror, an active secondary mirror, light baffles, the focal plane shutter and filter wheel, and the 2048 $\times$ 2048 pixel, thinned, back-illuminated CCD. As with SDO/AIA, an active, tip-tilt secondary mirror as-

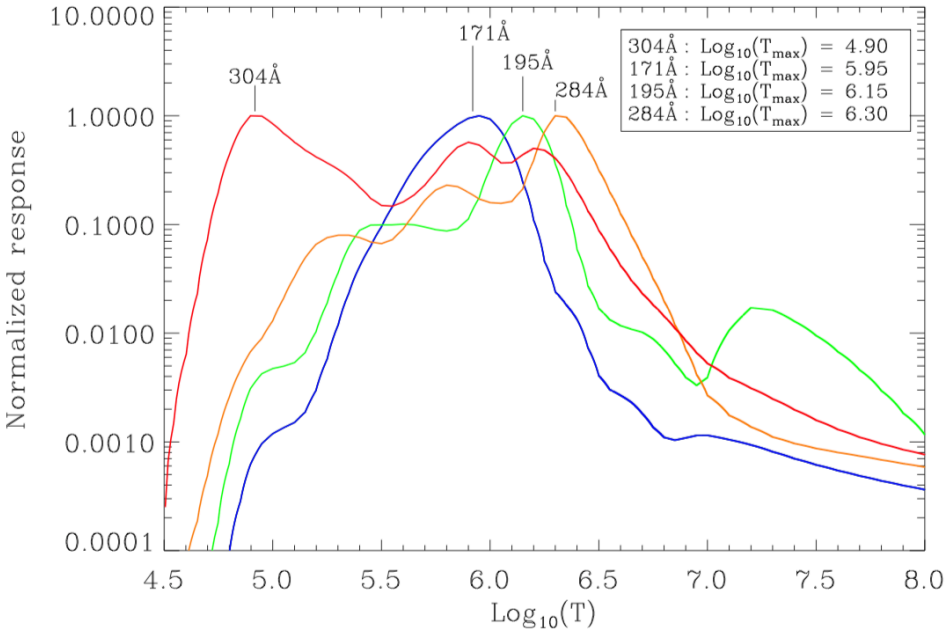

Figure 3.16: Temperature response curves of the EUV passbands imaged by EUVI. Approximate heights of formation for a given temperature are the same as shown in Figure 3.10. Taken from Long (2012).

sembly ensures that the image of the Sun is always centred on the CCD to account for jitter in the main telescope pointing.

Unlike SDO, the data that are downlinked from STEREO are not pre-processed prior to the release to the general scientific community. The raw, level-0 data are downlinked and reformatted into FITS files for ease of access and stored as level-0.5 data. The responsibility of processing the data are then that of the users. The freely available IDL SSW package contains the secchi_prep.pro function, designed to be used to process any of the data that are recorded by the instruments that are a part of the SECCHI suite. The pipeline for processing EUVI data are as follows:

1. Identify and remove cosmic ray hits and bad pixels that are the result of hardware failure or transmission loss.

2. Normalisation of the image by a pre-defined factor that is different for each observed passband.

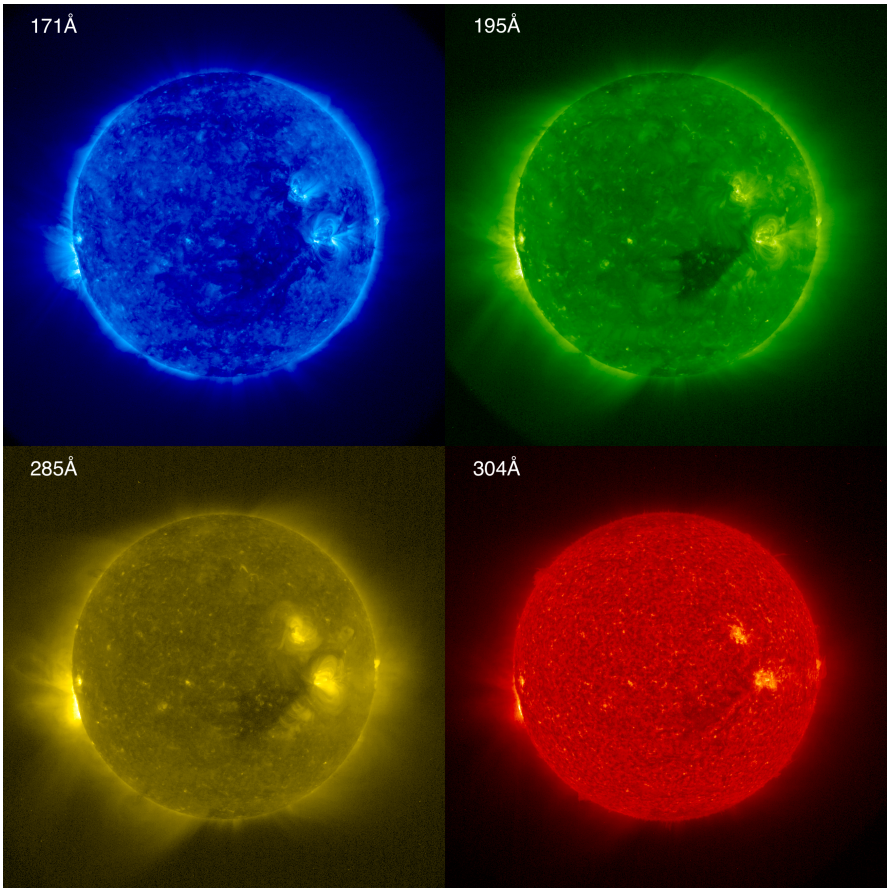

Figure 3.17: Sample set of observations taken by STEREO/EUVI. Each passband has been false-coloured to a standard for user-friendliness. (Picture courtesy *www.stereo.gsfc.nasa.gov*).

3. Removal of mean and SECCHI Electronics Board (SEB) bias and the SEB image summing.

4. Normalisation of the image by the exposure time.

5. Apply the calibration and photometric correction to an image based on its passband (Flat field, vignetting, DN-photon count).

The last step is to rotate the image of the Sun so that solar north is at the top of the image. After this, the data have been sufficiently processed for scientific study.

The primary product of EUVI is a 2D intensity image in discrete broadband passbands of the full solar disk, viewed at multiple points within the heliosphere depending on where each STEREO spacecraft is in time, and from a distance similar to the Earth's. The temperature response curves of the EUV passbands of EUVI

shown in Figure 3.16 highlight the ability of STEREO/EUVI to observe the intensity of the solar atmosphere at a range of temperatures. As EUVI observes emission/absorption at EUV wavelengths, prominences are also well observed using this instrument. An example set of intensity observations made using EUVI are shown in Figure 3.17. The primary scientific goal of STEREO is to image the Sun - Earth connection using stereoscopic methods with EUVI providing the on-disk component of this connection. As previously discussed, the separation between the STEREO spacecraft and the Earth increases at a rate of $\sim$ 22 degrees a year. This means that on 24 January 2009 the two spacecraft were 90 degrees apart from each other, a condition known as quadrature. Observations of the Sun-Earth connection by spacecraft positioned with a 90° separation enables the de-projection of structures observed therein with a particularly good example of this presented in Kienreich et al. (2009). In February 2011, the two spacecraft were at 180 degree separation and the entire Sun was simultaneously imaged for the first time. In October 2014, communication with STEREO-B was lost during a test ready for solar conjunction, the period of time when the spacecraft is travelling behind the Sun and out of direct contact with the Earth. As of August 2016, the spacecraft remains in an uncontrolled spin but conditions are such that additional attempts for recovery will be made when the spacecraft approaches the Earth.

3.2.2 Ground-based Instrumentation

3.2.2.1 The Dunn Solar Telescope (DST)

The (*Richard B.*) *Dunn Solar Telescope* (DST) is a ground-based solar telescope built in 1969 and located in Sunspot, New Mexico, USA. The telescope is uniquely built into the ground such that 41.4 m (67.1 m) are above (below), and all of the telescope internals (mirrors, coudé table, instruments, computers, etc.) lie on a rotating 'spinning top'-like structure, suspended by a mercury float at the top of the telescope that allows it to rotate freely, see panel a of Figure 3.18.

The telescope's beam path is shown in Figure 3.18 and has a total beam focal length of 54.86 m. With a primary mirror diameter of 1.6 m, and a beam diameter of 76 cm, observations taken at the DST are diffraction limited at all observed

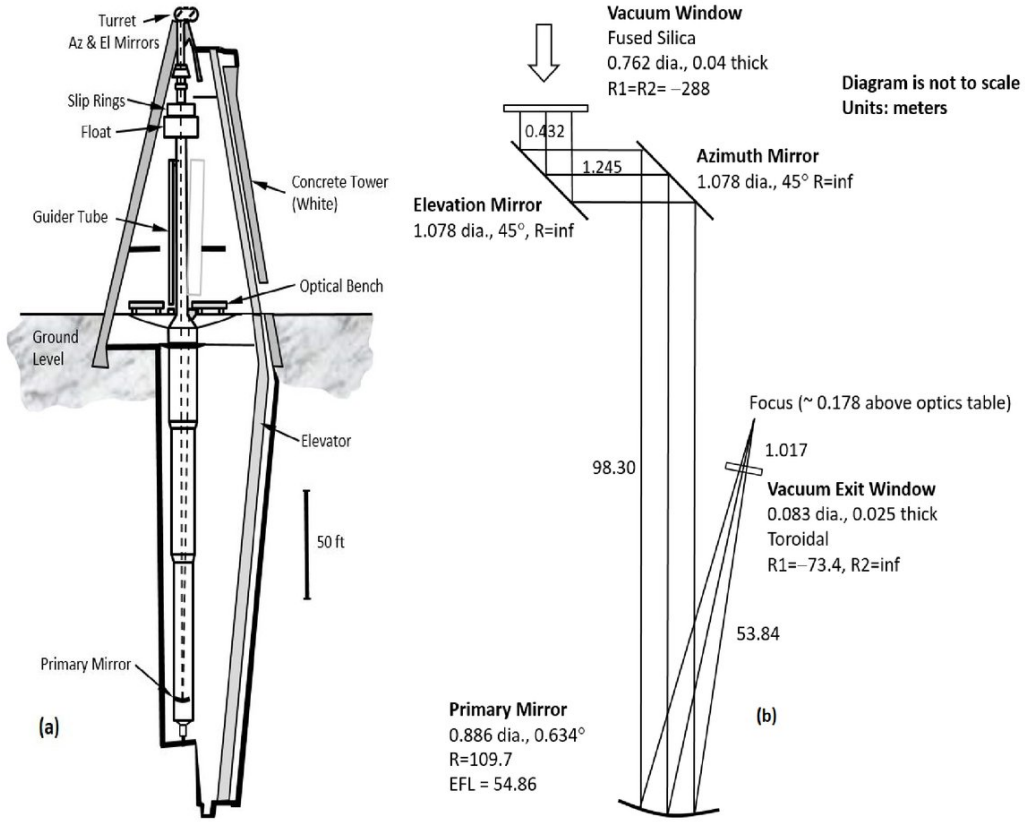

Figure 3.18: A sketch of the Dunn Solar Telescope and its optical layout. Taken from Underwood et al. (2017).

wavelengths, *e.g.*, 0.18″ at 6000 Å (Sankarasubramanian et al., 2004). However, there are a number of factors that affect the availability of diffraction limited observations, most notably the effect of thermal turbulence both interior and exterior to the telescope.

Turbulent motions of the air cause fluctuations in the refractive index of the air volume, causing a variation in the speed of the light passing through. This causes the plane waves incident on the volume of air to be converted into distorted wavefronts. A lot of the volumetric/thermal fluctuations responsible for affecting the "seeing" of the telescope are high up in the atmosphere and as such cannot be easily mitigated (*e.g.*, the jet stream at $\approx$ 10 - 15 km). In order to minimise the effect of the more localised "seeing" conditions at the DST, a number of steps have been taken to passively minimise the thermal variation inside and outside the telescope.

1. As the day goes on, the ground layer is heated by the Sun, in turn causing the local air surrounding the telescope to heat. This is mitigated at the DST in the same way as many other solar telescopes; the primary structure is that of a tower built on a large hill/mountain with the primary mirror mounted at the top of the tower, as far away from the heated layer as possible.

2. The light entering the telescope is sourced from the entire solar disk before being reduced to a $180''$ circular FOV by a circular field stop. This equates to an $\approx 95\%$ decrease in incident radiation that is absorbed by the field stop itself, causing it to heat significantly. To mitigate the effect of this hot component of the beam path, the entire guider tube surrounding the beam path and the field stop is evacuated of air.

3. After the primary mirror, the light beam leaves the evacuated portion of the telescope and enters the remaining optics that are not evacuated. In order to ensure that the temperature within the telescope remains stable, the telescope exterior is painted white to reflect as much energy as possible. This, in combination with an air-conditioning unit, ensures that the interior of the telescope remains at a constant temperature throughout an observing campaign.

Despite these steps, and as previously mentioned, the influence of the conditions in higher atmospheric layers remain present as waveforms in the cross-section of the light beam. More recently, the telescope was equipped with a high-order adaptive optics (AO; Rimmele, 2004) system as an active method of correcting for this. AO acts to compare n subapertures ($n = 97$ for the DST) evenly distributed across the beam cross-section to a reference image captured some time prior. The deviation in each subaperture from the reference image caused by a deformation in the wavefront is then corrected for by actuators (equal in number to the subapertures) attached to the back of a deformable mirror in the lightbeam. AO acts to return a distorted wavefront to as close to its previously undisturbed plane state as possible (for a more detailed description, see Rimmele, 2004)

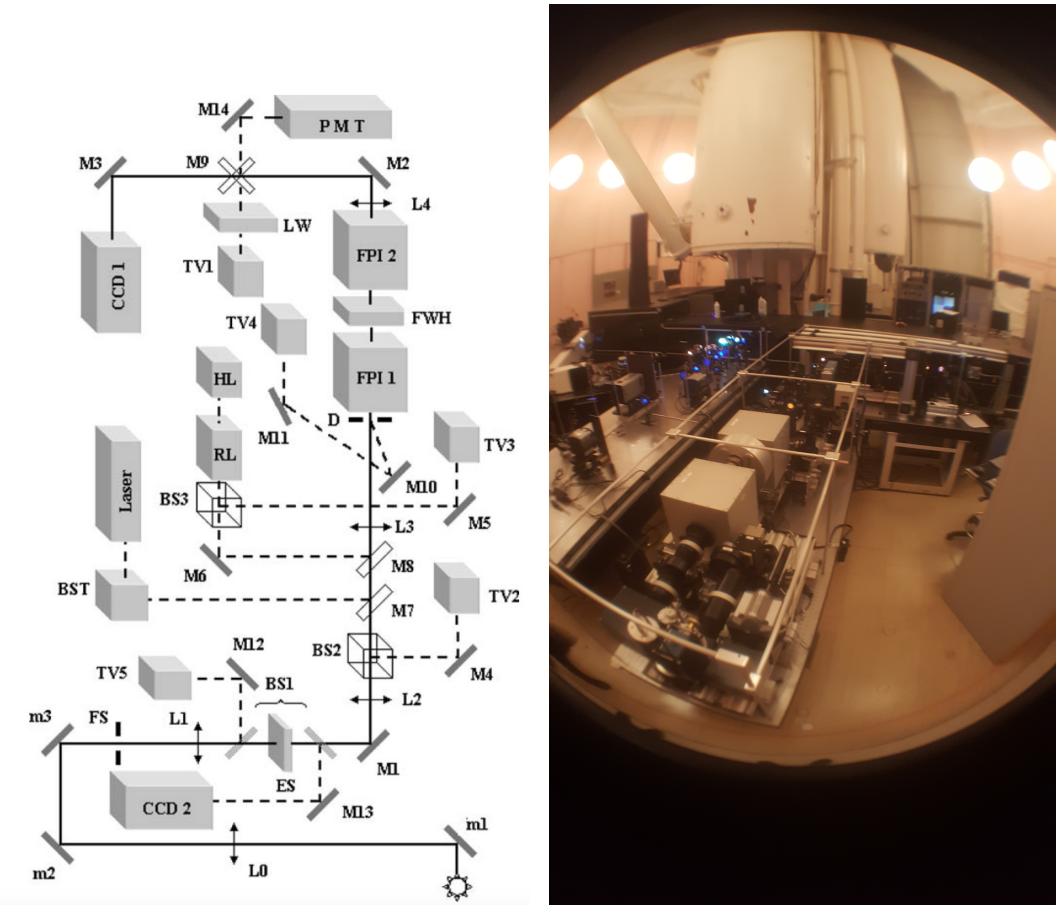

Figure 3.19: *Left;* The optical layout of the IBIS instrument. The primary light beam is shown by the solid line, the secondary light beams are shown by the dashed lines. The insertable/removable components are represented as transparent objects. The labels are defined as follows. M/m: mirror, FS: field stop, L: lens, ES: electronic shutter, BS: beamsplitter, BST: beam steering, FPI: Fabry-Perot interferometer, FWH: filter wheel, CCD: CCD camera, HL: halogen lamp, LW: lens wheel, PMT: photomultiplier, RL: relay lenses, TV: TV camera, W: window. Taken from Cavallini (2006). *Right;* An image I took of the IBIS instrument installed at the DST during our observing campaign there.

The telescope is currently operated/accessed by the members of a consortium headed by the New Mexico State University (NMSU). Prior to this, it was operated by the *National Solar Observatory* (NSO) and the telescope's time allocation committee (TAC) competitively selected exceptional observing proposals from Principle Investigators (PI) across the world; the observations presented and studied in Chapter 6 were obtained on such a basis.

Peak wavelengths of the interference filters (Å)	t_i (ms)	τ_T	t_e (ms)
5896	16	0.43	37
6302	18	0.38	47
7090	11	0.34	32
7224	11	0.33	33
8542	11	0.22	50

Table 3.3: Commonly used IBIS pre-filter wheel properties. t_i: shortest allowed exposure time assuming perfect telescope transparency ($\tau_T = 1$), τ_T: actual telescope transparency, t_e: effective exposure time from actual telescope transparency. In addition to the five interference filters in the filter wheel, the sixth and seventh filter positions are open and dark. Adapted from Cavallini (2006).

The Interferometric Bidimensional Spectropolarimeter (IBIS)

The Interferometric Bidimensional Spectropolarimeter (IBIS; Cavallini, 2006) is a dual Fabry-Pérot (FPI) system installed at the DST, capable of spectroscopic and spectropolarimetric observations of the Sun in high spectral, spatial ($\geq 0.2''$), and temporal resolution (several frames s^{-1}). IBIS is designed to study the evolution of the solar surface/atmosphere at wavelengths between 5800 Å and 8600 Å; discrete pre-filter wavelengths commonly used at the DST are summarised in Table 3.3. For a given observing run, the number of pre-filters that can be used in a sequence is limited by the seven windows available in the pre-filter wheel, six of which contain narrowband interference filters, although the number of wavelengths scanned per pre-filter is not limited. This allows the user to independently specify the position and number of wavelengths to be observed when scanning along the emission/absorption lines of interest. The total cadence of a cycle of observations is then dependent on the number of filters to be used and the number of positions chosen in the scan of each pre-filter curve.

The optical path of the IBIS instrument can be seen in Figure 3.19. From the high-order AO, the main path of the light is shown by the solid line and is incident on CCD 1 after passing through various mirrors, lenses, and the classically mounted double FPI. CCD 1 contains 1317 × 1035 pixels and is responsible for recording the main, narrowband scientific data. CCD 2 contains 1024 × 1024 pixels and is part

of the secondary, dashed optical path as an optional addition employed to record the broadband (100 Å passband centred on 7200 Å) counterpart to the observations recorded in CCD 1. The broadband observations captured by CCD 2 are for the purpose of aligning each narrowband spectral scan; a full, perhaps dense, scan is not instantaneous and exact pointing throughout the duration of a whole scan cannot be guaranteed.

When in spectroscopic mode, the FOV is set to circular to avoid over-illumination of the CCD chip and to preserve the symmetry of the instrumental wavelength shift over the FOV. This is achieved by inserting a circular mask in the focal entrance plane of the instrument. When combined with the 21.3 mm field stop the FOV diameter is set to approximately $80''$, although the exact FOV may be specified by the user. In standard spectropolarimetric mode, a rectangular mask is used instead and sets the FOV to approximately $80'' \times 40''$. The spectropolarimetric mode was not used in this work and so lies outside of the scope of this thesis.

Before the raw data from IBIS is suitable for scientific study, it is subject to pipeline processing[3]. In addition to the raw data, dark current, flat-field, and grid/dot images are required for the pipeline processing. Such observations should be taken during the same observing runs as the scientific data to ensure that the same light conditions are the basis for observing both the scientific data and the complementary calibration data. The order of the pipeline process for observations made in standard spectroscopic mode is as follows.

1. Grid/dot images are constructed by inserting a slide into the focal plane of the telescope that contains regularly spaced grids or dots. As the slide is inserted in the focal plane before the instrument, the relative orientation/plate-scale of the broadband and narrowband observations can be removed, facilitating alignment.

2. Dark current images are constructed by inserting a block in the main light beam such that the CCD receives no illumination. Any signal recorded by the CCD under such conditions is then a result of the electronics associated

[3] https://www.nso.edu/wp-content/uploads/2018/05/ibis_tn_005.pdf

with the CCD itself. The dark current maps are wavelength independent, and integration time dependent. Therefore, the dark current exposures have to be taken with the same integration time as the science observations. The dark current maps are removed from the science observations.

3. Broadband and narrowband flat-field images are traditionally constructed by moving the pointing of the telescope in a random fashion, whilst simultaneously deforming the AO mirror such that all pixels within the CCD receive all *possible* intensity variations. This results in the CCD experiencing uniform illumination and any residual differences are a consequence of pixel-to-pixel transmission irregularities in the CCD itself. If any clouds are present during the obtaining of the flat field data, the frames containing cloud signatures must be manually removed to ensure the flat-field is not contaminated. Flat-field observations are wavelength and integration time dependent. Therefore, the flat-field exposures have to be taken at the same wavelength positions, and integration times, as the science observations. The flat-field maps are removed from the science observations.

4. The collimated mounting of the FPI imprints a systematic wavelength shift across the FOV due to the shape of the lenses. This is corrected for by locating the line core position in each pixel of the narrowband averaged flat-field exposures and shifting accordingly.

The final step, in addition to but not a part of the standard pipeline, is correction for the pre-filter curve. This is completed as a separate step to the pipeline as this calibration step can be defined in different ways and is dependent on the aim of the scientific observations. More details on this can be found in Chapter 6. After completing these steps, the raw data taken in standard spectroscopic mode is now in a format that is ready for scientific analysis.

The primary observable of IBIS is an instantaneous, full-FOV variation in intensity of one-of-n wavelengths across a given interference pre-filter. Completing the n wavelength scans across the full pre-filter produces a 3D (x:1024,y:1024,z:n)

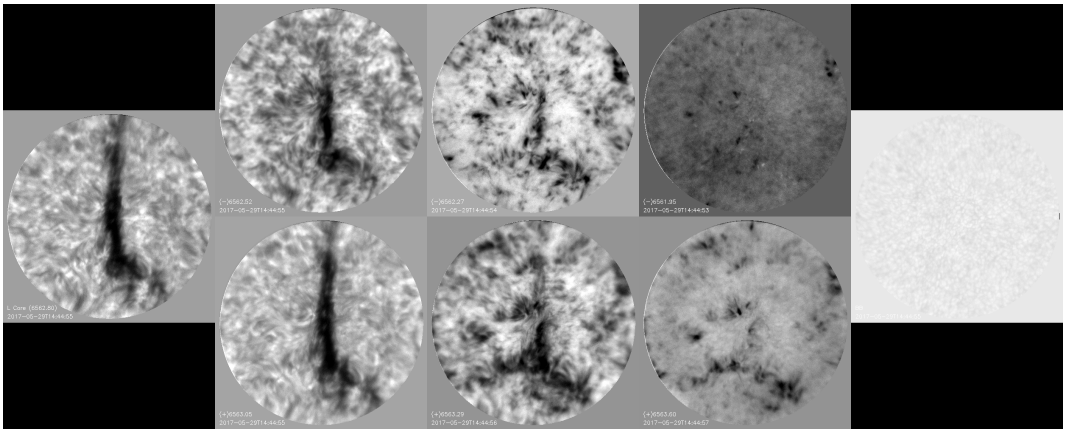

Figure 3.20: Sample set of H-α observations taken by DST/IBIS. From left to right, we move from the line core to the continuum level. The upper branch is the left wing, the lower branch is the right wing. Imaged is the footpoint of a filament with a circular FOV of 95″.

datacube where a specific column in z – (x,y,*) where * signifies all entries – returns the full spectral scan of the given interference pre-filter for that specific position within the FOV. A sample set of eight observations from the line core to the wings and continuum of the H-α (6563Å) absorption line are shown in Figure 3.20. These full spectral scans can be used to derive some of the properties of the plasma that is emitting/absorbing within the FOV, as detailed in Section 3.1.

3.3 Summarising Overview

This section concludes the description of the instruments used in this thesis by briefly combining and comparing the observables of the multiple instruments that have just been described. Figure 3.21 details the relative FOV of the SDO/AIA/HMI, STEREO/EUVI, and DST/IBIS instruments relative to a full-disk image taken by STEREO/EUVI. Table 3.4 then details the resolution, cadence, diagnostics, and height of formation for each of these instruments and wavelengths therein.

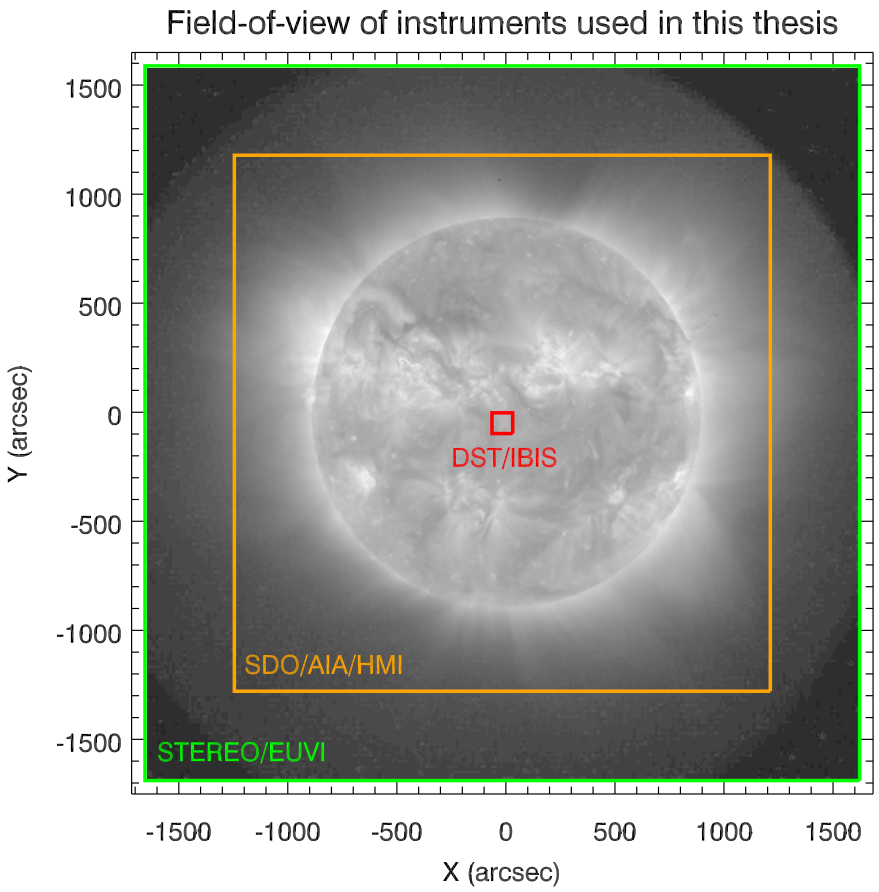

Figure 3.21: The FOVs of instruments used in this thesis, overlaid on a sample image taken by STEREO/EUVI. The FOV of STEREO/EUVI is shown in green, SDO/AIA/HMI in orange, and DST/IBIS in red.

Instrument/ Passband	FOV	Spatial Sampling ($''$ pix^{-1})	Cadence (s)	Diagnostic used	Region Probed (approx.)
SDO					
AIA	Full-disk				
	$2457'' \times 2457''$	0.6	12		
171 Å	”	”	”	Intensity	Transition Region
193 Å	”	”	”	Intensity	Corona
304 Å	”	”	”	Intensity	Chromosphere
HMI	Full-disk				
	$2457'' \times 2457''$	0.505	45		
6173 Å	”	”	”	Magnetogram	Photosphere
STEREO					
EUVI	Full-disk				
	$3277'' \times 3277''$	1.6	300		
195 Å	”	”	”	Intensity	Corona
DST					
IBIS	$95''$ circular	0.09471	13		
6563 Å	”	”	”	Spectral scan	Chromosphere
8542 Å	”	”	”	Spectral scan	Chromosphere

Table 3.4: Summarising overview of the observations used in this thesis.

Chapter 4

Evidence of Mass-Draining Leading to a Prominence Eruption

This chapter establishes observational evidence that the evolution of the gravitational force acting on a case-study solar prominence was capable of influencing its stability. The prominence, observed from 5-11 December 2011 by the SDO spacecraft, displayed a highly dynamic plasma motion just before it became unstable and partially erupted on 11 December 2011. At the time of the eruption, the STEREO-B spacecraft was approximately 107° behind the Earth in its orbit and so the eruption of the prominence was viewed at approximately 90° to its propagation direction. This combination of perspectives was used to remove the LOS projection effects that typically complicate the attempts to correlate the effect of internal plasma dynamics with the evolution of the prominence height. It is suggested that flux cancellation and nearby flux emergence that occurred in advance of the eruption played a role in increasing the height of the prominence. The two viewpoints are used to deduce that the large plasma motion was, in fact, directed towards the surface and out of the prominence, and enable the quantitative estimation of a large 'mass-draining', the subsequent radial expansion, and the eruption of the prominence to be investigated. The analysis shows that a distinct shift in the radial evolution of the prominence occurred after the initiation of the mass-draining. Order-of-magnitude estimates of the ratio of gravitational and magnetic tension forces that acted on the prominence's host flux rope at this time are evaluated. Lower-limit values of be-

tween 1.8 and 4.1 indicate that the gravitational forces supplied to the prominence's flux rope were capable of upsetting the equilibrium. As a result, it is concluded that the draining of 70 % of the prominence mass was responsible for the transition of the host flux rope from equilibrium to loss-of-equilibrium. The work presented within this chapter was published in the *Solar Physics* journal by Jenkins et al. (2018).

The density measure estimation code was applied to the observations by J. Carlyle (European Space Research and Technology Centre). All remaining computation and analysis was carried out by myself. J. Carlyle, D. M. Long (University College London), and L. van Driel-Gesztelyi (University College London) all aided in the context and interpretation of the results.

4.1 Introduction

As outlined in Section 2.4, the destabilisation of a prominence's host magnetic field can occur in response to a plethora of observed magnetic coronal dynamics. In particular, the flux cancellation, flux emergence, and ideal and non-ideal instability mechanisms have received much attention in recent years, whereas the influence of the mass of a prominence has been largely ignored. The many attempts to analytically or numerically model and simulate the evolution of the coronal magnetic environment in the absence of prominence material have successfully replicated the observed behaviour of many solar structures (see Cheng et al. (2017) for a review of the state of such models/simulations). However, with growing observational evidence suggesting that mass can influence the observed dynamics (*e.g.*, Seaton et al., 2011; Bi et al., 2014; Reva et al., 2017), it remains unclear how exactly the magnetic field and plasma of a prominence interplay, and why observations appear to suggest one thing whilst the models and simulations assume another.

The models that address the destabilisation of a prominence's host magnetic field tend to indicate the requirement of an ideal instability to drive the expulsion of the magnetic field and plasma into the heliosphere (cf. Kliem and Török, 2006). Although previous discussions on the topic exist (*e.g.*, Klimchuk, 2001), it is un-

likely, if not impossible, that the gravitational forces supplied to the magnetic field as a result of *e.g.*, the complete removal of mass could *drive* a solar eruption (cf. Forbes, 2000; Emslie et al., 2004; Aulanier et al., 2010). Nevertheless, this does not preclude the possibility that the evolution of mass is capable of influencing the pre-eruptive evolution, typically represented as a migration through quasi-static equilibria. However, to establish the magnitude of force exerted on the prominence as a result of the mass evolution, observationally-constrained estimates to both the total, and evolved mass must first be made.

Such estimates to the total mass of prominences are typically carried out using EUV absorption diagnostics in which off-limb prominence plasma, assumed to be majority $H^{(0)}$, $He^{(0)}$, and $H^{(1)}$, absorbs the emission from behind it. The degree of absorption is then proportional to the density, and therefore mass, of this plasma along the LOS. Gilbert et al. (2005, 2006) carried out a statistical study of prominence masses using such a method, yielding results of total prominence mass of between 10^{14} and 10^{15} g. More recently, Bi et al. (2014) have used the methods of Williams et al. (2013) and Carlyle et al. (2014) to study the mass flow of a filament, yielding a comparable mass of 1×10^{15} g. Bi et al. (2014) concluded that the eruption of their observed prominence was a result of this sudden flowing of material towards one of its ends. However, as no evolution in mass measurements is presented, or indeed ever has been, the evolution in the forces at play could not be explored.

In this chapter, a partial prominence eruption that displayed significant flows immediately prior to its eruption is studied to ascertain whether these flows were the cause. EUV and magnetic (magnetogram) observations and diagnostics taken with multiple spacecraft are used to study the evolution in the surroundings of the prominence, and to correlate the internal and global prominence plasma evolution in the lead up to its eruption. An overview of the chapter is outlined in Section 4.2. The observations and analysis are presented in Section 4.3, before a discussion of the results, and conclusions are offered in Sections 4.4 and 4.5, respectively.

4.2 Overview

This chapter will begin with a brief summary of the observations made in an effort to make the key events described in this chapter easier to follow. The partial prominence eruption studied here was observed on 11 December 2011 in the north-eastern quadrant of the solar disk by SDO and at the north-western limb by STEREO-B, as shown in Figure 4.1. The multi-scale Gaussian normalisation (MGN; Morgan and Druckmüller, 2014) technique, applied to the STEREO-B images, is an image processing technique that aims to enhance images without introducing artefacts. MGN utilises n 2D Gaussian kernels of n varying dimensions to isolate structures within an image that are equal in extent to each kernel size. The set of n images that contain the features of varying dimensions are then added, according to scaled weightings, to the original normalised image. The result is an image that has the finer scales enhanced without a loss of global context.

The analysis described here focuses on the period leading up to the eruption, specifically from 12:00 UT on 10 December to 08:00 UT on 11 December 2011.

i) The prominence of interest was one of several located in a large prominence channel that spanned approximately half of the solar disk visible from SDO/AIA. Line-of-sight magnetic field observations from HMI show that the prominence channel was flanked by a very diffuse bipolar photospheric field, common for quiescent prominence channels (Mackay et al., 2008). Approximately 18 hours before the eruption, a reduction in total unsigned flux was recorded along the PIL of this weak bipolar field, interpreted as flux cancellation. During this time, observations from STEREO-B/EUVI showed the prominence of interest increasing in height. The flux cancellation along the PIL was then seen to have ceased approximately 12 hours before the eruption. The associated analysis is explored in more detail in Section 4.3.1.

ii) Approximately nine hours prior to the eruption, a small bipole was observed to have emerged to the north-west of the prominence. The orientation of the bipole was perpendicular to the axis of the prominence channel. This

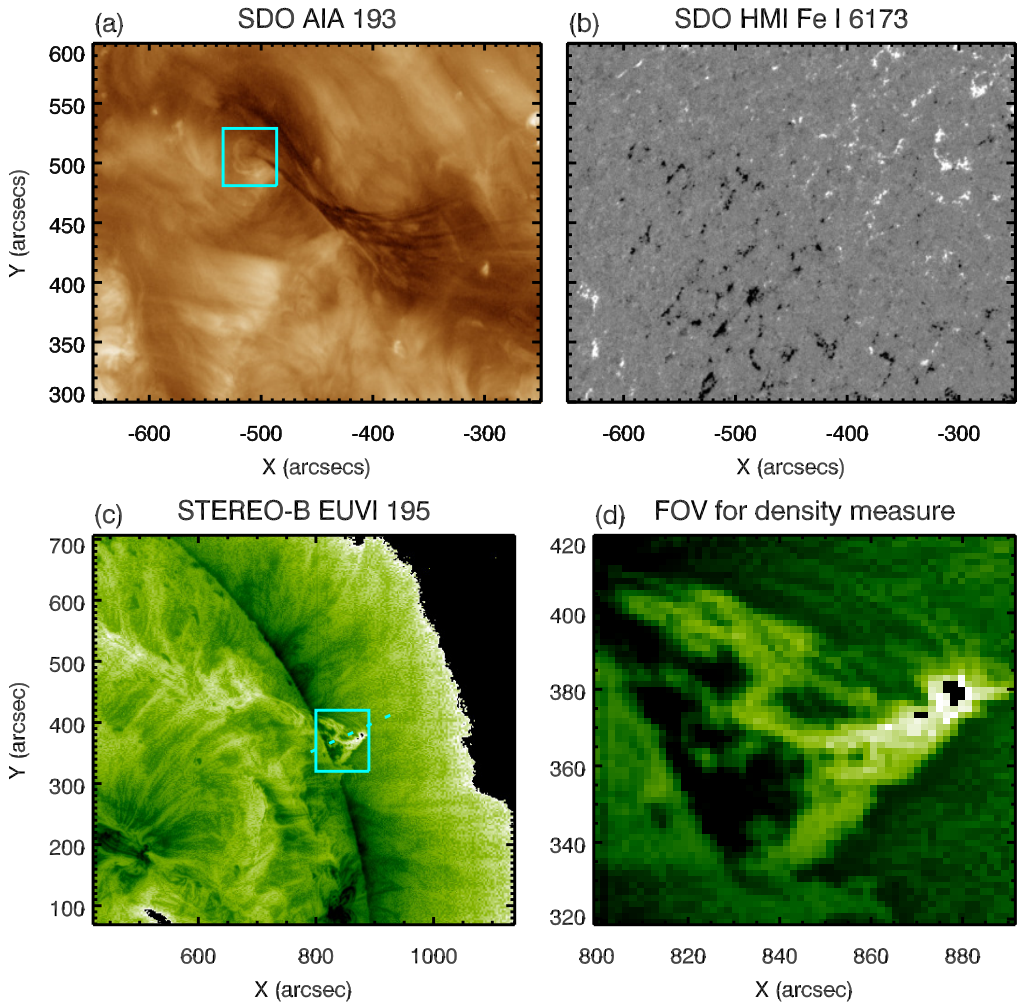

Figure 4.1: The prominence and its photospheric magnetic field environment as seen from the perspective of STEREO-B and SDO. *Panel a*; The prominence as seen in the SDO/AIA 193 Å passband. The cyan box represents the FOV used for the density measures of Figure 4.7. *Panel b*; The same FOV as in *a* from the SDO/HMI instrument showing the LOS magnetic field saturated to $\pm$ 100 G. *Panel c*; The prominence (indicated by the cyan box) as seen on the limb by the STEREO-B/EUVI 195 Å passband using a reversed color table. The cyan-dashed line indicates the location of the stack line for Figure 4.9. The cyan box represents the zoomed in FOV shown in *panel d* and used for the density measures of Figure 4.8. All EUV images have the time stamp of 04:51 UT on 11 December 2011 and the STEREO-B/EUVI images have been processed using the Multi-scale Gaussian Normalisation (MGN) technique.

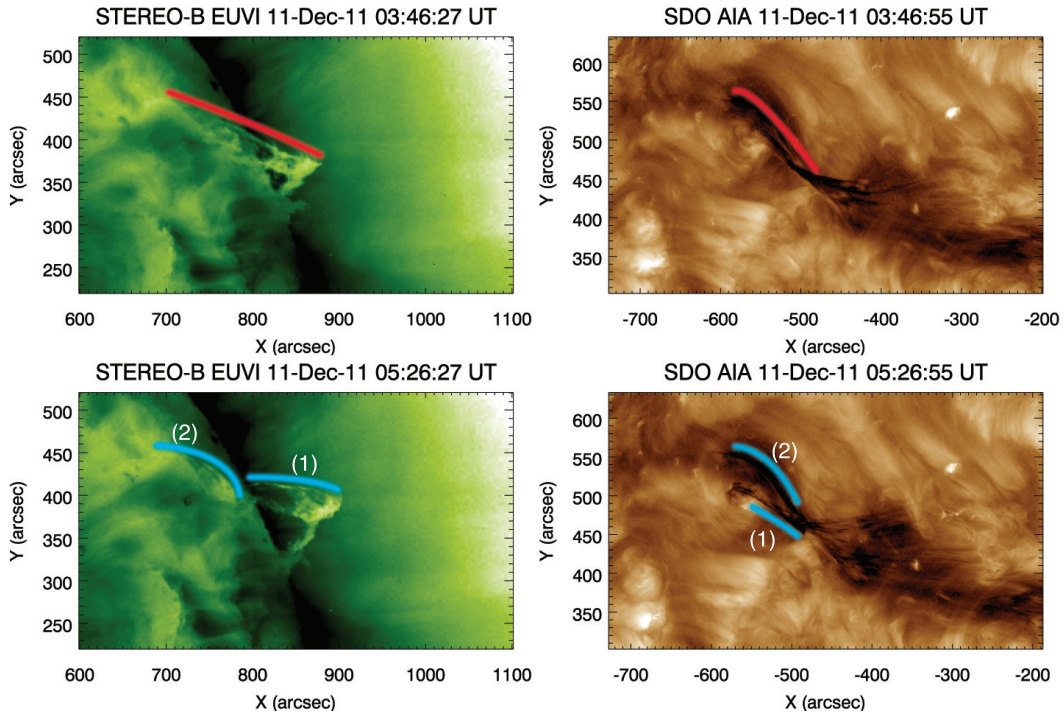

Figure 4.2: The splitting of the prominence during its eruption as seen by STEREO-B (left, reverse colour table *i.e.,* white – green – black instead of black – green – white) and SDO (right), the same passbands are used as in Figure 4.1. *Upper*; The red line traces the connection between the upper and lower branches of the prominence (STEREO-B) and the south-western and north-eastern portions of the prominence (SDO), indicating a magnetic connection highlighted by the illuminating material. *Lower*; The blue lines trace the edges of the two distinctly separated prominence structures, (1)–dynamic portion (2)–restrained portion, just prior to the eruption of the dynamic portion of the prominence.

small bipole grew in extent, reaching its peak value approximately five hours before the eruption of the prominence, before subsequently decaying. As the bipole approached its peak flux the prominence ceased rising, remaining stationary for approximately one hour. The associated analysis is explored in Section 4.3.2.

iii) The prominence was then seen to become unstable, potentially due to the associated flux rope becoming kink-unstable, and began a shallow-exponential expansion through the corona. Observations from STEREO-B/EUVI suggest that the rising prominence did not remain parallel to the surface during this expansion; see Figure 4.2. Shortly after the expansion of the prominence restarted, mass was observed to flow from the apex of the prominence towards

the north-eastern footpoint as observed by SDO. When the prominence apex reached a height of approximately 65–70 Mm, approximately one and a half hours prior to the eruption, a large mass flow was observed to drain from the apex down to the north-eastern footpoint of the prominence. Shortly after the initiation of the large mass flow the radial expansion of the prominence dramatically accelerated. This is analysed in detail in Sections 4.3.4 and 4.3.5.

During the eruption, the prominence was observed to split in two, shown in Figure 4.2, suggesting that the magnetic structure containing the prominence also split. As the higher, dynamic part of the prominence reached a height of approximately 100 Mm, flare ribbons and two large EUV dimmings (cf. Thompson et al., 2000) that spanned supergranular boundaries formed in the low solar atmosphere, indicating the successful eruption of this portion of the prominence. In addition to the brightenings on the surface, brightenings that appear to trace the outside of the magnetic structure suspending the prominence were observed during the eruption. The remaining portion of the split prominence was visibly perturbed at this point but was unable to successfully erupt, ultimately appearing to have reformed a part of the original prominence a few hours later. Therefore, the part of the prominence that has been focused on in this study, and used to define the eruption of the prominence, is the dynamic portion that successfully erupted into the heliosphere at 05:53 UT on 11 December 2011.

4.3 Observations

In this section, the individual observations are presented in chronological order and their analysis outlined accordingly. Discussions and interpretations are offered in the following Section 4.4.

4.3.1 Flux Evolution of Prominence Channel

According to work completed by authors such as van Ballegooijen and Martens (1989) and Litvinenko and Wheatland (2005), the formation and evolution of a prominence can be inferred by tracking the disappearance of surface magnetic polarities along the related PIL. Such tracking can be carried out manually by select-

ing a pair of obviously cancelling features or, more recently, automatically by using algorithms that track all evolution within a defined region-of-interest (ROI) (*e.g.*, Yardley et al., 2016; Dacie et al., 2016; James et al., 2017). All magnetic data used in this chapter have been radialised inline with the assumption that the LOS magnetic field is radial at photospheric heights, de-rotated to zero longitude for ease of tracking, and studied using automated procedures.

Tracking the evolution of, or along, a PIL between strong surface field concentrations is relatively trivial as its position and extent is well defined. However, the prominence was located within the quiet-Sun where the magnetic flux is much more diffuse and the position and extent of the associated PIL was not so clear. The associated PIL was therefore isolated by first choosing a ROI within the FOV of HMI that bound the estimated location of the PIL, in addition to a small area of the positive and negative polarity regions either side. This ROI is shown in panel a of Figure 4.3 as the area bound by the horizontal-blue lines. This sub-area was then successively smoothed by 1000 iterations of a $4.5''$ width window, allowing the positive and negative regions to slowly converge on the location of the PIL whilst also taking into account the larger influence of the stronger flux regions. The image containing the now-clear PIL is shown in panel c of Figure 4.3, the curvature therein is due to the aforementoned iterative approach to smoothing the magnetogram. The shape of the constructed PIL was then compared to the shape of the prominence as seen in the SDO/AIA 193 and 171 Å passbands to confirm an accurate trace; see panel b of Figure 4.3.

The extent of the PIL is typically best defined by manually identifying features that indicate the limit of the magnetic structure to be studied. For example, in active regions the well-illuminated loop footpoints observed in EUV images serve well in aiding to define such a boundary. However, in the quiet-Sun this is not as trivial a task. Instead, the dimensions of the region bound by the dashed-red box in panels a and b of Figure 4.3 were set by identifying features connected to the prominence channel as seen in the 193 Å and 171 Å passband observations. The upper bound was set to include the western end of the prominence and exclude the small can-

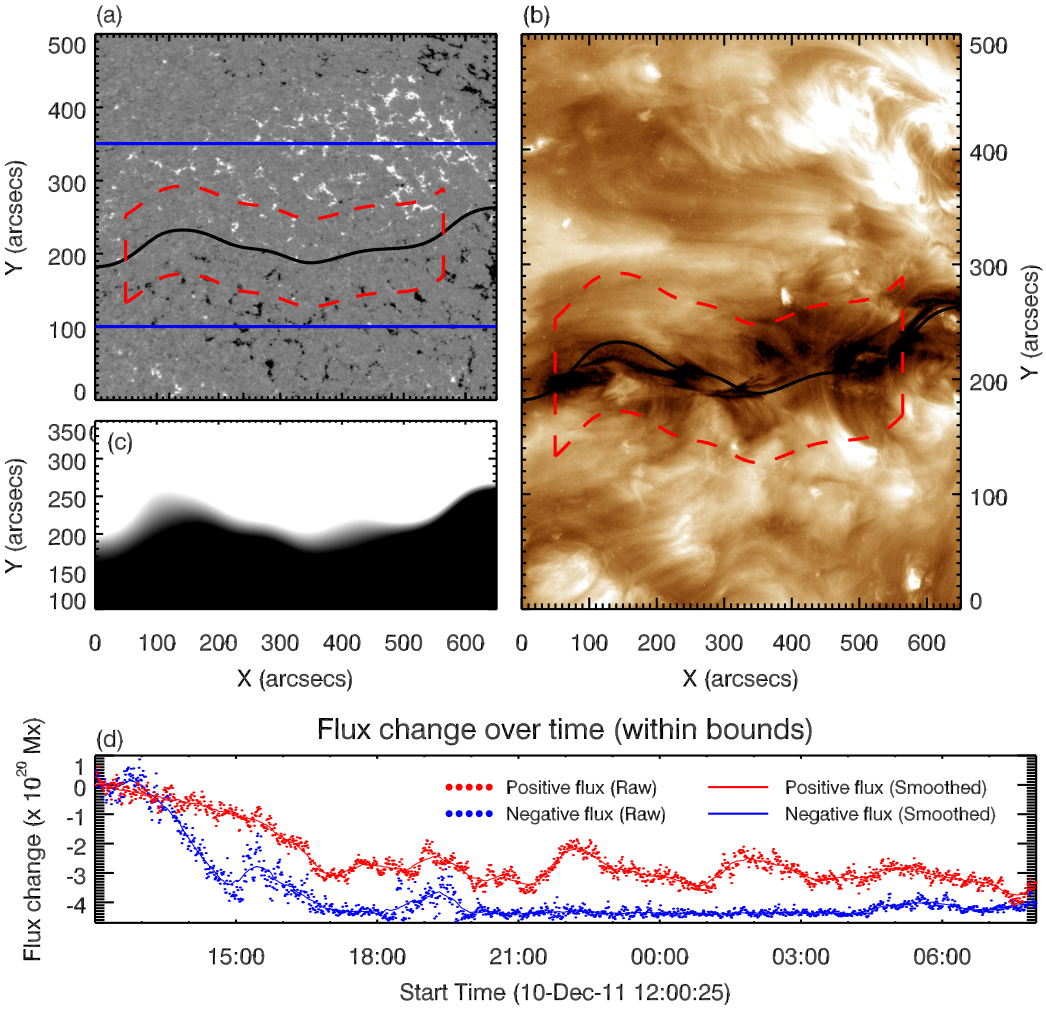

Figure 4.3: The magnetic field evolution within the prominence channel. *Panel a*; HMI LOS magnetogram rotated to disk centre. The solid-blue lines show the bounds of the LOS magnetogram smoothed to define the position of the PIL as in *c*, the solid-black line shows the position of polarity inversion line (PIL) based on smoothing regime, the dashed red lines define the bounds of summation defined by features associated with the prominence observed in AIA 193 Å and 171 Å passbands, as in *b*. *Panel b*; AIA 193 Å passband image corresponding to same FOV as the HMI image in *a*, used to define the region enclosed by the red-dashed line. The EUV image has been saturated to emphasise prominence material. *Panel c*; Result of the smoothed HMI LOS magnetogram that defines the location of the PIL. *Panel d*; The evolution of flux contained within the boundaries defined in *b*. The magnitudes of the raw (non-smoothed) positive and negative flux are both set to zero at 12:00 UT and the evolution after that time is referred to as the 'Flux change'. Cancellation is present within the specified bounds until $\approx$ 18:00 UT, after which the trend plateaus and remains near-constant.

celling bipole, indicated by the stronger EUV emission present at $\approx (390'', 270'')$ in panel b of Figure 4.3. The lower bound was set at the position where an absorption structure related to the prominence was seen to brighten; see Section 4.3.3. The east and west boundaries were defined by the absorption signature of the prominence material itself. This approach assumes that as much as possible of the flux contained within the prominence channel was included. However, this does not account for the inclusion of additional flux which may have been unrelated to the prominence.

The position of the PIL was redefined for each time step of the observation period to account for a slowly changing PIL. The extent of the prominence channel *i.e.*, the dimensions of the summation box, was fixed for all time steps. This allowed the variation in the shape of the PIL to passively track the photospheric changes that caused the change in shape. The total amount of signed ($\pm$) flux density, $|B| > 30$ G, contained within the bounds was then recorded for each time step. The threshold of $\pm$ 30 G was set to reduce the signal of noise ubiquitous to observations using HMI. Finally, the timeseries of the positive and negative flux variation were smoothed over time using a 50 point moving average to suppress the small-scale variation and isolate an average trend.

Figure 4.3d shows a large decrease in flux present within the specified bounds at the beginning of the observation period (12:00 – ≈18:00 UT). This decrease corresponds to a value of $\approx 3.5 \times 10^{20}$ Mx of unsigned flux. This decrease is consistent with the theory of cancellation having occurred at the location of the PIL. However, this signature of a decrease in flux can also be a signature of flux density having diffused to the point that it is no longer included in the summation *i.e.*, values in individual pixels may have dropped to below $\pm$ 30 G. If the measured decrease was entirely a result of diffusion, $\approx$ 7 % of pixels in the FOV would have to have dropped to below $\pm$ 30 G. However, at 12:00 UT on 10 December 2011, only 5 % of the pixels in the FOV contained values greater than 30 G. Assuming only 10 % of these pixels with values $B > \pm$ 30 G diffused, that would contribute a decrease of only $\approx 2.5 \times 10^{19}$ Mx, 14 times less than that observed. Therefore, it is possible

that diffusion contributed to the observed decrease but it cannot account for the entire decrease measured, indeed a faster process must have been involved. The flux cancellation along the PIL was observed to have plateaued after $\approx$ 18:00 UT on 10 December 2011 and remained nearly constant for the rest of the observation period up to and after the eruption.

4.3.2 Bipole Emergence

A few hours prior to the eruption of the prominence of interest, bright, small-scale loops observed in EUV were seen to have formed close to the north-western edge of the prominence channel. This was also observed in HMI photospheric magnetograms as opposite polarity signatures growing and separating to the north-west of the PIL. This small bipole was formed within the positive side of the diffuse bipolar region that hosted the studied prominence. This bipole, located at -32° longitude and +33° latitude at 21:00 UT, was oriented such that its negative polarity was closest to the PIL of the region.

The magnetograms from HMI were treated in the same way as in Section 4.3.1 *i.e.*, de-radialised and de-rotated to disk centre. The ROI was then restricted to $\pm 12''$ in x and 528 - 557$''$ in y, as seen in panel b of Figure 4.4, and the sum total of the LOS magnetic field strength at $|B| > 30$ G within the enclosed area was calculated and repeated for all time steps. The size and position of this ROI was chosen to include just the region that the bipole emerged into; no flux crossed the boundary over the specified observing period. The positive and negative flux evolutions were then smoothed by a 50 point moving average to suppress the small-scale variations and isolate just the overall trend. Finally, the values of raw (non-smoothed) positive and negative flux within the ROI at 20:00 UT on 10 December were set to zero to isolate the emergence of the bipole. The evolution of the flux attributed to the bipole emergence is shown in panel c of Figure 4.4.

The emergence began at approximately 21:00 UT on 10 December 2011, as indicated by the increase in both positive and negative flux. The larger values of positive flux compared to negative flux could be an artifact of the simple assumption used in the calculation of the radial component, therefore introducing a flux

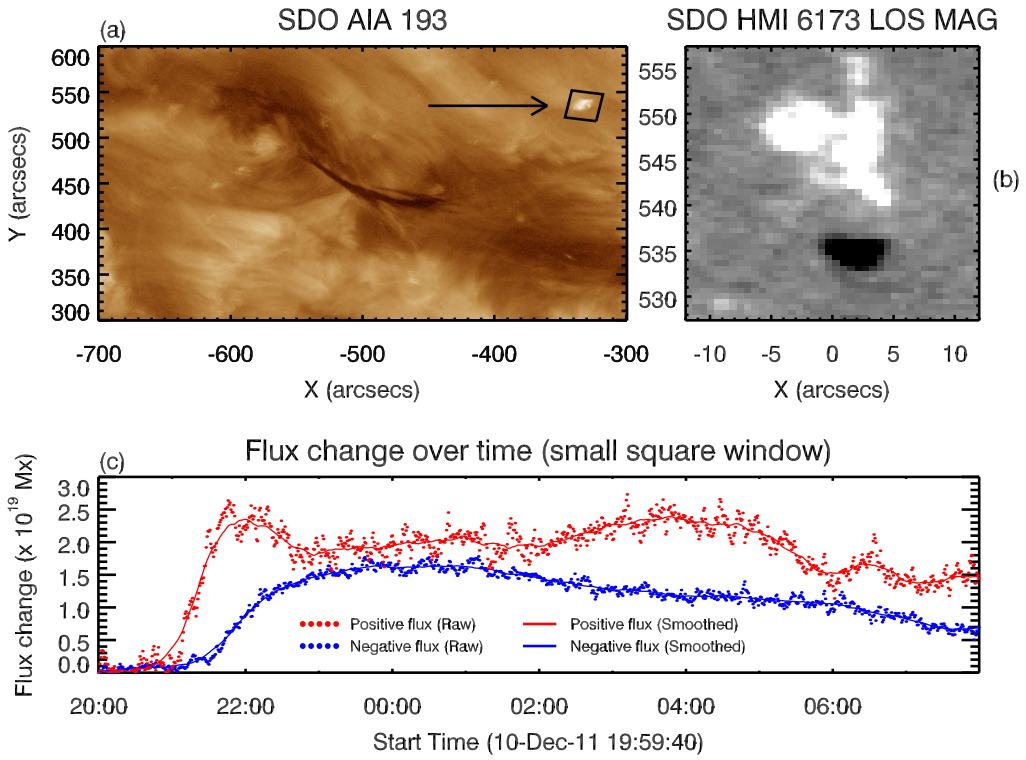

Figure 4.4: The evolution of a small-scale emerging flux region at the edge of the prominence channel. *Panel a*; Location of the bipole emergence with respect to the prominence of interest, as indicated by the arrow and black box. *Panel b*; The ROI, corresponding to the black box in *a*, used for flux summation of the bipole emergence (positive=white, negative=black). Note that the bipole is surrounded by a positive-polarity magnetic environment. *Panel c*; The evolution of the positive and negative flux contained within the small box surrounding the emerging bipole seen to the north-west of the prominence. Emergence began at approximately 21:00 UT on 10 December 2011 and negative flux, associated with the emergence only, peaked at 00:30 UT on 11 December 2011. Both AIA and HMI images have timestamps of 00:41 UT.

imbalance into the photospheric field measurements. It is also clear that the evolution of the positive flux and negative flux were non-identical. The initial increase in positive flux within the ROI is clearly in excess of the initial increase of the negative flux (21:00 – 23:00 UT), before decreasing and becoming more aligned with the evolution of the negative flux (23:00 – 02:00 UT). Prior to the emergence of this bipole, the ROI was populated with positive flux. During the emergence of the bipole the positive polarities of the pre-existing flux and the emerged flux were observed to first coalesce before spreading out. Therefore, the portions of each flux concentration that were below the 30 G threshold will have temporarily increased.

This suggests that the trend shown by the negative flux is more representative of the emergence of just the bipole into the ROI, as its flux evolution only corresponds to that of the emergence. The negative flux can be seen to have peaked at approximately 00:30 UT on 11 December 2011 with a value of $\approx 1.6 \times 10^{19}$ Mx of unsigned flux emergence recorded.

4.3.3 Morphological Analysis of Flows

In the hours leading up to the eruption of the prominence, intensity variations were seen by SDO/AIA to have propagated away from the middle of the prominence. As these signatures propagated, they appeared to travel along a previously unidentified path that led away from the spine of the prominence. Although the intensity variations were seen as dark "blobs", the EUV emission images captured by SDO/AIA are sensitive to both density and temperature variations. Therefore, any intensity variations observed could be temperature variations of the observed plasma, its environment, or physical density variations and therefore plane-of-sky motions of either the prominence plasma itself or additional absorbing material along the LOS.

By plotting the intensity of pixels along a line against time it is possible to isolate how these intensity variations evolved along the given line. This produces a 2D plot typically referred to as a stack-plot. The line A – B drawn in solid-white in panel a of Figure 4.5 is a trace along the average path that the intensity variations were observed to take. A width of two pixels (870 kilometres) was then set and the intensity at a given distance along the line is then an average across this width. This average was introduced to reduce the noise in the recorded value of pixel intensity and to increase the signal of the intensity variations against the background intensity. The resulting stack-plots, shown in Figures 4.5b,c, detail the evolution of intensity variations recorded along the static, solid-white line A – B.

The first large intensity variation was observed at $\approx$ 01:30 UT to travel from the middle of the prominence towards its north-eastern end. This is seen in panels b and c of Figure 4.5 as a darker feature originating at $\approx$ 85 Mm along the track and brightening an hour later at $\approx$ 30 Mm, highlighted with the use of the white dash-dotted line. However, the connection between these dark and bright features is not

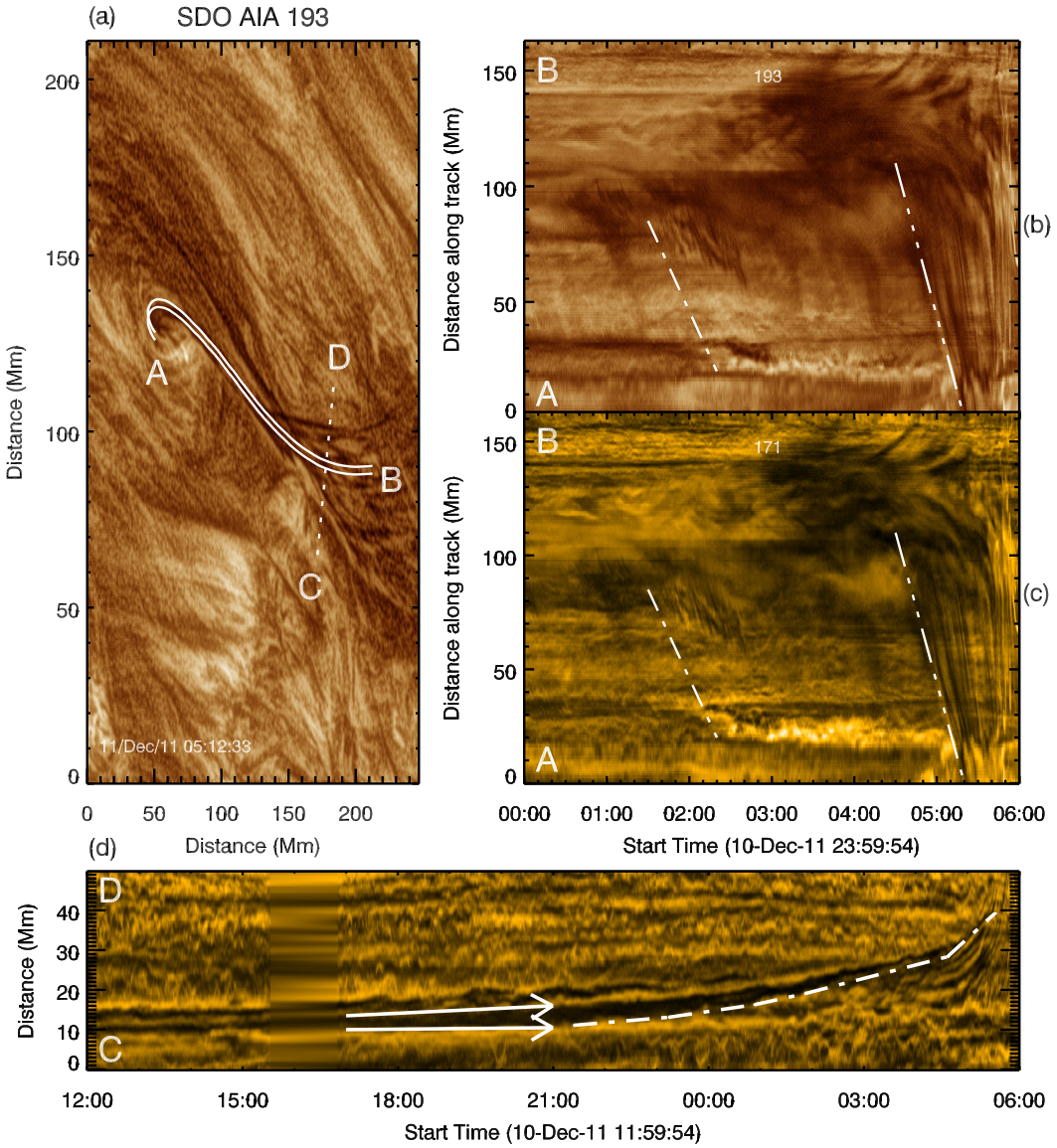

Figure 4.5: Tracking intensity variations along and perpendicular to the prominence axis. *Panel a*; The de-rotated ROI used to specify the lines that trace the motions of interest. The region contained within the white-solid lines (A - B) was used to construct the stack-plots shown in panels *b* and *c*. The dotted-white line (C - D) indicates the location of the line used to construct the stack-plot shown in panel *d*. *Panel b*; The temporal variation in pixel intensity, averaged across the width of separation of the two lines, along the axis of the flows over time for the 193 Å passband. *Panel c*; The same as *b* but for the 171 Å passband. The white dash-dotted and dash-dot-dot-dotted lines in panels *b* and *c* indicate start of the initial and the large mass flow episodes, respectively. *Panel d*; The temporal variation of pixel intensity along the dotted-white line (C - D) in panel *a*. Passbands were processed using the MGN technique to isolate the fine structure of the flows.

obvious *i.e.*, there are no continuous dark streaks connecting the two regions until $\approx$ 05:00 UT. This is because the curved path traced by the intensity variation was highly dynamic over its lifetime. As a result, the static line A – B was not always able to capture the full dynamic evolution of all intensity variations from the middle of the prominence to its eastern end.

The bright structure was, however, persistent throughout the lead-up to the eruption and was particularly well captured between 20 and 30 Mm from 02:30 to $\approx$ 05:00 UT in panel c of Figure 4.5, suggesting the process causing the intensity variations may have varied in extent but did not cease. The intensity variations were then seen to darken and expand from the prominence middle to the north-eastern end, approximately one hour before eruption ($\approx$ 04:40 UT). These are identified in Figures 4.5b,c by the grouping of linear streaks angled towards 0 Mm and traced by the dash-dot-dot-dotted line. These larger-scale variations then continued throughout the final hour leading up to the eruption. Although intensity variations were also observed to propagate from the middle of the prominence to its western end *i.e.,* the bottom right of the prominence as viewed in panel a of Figure 4.1, these were far less intense or dynamic. Those on the western side remained constant after their initiation at 02:50 UT, persisted until the eruption of the prominence, and simply served to highlight the location and extent of the western end of the prominence.

In addition to the stack-plots made from the line A – B in panel a of Figure 4.5, the second line C – D is a perpendicular bisect of the length of the prominence. The change in the orientation of the dynamic portion of the prominence over time is presented in Figure 4.5d. Between $\approx$ 17:00 and 21:00 UT on 10 December the prominence can be seen to have widened, as highlighted by the arrows. After the expansion of the prominence, the entire prominence appears to have undergone a bulk, anti-clockwise rotation that persisted up to the partial eruption of the prominence at $\approx$ 05:53 UT on 11 December.

If the temperature of the material within the prominence was heating/cooling so as to produce the observed intensity variations, their signatures in the 171 Å (0.63 MK) and 193 Å (1.3 - 2 MK) passband stack-plots of Figure 4.5 would be

offset in time. As the variations were seen to be contemporaneous, this demonstrates that they were not temperature but density variations *i.e.*, temperature variations would be recorded in observations using different passbands as bright structures with similar structure but offset in time. Considering the possibility that this was plasma other than that of the prominence's, in order for the absorption signature to be recorded the plasma pressure (and therefore density) has to be high enough (Heinzel et al., 2015). Presumably, plasma at great heights would be far less-dense than that of plasma within the prominence, hence indicating the movement of plasma was most likely within the prominence. The density of these flows can now be considered, in particular with respect to the density of the rest of the prominence structure.

4.3.4 Density Evolution

4.3.4.1 Monochromatic

The cool, dense chromospheric material of a prominence appears in absorption in extreme ultraviolet (EUV) wavelengths below the Lyman continuum limit at 912 Å; photons are removed from the LOS predominantly by photoionisation (Williams et al., 2013), so the efficiency of this removal is a function of wavelength. The temperature of this material, however, is low enough to assume there is negligible emission occurring at these wavelengths (Landi and Reale, 2013). In this case, the optical thickness of the material τ is defined by the column number density N multiplied by the cross-sectional area of photoionisation σ,

$$\tau = N\,\sigma(\lambda), \tag{4.1}$$

which will reduce the intensity of radiation passing through the material as,

$$I_{\rm obs} = I_{\rm b}\exp\{(-\tau)\}, \tag{4.2}$$

where $I_{\rm obs}$ is the final observed intensity and $I_{\rm b}$ is the intensity before passing through the material ('background'). The cross-sectional area of hydrogen and both

neutral and singly-ionised helium is very similar at wavelengths below 227 Å when weighted by the solar chemical abundances given by Grevesse et al. (2007) ($A_H = 1$, $A_{He} = 0.085$), allowing the column number density of hydrogen to be calculated from the total optical thickness,

$$N_H(\lambda) \geq \frac{\tau}{2A_{He}\sigma_{He\,II}(\lambda)}, \tag{4.3}$$

(see Williams et al., 2013, for a rigorous derivation) .

The total optical thickness of such material may be estimated provided the "background", or rather the unattenuated radiation field[1], can be reasonably approximated. This may be done for highly dynamic material by taking an image co-spatial to the examined material some moments in time before or after the material is in that particular FOV. For less dynamic material, the background could be estimated from surrounding areas which are unobscured by cool, dense material. Therefore, provided two suitable images exist (one of the material to be measured, and one to estimate the unattenuated field), a lower limit on the hydrogen column number density may be calculated.

4.3.4.2 Polychromatic

Should the prominence material be observed in $\geq$ three wavelengths below 227 Å (the cross-section of ionisation limit for He II), the optical thickness can be used to constrain a model that includes the fraction of emission, as the unattenuated radiation field includes not only background radiation but also emission from hot coronal material between the prominence material and observer. Furthermore, the fine structuring of the prominence material may be smaller than the pixel dimensions and so a given pixel may contain background emission that was allowed to pass through the prominence material unobstructed, and as such a pixel-filling factor should be considered (assumed equal to unity for the monochromatic method). Therefore, the

[1] 'unattenuated radiation field' refers to the emission from behind and in front of the material in question; the radiation field as it would appear to an observer in the absence of the material would not be reduced in intensity by any absorption as there is no material there to absorb, or 'attenuate' the background intensity.

intensity observed is given by,

$$I_{\rm obs} \;=\; I_{\rm b}(f\exp\{(-\tau)\} \;+\; (1 \;-\; f)) \;+\; I_{\rm f}, \tag{4.4}$$

where f is the pixel-filling factor (*i.e.* the fraction of each pixel occupied by material) and $I_{\rm f}$ is the foreground emission. Rearranging, we have.

$$1 \;-\; \frac{I_{\rm obs}}{I_{\rm b} \;+\; I_{\rm f}} \;=\; f\frac{I_{\rm b}}{I_{\rm b} \;+\; I_{\rm f}}\,(1 \;-\; \exp\{(-\tau)\}), \tag{4.5}$$

where the unattenuated radiation field is approximately equal to $I_{\rm b} \;+\; I_{\rm f}$ (emissivity blocking, the emission which would be emanating from the hot corona in the location of the prominence material were it absent, is negligible due to the small volume relative to the rest of the corona), and so the left-hand-side of Equation 4.5 is measurable, denoted as $d(\lambda)$. On the right-hand-side, a substitution can be made,

$$f\frac{I_{\rm b}}{I_{\rm b} \;+\; I_{\rm f}} \;=\; G. \tag{4.6}$$

This reduces the RHS to two coupled parameters (G,$N_{\rm H}(\lambda)$), if d is measured in three or more wavelengths, the model may be constrained by using a least-squares fit. Although the multiple wavelengths below 227 Å required by this technique are captured by SDO/AIA, from this point-of-view (POV) the prominence is viewed with the backdrop of the solar disk. Therefore, the unattenuated radiation field is not only more dynamic but also more structured. This introduces uncertainties in the estimated radiation field and hence the calculated density. For more detail on this method; see Heinzel et al. (2008), Williams et al. (2013), and Carlyle et al. (2014).

Here, the polychromatic method was first applied to the dynamic portion of the prominence, specifically the observations taken in the 94, 131, 171, 193, and 211 Å passbands of SDO/AIA, prior to its eruption and the results are shown in Figure 4.6. A mosaic approach was taken to minimise the effect of spurious pixels, as computing the column number density for a square of this size would have been

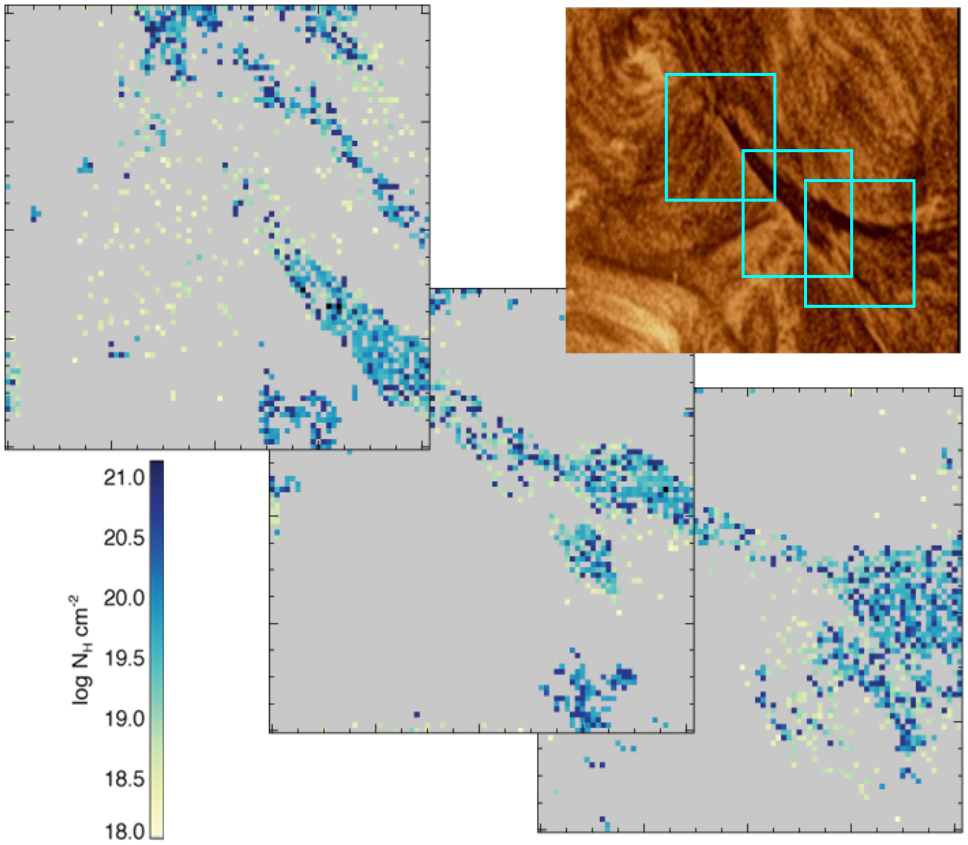

Figure 4.6: *Top right*; A 193 Å intensity image of the dynamic portion of the prominence as seen at 01:51 UT by SDO/AIA. The three panels indicated in the top-right image using cyan boxes are presented as mosaic maps of column number density within the dynamic portion of the prominence, calculated using the polychromatic method. The mosaics have a $48'' \times 48''$ FOV, with each tick separated by $3''$.

much more computationally demanding. Similarly the corners of the ROI were of no interest and as such it was deemed unnecessary to compute over the full area. Furthermore, the assumption of an unattenuated background is more difficult to satisfy over a larger area, as the Sun is highly dynamic and structured, so using three similar, smaller frames increases the reliability of the results. The requirement for an unattenuated background field (*e.g.*, unstructured, not varying significantly across the FOV, close to the observed prominence) was best satisfied at 01:51 UT, which is why this time was chosen for the analysis.

Next, the polychromatic method was applied to observations of the large density flow that occurred shortly before the eruption of the dynamic portion of the prominence. From the previous section, this flow was identified to have travelled

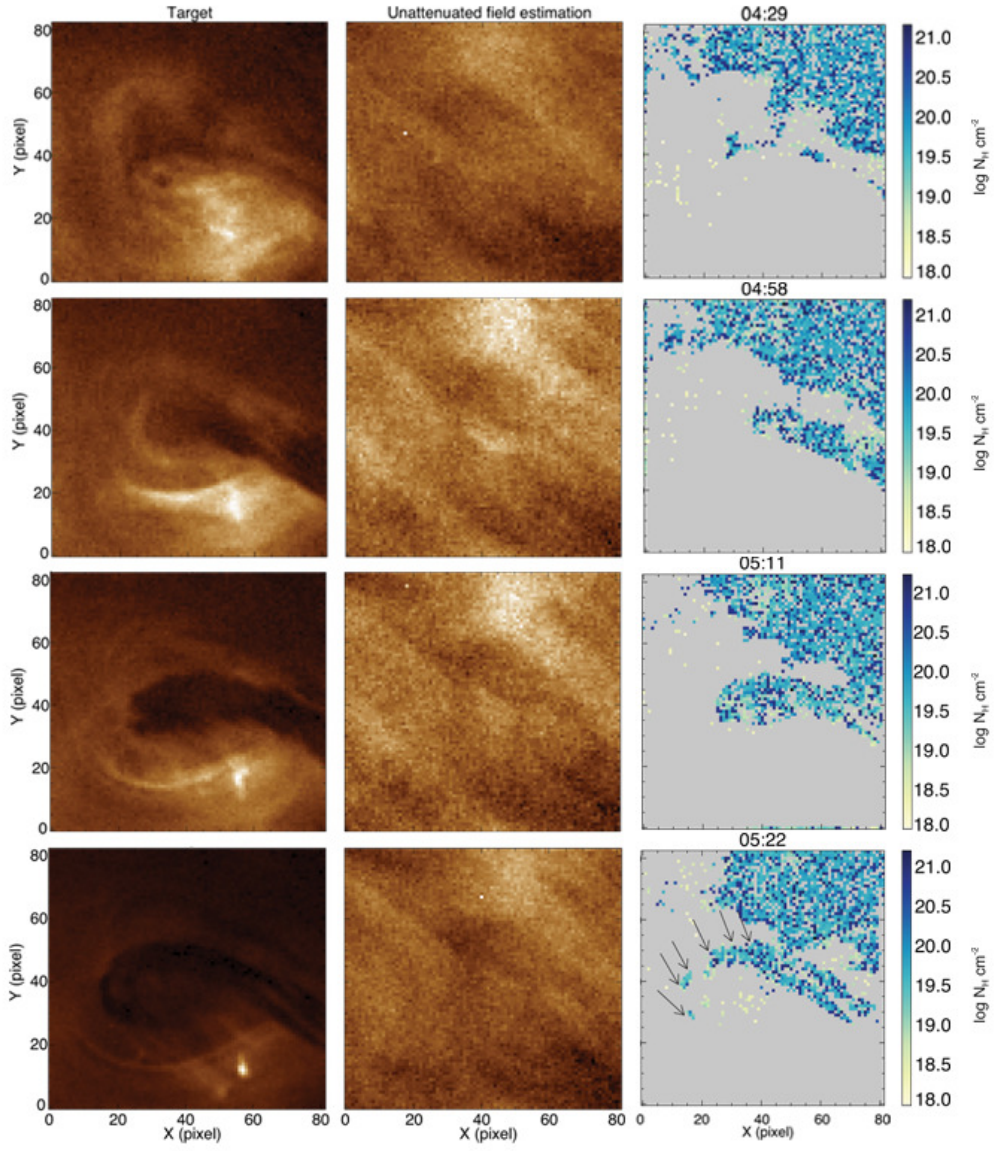

Figure 4.7: Density evolution of the large mass flow between 04:29 and 05:22 UT on 11 December 2011, using the polychromatic method applied to SDO/AIA data. *Left*; FOVs used in the density determination method that include the end of the large mass flow, defined in Figure 4.1a. *Middle*; Unattenuated radiation field estimation for each intensity image shown on the *left*. *Right*; Results of the density determination method based on the specified target and unattenuated field estimate. The hooked shape of the dense object at 05:22 UT is indicated by the arrows. All times indicated above the panels are in UT. Resolution is $\approx 0.6''$ per pixel.

from the middle of the prominence towards its north-eastern end. As before, a small ROI was specified around the north-eastern end of the prominence and a few frames around the time of the flow were analysed to track the evolution of this flowing material. The results are shown in Figure 4.7. Material is clearly seen to enter the FOV from the middle of the prominence in the centre-right of each image and follow a curved path, indicated by the arrows in the 05:22 UT panel of Figure 4.7.

The polychromatic method applied in Figures 4.6 and 4.7 to the SDO/AIA observations of both the entire dynamic portion of the prominence, and the large mass flow, returns a mean column number density of 1×10^{20} cm^{-2}. However, this value is a lower-limit estimate for two main reasons. The first is that in order for an absorption signature to be detected in the EUV passbands, or indeed any EUV observations, *enough* material has to be present along the LOS. Hence, there is almost certainly more material within the prominence than can be detected. The second is, of the material that can be detected, the EUV absorption method used here is only sensitive up to populations of He II, as detailed in Section 4.3.4.2. Although the majority of solar plasma is comprised of species of hydrogen and helium, heavier elements are also present that can not be probed using this method (see Parenti, 2014).

On 11 December 2011, STEREO-B was situated in its orbit approximately 107° behind the Earth. The eruption occurred at $\approx$ -30° longitude from the perspective of SDO/AIA, hence, the eruption was seen by STEREO/EUVI to have evolved approximately in the plane-of-the-sky ($\approx$ 77° to the LOS). This provided a rare opportunity to view an eruption contemporaneously both on-disk (SDO/AIA) and off-limb (STEREO-B/EUVI), and help disentangle the structure of the prominence that would otherwise have been unachievable with single-perspective observations.

From the point-of-view of STEREO-B, the prominence was projected against a slowly-changing background of the corona. Therefore, the unattenuated background radiation field estimate required for the density measure methods could be well approximated by using an image taken in the location of the prominence following its eruption. Unfortunately, due to the large distance, and therefore low

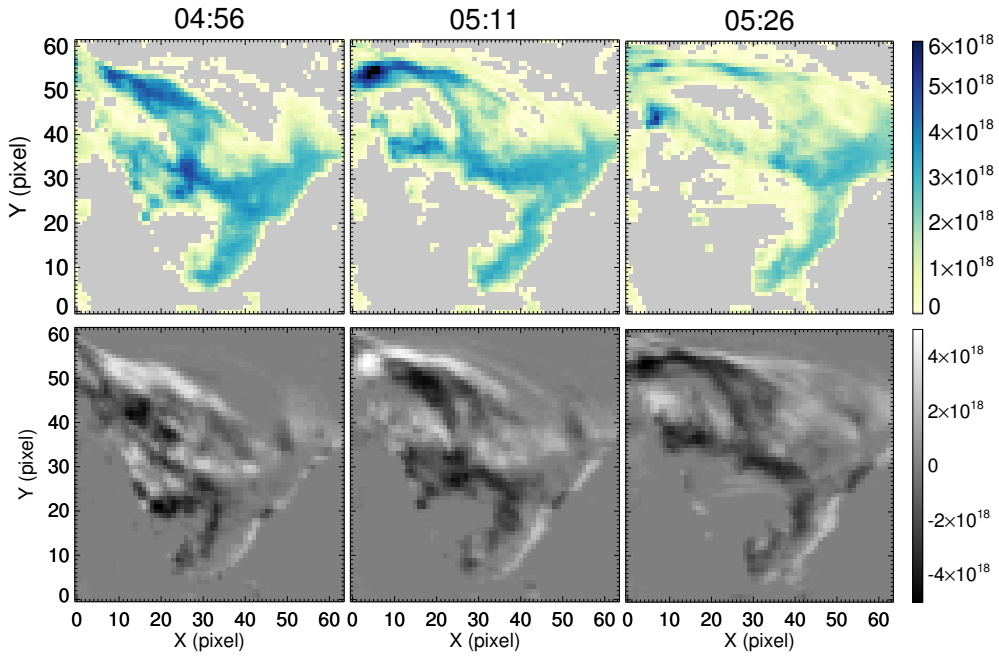

Figure 4.8: The evolution of column number density and flows in the dynamic portion of the prominence as seen from STEREO-B/EUVI. *Top row*; Evolution of column number density, measured in N_H cm^{-2}, detailing the mass flow initiated at $\approx$ 04:40 UT on 11 December 2011. This large mass flow can be seen as an increase in column number density at the top-left of the image. *Bottom row*; Running difference images of the column number density evolution measured in ΔN_H cm^{-2}. Features becoming more (less) dense in time appear white (black). The running difference image for 04:56 UT was constructed by subtracting the column number density map at 04:41 UT. This further highlights that the mass was moving towards the north-eastern footpoint of the prominence (top-left of each image). Resolution is $\approx 1.6''$ per pixel.

data-rate, between the Earth and the STEREO spacecraft in 2011, it was only taking high-cadence observations in a single passband at this time. Therefore, using the observations taken in the 195 Å passband alone, it was only possible to apply the simpler, less-well constrained monochromatic method to extract densities and masses of the prominence plasma.

The method was applied to the STEREO observations, specifically those within the ROI indicated in panel d of Figure 4.1, from 19:26 UT to 05:56 UT on 10-11 December, respectively. Figure 4.8 details the results and shows the evolution of the column number density within the ROI for three snapshots centred on the period of time that the largest material flow was observed (04:45 – 05:26). The dynamic portion of the prominence appears as a triangular shape, where the straight edge

to the bottom-left of the image corresponds to the limb of the Sun. The average value for the prominence's column number density, measured across the ROI, was approximately 4.5×10^{18} cm^{-2}, as seen in the top panels of Figure 4.8.

In the 04:56 UT panel of Figure 4.8, a large dense structure can be seen in the upper-left quadrant of the ROI. At 05:11 UT, this dense structure can be seen to have concentrated and elongated slightly, with the densest portion seen close to the position of the solar limb. Then, at 05:26, this dense structure seems to have disappeared, leaving a thin dense structure behind in its place. This has been further highlighted using *running density difference* images shown in the bottom panels of the same figure. In each case, these are constructed by subtracting each column number density map from the previous one. The observed motion of the blob towards the top-left from the perspective of STEREO corresponds to motion towards the north-eastern end of the prominence as viewed by SDO/AIA. Therefore, combining the observations captured by both spacecraft it is highly probable that the material was flowing out of the prominence and towards the surface. This is indicated by the material having flowed along curved paths oriented towards the surface, as if being guided by the host prominence field, and the brightenings described in Figure 4.5 would therefore be consistent with the material heating as it approached lower altitudes.

The column number density measurements are then converted to a mass estimate for each snapshot according to the method of Carlyle et al. (2014) *i.e.*, by multiplying by the mass of hydrogen and the plane-of-sky area of a STEREO pixel (assuming a distance of 1 Astronomical Unit). The results show that the total mass within the ROI gradually increased from 4×10^{13} g to 8.8×10^{13} g over approximately eight hours, shown in panel c of Figure 4.9, consistent with the prominence having slowly risen above the solar limb due to solar rotation. This apparent increase in mass within the ROI has partially masked the initiation of the smaller-scale material flow previously noted to have started at 01:30 UT. Then, the large material flow previously identified to initiate at 04:40 was measured to have reduced the total target mass to 2.2×10^{13} g in just over an hour.

These results indicate that the prominence studied here was large and dense throughout the lead-up to its eruption. A large and sudden flow of dense material from the prominence apex towards the north-eastern footpoint decreased the density of the material contained within the prominence. It is therefore evident that from 04:00 UT onwards to eruption the total mass in the prominence's measurable portion decreased by more than two thirds ($\approx 6.6 \times 10^{13}$ g).

4.3.5 Prominence and Plasma Kinematics

In the previous sections several large, dense pockets of material have been tracked moving away from the apex/middle of the prominence structure and down towards the surface. The 1D velocity estimate, derived from the stack-plots in Figure 4.5, of the large mass-deposit that left the apex of the prominence at 04:40 UT is ≈ 28 km s^{-1}. The second perspective offered by STEREO-B/EUVI shown in Figure 4.8 indicates that the large mass deposit originated from a height of ≈ 40 Mm, ≈ 30 minutes earlier than suggested in the stack-plots of Figure 4.5. This combination of the stack-plot observations made from both spacecraft indicates that the mass-deposit had a 2D linear acceleration of ≈ 12 m s^{-2}, and reached a velocity of ≈ 31 km s^{-1} as the material approached the surface. Note that the acceleration of the mass flow was an order of magnitude lower than free-fall at the solar surface, caused by *e.g.*, a non-vertical flow vector and/or the flow encountered an increased background density as it travelled towards the surface facilitated by the constricting magnetic field of the low solar atmosphere.

As previously stated in Section 4.2, the dynamic portion of the prominence erupted whilst the restrained portion did not. Panel a of Figure 4.9 shows the height - time evolution of this dynamic portion of the prominence from the perspective of STEREO-B. The line used to construct this stack-plot is radial and specified in Figure 4.1c. The evolution of the prominence height with time was measured by manually selecting the leading edge of the prominence. This was repeated six times to minimise user bias and provide an average position. The contribution to the height - time evolution due to solar rotation was then removed, revealing four

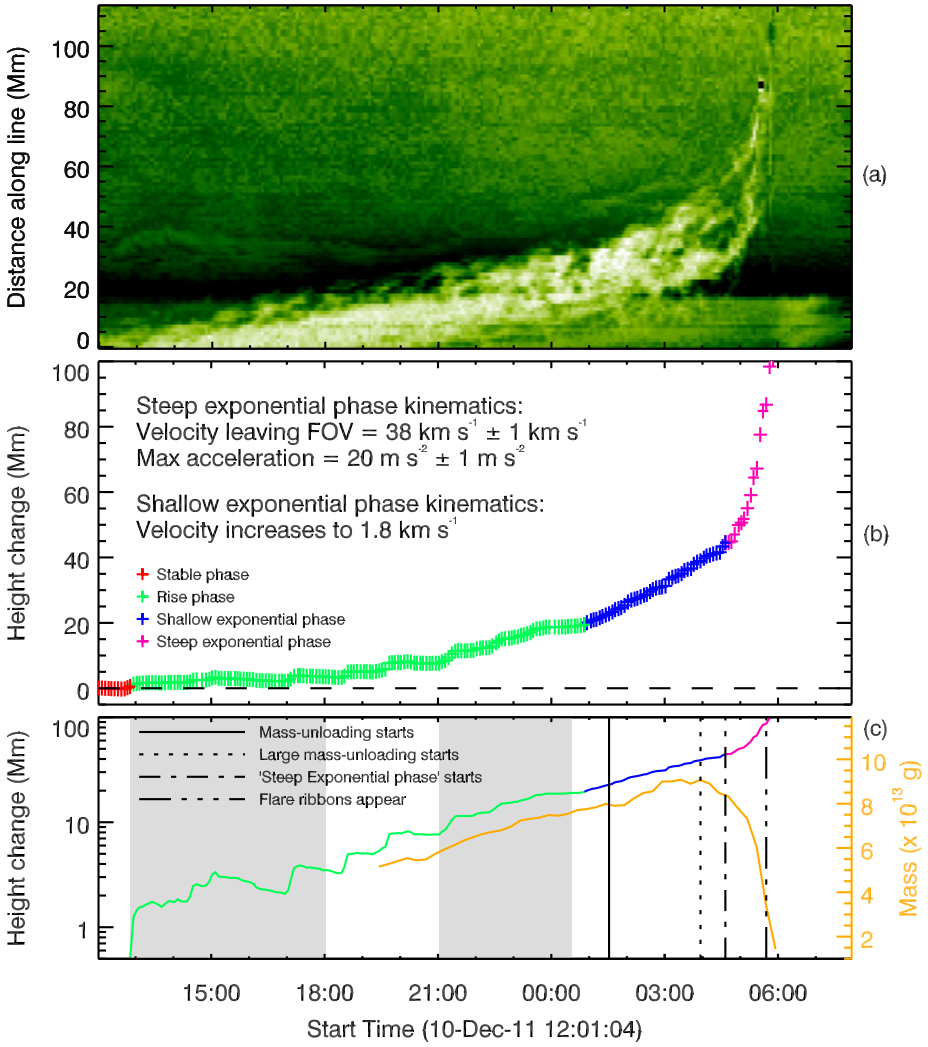

Figure 4.9: The evolution of the prominence height and mass with time. *Panel a*; The height–time stack-plot taken along the line specified in Figure 4.1c shown using a reversed colour table. *Panel b*; The solar-rotation-removed evolution of the dynamic portion of the prominence as it evolved and erupted. Red indicates the stable phase, green indicates the rise phase, blue indicates the shallow-exponential phase, and magenta indicates the steep-exponential expansion phase. Kinematics are derived from the fitting of an exponential function to the magenta region of evolution, and a linear line to the blue region. *Panel c*; The height - time profile as in *b* but with a logarithmic scaling, compared to the evolution of mass contained within the FOV enclosing the prominence over time, as seen by STEREO-B/EUVI. The initial increase in mass corresponds to larger portions of the prominence being visible above the limb over time due to solar rotation, and can therefore be considered to be artificial. Shaded patches indicate the times of flux cancellation recorded along the PIL and the nearby bipole emergence. Vertical lines indicate (from left to right) time of first visible mass flow, the time of the largest mass deposit, start of the steep-exponential expansion, and initial appearance of the flare ribbons and twin EUV dimmings.

main evolution domains within the lead-up to the eruption that are summarised in Figure 4.9b:

i) A stable phase (red). The horizontal trend suggests the evolution seen in the stack-plot at this time was due to solar rotation alone. The average position of these points was set as the origin of the y-axis. Therefore, any evolution in the prominence caused by anything other than solar rotation can be easily identified.

ii) A rise phase (green). This region describes the deviation from stable phase and the initial slow rise of the prominence through the solar atmosphere.

iii) A shallow-exponential phase (blue). So named as the height - time evolution is approximately linear when plotted on a logarithmic scale as in Figure 4.9c, suggestive of a marginal instability (a very shallow exponential).

iv) A steep-exponential phase (magenta). Fitting this phase of the height - time profile with the exponential function results in a final radial velocity estimate of the prominence of $v \approx 38 \pm 1$ km s^{-1}, a larger-than-average velocity for a quiescent prominence eruption according to Loboda and Bogachev (2015). After the mass draining the prominence was then seen to accelerate with a value of $a \approx 20 \pm 1$ m s^{-2}, indicating the initiation of the impulsive acceleration phase of a CME *i.e.*, the prominence began to erupt (Schrijver et al., 2008).

Figure 4.9c compares the height - time profile of the prominence using a logarithmic scale, with the evolution of its mass derived from the hydrogen column number density measurements of Section 4.3.4. It is shown that the expansion of the prominence between $\approx$ 01:00 UT and 04:40 UT was near-exponential, as indicated by the near-linear gradient. Interestingly, the total mass of the prominence began to decrease at $\approx$ 04:00 UT, approximately 40 minutes before the prominence was seen to accelerate significantly. Therefore, it appears that after a large amount of the mass had drained from the system the radial evolution of the prominence accelerated to a larger exponential expansion.

4.4 Discussion

In this chapter, a case study of a prominence that experienced large-scale plasma flows immediately prior to its eruption was undertaken to ascertain whether these flows were responsible for its eruption. However, additional magnetic dynamics were observed in the lead up to the eruption that have previously been shown to facilitate prominence eruptions and so these dynamics also required attention. In summary, the observed dynamics were,

- Flux cancellation along the PIL underneath the prominence (cf. Zhang et al., 2001). Observed to have occurred between 17 and 12 hours prior to the eruption.
- The nearby emergence of a small, favourably-oriented magnetic bipole (cf. Chen and Shibata, 2000). Observed to have occurred between 9 and 5.5 hours prior to the eruption.
- Large-scale flows seen to originate at the middle of the prominence and propagate towards the surface (cf. Low, 1996). Observed to have occurred between 4.5 hours and immediately prior to the eruption.

At the start of the period chosen for the analysis of the prominence eruption (12:00 UT on 10 December) a decrease in surface flux was recorded along the PIL that lay underneath the prominence of interest. This indicates the occurrence of flux cancellation and the concentration of non-potentiality along the PIL during this time. Unfortunately, the easternmost border of the summation bound in Figure 4.3 lay at $\approx 60°$. Therefore, due to the increased noise in LOS magnetic data past the 60° limit (Hoeksema et al., 2014), the evolution in flux could not be studied further back in time. Hence, it is only possible to *suggest* that the observed flux cancellation was related to the flux rope formation process described in van Ballegooijen and Martens (1989). Furthermore, as the prominence was observable for several days prior to the observation period studied in this chapter, the recorded flux cancellation cannot be related to the *initial* formation of the prominence. If there had

been a preexisting flux rope present above the PIL, as indicated by the pre-existing prominence, then the negative trend of total flux implies the injection of additional flux into the flux rope system.

As suggested by the model of van Ballegooijen and Martens (1989), the plateauing trend in the flux evolution indicates that the reconnection injecting additional flux into the proposed flux rope had ceased by or just after 18:00 UT on 10 December. This injection of free energy would have caused the flux rope to increase in height and expand in order to find a new equilibrium with its surroundings. It is possible that the widening of the prominence (Figure 4.5d) is the observational signature of the prominence rising/expanding. Unfortunately, due to the data gap in the AIA 171 Å passband observations between 15:32 and 16:50 UT on 10 December it is not possible to extrapolate this backwards in time.

The emergence of the nearby bipole studied in Section 4.3.2 began at $\approx$ 21:00 UT, after the flux cancellation recorded along the PIL had plateaued. The work by *e.g.*, Feynman and Martin (1995) and Chen and Shibata (2000) suggests that such an emerging bipole was favourably-oriented for reconnection with the field overlying the prominence of interest, *i.e.*, the negative polarity of the bipole was closer to the negative polarity of the hosting bipolar field (recall Figure 2.12). Indeed, if there was an interaction between the two systems then the overlying field above the prominence would have been weakened as a result of the proposed reconnection, as in Williams et al. (2005). The prominence would then have been able to expand to a higher height within the corona at a speed proportional to the reconnection rate between the bipole and the field overlying the prominence. Based on the stack-plot presented in Figure 4.9a, panels b & c of the same figure show that the prominence appeared to have been in equilibrium for approximately an hour prior to 21:00 UT. After 21:00 UT, and the beginning of the emergence of the bipole, the same plots describe the prominence as having resumed its expansion through the corona. The height - time evolution of the prominence is then seen to have plateaued at 23:30 UT. At this time, the nearby bipole was approaching the peak of its emergence (see Figure 4.4, actual peak 00:30 UT on 11 December) and

therefore it can be envisioned that the reconnection rate between the two systems would have reduced and ultimately stopped.

It is worth noting that an additional, smaller bipole was seen to have emerged at $\approx$ 20:30 UT beneath the western portion of the prominence. Observationally it appears there was also some re-organisation of the field topology in the vicinity of this flux emergence, as indicated by the sporadic, bright extensions away from the location of the bipole. However, the orientation of this smaller bipole with respect to the surrounding field suggests that it was not favourably oriented for reconnection, as was the case with the larger bipole that has been studied in Section 4.3.2. Nevertheless, it is possible that this smaller bipole was involved in the evolution of the system, even if to a currently unmeasurable degree.

Although the presented analyses suggest a tenuous connection between the noted emergences and the evolution of the prominence, the post-eruption large twin EUV dimmings typically associated with the footpoints of the proposed flux rope (cf. James et al., 2017) are seen to have migrated counter-clockwise and the western dimming is seen to have approached and eventually enveloped the location of the bipole studied in Section 4.3.2, indicating a relationship between the bipole and the footpoints of the erupting CME. However, it is unlikely that such small bipoles were the sole influences on the evolution of the prominence height after 21:00 UT on 10 December.

The prominence of interest was located within the northern hemisphere and, according to the combined EUV and magnetogram observations from AIA and HMI respectively, it was rooted in a positive-leading and negative-trailing bipolar region. This, in combination with the EUV observations of the post-eruption surface brightenings, suggests the proposed flux rope containing the prominence would have been left-handed with a negative chirality (cf. Mackay et al., 2010). Green et al. (2007) suggested a flux rope in this configuration should rotate anti-clockwise about its PIL as it expands. Figure 4.5d is a stack-plot defined by a line that is a perpendicular bisector of the axis of the dynamic portion of the prominence. In this plot, at $\approx$ 21:00 UT on 10 December, the prominence was seen to have started rotat-

ing counter-clockwise about its PIL. The combination of this observation and the previously discussed expansion of the prominence beginning at approximately the same time is consistent with those conclusions presented by Green et al. (2007). In addition to this, the counter-clockwise rotation can be seen to continue throughout the period leading up to the eruption at 05:53 UT on 11 December, whereas the emergence of the bipole – the possible cause of the height increase from 21:00 UT on 10 December – ceased by 00:30 UT on 11 December. This suggests that the observed persistence in rotation could be due to the proposed flux rope having become kink-unstable. Nevertheless, this does not necessarily override the role of the emerging bipole in the expansion of the prominence, as the combination of the two mechanisms are likely to have influenced the temporal evolution of the height of the studied prominence.

Up to this point, it has been assumed that the prominence was suspended by a flux rope topology. However, the event described here lacks certain features that are usually identified in observations when a flux rope is present; for example, there is little evidence of a cavity in SDO/AIA 193 Å images that would outline the shape of a possible flux rope when passing the eastern limb. The only explanation for this is that the angle that the prominence made with the LOS of either SDO or STEREO-B was not optimal for a cavity observation, *i.e.*, the structure was not observed along its axis (cf. Gibson et al., 2006; Forland et al., 2013). However, the combined observations of flux cancellation in the prominence channel, the suggested onset of kinking, the post-eruption twin EUV dimmings, and the brightenings along the length of the prominence during the eruption that appear to outline helical field are most consistent with the flux rope theory.

Interestingly, the prominence can be seen to have fanned out during this kinking. This was most evident on the western side of the prominence as the field lines associated with the fanning were highlighted by material suspended along their length, as previously stated in Section 4.3.2. The flows appeared to trace the curvilinear paths of the fanning field lines from $\approx$ 01:30 UT until eruption. The magnetic topology of a flux rope has been adopted in order to explain the observed

dynamics of the prominence, however it is difficult to reconcile how the highly twisted field lines of these studied flux ropes could produce the near-linear motions of plasma observed in this event (*e.g*, Roussev et al., 2003; Mei et al., 2017; Guo et al., 2017). Interestingly, extrapolations of less-twisted flux ropes, such as those by Su et al. (2011) and Jiang et al. (2014), are easier to compare to the observations as they contain very weakly twisted field lines that pass through the axes of the extrapolated flux ropes. However, as pointed out by Aulanier and Démoulin (1998), the location of the dips that contain the cool, dense material of a prominence are unlikely to reach entirely up to the axis of the flux rope, with the majority of the material lying in the lower portions (cf. Gunár and Mackay, 2015). Nevertheless, the assumption that the prominence material lies entirely within the dips of the magnetic flux rope is a first order approximation. With the inclusion of the thermodynamic instability, theorised to occur in the solar environment (Field, 1965), material may be able to be suspended in higher portions of a flux rope including the more weakly twisted field of the flux rope axis. In addition, work completed by Su et al. (2011), and more recently by Polito et al. (2017), successfully reconstructed the diffuse footpoints of flux ropes, as their observations had initially indicated, a feature not currently achievable through simulations. Therefore the combination of magnetic dips, the thermal instability, and the possibility of a diffuse flux rope footpoint offer explanations to the observations presented in this chapter, *i.e.*, that the material was seen to travel along curvilinear field lines associated with the flux rope and have footpoints that spanned supergranular boundaries.

Continuing with the evolution of the prominence, Figure 4.9 suggests that the proposed flux rope containing the prominence became marginally unstable at 01:00 UT on 11 December, as indicated by the linear height–time evolution on the logarithmic scale of Figure 4.9c. As a consequence of flux rope expansion, flux rope field lines that suspend prominence material above the surface increase in their gradient with respect to the surface. At some time, this would cause the concave-up sections of the field lines to become more shallow or even disappear and therefore no longer be capable of supporting the prominence material against

gravity (*e.g.*, Fan, 2017, 2018). Prominence material within such a flux rope would then drain from the system as it continued to expand (Mackay et al., 2010). For the event presented in this chapter, the first obvious observation of 'mass-draining' is seen to have initiated on the north-eastern side at $\approx$ 01:30 UT. Then, after approximately three hours of sporadic and varied mass motions, the largest mass deposit was observed at $\approx$ 04:30 UT by SDO/AIA to have propagated towards position A, as shown in Figure 4.5. Interestingly, this large decrease in mass is shown in Figure 4.9 to have actually initiated at 04:00 UT ($\approx$ 30 minutes prior) although this discrepancy is likely due to difficulties in isolating the initiation of the mass motion among all of the additional, unrelated intensity variations shown in Figures 4.5b,c. Therefore, it is concluded the large mass flow began at 04:00 UT. This rapidly reduced the mass contained within the prominence, preceding the beginning of the 'steep-exponential phase' of the height - time profile of Figure 4.9, and the splitting of the prominence into two separate structures.

It has been established in the last few decades that the eruption of flux ropes is readily triggered and driven by ideal magnetic instabilities such as the kink and torus instabilities, respectively (Török and Kliem, 2005; Kliem and Török, 2006). However, this does not necessarily preclude the role of mass in being able to modify the pre-eruption equilibrium. Indeed, if the observed 'mass-draining' were responsible for the change between the two exponential expansions observed for the prominence studied in this chapter, then the ratio between gravitational forces supplied to the flux rope *vs.* the forces acting down on the flux rope from above *must* have been on the order of or greater than one. *i.e.*, the buoyed flux rope had to have been able to overcome the restricting magnetic-tension forces in order for the system to have accelerated as observed. This can be explored through an order-of-magnitude estimation of the magnetic-tension force, as outlined in the derivation presented in Equation 6.2.18 of Aschwanden (2005). The resulting ratio between

the gravitational forces and magnetic forces is then,

$$\text{ratio} = \frac{\rho(m,V)g}{\left(\frac{B^2}{\mu_0 r_c}\right)}, \tag{4.7}$$

where ρ is plasma density, a function of plasma mass m and volume V, g is acceleration due to gravity, μ_0 is the permeability of free space (substituted for 4π when considering cgs units), and B and r_c are the magnitude and radius of curvature of the overlying magnetic field (loops), respectively, that supply the tension acting down on the flux rope.

The mass of the drained plasma was estimated in Section 4.3.4. The EUV observations taken by STEREO and SDO were used to measure the dimensions, and therefore the volume, of the prominence; a prominence slab was assumed with approximate dimensions of, 2×10^8, 20×10^8, and 200×10^8 cm. Therefore, the density of the prominence is estimated to have decreased by 8.25×10^{-15} g cm^{-3}. The acceleration due to gravity was taken as that at the solar surface, 2.74×10^4 cm s^{-2}. The magnitude of B for the field overlying the flux rope was estimated by computing a potential-field-source-surface (PFSS) model at 06:04 UT, at the start of the eruption (*cf.* Schrijver and De Rosa, 2003). The PFSS model of the coronal magnetic field was extrapolated using photospheric boundary conditions that are updated in six-hour intervals. Although the extrapolation was carried out on a post-eruption photospheric magnetic field, eruptions themselves do not perturb the photospheric configuration of the field (recall from Figure 1.5 that $\beta > 1$ in the photosphere). Hence, the photospheric field configuration at this time was deemed to have more closely matched the photospheric conditions at the time of mass-draining than those present in the magnetogram taken $\approx$ five hours prior. The radius of curvature for the overlying field was taken as a range, with the lower bound being the height at which the height - time profile changed from the shallow-exponential to the steep-exponential phase, as seen by STEREO-B. With $r_c \approx 70$ - 90 Mm, this yields a magnetic field strength B for the apex of the potential field overlying the flux rope of between 3 and 2.2 G. From Eq. 4.7, the ratio between gravitational and

magnetic-tension forces is found to have been between 1.8 to 4.1 respectively at 04:40 UT, *i.e.*, the change from shallow- to steep-exponential phase. Therefore the height increase temporally associated with the mass-draining shown in Figure 4.9 is interpreted as this expansion of the magnetic field due to the weakening of the anchoring force supplied by the large, dense, and heavy prominence. In addition, the gravitational and kinetic energies of the plasma blob are calculated to have decreased by 1.1×10^{28} ergs and increased 4.8×10^{26} ergs respectively, suggesting the non-gravitational energy of the system (the flux rope + prominence) must have increased (in some way) by the difference.

In order to determine the evolution in the prominence density in the lead up to its eruption, the monochromatic and polychromatic column number density determination methods of Williams et al. (2013) and Carlyle et al. (2014) have been used. Of the two methods, the monochromatic method inherently returns a lower estimate of the column number density (which in itself is already a lower limit) than the polychromatic method as the simpler model does not account for filling factor and foreground fraction of emission; see Section 4.3.4 for specific details. Therefore, the absolute values calculated using the monochromatic method will have contained a systematic error, albeit currently unquantified, and could only be treated as estimations. In order to approximate this systematic offset, a multi-wavelength, multi-method study would have to be carried out on a single quiescent prominence projected above the limb and observed from a single perspective *e.g.*, using SDO/AIA. Nevertheless, the internal mass structure was well highlighted by examining the results of the monochromatic method applied to the target at multiple times, and an evolution in mass was estimated in Figure 4.9.

Although the polychromatic method applied to the SDO/AIA observations was able to constrain filling factor and foreground emission, and hence give a more certain lower-limit on column number density, it was not possible to infer a mass for the whole prominence in this instance due to the uncertainty of the unattenuated radiation field behind the prominence. Interestingly, the column number density estimates of portions of the prominence material derived using the polychro-

matic method were found to be almost two orders of magnitude greater than for the monochromatic technique. This suggests that either this prominence was far more dense than the STEREO-B data indicated, or the prominence structure resembled a slab topology, and SDO was simply observing a thicker structure from above than STEREO-B was from the side. Hillier and van Ballegooijen (2013) provide a topological description of such a possible slab structure from the magnetic dips in a flux rope. Nevertheless, if the density estimates of SDO were more representative of the prominence, the ratio of gravitational forces to magnetic forces would increase by the corresponding orders of magnitude, indicating that the mass-draining played a significant role in the final evolution of the prominence.

Finally, the prominence is seen to have split into two distinct structures in the lead up to its eruption; the dynamic portion that erupts and the restrained portion that remains. Gilbert et al. (2001) describes a partial prominence eruption that they observed, and offer an explanation to how the magnetic environment, in their case a flux rope, can evolve and separate during an eruption. Unfortunately, no spectroscopic observations are available for the event that has been presented here, therefore the identical types of observations are not available for study and so the applicability of their model to the available obervations cannot be directly tested. However, as both of the split prominences are assumed to involve flux ropes, it is reasonable to assume that this event may share some similarity to theirs. According to Figure 4.2, the separation can be seen to have occurred by $\approx$ 05:26 UT on 11 December, after the initiation of the large mass-draining. As demonstrated above, it has been suggested that the mass-draining was responsible for the change in the nature of the expansion of the prominence from a shallow to steep-exponential rise. It also appears that the mass-draining was located at the apex of the dynamic portion of the prominence, reducing the anchoring force of this region of the prominence to the surface. With no noticeable mass-draining having occurred within the region that becomes the restrained portion, it is reasonable to assume that this region did not experience the same reduced anchoring force and expansion that the dynamic portion underwent. Therefore, during the expansion of the dynamic portion, it is

possible that the magnetic structure underwent some form of vertical reconnection due to the rise, as in the model presented by Gilbert et al. (2001), and this permitted the splitting of the proposed flux rope into two. Interestingly, the material suspended in the restrained portion of the proposed flux rope, in the event presented here, was visibly perturbed during the eruption of the dynamic portion. This perturbed material was seen to then reform the restrained portion of the prominence some hours after the eruption, suggesting that the magnetic structure of the restrained portion did not reconfigure to a significant degree, or lose much mass, during the nearby eruption and perturbation.

4.5 Conclusions

A multi-wavelength study of the pre-eruption period of the partial prominence eruption on 11 December 2011 has been presented using data from two spacecraft. The use of multiple viewpoints has revealed the evolution of the prominence height in response to the material dynamics within; a separation otherwise unachievable from a single perspective. Four main stages of evolution have been isolated: a stable phase (12:00 - $\approx$ 13:00 UT), a rise phase (13:00 - 01:00 UT), a shallow-exponential phase (01:00 - 04:40 UT), and a steep-exponential phase (04:40 UT onwards).

The initial rise phase coincided temporally with flux cancellation along the PIL below the prominence. The further rise of the proposed flux rope is shown, through temporal coincidence, to have been facilitated by both a nearby bipole emergence and the kink instability. This highlighted the cancellation, emergence, and kinking as the potential triggers for the partial eruption (Wang and Sheeley, 1999; Török and Kliem, 2005). The proposed flux rope that contained the prominence was then seen to have become marginally-unstable, as demonstrated by a shallow-exponential evolution in the height of the prominence starting at 01:00 UT. A few hours later, at 04:00 UT, a large mass flow was observed to have travelled from the prominence body towards its footpoint that was measured to have drained $\approx$ 70 % of the entire prominence's mass (a larger percentage than those reported previously by Bi et al. (2014) and Fan, 2017). Taking a ratio between the reduced gravitational force and

the magnetic-tension force that acted on the flux rope, a lower-limit range of 1.8 to 4.1 was found, indicating gravitational dominance at the time of the flow. The expansion of the dynamic portion of the prominence was then seen to accelerate to a large exponential and ultimately erupt from the solar atmosphere.

These results suggest that the magnetic evolution associated with the evolution of the proposed flux rope occurred far in advance of the eruption of the prominence. However, the significant amount of mass measured to have drained from the prominence occurred immediately before the acceleration and eruption of the prominence. Therefore, it is concluded that the observed mass-draining was responsible for the transition between the two exponential expansions of the prominence, and triggered its eruption.

In this chapter, it has been established through an observational case-study that the removal, or draining, of (prominence) mass from a flux rope can cause it to lose global stability, and erupt into the heliosphere. This has been achieved using order-of-magnitude estimates to the forces involved assuming that the flux rope was close to its loss of equilibrium *i.e.*, that the gravitational and magnetic-tension forces were majority-responsible for the maintained equilibrium. Although a reasonable assumption, by definition this approach did not account for the *full* equilibrium as the flux rope self- (hoop) force was neglected in its entirety. Similarly, this has been shown for a single event and it is not clear whether this is a ubiquitous effect or an isolated incident. Therefore, a more general model that includes the equilibrium of all forces acting on the flux rope is required and presented in the next chapter.

Chapter 5

Modelling the Effect of Mass-Draining on Prominence Eruptions

In this chapter a simple model is presented to further explore the observational conclusions of Chapter 4, and quantify the effect of "mass-draining" during the pre-eruptive height-evolution of a solar flux rope. Whereas the previous chapter focused on a specific case-study, the model presented here builds evidence for a more general relationship between a flux rope and the evolution of mass within. The flux rope is modelled as a line current suspended within a background potential magnetic field. It is first shown that the inclusion of up to 10^{12} kg of mass can modify the height at which the line current experiences loss-of-equilibrium by up to 14%. Next, it is shown that the rapid removal of this mass prior to the loss-of-equilibrium enables the height of the flux rope to increase sharply as it approaches this loss-of-equilibrium point, and without upper bound (*i.e.*, eruption) if the height increase ends above the critical height. This indicates that the critical height for the loss-of-equilibrium can occur at a range of heights depending explicitly on the amount and evolution of mass within the flux rope. Finally, it is demonstrated that for the same amount of drained mass, the effect on the height of the flux rope is up to two orders of magnitude larger for quiescent than for active region prominences.

The work presented within this chapter forms the basis of the work published in *The Astrophysical Journal* by Jenkins et al. (2019).

The analytical derivation presented in Section 5.3.4 was assisted by G. Aulanier, P. Démoulin (Observatoire de Paris), and G. Valori (University College London). The numerical computations were carried out by M. Hopwood (University of Adelaide & University of Birmingham). All remaining computation and analysis was carried out by myself. D. M. Long and L. van Driel-Gesztelyi assisted in the context and interpretation of the results.

5.1 Introduction

In the simplest sense, a prominence exists in the solar atmosphere as a result of the equilibrium between the upward Lorentz force of its host flux rope, the downward Lorentz force of the background magnetic field, and the downward gravity force of the prominence material within the flux rope. The study of the evolution and eruption of a flux rope within the solar atmosphere is essentially a study of the balance/evolution of these forces in 1 – 3D, and either statically or in time.

In order to isolate the mechanism responsible for solar eruptions, work was carried out using data-informed, order-of-magnitude models aimed at quantifying the total amount of energy (magnetic, kinetic, gravitational) involved in eruptions, and the sources therein (*e.g.*, Low, 1981; Démoulin and Priest, 1988; Martens and Kuin, 1989; Démoulin et al., 1991; Forbes and Isenberg, 1991). The results of the studies by Martens and Kuin (1989) and Démoulin et al. (1991), in particular, concluded that the influence of the gravity term is negligible assuming "typical" values for prominence mass; gravity is unlikely to be able to perturb the equilibrium dominated by the magnetic pressure and tension forces. As a result, the majority of complex, time-dependent MHD models and simulations that have followed have assumed a force-free magnetic flux rope that satisfies the zero-β approximation (*i.e.*, the environment surrounding and within the flux rope contains either zero mass or temperature, *e.g.*, Titov and Démoulin (1999) and Filippov, 2018). Hence, such modelled/simulated flux ropes do (can) not contain the cool, dense plasma

that comprises a prominence (as summarised by *e.g.*, Cheng et al. (2017), Gibson (2018), and references therein).

However, novel observations, magnetohydrostatic (MHS), and MHD modelling in addition to the results presented in Chapter 4 are beginning to suggest that mass may be able to influence the local and global properties of magnetic flux ropes (*e.g.*, Low et al., 2003; Petrie et al., 2007; Seaton et al., 2011; Blokland and Keppens, 2011; Gunár et al., 2013; Bi et al., 2014; Reva et al., 2017; Fan, 2018). Of those, the conclusions by Bi et al. (2014), Reva et al. (2017), and Chapter 4 are based on observations of large flows within quiescent prominences that are suggestive of material having been evacuated/drained out of the host flux rope immediately prior to its eruption. Then, the Shafranov shift (cf. Shafranov, 1958) as explored by Blokland and Keppens (2011), and based on work by Petrie et al. (2007), details how varying the gravity term in their 2.5D MHS model can cause the axis of their stable flux rope to decrease in height. Similarly, Gunár et al. (2013) discussed how a significant amount of mass loaded onto field lines in their 3D MHS simulation of a prominence-flux rope system, required an increase in the radial component of the host magnetic field to maintain the suspension of the plasma. Then, the fully 3D MHD simulation of a prominence eruption by Fan (2018) demonstrated for the first time that a comparison between two identical simulations - aside from one simulation containing prominence mass and the other not - reveals that the eruption of the mass-loaded flux rope can be delayed by almost a day in comparison to the eruption of the massless flux rope. However, this was shown for a single case-study, with a single set of initial conditions and considering this is a fully MHD simulation, a parametric study has not been carried out. Similarly, it is unclear how well the model scales between conditions representative of different regions within the solar atmosphere.

Before the advent of such advanced, 3D MHD simulations, early work by van Tend and Kuperus (1978) presented a 2D analytical model in which the flux rope was approximated as a straight line current suspended at equilibrium in a background potential magnetic field. Although a simplified setup was employed, the

authors qualitatively demonstrated that increasing the magnitude of the line current causes its height above the solar surface to increase. This relationship between the current and height of the line current can be represented with an equilibrium curve. In addition, they concluded that there is a point at which an increase in the strength of the line current would no longer result in a solution on the equilibrium curve. At this time, the line current was said to have experienced 'loss-of-equilibrium'. Importantly, such a simple 2D line current model is, as demonstrated by Démoulin and Aulanier (2010), identical in its equilibrium conditions to its fully 3D MHD counterpart (see also Kliem et al., 2014) and, as analytical solutions can exist, requires a fraction of the computational solving power.

It was concluded in Chapter 4 that the mass-draining triggered the eruption of the case-study prominence by using a quantitative estimation based on the Lorentz force equation, specifically the ratio between the modification of the gravitational force due to the reduction in mass and the force of the background magnetic tension restricting the height-evolution of the flux rope. However, this order of magnitude estimate of the importance of the mass-draining does not account for the full equilibrium conditions of the host flux rope. Therefore, in this chapter, an extension to the model developed by van Tend and Kuperus (1978) is presented that enables such a study of the role of mass in the evolution of a line current in quasi-equilibrium. First, a comparison is made between the mass-loaded and mass-less line current configurations, highlighting the effect of mass on the global stability criteria. Next the removal of mass (or "draining") from a pre-eruptive line current is explored to identify whether mass can modify the global height of the line current within the solar atmosphere. As the stability criteria of a 2D line current and a 3D flux rope are identical, to avoid confusion by using both terms interchangeably the line current will henceforth simply be referred to as a flux rope unless explicitly referring to the model. The general model is described in Sections 5.2 and 5.3, and applied in Section 5.4 to a bipolar background potential magnetic field. In Section 5.5, the model is further constrained with measurements made from the observations presented by

both Seaton et al. (2011) and in Chapter 4. Finally, a discussion and summary are presented in Section 5.6.

5.2 Model Concept

Following the formulation outlined in Démoulin and Aulanier (2010), hereafter DA10, a flux rope can be modelled in cartesian coordinates as a magnetic field generated by an infinitely long line current I at a given height h above the photosphere. It can be assumed that the majority of curvature of a magnetic flux rope that hosts a prominence is localised to its footpoints, otherwise a prominence would drain along the inclined field lines. Therefore, as this curvature is located far from the centre of the prominence, the host flux rope in the vicinity of the middle of the prominence can be represented by a straight line current. An "image" line current *-I* is introduced under the photosphere that runs anti-parallel to the "real" line current. Following van Tend and Kuperus (1978), the additional image magnetic field beneath the surface results in no modification to the vertical, z, component of the photospheric magnetic field. This "image" current acts to increase the height of the "real" line current. The straight line current is then added to a background potential magnetic field $B_{\rm ext}$ that acts to force the line current towards the photosphere. A cartoon representation of these different field contributions is shown in Figure 5.1. The total field has an inverse configuration because of the presence of a flux rope (e.g., similar to the configuration of Figure 1a within Petrie et al., 2007). The line current is then in equilibrium if the sum of forces is zero,

$$\sum f = 0 \leftrightarrow f_{\rm u} = f_{\rm d} \Rightarrow IB_{-\rm I} = IB_{\rm ext}, \tag{5.1}$$

where $f_{\rm u}$ is the sum of the upward magnetic forces, the so-called *hoop force*, $f_{\rm d}$ is the sum of the downward magnetic forces, I $(-I)$ is the real (image) current, $-B_{\rm ext}$ is the horizontal background magnetic field component orthogonal to the current at height h, and B_{-I} is the strength of the magnetic field as a consequence of the

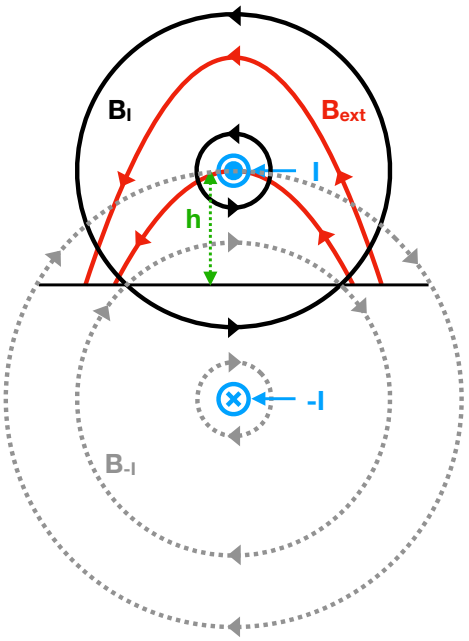

Figure 5.1: Cartoon diagram of the model set-up. The inverse magnetic configuration is formed by the superposition of three fields: the external potential field $B_{\rm ext}$ (solid-red), and the field generated by the line current (located at z=h) and its image (located at z=-h), drawn with solid-black and dashed-grey lines respectively. The line current at z=h is maintained by the balance of two Lorentz forces, an upward (hoop) force due to the magnetic field generated by the image line current, and a downward force from a stabilizing external potential field $B_{\rm ext}$. Model concept is identical to that presented by van Tend and Kuperus (1978).

image line current. The image magnetic field $B_{-\rm I}$ is derived from Ampère's law,

$$\begin{aligned} \oint B_{-\rm I} \cdot dl &= \mu_0 I, \\ \Rightarrow B_{-\rm I} &= \tfrac{\mu_0 I}{2\pi R}, \end{aligned} \tag{5.2}$$

where the strength of the magnetic field $B_{-\rm I}$ is measured at a point in space that is at a distance/height $R = 2h$ away from the line current, and μ_0 is the permeability of free space equal to $4\pi \times 10^{-7}$ in MKS units.

In order to simulate the existence of a prominence within a flux rope, the van Tend and Kuperus (1978) model is extended to include mass that is set to exist at the same point as the line current, *i.e.*, at height h. The inclusion of mass into the system results in an additional downward force that acts to further anchor the line

current. With the inclusion of mass, Eq. (5.1) becomes,

$$IB_{-\mathrm{I}} = IB_{\mathrm{ext}} + mg, \tag{5.3}$$

where m is the mass of the suspended plasma per unit length and g is the acceleration due to gravity. g is taken independent of h (since $h \ll r_\odot$, where $r_\odot$ is the solar radius) except where explicitly stated. All quantities in Eq. (5.3) are defined positive.

5.3 General equations

5.3.1 Equilibrium Current

Here, the general form of equations are established that will be applied to a specific B_{ext} in the following sections. The force f on the flux rope, per unit length, according to Eq. (5.2) and Eq. (5.3) is,

$$f = \frac{\mu_0 I^2}{4\pi h} - IB_{\mathrm{ext}} - mg, \tag{5.4}$$

where B_{ext} is a function of h (as well as other parameters depending on the selected model). $B_{\mathrm{ext}} > 0$ is set so that the external magnetic field creates a force oppositely directed to the hoop force, $\mu_0 I^2/4\pi h$, and an equilibrium exists in the limit $m = 0$.

The electric current needed for equilibrium is given by solving Eq. (5.4) for I with $f = 0$,

$$I_{\mathrm{eq,m}} = \frac{2\pi h B_{\mathrm{ext}}}{\mu_0} \pm \sqrt{\left(\frac{2\pi h B_{\mathrm{ext}}}{\mu_0}\right)^2 + \frac{4\pi}{\mu_0} m g h}, \tag{5.5}$$

where the lower index m has been added to indicate that the equilibrium current depends on the mass.

With finite mass, Eq. (5.5) provides two equilibria corresponding to the sign selection in front of the square root. With a negative sign selected, $I_{\mathrm{eq,m}} < 0$, which implies that both magnetic forces are upward and opposite to the gravity force in Eq. (5.4). This case has a vanishing current in the limit of a vanishing mass and does not correspond to a force free equilibrium with a flux rope (*i.e.*, $I \equiv 0$, therefore no

flux rope exists). Therefore, only the second case with a positive sign in front of the square root of Eq. (5.5) is considered,

$$I_{\mathrm{eq,m}} = \frac{2\pi h B_{\mathrm{ext}}}{\mu_0} + \sqrt{\left(\frac{2\pi h B_{\mathrm{ext}}}{\mu_0}\right)^2 + \frac{4\pi}{\mu_0} m g h}, \tag{5.6}$$

Supposing that $B_{\mathrm{ext}}(0)$ is finite, then for small enough h values such that $h \ll (\mu_0 m g / \pi B_{\mathrm{ext}}^2)$,

$$I_{\mathrm{eq,m}} \approx \frac{2\pi h B_{\mathrm{ext}}}{\mu_0} + \sqrt{\frac{4\pi}{\mu_0} m g h}. \tag{5.7}$$

Then, $I_{\mathrm{eq,m}}$(h) has a $h + \sqrt{h}$ dependence when h is small enough and $m > 0$. This behavior changes to a linear dependence when $m = 0$.

With $m = 0$, $I_{\mathrm{eq,0}}(0) = 0$, and since B_{ext} typically decreases faster than $1/h$ for large h values, $I_{\mathrm{eq,0}}(h) = (2\pi/\mu_0) h B_{\mathrm{ext}}$ will tend towards zero at large heights. This implies that $I_{\mathrm{eq,0}}(h)$ has a maximum (at least one) between small and large heights. However, if $m > 0$, $I_{\mathrm{eq,m}}(h)$ is dominated by the gravity term at large h values once B_{ext} has sufficiently decreased, then $I_{\mathrm{eq,m}}(h) \approx \sqrt{(4\pi/\mu_0) m g h}$ is a growing function of h for constant g. At even larger h values, as g is inversely proportional to $(r_\odot + h)^2$, then $I_{\mathrm{eq,m}}(h)$ will again tend towards zero, even for large mass values. Nevertheless, for low enough m and h values, $I_{\mathrm{eq,m}}(h)$ will still have a minimum at $h = 0$ and large heights, and a maximum (at least one) somewhere in between. It is the response of the flux rope to mass within this region that is the focus of this study.

5.3.2 Dependence of the Equilibrium current on Mass

Here, the effect of m on $I_{\mathrm{eq,m}}$ is investigated keeping all other quantities fixed,

$$\frac{\partial I_{\mathrm{eq,m}}}{\partial m} = g h \Big/ \sqrt{(h B_{\mathrm{ext}})^2 + \frac{\mu_0}{\pi} m g h} \geq 0. \tag{5.8}$$

Increasing the mass m requires the magnitude of the current to be increased so as to reach a given height (*i.e.*, to increase the hoop force).

Next, supposing $mgh \ll (\pi/\mu_0)(hB_{\text{ext}})^2$, a first order Taylor expansion of Eq. (5.6) provides,

$$I_{\text{eq,m}} \approx I_{\text{eq,0}} + mg/B_{\text{ext}}. \tag{5.9}$$

Then, the equilibrium current is comparatively increased by adding a term proportional to the mass and to $1/B_{\text{ext}}$. Since $B_{\text{ext}}(h)$ is typically a decreasing function of h, this implies that $I_{\text{eq,m}}$ is increasingly separated from $I_{\text{eq,0}}$ with height.

5.3.3 Mass-draining

Finally, the draining of prominence mass is studied to ascertain its effect on the host flux rope's equilibrium height and, possibly, its eruption. It is assumed that the draining is fast enough that there is a negligible evolution, through for example, diffusion (*e.g.,* van Driel-Gesztelyi et al., 2003), of the vertical component of the photospheric field distribution. This is modelled with the image current and implies that the associated potential field, B_{ext}, is unchanged. It is also assumed that this short-term evolution is done without reconnection. This implies that the magnetic flux, F, passing below the flux rope bottom (located at $z = h - a$, where a is the radius of the flux rope / line current) and the photosphere (at $z = 0$) is conserved.

van Tend and Kuperus (1978) suggested that a flux rope would experience loss-of-equilibrium if the current magnitude exceeded the maximum of the $I_{\text{eq,0}}(h)$ function, as with a classical electric circuit. DA10 (see also Démoulin et al., 1991; Lin et al., 2002) expanded on this by imposing a short-term MHD evolution with flux conservation to study the loss-of-equilibrium of a flux rope. The hybrid MHD / line current approach uses pseudo-time long-term evolution of model parameters, *e.g.*, photospheric flux density ϕ or average coronal twist T, to overcome the limitations of the classical approach. The evolution of one of the model parameters in this way enables the construction of a family of constant F curves which describe the short-term evolutions. The intersection of these curves with $I_{\text{eq,0}}$ details how a flux rope evolves as a function of the evolving parameter.

Two equilibrium curves, $I_{\text{eq,m}}(h)$ and $I_{\text{eq,0}}(h)$ are shown in Figure 5.2 together with five curves of fixed magnetic flux F, differing from each other as a result of

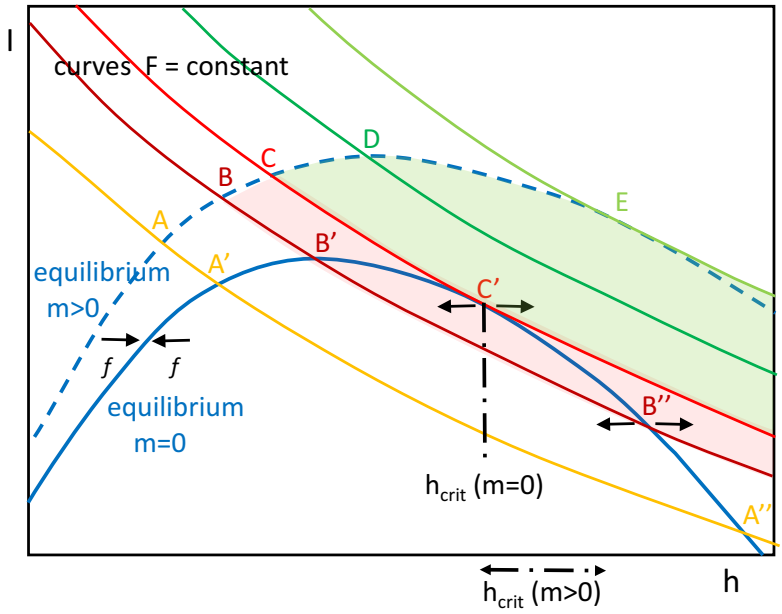

Figure 5.2: Schema showing the possible evolutions with mass-draining. The equilibrium curve with $m = 0$, $I_{\mathrm{eq},0}(h)$, is shown with a continuous dark blue line. The equilibrium curve with mass, $I_{\mathrm{eq,m}}(h)$, is above with a dashed line. The constraint of magnetic flux conservation, Eq. (5.12), is shown with the other coloured curves representing different starting points along $I_{\mathrm{eq},0}(h)$ for draining mass. If the draining mass starts between points C and E, no equilibrium can be reached without mass (region shaded in light green), while if draining is realized before point C (*e.g.*, at point A), another stable equilibrium could be reached. In the region shaded in pink, the finite kinetic energy accumulated may enable the line current to reach the unstable equilibrium without mass (such as point B″). The small black arrows indicate the direction of the total force when the line current is slightly shifted away from the equilibrium curve. The critical height(s) h_{crit} of the $m = 0$ ($m > 0$) line current is indicated with the vertical (horizontal) black-dash-dotted lines.

an evolution in, *e.g.*, B_{ext}. Assuming that the coronal configuration begins as nearly potential, the prominence and its flux rope would first evolve quasi-statically along the stable equilibrium curve of $I_{\mathrm{eq,m}}(h)$, with a height growing slowly with time as a result of the evolution of B_{ext}. At some point during this evolution, the draining of the full mass is assumed to occur fast enough to keep both B_{ext} and F unchanged, then the evolution is along the corresponding $F =$ constant curve towards larger heights. The general form of the $F =$ constant curve (Eq. (9) of DA10) for an

evolving $B_{\rm ext}$, hereafter defined as $I_{\rm evol}(h)$ is,

$$I_{\rm evol}(h) = \frac{2}{L_{\rm s}}\left(F + \iint_S B_{\rm ext}\,{\rm d}y\,{\rm d}z\right), \tag{5.10}$$

where S is the plane between the photosphere and the underside of the current channel (of radius a), and $L_{\rm s} = \frac{\mu_0 \Delta y}{\pi}(\ln(2h/a) + l_{\rm i}/2)$ and $l_{\rm i}$ are the external inductance and normalised internal inductance, respectively. For this set-up in which the current is focused at the edges of the current channel, $l_{\rm i} = 0$.

The effect of draining the mass depends on the location where it occurs. If it occurs at point A of Figure 5.2, or a nearby one, then a stable equilibrium $I_{\rm eq,0}$ exists at the intersection with the $I_{\rm evol}$ flux curve (at point A$'$). Comparing the height of stable equilibrium with and without mass linked by the same $I_{\rm evol}$ curve, the equilibrium with mass is always at a lower height (*e.g.*, $h_{\rm A} < h_{\rm A'}$) which is due to the downward gravity force compressing the $B_{\rm ext}$ configuration. As the draining point is shifted to larger heights, *e.g.*, at point B, the new equilibrium on $I_{\rm eq,0}$ curve is further away, at a larger height, from the initial one on $I_{\rm eq,m}$ curve. This is the case until the point C where the $I_{\rm evol}$ flux curve only touches the $I_{\rm eq,0}$ equilibrium curve tangentially. Equation (20) of DA10 demonstrates that the equilibrium is linear neutral at this tangent point C$'$, but it is unstable with the non-linear perturbation term taken into account (graphically the $I_{\rm evol}$ curve is extending to the right in the region where the force f is pointing towards large h values, so away from the equilibrium curve).

After the mass-draining occurs at a point such as A, the total magnetic force will be directed upward, accelerating the flux rope towards the equilibrium curve $I_{\rm eq,0}$. However, this equilibrium will be reached with a finite kinetic energy, enabling the line current to continue evolving along the $I_{\rm evol}$ curve. The line current will then continue on the other side of the equilibrium point with a change in sign of the total magnetic force. Finally, at some point, the motion will stop and reverse direction leading to an oscillation of the flux rope. This scenario also envisages damped oscillations towards the $I_{\rm eq,0}$ curve as the extra energy is progressively ra-

diated away by fast MHD waves. Such results have been reported in both 2D and 3D numerical simulations of prominence oscillations (*e.g.*, Schutgens and Tóth, 1999; Zhou et al., 2018, respectively).

Furthermore, the $I_{\rm evol}$ curve can also cross the other branch of the $I_{\rm eq,0}$ curve past the point C$'$, such as at points A$''$ and B$''$ in Figure 5.2. Since these equilibria are unstable to perturbations (see the f arrows in Figure 5.2, reproduced from DA10), there is the possibility of an eruption if the system has sufficient energy to reach this unstable part. This region is indicated qualitatively with a pink area in Figure 5.2. Its extension towards the side with small h values is limited by the ability of the magnetic force to decrease the kinetic energy before the unstable region, at larger h values, is reached. This particular aspect is not studied any further since it is expected to be an effect localised to the family of $I_{\rm evol}$ curves near to point C$'$ and this would need a detailed analysis (it depends both on m and $B_{\rm ext}(h)$). It is simply important to point out that an eruption may be started, by draining mass, before the line current evolves to the limiting curve $I_{\rm evol}$ that passes the first unstable point, C$'$, of the $I_{\rm eq,0}$ curve.

5.3.4 Modification of the Equilibrium Height

To study the effect of mass-draining, the notations $(h_{\rm m}, I_{\rm m})$ and (h_0, I_0) are introduced to represent the mass and mass-less equilibria, respectively, that are related by a common constant $I_{\rm evol}$ curve. The total flux passing between the bottom of the flux rope and the surface is,

$$F(h) = \frac{\mu_0 I}{2\pi} \ln\left(\frac{2h}{a}\right) - \int_0^{h-a} B_{\rm ext}(z)\,{\rm d}z\,. \tag{5.11}$$

Conserving flux passing below the flux rope per unit length Δy during the mass-draining requires that $F(h_{\rm m}) = F(h_0)$, hence,

$$\begin{aligned} \int_0^{h_{\rm m}-a} B_{\rm ext}(z){\rm d}z \;&-\; \frac{\mu_0}{2\pi} I_{\rm m} \ln(2h_{\rm m}/a) \\ &= \int_0^{h_0-a} B_{\rm ext}(z){\rm d}z - \frac{\mu_0}{2\pi} I_0 \ln(2h_0/a)\,, \end{aligned} \tag{5.12}$$

where it is assumed that the flux rope radius, a, is small compared to its height, and that a remains unchanged by the mass-draining to simplify the expressions as evolution in a has a low effect on the results (similar to the case $m = 0$ in DA10 where a did not evolve). Equation (5.12) explicitly states that the two equilibria are on the same $I_{\rm evol}(h)$ curve of Eq. (5.10).

It is then assumed that the two equilibria $(h_{\rm m}, I_{\rm m})$ and (h_0, I_0) are close enough, so that the mass has a small effect on the force balance ($mgh \ll (\pi/\mu_0)(hB_{\rm ext})^2$). The equilibrium without mass is taken as a reference to express all terms of the Taylor development and define the variation quantities: $\Delta h = h_0 - h_{\rm m}$, $\Delta I = I_0 - I_{\rm m}$. From Figure 5.2, $\Delta h > 0$ and $\Delta I < 0$.

With a Taylor development to first order in Δh and ΔI of Eq. (5.12), the conservation of flux imposes the relationship,

$$\frac{\Delta h}{h_0} = -2\ln(2h_0/a)\,\frac{\Delta I}{I_0}\,. \tag{5.13}$$

The equilibrium curve without mass satisfies,

$$0 = \frac{\mu_0 I_0^2}{4\pi h_0} - I_0 B_{\rm ext}(h_0)\,, \tag{5.14}$$

and the force balance with mass m satisfies,

$$\Delta f = \frac{\mu_0 I_{\rm m}^2}{4\pi h_{\rm m}} - I_{\rm m} B_{\rm ext}(h_{\rm m}) - mg\,. \tag{5.15}$$

With ΔI rewritten as a function of Δh with the flux conserved, Eq. (5.13), with $I_0 = (4\pi/\mu_0) h_0 B_{\rm ext}(h_0)$, the first order expansion around (h_0, I_0) of Eq. (5.15) is,

$$\begin{aligned} \Delta f \;\; = \;\; & -mg + \Delta h\,\frac{4\pi}{\mu_0}\,B_{\rm ext}^2 \\ & \left(1 + \frac{2\pi}{\mu_0 \ln(2h_0/a)} + \left.\frac{\partial \ln B_{\rm ext}(h)}{\partial \ln h}\right|_{h=h_0}\right)\,. \end{aligned} \tag{5.16}$$

With $m = 0$, Eq. (5.16) describes the test of stability of the equilibrium around the point (h_0, I_0). Then, the following notations are introduced as,

$$n = -\left.\frac{\partial \ln B_{\text{ext}}(h)}{\partial \ln h}\right|_{h=h_0}, \tag{5.17}$$

for the negative logarithmic derivative of the external field component, commonly referred to as the decay index (Bateman, 1978; Filippov and Den, 2001; Török and Kliem, 2005; Zuccarello et al., 2016), and,

$$n_{\text{crit}} = 1 + \frac{2\pi}{\mu_0 \ln(2h_0/a)}, \tag{5.18}$$

which is Eq. (33) of DA10 (with $n_{\text{a}} = 0$ since a is a fixed value). Then, Eq. (5.16) is rewritten as,

$$\Delta f = -m g + \Delta h \frac{4\pi}{\mu_0} B_{\text{ext}}^2 (n_{\text{crit}} - n). \tag{5.19}$$

With $m = 0$, the equilibrium at (h_0, I_0) is stable if Δf is oppositely directed to the displacement $-\Delta h$ from h_0 to h_{m}. This is achieved for $n < n_{\text{crit}}$, as expected.

Supposing that the extra energy is somehow dissipated, *i.e.*, $\Delta f = 0$, Eq. (5.19) also describes the mass-draining from the equilibrium at $(h_{\text{m}}, I_{\text{m}})$ to the equilibrium at (h_0, I_0). This draining implies the shift in height,

$$\Delta h = \frac{m g}{\frac{4\pi}{\mu_0} B_{\text{ext}}^2 (n_{\text{crit}} - n)}, \tag{5.20}$$

to the new equilibrium (h_0, I_0) which exists only for $n < n_{\text{crit}}$. This quantifies the graphical description of Figure 5.2. In particular, it shows that Δh is proportional to the loaded mass m and inversely proportional to distance to the loss-of-equilibrium point (*i.e.*, in terms of the decay index, where $n = n_{\text{crit}}$). Finally, the strength of the external field has a strong effect on Δh since a factor 10 on B_{ext} decreases Δh by a factor 100 (this factor 10 on B_{ext} is the order of magnitude for the ratio between the field present in active and quiescent prominences for example). Therefore, it is concluded that the draining of a given mass m could cause the height of the prominence to increase from a tiny to a very large amount (up to the loss-of-equilibrium

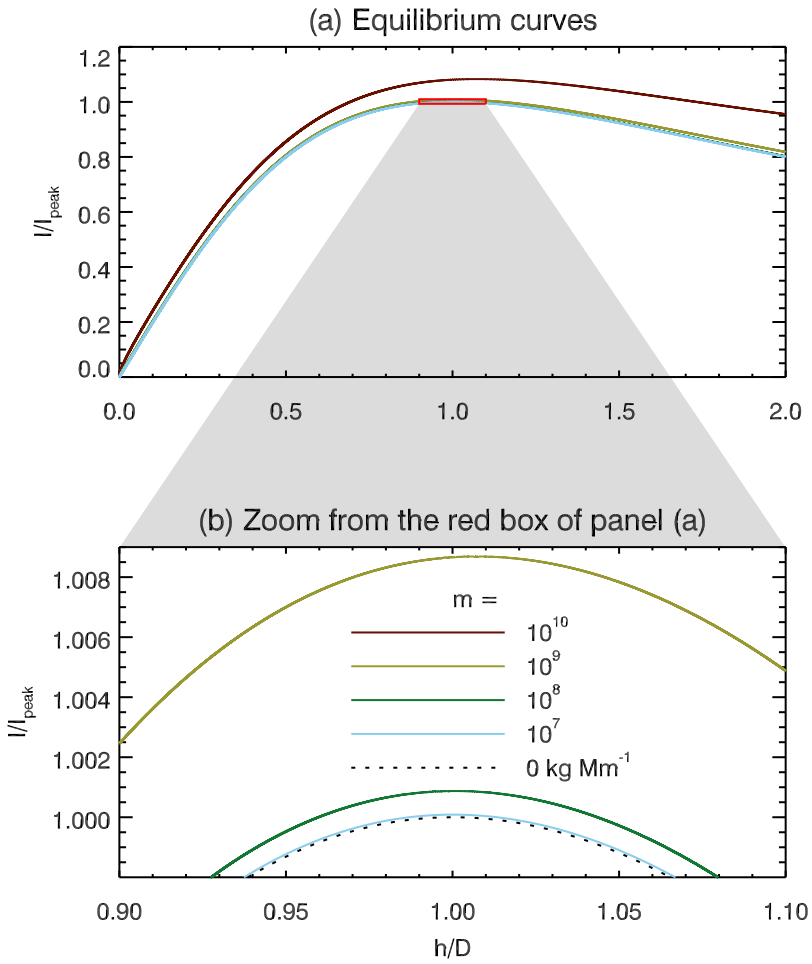

Figure 5.3: Equilibrium curves demonstrating Eq. (5.24), the relationship between electric current magnitude and height of the line current suspended within a bipolar background potential magnetic field generated by a 4 G mean surface field. These equilibrium curves are calculated assuming a range of prominence mass between 10^7 – 10^{10} kg Mm^{-1}. The dotted-black line corresponds to no mass within the system, comparable to the solid-black line in Figure 2c of Démoulin and Aulanier (2010).

and resulting eruption) depending on precisely where this draining occurs along the equilibrium path and on the strength of the external field.

5.4 Results

5.4.1 Bipolar Background Field

First, the case investigated in DA10 is expanded to explore the effect of including mass on the evolution of the flux rope, suspended within a bipolar background magnetic field, up to its loss-of-equilibrium. Here, the bipolar background magnetic

field is supplied by two infinitely long polarities at distance $\pm D$ from the position of the line current (DA10),

$$B_{\rm ext} = 2\phi D(\pi(h^2 + D^2))^{-1}, \tag{5.21}$$

where ϕ is the magnetic flux per unit length in the invariant direction. Substituting Eqs. (5.21) and (5.2) into (5.4), the condition for the system in equilibrium with $f = 0$ is,

$$\frac{\mu_0 I^2}{4\pi h} - \frac{2\phi D I}{\pi(h^2 + D^2)} - mg = 0. \tag{5.22}$$

The equilibrium curve for the massless flux rope is,

$$\frac{I_{\rm eq,0}(h)}{I_{\rm peak}} = \tilde{I}_{\rm eq,0}(\tilde{h}) = \frac{2\tilde{h}}{(\tilde{h}^2 + 1)}, \tag{5.23}$$

where $I_{\rm eq,0}(h)$ is normalised by its maximum value, $I_{\rm peak} = \frac{\phi}{\pi}$, occurring at height $\tilde{h}_{\rm peak} = h_{\rm peak}/D = 1$. Note that Equation (5.23) corrects a typo of DA10. For the case where a flux rope does contain mass, $\tilde{I}_{\rm eq,m}(\tilde{h})$ takes the form similar to Eq. (5.6),

$$\tilde{I}_{\rm eq,m}(\tilde{h}) = \frac{2\pi^2 \tilde{h} D}{\mu_0 \phi}\left(B_{\rm ext} + \sqrt{(B_{\rm ext})^2 + \frac{\mu_0 m g}{\pi \tilde{h} D}}\right). \tag{5.24}$$

In Figure 5.3, a comparison is shown between normalised equilibrium curves of flux ropes suspended within a "typical" quiet-Sun region of average surface field strength equal to 4 G and loaded with a range of masses. The properties of the masses used are presented in Table 5.1, assuming a typical quiescent prominence of length = 100 Mm, height = 30 Mm, and width = 4 Mm (Labrosse et al., 2010; Xia et al., 2012).

5.4.2 Effect of Mass on Line Current Equilibrium

Here, the flux evolution analysis, as described in Section 5.3.3, is imposed on the equilibrium curves presented in Figure 5.3 to study the effect of mass on the equilibrium of the host line current. The reference state with fluxes $\tilde{F}_0$ and ϕ_0 is defined

N_H (Total) (cm^{-3})	Mass (Total) (kg)	Mass (Per unit length) (kg Mm^{-1})
5×10^7	10^9	10^7
5×10^8	10^{10}	10^8
5×10^9	10^{11}	10^9
5×10^{10}	10^{12}	10^{10}

Table 5.1: The properties of the masses loaded onto the flux ropes presented in Figure 5.3. It is assumed that all mass within a prominence is cool (low ionisation ratio), therefore N_H is the number density of neutral hydrogen assuming the range of masses within the second column (Labrosse et al., 2010).

at the maximum of the $\tilde{I}_{eq,0}(\tilde{h})$ curve (DA10, and references therein),

$$\tilde{F}_0 = \frac{\mu_0}{2\pi}\tilde{I}_{peak}\ln\left(\frac{2\tilde{h}_{peak}}{\tilde{a}}\right) - 2\tan^{-1}\left(\tilde{h}_{peak} - \tilde{a}\right), \tag{5.25}$$

where $\tilde{I}_{peak}$ is the maximum value of $\tilde{I}_{eq,0}(\tilde{h})$, and $\tilde{a}$ is the normalised radius of the flux rope ($\tilde{a} = a/D = 0.1$ hereafter). Then, $\tilde{I}_{evol}(\tilde{h})$ is found from Eq. (5.10),

$$\tilde{I}_{evol}(\tilde{h}) = \frac{\tilde{F} + 2\tan^{-1}\left(\tilde{h} - \tilde{a}\right)}{\frac{\mu_0}{2\pi}\ln\left(\frac{2\tilde{h}}{\tilde{a}}\right)}, \tag{5.26}$$

where $\tilde{F} = \tilde{F}_0/f_\phi$.

The intersection of $\tilde{I}_{evol}(\tilde{h})$ and $\tilde{I}_{eq,0}(\tilde{h})$ for the case of $f_\phi = 1$ for the massless flux rope is shown in Figure 5.4a. The orange curve in Figure 5.4b then corresponds to $f_\phi = 0.986$ (1.4% reduction in ϕ_0, the strength of the photospheric polarities) applied, also, to the case of a massless flux rope, indicating a single point of intersection between the two $\tilde{I}(\tilde{h})$ curves, at $h/D = 1.15$. Any further reduction in f_ϕ results in no intersection between the two $\tilde{I}(\tilde{h})$ curves. DA10 demonstrate that such a flux rope experiences an ideal-MHD instability and an outward force drives the eruption of the flux rope.

In Figures 5.3 and 5.4b it is shown that an increase in the amount of mass loaded onto the flux rope results in a shift in the maximum value of I/I_{peak} and

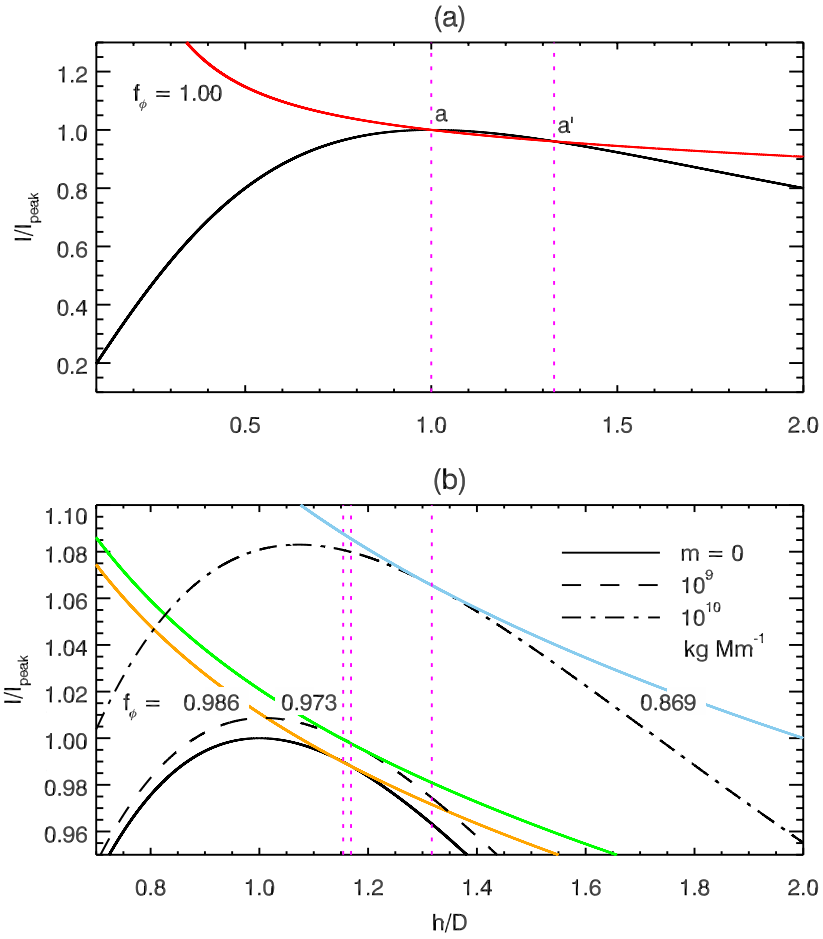

Figure 5.4: The effect of mass on the stability of a flux rope suspended within a bipolar background potential field. *Panel a*; intersection of $\tilde{I}_{\mathrm{eq},0}(\tilde{h})$ and $\tilde{I}_{\mathrm{evol}}(\tilde{h})$ with $f_\phi = 1$ indicating two equilibrium positions, $\tilde{h} = 1, 1.33$, as in Figure 2c of Démoulin and Aulanier (2010). *Panel b*; orange, green, and blue curves correspond to the last point-of-intersect, with f_ϕ decreasing, between $\tilde{I}_{\mathrm{eq,m}}(\tilde{h})$ and $\tilde{I}_{\mathrm{evol}}(\tilde{h})$, with $f_\phi = 0.986, 0.973$ and 0.869 for line currents loaded with mass equal to 0, 10^9, and 10^{10} kg Mm^{-1}, respectively. The vertical magenta-dotted lines indicate the h/D value for this last intersection, in each case, between the two $\tilde{I}(\tilde{h})$ curves. The h/D value is seen to increase as more mass is loaded.

its corresponding h/D value. As with the orange curve, the green and blue curves are the last point of intersect between $\tilde{I}_{\mathrm{eq,m}}(\tilde{h})$ and $\tilde{I}_{\mathrm{evol}}(\tilde{h})$ where a flux rope is loaded with 10^9 and 10^{10} kg Mm^{-1}, respectively. This implies that the flux of the photospheric polarity must decrease further than for the massless case in order for the mass-loaded flux rope to experience an ideal-MHD instability. For a flux rope loaded with 10^9 or 10^{10} kg Mm^{-1}, ideal-MHD instability occurs after ϕ has decreased by 2.7% and 13.1%, respectively, at a height of $h/D = 1.17$ and 1.32. Therefore, the simple model presented here appears to demonstrate that a mass-

loaded flux rope can be significantly anchored as a result of the inclusion of mass (cf. Blokland and Keppens, 2011), requiring additional current within, photospheric flux decay below, and height for the flux rope to experience loss-of-equilibrium.

Fan (2018) recently published the first example in which a prominence comprised of mass on the order of 10^{12} kg erupted in a fully MHD simulation. Interestingly, the existence of this prominence was shown to have a significantly stabilising effect on its host flux rope when compared to an identical flux rope without prominence formation induced. Specifically, the prominence was shown to inhibit the initiation of the kink instability prior to a successful eruption. The work presented here shows that a similar conclusion can also be reached with the torus instability using significantly simplified conditions.

5.4.3 Effect of Mass-Draining on the Pre-Eruptive Evolution of the Line Current

Blokland and Keppens (2011) showed that the inclusion of mass within their MHS model caused the centre of their flux rope to be pulled downwards, an effect known as the Shafranov shift (see also Shafranov, 1958). Further to this, in the previous section it was established that the inclusion of mass within the simple model presented by van Tend and Kuperus (1978) and expanded by DA10, can result in a non-negligible modification to the equilibrium curves and implies additional stability. It is therefore reasonable to suggest that the removal of this mass from a pre-loss-of-equilibrium flux rope will also result in a modification to its evolution, perhaps identical to the Shafranov shift but in the opposite direction, as suggested in Chapter 4 and several observational case studies of prominences (*e.g.*, Seaton et al., 2011; Bi et al., 2014; Reva et al., 2017).

First, to test this hypothesis and simulate the draining of prominence mass from a flux rope, the general, first-order development described in Section 5.3.3, specifically Eq. (5.20), is applied assuming the specific bipolar background magnetic field of Eq. (5.21). The results are presented in Figure 5.5 as the dashed-black lines. Δh is larger when h_{m} is closer to the loss-of-equilibrium point (*i.e.*, $n = n_{\mathrm{crit}}$). How-

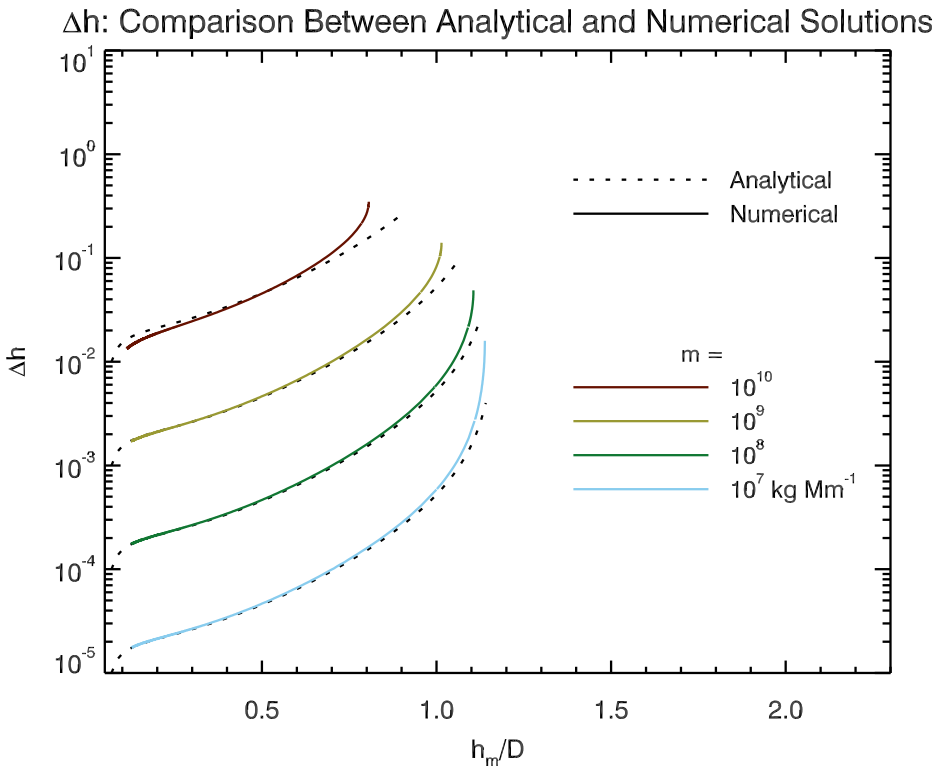

Figure 5.5: The change in the height of a flux rope due to a range of mass-draining, assuming a bipolar background potential magnetic field generated by an average surface field of strength 4 G. Analytical solutions to Eq. (5.20) are plotted for each mass as dashed-black lines. Overplotted on these dashed lines are the solid-coloured lines representing the numerical solution. The analytical solution works well for small h and m values, but clearly deviates from the numerical solution at larger values.

ever, Eq. (5.20) is derived with a Taylor expansion in Δh, so it cannot describe large Δh values.

Therefore, the "Chebfun" package (see, Driscoll et al., 2014) implemented in MATLAB has been used to solve numerically for the intersects between $\tilde{I}_{\mathrm{eq,m}}(\tilde{h})$, $\tilde{I}_{\mathrm{eq,0}}(\tilde{h})$, and $\tilde{I}_{\mathrm{evol}}(\tilde{h})$ for a range of values of f_ϕ. These solutions are presented in Figure 5.5, plotted over the analytical solution for comparison. Although the main trend is accessible via both the analytical and numerical solutions, the numerical solution emphasises the sensitivity of the equilibrium to mass evolution when the flux rope is close to its loss-of-equilibrium.

5.5 Implications for Observations

Although the model has been explored in a general sense, it is important to also compare the model results to actual observational cases where mass evolution was suggested to have played an important role in the observed global evolution of a prominence. Here, a basic comparison is carried out between the model and the observations of both Chapter 4 and Seaton et al. (2011). The simple model shows that some of the quantities may be very sensitive to the value used in their computation, see *e.g.*, Figure 5.5 for large h_{m}/D. The model input parameters (prominence dimensions, height, mass, and external field as a function of time) require indirect, often complex methods to enable an estimate to be made from observations, and are subject to different types of errors. Therefore, the intention is to establish an order-of-magnitude indication to the importance of mass-draining in these two cases, not an exact measure. Furthermore, it is found that varying the value of a/D between 0.1 and 0.5 results in modifications to the stability of the flux rope of only a few %. Therefore, for this comparison the assumption of a thin flux rope is maintained and $a/D = 0.1$ remains fixed.

First, we refer back to Chapter 4 where the column density estimation technique of Williams et al. (2013) and Carlyle et al. (2014) was used to study the draining of mass from an erupting quiet-Sun prominence. Recall that shortly prior to the onset of the prominence eruption there, the total mass within the FOV reduced by at least 1×10^{10} kg, equal to 15% of the initial mass within the FOV. The additional properties of the erupting prominence were estimated from observations taken using SDO/AIA to be,

$$
\begin{aligned}
D &= 65\ \mathrm{Mm} \\
L_{\mathrm{y}} &= 260\ \mathrm{Mm} \\
B_{\mathrm{Phot}} &= 4.6\ \mathrm{G} \\
\phi &= \frac{\pi D B_{\mathrm{Phot}}}{2} \\
\delta m &= 1\ \times\ 10^{10}\ \mathrm{kg},
\end{aligned}
$$

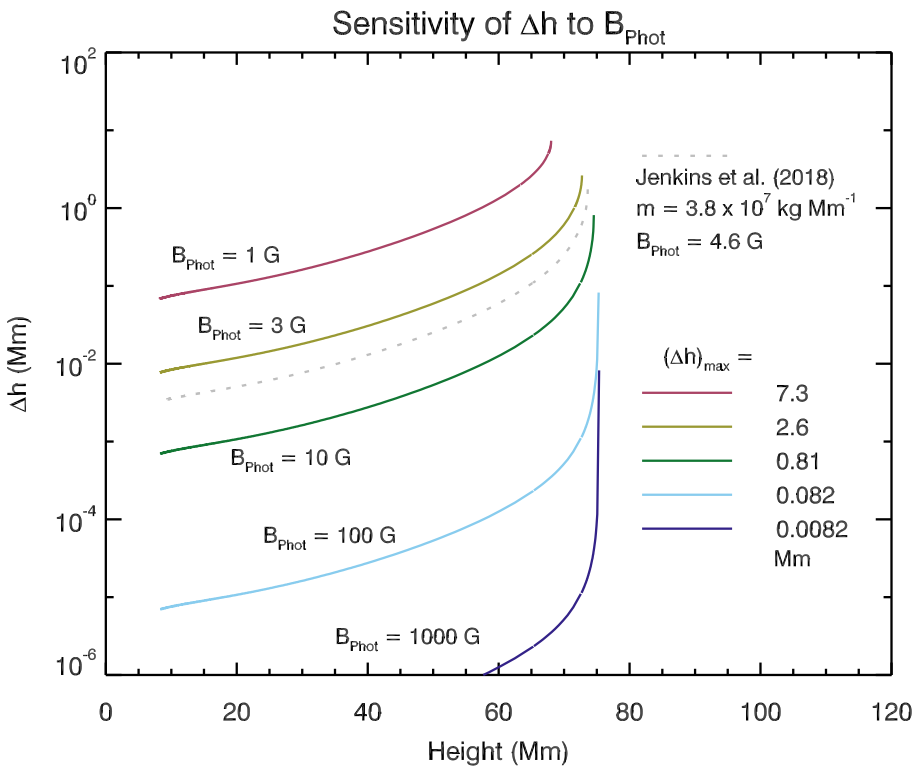

Figure 5.6: The modification to the height of the flux rope assuming a draining equal to 1×10^{10} kg of prominence mass at a range of photospheric magnetic field strengths. Quiet-Sun surface field strengths result in a significantly larger change in height due to mass-draining than field strengths similar to those observed in active regions.

where L_y is the length of the prominence. D is half the width, and L_y the length, of the red-dashed box in Figure 4.3a. The value of $B_{\rm Phot}$ is the average strength of the magnetic field within the bounds of the red-dashed box in Figure 4.3a. The results of the application of these values to the model are shown in Figure 5.6.

In the application of these observations to this model the initial mass has been set equal to 9×10^{10} kg and final mass equal to 8×10^{10} kg. In the observations, the prominence was seen to become unstable, inferred by the sudden and large acceleration, once it had reached a height of $\approx$ 45 Mm. According to the model, such a flux rope would need to reach a height of $\approx$ 75 Mm (MAX($h + \Delta h$) of the deshed-grey line in Figure 5.6) to lose stability, $\approx$ 30 Mm higher than observed. In fact the comparison between model and observations cannot be precise because of the approximate values derived from observations and the simplicity of the model. Moreover, all of the mass present in the model exists at the height of the line current,

a location representative of the axis of a flux rope. As it is commonly assumed that prominence material resides below this height in the dips of the magnetic field of a flux rope (*e.g.*, Aulanier et al., 1998; Gunár and Mackay, 2015), it is expected that the model height corresponding to loss-of-equilibrium would always be larger than any observed prominence height (see also, Zuccarello et al., 2016).

The increase in height of the prominence, shown in Figure 4.9, after the prominence underwent mass-draining was $>$ 60 Mm before leaving the FOV. The simple model described here predicts the maximum possible increase in height for the same amount of mass-draining to be up to 1.7 Mm, assuming the final state is also in equilibrium. It was noted in the analysis and conclusions of Chapter 4 that the flux rope associated with the prominence was at a point of marginal instability when the mass-draining initiated. Indeed, it has been shown that the simple model described here predicts the largest increases in height due to mass-draining to occur as the flux rope approaches its loss-of-equilibrium. Hence, the large increase in the height of the observed prominence (60 Mm) shortly after the draining of mass could be interpreted as being caused by the flux rope losing equilibrium and erupting into the heliosphere due to the torus instability. Indeed, this was the main conclusion of Chapter 4 and Jenkins et al. (2018). The prominence observed in Chapter 4 did successfully erupt and was later observed as a CME by multiple coronagraphs.

The mass estimates of the prominence material from Chapter 4 were derived using the monochromatic method applied to single wavelength observations captured using STEREO/EUVI. As previously mentioned, these values are underestimated compared to the results of the polychromatic method that better constrains the filling factor and foreground emission fraction within the model. Therefore, the derived values of total mass and mass drained using the monochromatic method are taken as lower-limits, and in turn all values of Δh are taken to be lower-limit estimates to the increase in the height of the prominence.

Similarly, this model can be applied to a prominence originating within an active region by using the example presented in Seaton et al. (2011), in which the observed mass-draining was concluded to have been responsible for the $\approx$ 35 Mm

increase in prominence height. In this case, the decaying active region was observed to have had an average surface magnetic field strength of $\gtrsim$ 100 G according to magnetogram observations taken using MDI on board the *Solar and Heliospheric Observatory* (SOHO; Domingo et al., 1995). The simple model of this chapter can test this conclusion by assuming the same degree of mass-draining as was observed in Chapter 4, and modifying B_{Phot} to test the sensitivity of the model to a range of surface fluxes.

In the solar context, higher values of B_{Phot} are associated with smaller values of D, in turn reducing the critical height of the flux rope. Indeed, this is a commonly observed and well studied relationship between prominence height and magnetic domain (*e.g.*, Rompolt, 1990; McCauley et al., 2015; Filippov, 2016, and references therein). However, in order to meaningfully vary D with B_{Phot} within this model, additional assumptions would have to be made *e.g.*, the effect of scaling between different topologies of surface fluxes. Therefore, to facilitate a simple comparison between the two observational case-studies and the additional range of realistic surface flux values, conditions are compared for a "normalised filament", fixing D as in Chapter 4 and simply varying B_{Phot}.

The results, shown in Figure 5.6, suggest that increasing the surface magnetic flux results in a stronger background potential magnetic field, and reduces the effect that mass-draining can have on the height change Δh. According to the model, draining 1×10^{10} kg from a line current embedded within a bipolar background potential magnetic field that has a surface magnetic field strength of $\gtrsim$ 100 G would result in a very small maximum change to the height of the flux rope unless the configuration is very close to loss-of-equilibrium. It is therefore unlikely that the mass-draining was directly responsible for the observed $\approx$ 35 Mm increase in the height of the prominence. Nevertheless, as appears to have been the case for the prominence studied in Chapter 4, the mass-draining may have been responsible for perturbing the equilibrium towards the non-equilibrium point.

A similar result to this has previously been reported by Reeves and Forbes (2005), in which the authors concluded the effect of mass was likely to be negligible

in a system restricted by a background field stronger than 6 G. The result presented in Figure 5.6 is complementary to this by providing a quantitative comparison for a range of surface fluxes and masses.

5.6 Discussion and Summary

The general model described in this chapter has enabled the detailed exploration of how the inclusion of realistic prominence masses and complete draining of this mass from a flux rope can have both stabilising and destabilising effects. Returning to Figure 5.2 for comparison, a flux rope that drains total mass at point A, for example, would move along the constant F curve to A$'$, resulting in damped oscillations around A. In such a case, the flux rope does not experience a loss-of-equilibrium; the draining of mass has simply enabled the flux rope to increase in height to a new equilibrium and further evolution of other parameters would be required for a successful eruption to occur. Considering, now, a flux rope evolving from C to C$'$ due to complete mass-draining, the flux rope would become unstable to an ideal-MHD instability as it reached point C$'$, and the flux rope would experience a loss-of-equilibrium triggered by the draining of mass.

The mass draining can also be partial and can also occur during the aforementioned oscillations. Indeed, Zhou et al. (2018) showed that the oscillation of the prominence in their 3D MHD simulation resulted in the draining of mass from the structure due to the periodic increase in height of field lines during the oscillation. The authors also note that this can cause the height of individual field lines to increase due to the reduction in the gravitational force, although this is studied locally for a few field lines.

For a line current that drains a partial amount of the total mass loaded, the height of the flux rope would increase accordingly, as has already been discussed in Section 5.4.3. If this is realised at point A or B of Figure 5.2, the flux rope would not evolve all the way to point A$'$ or B$'$, rather a point on the constant F curve that is in-between and dependent on the degree of draining.

Considering point D, a point that is not sampled using the methods outlined in this chapter, then the partial or complete draining of total mass may result in the flux rope either reaching a stable equilibrium again or experiencing a loss-of-equilibrium. In this case, the nature of the flux rope post mass-draining would depend on the degree of mass drained. Graphically, for a flux rope to experience loss-of-equilibrium the constant F curve cutting the mass-loaded flux rope equilibrium curve at point D would have to touch the mass-drained equilibrium curve tangentially or not at all. Defining m_{drained} as the amount of mass drained and m_{min} as the minimum amount of mass-draining required to destabilise a flux rope at point D, if $m_{\text{drained}} < m_{\text{min}}$ the final state of the flux rope would be equilibrium. Assuming no more mass-draining occurred, the additional physical parameters of the system would be required to evolve for a successful eruption to occur. It then follows that if $m_{\text{drained}} \geq m_{\text{min}}$ the flux rope would experience loss-of-equilibrium as a result of the mass-draining.

At point E the flux rope is already unstable to an ideal-MHD instability without any draining of mass. If mass draining was to occur at this point, the draining of total or partial mass would not contribute to the initiation of the loss-of-equilibrium but would instead contribute an additional accelerating force to the erupting flux rope.

Finally, applying specific conditions to the general case, it is shown that:

- For a flux rope suspended within a bipolar background field generated by a surface field of 4 G, the inclusion of typical prominence masses can increase the height at which the flux rope experiences an ideal-MHD instability by up to 14%, indicating that the mass provides a larger anchoring effect than is typically assumed.

- The draining of the larger masses from a flux rope can cause a non-negligible increase in the height of the flux rope without upper bound, with the largest height increase observed as the flux rope approaches its loss-of-equilibrium.

- Using the observational measurements of Chapter 4 as the input parameters, it is shown that the modification to the height of the flux rope due to mass-draining is as much as 1.7 Mm. This non-negligible increase in the height of the flux rope effectively demonstrates the ability for mass-draining to perturb the equilibrium of weak field quiescent flux ropes.

- Scaling the model for comparison with observations presented by Seaton et al. (2011), it is shown that draining mass from a flux rope suspended in a background field generated by up to kilogauss surface field results in only a negligible modification to the height of the flux rope.

In this chapter, the role that mass plays in the *global* evolution and eruption of flux ropes is explored, suggesting that it depends on four main parameters: the strength of the surface field generating the background potential field, how much mass is loaded into a flux rope, how much mass drains during its evolution, and when along a flux rope's equilibrium curve the mass drains. The effect of the *local* evolution of plasma within prominences is not discussed in this chapter, *i.e.*, the mass-draining that is studied here differs from the mass-loss due to the RTI that has been studied extensively in both observations and simulations (*e.g.*, Hillier et al., 2012b; Xia and Keppens, 2016; Hillier, 2018). In addition, Kaneko and Yokoyama (2018) pointed out that, in their case, the mass-loss from the prominence due to the RTI was balanced by new condensations into the prominence. A parametric study would be required in order to ascertain the effect of such local evolutions of mass on the global stability of a flux rope–prominence system.

Given the simple model and subsequent results presented and discussed here, it is concluded that the role of mass within solar eruptions, particularly those involving quiescent prominences, is greater than has been historically attributed, and requires a more in-depth analysis.

It has been established in the first two chapters of this thesis that the understanding of the commonly-assumed-negligible role of mass in the global pre-eruptive equilibrium/evolution of solar flux ropes is incomplete. Indeed, it has been

confirmed that the effect of mass within regions of strong surface flux *i.e.*, active region prominences, is small and the magnetic flux rope can be accurately prescribed as zero-β. In contrast, flux ropes sourced within the quiet-Sun *i.e.*, quiescent prominences, cannot be assumed to be force free and the role of mass should not be neglected.

Everything being equal, and as briefly mentioned at the end of this chapter, the effect of the local evolution of mass on the global stability of prominences is yet to be addressed. Consider, for example, the mass of a prominence becoming localised enough to trigger the RTI. Such localised, over-dense blobs of mass may ultimately be *lost* from the associated prominence, in turn ceasing to contribute any gravitational forces to the equilibrium (Berger et al., 2010, 2011; Hillier, 2018; Kaneko and Yokoyama, 2018). Although the initiation of the RTI has been studied under prominence-like conditions, most of these studies are isolated to theoretical endeavors informed from observations wherein the required plasma parameters have been inferred/assumed rather than directly measured. Indeed, obtaining the necessary observations is non-trivial, as are the methods required to extract this information from such observations. However, this will be the focus of the following chapter.

Chapter 6

The Small-Scale Structure and Motions Underneath an On Disk Solar Prominence

This chapter addresses the possible detection of an RTI-like process occurring underneath a quiescent prominence that was observed at the DST on 29 May 2017. To begin, the results of two different inversions applied to this prominence are introduced, the Hanle and Zeeman Light (HAZEL; Asensio Ramos et al., 2008) inversion of Wang et al. (2020) and the H-α inversion of Schwartz et al. (2019). The values of plasma and magnetic pressure that may be derived from these studies are used to calculate plasma β within the prominence at six positions along its body, producing a range of $0.02 - 0.23$. The Beckers' cloud model is then used to invert the full FOV of the H-α observation so as to establish 2D maps of the associated plasma's optical thickness, LOS velocity, and line width. Then, by adopting NLTE assumptions, the temperature stratification (with height) of the low Ca II corona is reconstructed across the full FOV. The co-incidence of grouped red-shifted and heated material in H-α, with increased magnetic field strength as measured in He I, the relatively hot monolithic structures (both inclined and vertical) within the Ca II inversion, and the position of photospheric polarity concentrations suggest the footpoint of the prominence was present within the FOV. Furthermore, the Ca II inversion is found to contain a thermal signature underneath the prominence body

that is seen to have propagated to significantly lower heights. However, considering the density of the surrounding atmosphere at such heights, it is concluded that this is not an observation of the RTI traditionally observed with respect to prominences but rather a plasmoid of currently unknown origin. It is further concluded that the NLTE slab inversion methods of HAZEL and Schwartz et al. (2019) are well-equipped to extract physical parameters of prominence plasma. However, in order to carry out further, more detailed observational studies of RTI-like phenomena, this requires the use and development of NLTE inversions that involve stratified plasma parameters at higher altitudes than was possible here.

The observations that will be presented in this chapter were collected at the DST in a campaign that was led by myself in collaboration with D. M. Long (University College London), J. Carlyle (European Space Research and Technology Centre), C. Beck (National Solar Observatory), and D. Choudhary (California State University Northridge). The NLTE H-α modelling was carried out by P. Schwartz (Astronomical Institute of Slovak Academy of Sciences) and has been published in *The Astrophysical Journal* under Schwartz et al. (2019). The HAZEL inversion was applied to the observations by S. Wang (New Mexico State University) and the associated paper is currently in preparation. The NLTE Ca II inversion code was applied by C. Beck (National Solar Observatory) with possible interpretations also offered. All remaining computation, analysis, and interpretation was carried out by myself.

6.1 Introduction

Prominences exist within the solar atmosphere as a balance between the Lorentz force of their host magnetic field and the gravitational force of the plasma itself. It has been suggested that prominence plasma resides in the dips of its host magnetic field, a concept confirmed by frequent observations of small-scale plasma motions within active region prominences that appear horizontal, aligned, and give the impression of threads (Kippenhahn and Schlüter, 1957; Anzer, 1969; Okamoto et al., 2016). However, although such studies have well established that the Lorentz force

must dominate the relationship throughout the prominence for suspension to persist (see also Hillier and van Ballegooijen, 2013), observations of vertical structuring within quiescent prominences have suggested that such a relationship may be more tentative than previously thought (*e.g.*, Berger et al., 2008). Specifically, such observations have been successfully interpreted as occurrences of the (magnetic) RTI (*e.g.*, Berger et al., 2010, 2011; Liu et al., 2012; Hillier et al., 2012a). Understandably, in order for such a process to occur within prominences, the hydrodynamic forces must have a non-negligible role to play in their internal structuring, most notably within those that are more quiescent.

The classical RTI occurs when two fluidic media are stratified such that the denser of the two lies (gravitationally) above the other and the interface between them is perturbed; the resulting dynamics are in the form of less-dense *plumes* that rise and more-dense *fingers* that fall (Hillier, 2018). For astrophysical phenomena, much interest lies in the evolution of the RTI when the system in question is permeated by a magnetic field (*e.g.*, supernovae, nebulae, magnetised stars, solar interior, solar prominences). For prominences specifically, Keppens et al. (2015) simulated the traditional case where the field was initially assumed perpendicular to the gravitational stratification. The horizontal assumption is assumed valid by considering a small-enough section of the dip of a flux rope such that curvature can be ignored (or more generally if comparing to observations *e.g.*, Casini et al., 2003). By including prominence-like material, the authors were then able to convincingly reproduce the vertical structuring similar to that observed within quiescent prominences at the limb; see Figure 6.1.

Interestingly, Liu et al. (2012) observed a prominence using the SDO/AIA instrument suite and noted vertically-oriented and downward-propagating plasma dynamics that bared a striking resemblance to their cartoon of the RTI process in 2D. The authors showed that the total mass of this prominence was seen to plateau despite simultaneous observations of ongoing plasma condensations supplying mass to the prominence. As a result, the authors interpreted the internal, downward-propagating, RTI-like motions as a process leading to material completely leaving

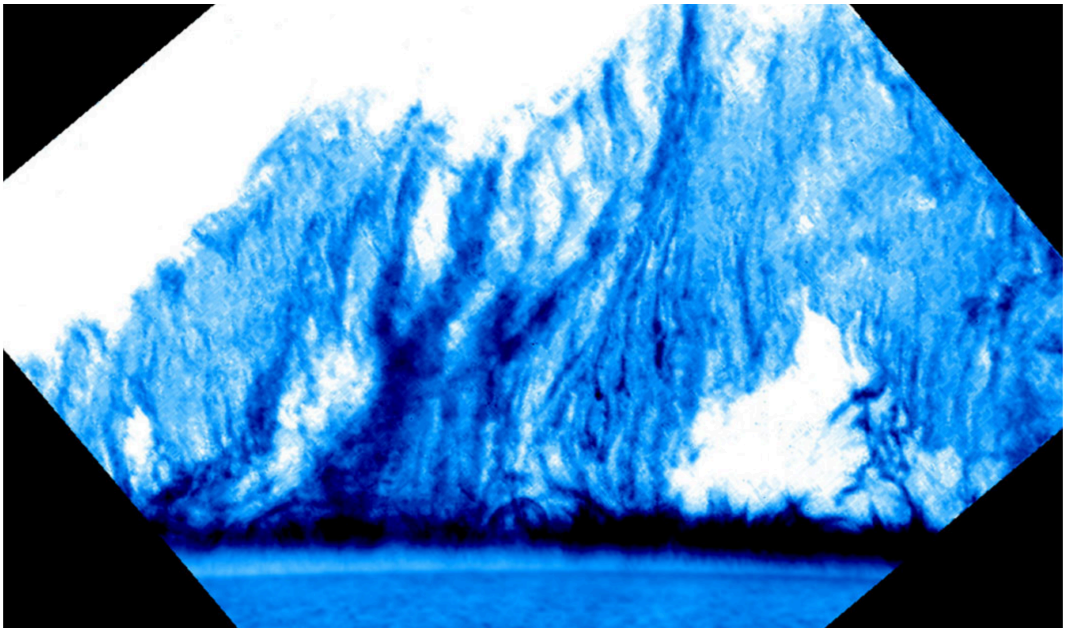

Figure 6.1: Observations of a quiescent prominence that appears to have a more vertical structuring than horizontal. Movies of the related dynamics indicate vertical velocity components that have been interpreted as being caused by the magnetic Rayleigh-Taylor instability. Image taken from Hillier (2018).

the prominence at a rate similar to the plasma condensations. Under this interpretation, the observations also suggested that the entire mass of the prominence could be *swapped-out* on the order of an hour. Hence, although prominences are long-lived structures within the solar atmosphere persisting for up to several rotations, such an observation suggests that the plasma of a prominence may not be similarly long-lived.

It was concluded in Chapters 4 & 5 that the mass of a prominence (both total and evolution therein) is of critical importance when considering the balance of gravitational and magnetic forces within. However, such conclusions only hold if the mass of the prominence remains within the global structure so as to impart a force on the global equilibrium. If the mass of a prominence is capable of draining via an ongoing RTI(-like) process then it is not immediately clear what implications this may have on our understanding of the aforementioned equilibrium. As was the case in Chapter 5, removal of mass through the RTI may contribute to the height-rise and destabilisation of the prominence. Conversely, the (instantaneous) total mass of the prominence studied by Liu et al. (2012) did not vary to a significant

degree during the mass-cycling that the authors observed. However, this was the case for a single case-study prominence in which the successful draining itself was only inferred.

It is therefore of particular interest that the work by Kaneko and Yokoyama (2018) explored the evolution of mass within a simulated prominence that was embedded within a *realistic* magnetic flux rope. The authors described the prominence as being in a *dynamic state* due to a combination of a condensation process that supplied mass to the prominence and an RTI-like process that included significant draining of material from the prominence body. It is important to note, however, that the thin fingers of the RTI that were observed by the authors to have extended to lower altitudes were only *assumed* to have been capable of completely removing blobs of mass from the associated prominence (a similar argument as was suggested by Liu et al., 2012). In actual fact, the authors speculated that their numerical set up, as with that of Keppens et al. (2015), forbid the material from completely evacuating the associated prominence due to the nature of the lower boundary of their simulation. Instead, the successful "removal" of plasma material from the prominence as described by Kaneko and Yokoyama (2018) was defined as the material that dropped below an arbitrarily set cut-off height. Furthermore, observations are yet to confirm the additional dynamics produced in the comparable simulation of Keppens et al. (2015) wherein the thin fingers were propelled to significantly higher altitudes in response to an interaction with the prominence's lower boundary. Therefore, despite the depth of these studies that were carried out to address whether the RTI (or a RTI-like mechanism) is capable of completely liberating plasma from prominences, this question remains unanswered.

In this chapter, a prominence observed using high-resolution, ground-based instrumentation is analysed with multiple inversion tools to reconstruct the small-scale properties and motions of the plasma within. In the first instance, these inversion codes are used to ascertain whether any RTI-like process may have been occurring within the observed prominence. The results of these traditional inversion methods are then compared with the 3D temperature structure of the solar atmo-

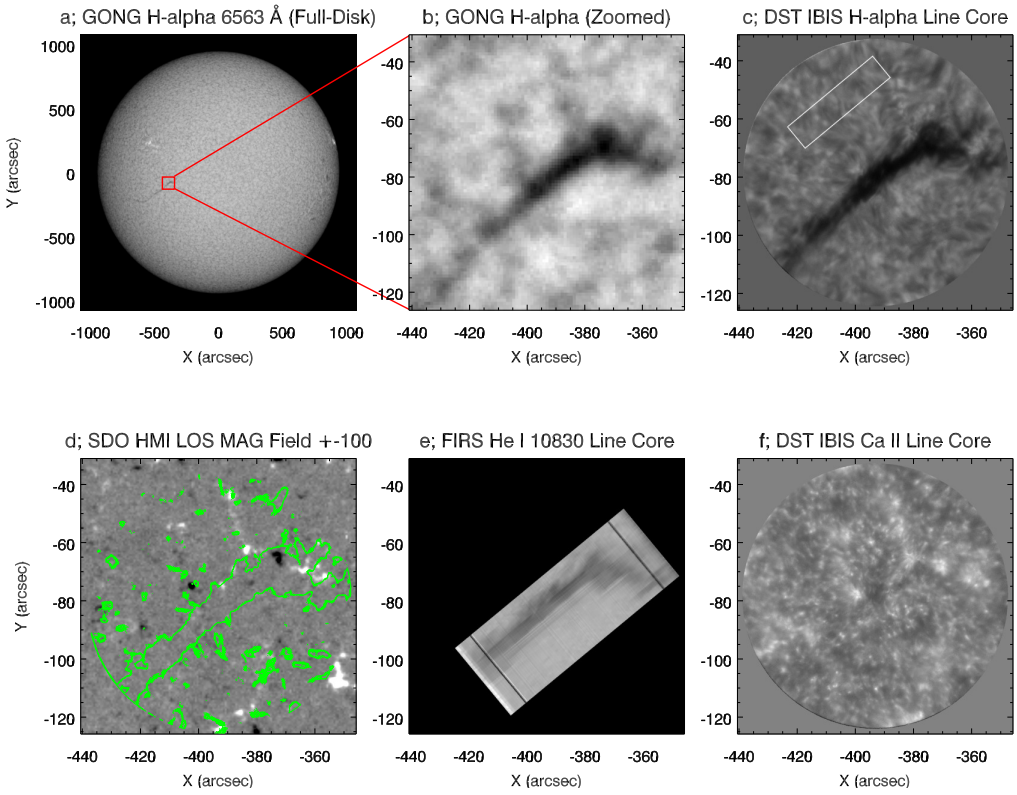

Figure 6.2: Overview of observations taken with the DST. *Panel a*; Full-disk image of the Sun in H-α, taken by GONG. *Panel b*; Zoomed FOV of the red box in (a) showing the prominence of interest. *Panel c*; The prominence of interest observed in the line core of H-α by the IBIS instrument at 14:44:55 UT at the DST. *Panel d*; the strength ($\pm$ 100 G) and the photospheric polarity underneath the prominence of interest, as observed by HMI at 14:45:00 UT, with the green contour outlining the absorption structure seen in panel c. *Panel e*; The prominence of interest observed in the line core of He I 10830 Å by the FIRS instrument at the DST. *Panel f*; The chromosphere underneath the prominence of interest observed in the line core of Ca II by the IBIS instrument at the DST.

sphere underneath the prominence, reconstructed using a novel inversion approach that includes stratifications in atmospheric parameters. The prominence observations are presented in Section 6.2. The results of the application of the various inversion models are then presented and discussed in Section 6.3. Finally, the interpretations of these inversion results are discussed in Section 6.4 before they are collated as summarising conclusions in Section 6.5.

6.2 Observations

The quiescent prominence shown in Figure 6.2 was observed on-disk on 29 May 2017 with a position of (-24.3°,-4.85°). Figure 6.2a is a full-disk context image

taken of the H-α line core at 6562.8 Å using the ground-based GONG network[1] (Harvey et al., 2011). Figure 6.2b is a zoom-in of the box in (a) showing the portion of the prominence observed using the instrumentation at the DST. Figure 6.2c shows the prominence as observed in H-α at 14:44:55 UT using the IBIS instrument, panel f of the same figure shows the same observation but in Ca II at 14:44:49 UT, also taken with IBIS. Panel d then shows the polarity of the photospheric magnetic field observed with HMI at 14:45:00 UT with contours of the H-α intensity from (c) overlaid in green. Figure 6.2e is the prominence as observed in the line core of He I 10830 Å using the *Facility Infrared Spectropolarimeter* (FIRS; Jaeggli, 2011) slit spectropolarimeter. FIRS was used to raster scan across the prominence to produce a 2D map starting at 14:41:33 UT at the left edge. In addition to IBIS and FIRS, observations were taken using the *Rapid Oscillations in the Solar Atmosphere* (ROSA; Jess et al., 2010) and the *Spectro-Polarimeter for Infrared and Optical Regions* (SPINOR; Socas-Navarro et al., 2006). However, in this chapter we focus only on the observations taken with IBIS and FIRS.

6.2.1 IBIS

As the target was a prominence, IBIS was used to scan the two lines of H-α at 6562.8 Å and Ca II IR at 8542.1 Å in spectroscopic mode with a non-equidistant spectral sampling of 27 and 30 wavelength points, respectively; see panels (a) and (b) of Figure 6.3. Non-equidistant spectral sampling was chosen so as to better-resolve the wells of each profile in comparison with the core and wings. The exposure time was 80 ms per image with a total cadence of 13 s for a complete scan of both lines. A circular FOV with a diameter of $95''$ was sampled with $\approx 0.1''$ pix^{-1} in both x and y. Data were acquired in three separate blocks from 13:59:38 to 15:30:36, 15:30:45 to 15:42:09, and 20:58:53 to 22:18:10 UT, with the gaps between observations due to weather limitations. The IBIS data were reduced with the standard data reduction pipeline[2]. In addition to the standard processing, the influence of the pre-filter transmission curve on the line profiles was removed. This

[1] http://halpha.nso.edu/index.html
[2] https://www.nso.edu/wp-content/uploads/2018/05/ibis_tn_005.pdf

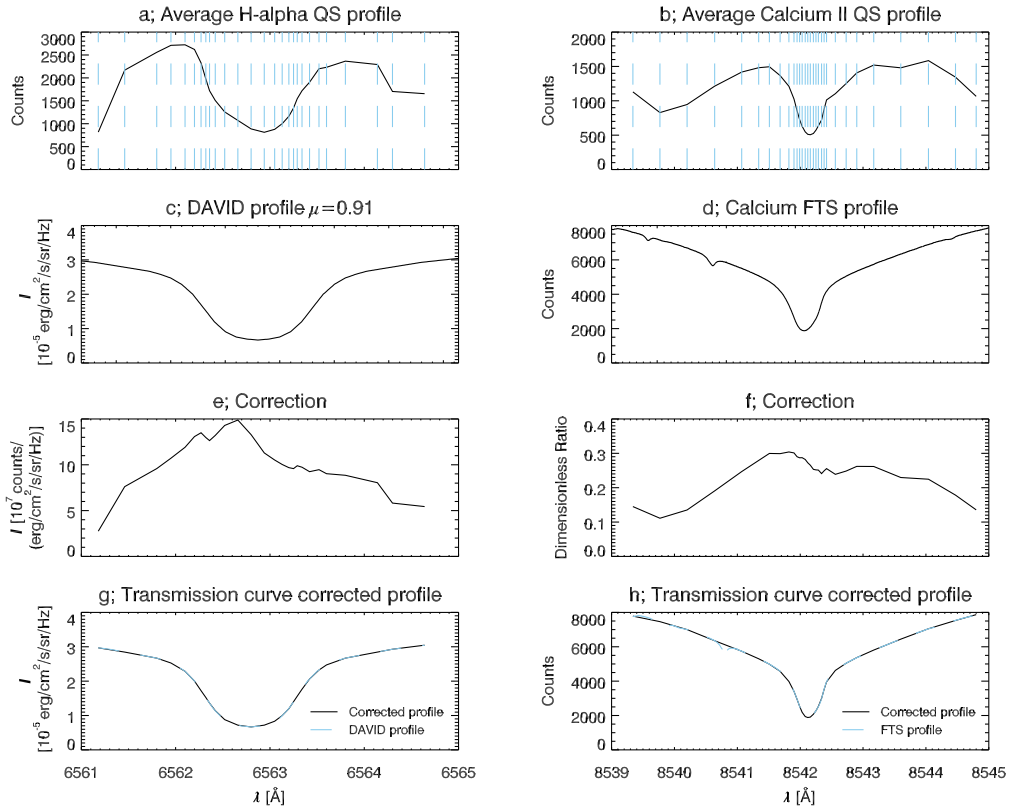

Figure 6.3: The method of pre-filter correction for the H-α and Ca II DST observations. *Panels a, c, e,* and *g* show the average profile defined within the white box of Figure 6.2c and the wavelength sampling positions in dashed-cyan, the assumed-rest H-α profile from David (1961), the correction between (a) and (c), and the resulting average H-α profile with the correction of (e) applied, respectively. *Panels b, d, f,* and *h* are the same as the left column but for Ca II and using the reference profile provided by the Fourier Transform Spectrometer atlas (FTS; Kurucz et al., 1984).

is achieved by forcing the average quiet-Sun profile, defined over the region bound by the square box shown in Figure 6.2c, into the shape of a reference profile given by the tables of David (1961) at $\mu = 0.91$ for H-α and the FTS atlas for Ca II; see Figure 6.3. The correction required for the average profile to match the reference profile was then applied to all other spectra across the FOV. For the H-α observations, this step also provides an absolute intensity calibration.

6.2.2 FIRS

FIRS was used to observe the chromospheric He I 10830 Å line using a 40-micron wide ($\approx 0.3''$), single slit of $75''$ length that was sampled with $0.15''$ pix^{-1} along the slit. A spectral range from 10817 to 10856 Å was covered with a spectral sampling

of 3.85 pm. The exposure time was 125 ms with a total integration time of 20s per scan step. The Coudé table was rotated such that the slit of FIRS was aligned along the axis of the prominence. The prominence was scanned with 100 steps of 0.3″ step width with a total duration of 40 min. Data were acquired from 14:41:33 to 15:21:30 UT, no data were taken during the third observing window of IBIS due to technical issues. The FIRS data were reduced with the standard data reduction pipeline[3]. In addition to the standard processing, a two-dimensional Fourier filter was applied to the data to reduce polarized interference fringes and a de-spiking routine to capture hot pixels over the FIRS spectra. Prior to the inversion, the data were re-binned to 0.9″ × 0.9″ per pixel to improve the signal-to-noise ratio.

6.2.3 Alignment

To ensure comparisons can be made between the various instruments, a robust alignment is necessary. For IBIS, the H-α observations were aligned to the synoptic GONG H-α observations (see also Schwartz et al., 2019). To account for slight misalignments within the IBIS instrument, the Ca II observations were aligned separately to the 1600 Å passband observations taken by the AIA on board SDO. The He I 10830 Å observations from FIRS were aligned to the H-α observations of IBIS as the absorption signatures of each observation are assumed to be morphologically similar. All alignment was carried out using a 2D cross-correlation algorithm implemented in the IDL coding language; this includes the step for isolating the correct orientation of each observation.

6.3 Results

6.3.1 Plasma β

As previously discussed in Section 1.5.1, the plasma β is defined as the ratio of plasma pressure to magnetic pressure. Typically, prominences are considered as structures that adhere to plasma $\beta \ll 1$ as this permits simulations to consider their host magnetic field (flux ropes) as force-free in all instances. By extension this suggests that the plasma of a prominence can only *respond* to the evolution

[3] https://www.nso.edu/wp-content/uploads/2018/05/firs_soft_manual.pdf

of the magnetic field. However, the numerous observations of an RTI-like process occurring within quiescent prominences suggests this cannot be the case (Berger et al., 2008, 2010, 2011). Furthermore, both simulation and observational studies of the RTI and its application to prominences have reported values of plasma β that explicitly contradict these assumed conditions within prominence-hosting flux ropes (*e.g.,* $0.16-1.13$ Hillier et al., 2012a; Keppens et al., 2015). Therefore, it may be possible to indicate, to first order, whether the plasma of a prominence is capable of undergoing an RTI (-like) process from the measured values of β alone. Unfortunately, estimating β using the geometrical method of Hillier et al. (2012a) is unsuitable as the prominence presented here is observed on-disk.

The observed prominence has previously been studied by Schwartz et al. (2019) wherein the plasma parameters of the H-α absorption signature were inverted assuming a 2.5D NLTE prominence model. Included in the extracted properties was the plasma pressure at six positions along the prominence's body. Similarly, an additional study is currently in preparation by Wang et al. (2020) in which the He I 10830 Å absorption of this prominence is studied using the HAZEL inversion code so as to establish the properties of the prominence's host magnetic field. As one of these properties includes the magnetic field strength, it is trivial to calculate the associated magnetic pressure using the relation,

$$p_{\mathrm{mag}} = \frac{B^2}{2\mu_0}, \tag{6.1}$$

where B is measured in Gauss, and μ_0 is substituted for 4π when considering cgs. Using the plasma and magnetic pressures measured in these studies it is possible to calculate the associated β. The relevant results of Schwartz et al. (2019) and Wang et al. (2020) are presented in Table 6.1 in addition to the resulting β.

The values of the magnetic and plasma pressure calculated for the six positions within the FOV suggest that the conditions within the prominence vary significantly from one position to another. Furthermore, the resulting values for β appear to vary by an order of magnitude across these six positions, with the largest values sitting within the range of values found in previous studies of the RTI. As the focus in

Schwartz et al. (2019)			Wang et al. (2020)	
Area	Solar (X,Y) (Arcsec)	Gas pressure (dyn/cm^2)	Magnetic field strength (G)	Plasma β
f1	(-408,-101)	0.28$\pm$43%	7.3	0.13$\pm$44%
f2	(-404,-98)	0.20$\pm$50%	4.9	0.21$\pm$53%
f3	(-398,-90)	0.42$\pm$67%	20.4	0.02$\pm$67%
f4	(-392,-88)	0.15$\pm$40%	4.0	0.23$\pm$45%
f5	(-398,-83)	0.16$\pm$56%	10.2	0.04$\pm$57%
f6	(-379,-79)	0.16$\pm$56%	4.5	0.20$\pm$59%

Table 6.1: Plasma β and associated errors in the six positions (f1-6) specified in the second column. The error in the magnetic field measurements is reported by the HAZEL code to be a constant error of 0.1 G.

this work is to address whether the RTI can be detected in on-disk prominences, particular interest lies in these larger values of β. Nevertheless, it is interesting, although perhaps unsurprising, that both small and large values of β exist in such close proximity. This is further evidence that prominences exist as the delicate and tentative balance of magnetic and plasma forces.

While these values of β are consistent with the understanding that the magnetic pressure dominates within solar prominences, they are also consistent with the case studies of the RTI carried out using simulations and observations. Indeed, the range of values of β that have been established by Hillier et al. (2012a) and Keppens et al. (2015) cannot be considered exhaustive as neither of these works involves a parametric study. Nevertheless, as the largest values in Table 6.1 lie only just within this range it is necessary to explore additional plasma parameters that may be indicative of an RTI (-like) process having occurred here.

6.3.2 Beckers' Cloud Model

6.3.2.1 The Model and its Validity

To date, observations of the RTI process within prominences are limited to those taken such that the prominence is projected above the limb and therefore observed from the side. In such instances, information about the behaviour of the plasma

involved within the RTI is extracted through analysis of the associated dynamics that are projected into the plane of the sky. As a result, any LOS measurements of the velocity of the plasma contain little, if any, information about the buoyant flows of the RTI. In the case of the prominence observed here, the problem is reversed and the orientation of the prominence is such that the motions of any plasma involved within any potential RTI would have a velocity component significantly aligned with the LOS. It then follows that if the plasma within the observed prominence was undergoing an RTI (-like) process, this may be detectable as LOS motions.

Values of the LOS velocity within the observed prominence have already been isolated using the NLTE H-α modelling of Schwartz et al. (2019). However, as the method presented by these authors requires careful handling of the background radiation for each position within the prominence, isolating unique and accurate solutions is time consuming and it would be impractical to use this method to invert the plasma parameters of the prominence within the entire FOV. The fastest method of extracting velocity information from spectral lines is to assume that the entire absorption signature is sourced in a single cloud moving with bulk velocity as under such assumptions the measured position of the line centre relative to its rest position provides a value of LOS velocity. However, Chae et al. (2006) have shown that the line centre method systematically underestimates the 'true' velocity of optically thick material. The authors advocate instead for Beckers' cloud model (BCM; Beckers, 1964), which was devised to provide a fast method of inverting large numbers of optically-thick spectral profiles without sacrificing physical accuracy.

The simplifying approximations adopted by Beckers (1964) reduce the number of dependent variables of the RTE to four,

- constant background intensity - The assumption that the background light incident across the studied pixel is constant, an assumption that may be less well-satisfied in more dynamic environments *e.g.*, active regions,
- constant source function - The assumption that the source function does not vary with height along the LOS,

- Gaussian-like optical thickness in wavelength - the assumption that the studied cloud is isotropic along the LOS,
- and a constant LOS velocity.

Each of these parameters may, of course, vary across the FOV. As such, the RTE of Eq. (3.8) reduces to the form,

$$I(\lambda) = I_0(\lambda)\mathrm{e}^{-\tau(\lambda)} + S\left(1 - \mathrm{e}^{-\tau(\lambda)}\right). \tag{6.2}$$

where,

$$\tau(\lambda) = \tau_0 \mathrm{e}^{-\left(\frac{\lambda_0 - \lambda}{\lambda_\mathrm{D}}\right)^2}, \tag{6.3}$$

and τ_0 is the thickness of the line centre (assumed constant), λ and λ_0 are as in Eq. (3.4), and λ_D is the Doppler width, otherwise known as the thermal width as in Eq. (3.3). Beckers (1964) went on to make a further, seemingly arbitrary, simplification of Eq. (6.2) to,

$$C(\lambda) \equiv \frac{I(\lambda) - I_0(\lambda)}{I_0(\lambda)} = \left(\frac{S}{I_0(\lambda)} - 1\right)[1 - \exp(-\tau(\lambda))], \tag{6.4}$$

referred to as the so-called *contrast profile*. However, by carrying out this additional step it became clear there were portions of an observation, or even entire observations, wherein the BCM would not apply. For example, Loughhead (1973), building on the success of Grossmann-Doerth and von Uexküll (1971) and Bray (1973), noted that the application of the cloud model to structures very far from the disk centre was questionable. Such contrast profiles tend to include large portions in emission *e.g.*, spicules, mottles, and prominences, producing nonsensical values of the source function and optical thickness (Cram, 1975). Hence, in addition to the initial assumptions discussed by Beckers (1964), the cloud model can only be reliably applied to features that can be assumed to be *completely* disconnected from the surface and appear in absorption alone *i.e.*, structures at disk centre.

One of the key assumptions in the model presented by Beckers (1964) is that the source function (formally dependent on the optical thickness of the cloud) re-

mains constant with height. Mein et al. (1996) tested this assumption by comparing the BCM with the outputs of a true NLTE model, showing that the optical thickness of the cloud was increasingly underestimated as the true optical thickness was increased. Therefore, unsurprisingly the results are clear in that the source function is not constant along the LOS. Nevertheless, the authors note that the inverted velocity is overestimated by only 20% and only in the thickest H-α clouds ($\tau > 5$).

In conclusion, despite the clear inaccuracy in the assumption that the source function is constant with height, the inverted velocity has been shown to be relatively insensitive to the optical thickness. Furthermore, the observations presented in this chapter are of a prominence located close to disk-centre and as there is little correlation between the linear polarisation of the He I 10830 Å and Si I 10827 Å observations (cf. Wang et al., 2020), the structure is believed to be significantly separated from the photosphere below. It is, therefore, assumed that the BCM is a suitable method for measuring the LOS velocity of the material within the prominence, with the understanding that the error in the inverted velocities varies as a function of optical thickness.

6.3.2.2 Application of the Model to the Data

The model is constructed assuming a single cloud along the LOS, as is typically assumed in the application of the BCM, with a uniform background illumination, I_0, assumed to be adequately modelled by the average profile measured within the box of Figure 6.2c *i.e.*, Panel g of Figure 6.3. All additional parameters used as inputs to the BCM are assumed constant along the LOS. The source function, τ, velocity, and line width are permitted to vary across the FOV within the bounds [0.01,0.4] W m^2 sr^1 Hz^1, [0,3], [-38,38] km s^{-1}, and [0.09,0.71] Å, respectively, following the successful application of these ranges within previous works (*e.g.*, Alissandrakis et al., 1990; Chae et al., 2006; Kuckein et al., 2016). The BCM is then only applied to the portions of the FOV containing deeper profiles than the assumed background, arbitrarily set at 0.58; see the green contour in panel a of Figure 6.4. The goodness-of-fit of the BCM to the observations is presented in the remainder of Figure 6.4. Panel b indicates the value of χ^2 for every profile inverted within

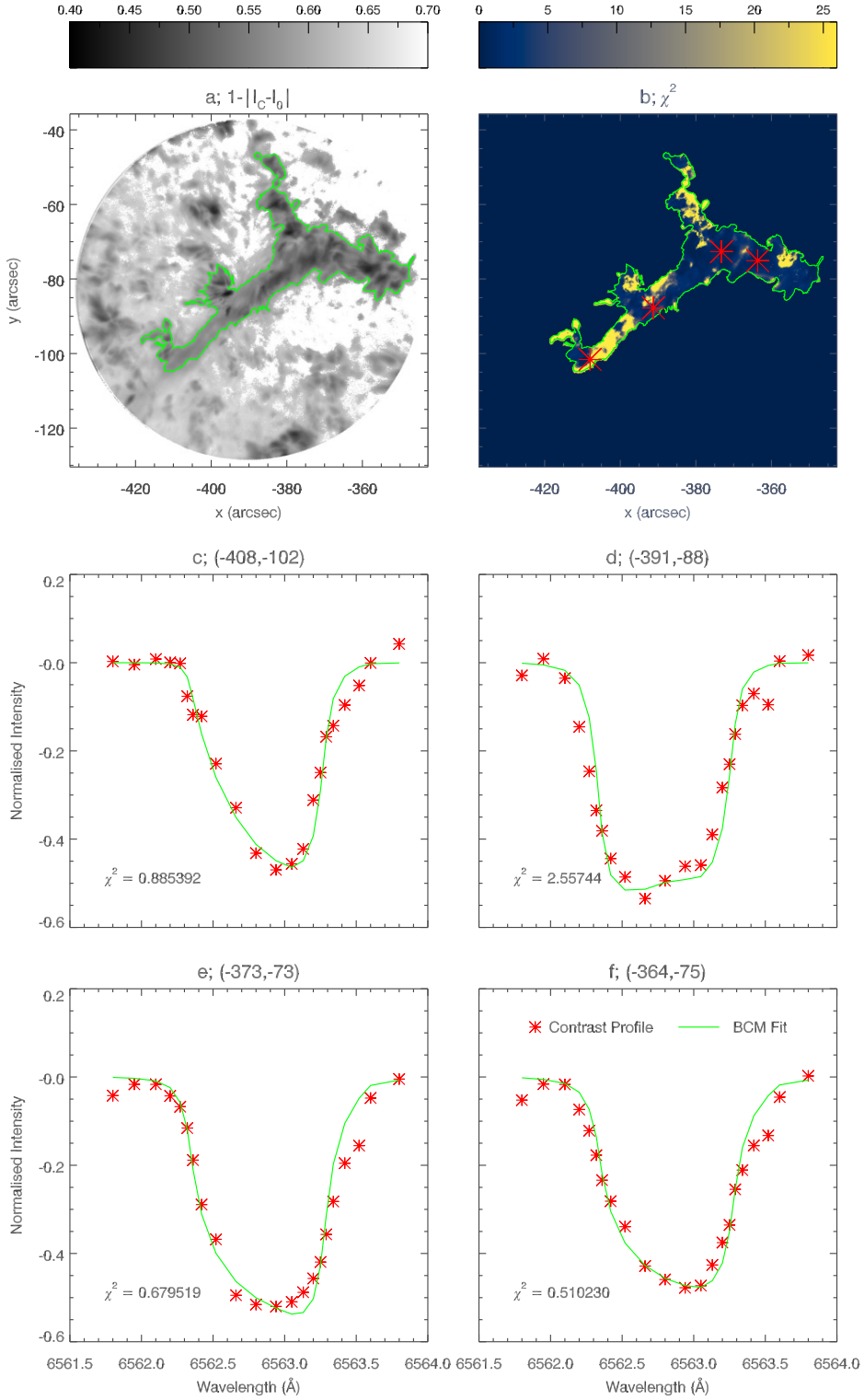

Figure 6.4: χ^2 fitting of the BCM model to the observations. *Panel a*; The absorption structure used to select the region of the FOV for inversion *i.e.*, the green contour outlines just the prominence. I_0 is the average profile from panel g of Figure 6.3, I_c is the line core intensity. *Panel b*; the χ^2 values across the FOV, saturated between 0 and 25.99. *Panels c, d, e and f*; sample fitting of four positions within the prominence. Red crosses indicate the measured contrast profile and solid-green line is the BCM fit. χ^2 value indicated in the bottom-left of each panel.

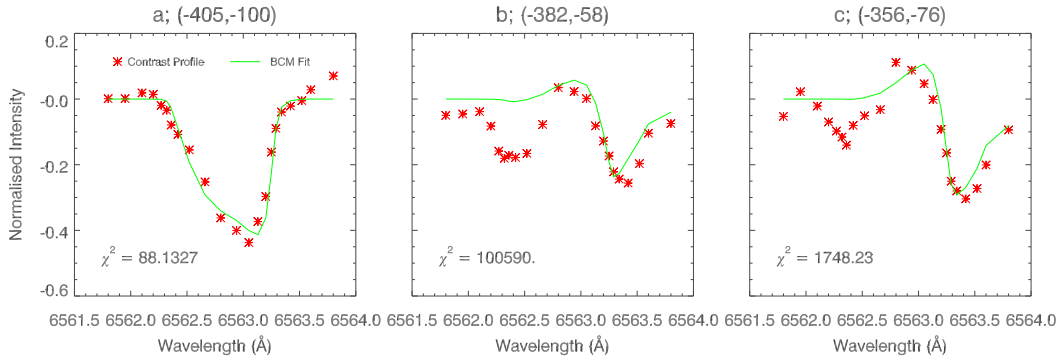

Figure 6.5: Examples of bad BCM fits in the positions indicated in the title of each panel. Red crosses indicate the measured contrast profile and solid-green line is the BCM fit. The χ^2 value for the fits are shown in the bottom-left of each panel.

the contour; saturated between 0 and 25.99 (P(0.9) for 18 degrees of freedom). The fitting and associated χ^2 for four arbitrarily-chosen positions within the prominence are then shown in panels c, d, e, and f of the same figure.

A large number of the pixels inverted using the BCM return χ^2 test values under 25.99, but a non-negligible portion of these pixels contain χ^2 values larger than 25.99 (in some positions significantly larger). The initial reason for this is believed to be due to the sparseness of the wavelength positions sampled in the observations. Although 27 wavelength points along the H-α line were scanned only 22 were used for fitting to the BCM. This is because the outermost points scanned were far into the wings of the profile. Here, the measured signal is significantly influenced by the prefilter with the result that the photon count in this region was extremely low. An example profile with an inconsistent wing profile is shown in panel a of Figure 6.5. However, for the other two profiles shown in the same figure, it is clear that the wing profiles are not responsible for the failed fit. Rather, it appears there exists a second absorption signature within some pixels that is incompatible with the assumption of a single cloud along the LOS. This is explored in more detail in Section 6.5, but for now the profiles that have failed to fit have been excluded from the following analysis. The results of the portions of the image that were successfully fitted are presented in Figure 6.6.

The values of the source function calculated within the contour have already been established to be physically unrealistic as the source function cannot be as-

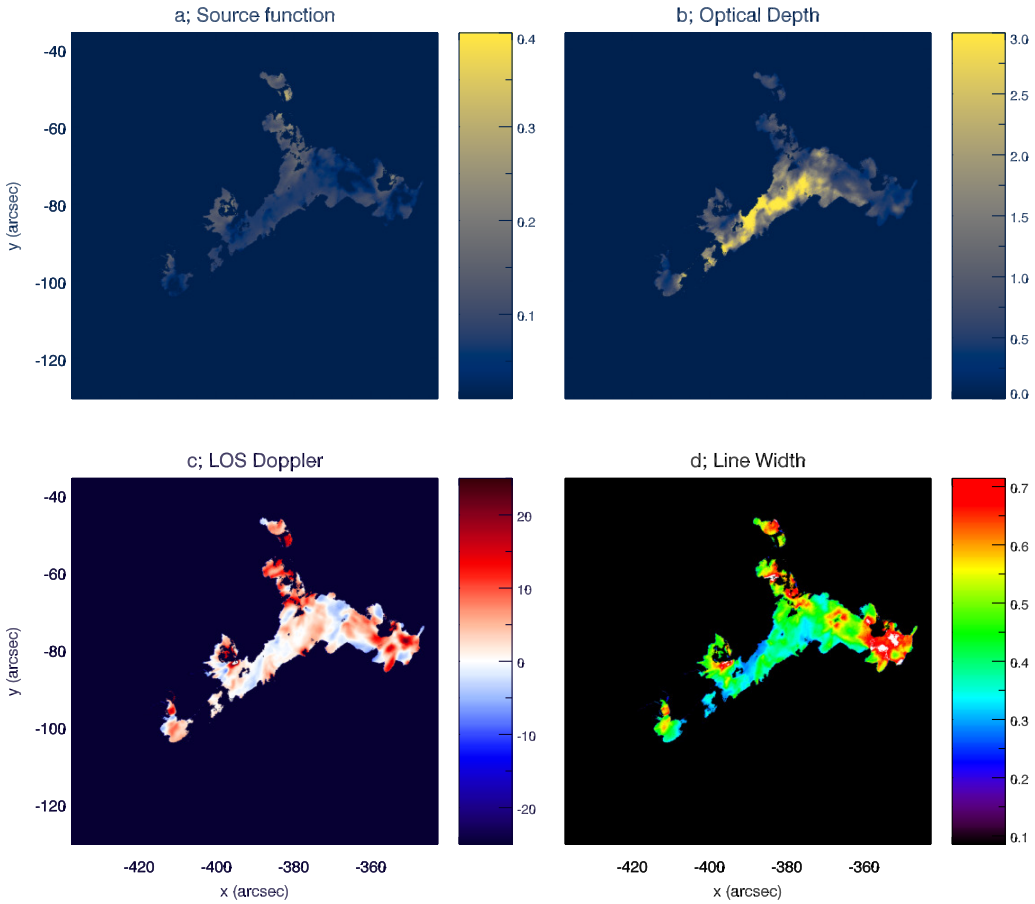

Figure 6.6: Plasma parameters of the observed prominence, inverted using the BCM code. *Panels a, b, c, and d*; the source function, optical thickness, LOS velocity [km s^{-1}], and line width [Å], respectively, measured across the prominence.

sumed constant along the LOS for a real prominence. This instead represents some average along the LOS that does not account for the true NLTE nature of the processed light; this is also the case for the optical thickness although to a lesser degree. The 2D map of the modelled source function presented in Figure 6.6a has therefore only been included to facilitate a comparison with previous studies (*e.g.*, Chae et al., 2006; Kuckein et al., 2016). The model optical thickness was permitted to vary between zero and three, although the majority of the points lie within this bound and towards the lower end, there are a number of saturated pixels indicating the model was unable to fit as the true optical thickness was presumably above the limit of three; see panel a of Figure 6.7. The pixels containing the larger optical thickness values in panel b of Figure 6.6 make a linear shape that traces the body of

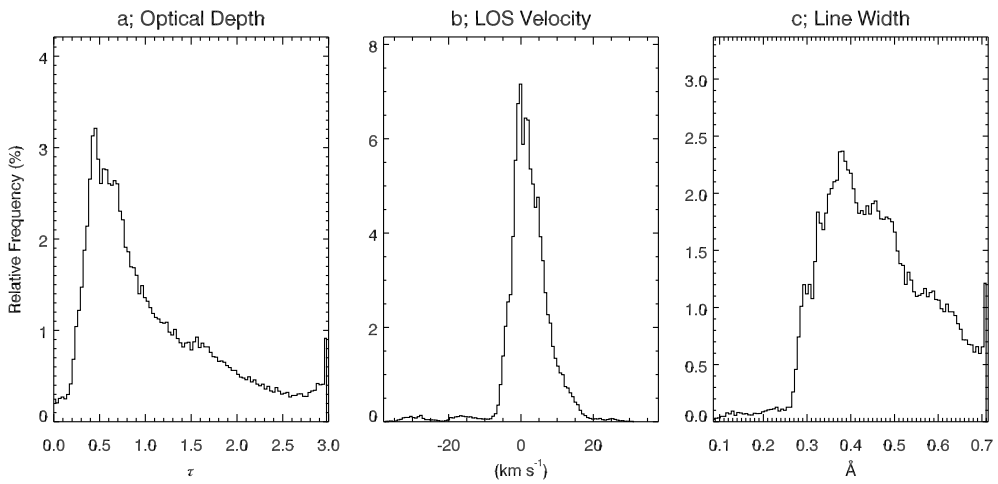

Figure 6.7: Frequency distributions of optical thickness, velocity, and line width within the prominence as derived using the BCM.

the prominence as seen in H-α absorption (cf. panel c of Figure 6.2), this section of the prominence is henceforth referred to as the spine (Chae et al., 2006).

As the majority of pixels indicate a small τ value, according to Mein et al. (1996) we may assume the deviation in the modelled velocities is small in comparison to that which would be returned from a truly NLTE model. The variation of the LOS velocity across the prominence in panel c of Figure 6.6 indicates the majority of the observed material was red-shifted with respect to the average profile. Comparing the magnitude of the modelled velocity to their positions within the prominence, it is immediately clear that the largest (by dimension) flows appear to have been located at the ends of the extensions away from the spine of the prominence. By likening the contoured structure to the shape "Y", these large velocities are concentrated at the top of such a shape with magnitudes in excess of 10 km s^{-1}. Two additional concentrations of strongly red-shifted velocities are present just to the left of the spine, one at the bottom and one midway along with the latter containing particularly strong flows of 25 km s^{-1}. The velocities in the spine of the prominence are measured by the BCM to have been between -10$< v <$10 km s^{-1}.

Panel d of Figure 6.6 details the variation in the observed profile's line width, across the prominence. Interestingly, the regions of larger-than-average red-shifted velocity that have been highlighted previously appear to coincide with regions of

larger-than-average line widths. Such broadenings are typically explained as some combination of local heating, collisions with increasingly dense material, and/or unresolved Doppler motions. The local heating of the plasma increases the width of the Maxwellian distribution and as such broadens the observed Gaussian. On the other hand, the collisional broadening takes the much thinner form of a Lorentz profile, and as such the effect of collisional broadening is likely negligible in comparison with thermal heating. As for Dopper broadening, estimates have previously been made as to the non-thermal velocities within prominences at the limb (*e.g.*, Stellmacher and Wiehr, 2015; Levens et al., 2015), whereas the effect this has on absorption profiles is seldom explored. Instead, a value of $5-15$ km s^{-1} (the ad-hoc 'microturbulent' velocity component *e.g.*, Labrosse et al., 2010) is typically assumed for the non-thermal velocity of the H-α plasma, causing a non-thermal broadening of the order expected for thermal broadening of H-α material at $\approx$ 10,000 K (Leenaarts et al., 2012). Hence, it is not possible to completely discount the possibility that the non-thermal velocities varied across the prominence without properly handling the expected thermal width of a H-α absorption profile, especially if these non-thermal velocities are caused by the Kelvin-Helmholtz instability sometimes associated with the RTI (see, *e.g.*, Berger et al., 2017). In any case, it can be said with certainty that line broadening is coincident with red-shifted velocites, an obervation that is consistent with the interpretation that prominence material was being heated as it propagated to lower altitudes. Hereafter, it is assumed that, as in previous studies, the microturbulent velocity within the prominence can be represented by a constant value of $5-15$ km s^{-1} and the measured variation in line width is then a consequence of varied heating of the prominence material. Comparatively, there appear to be regions of red-shifted velocity along the spine of the prominence that do not coincide with any broadening of the line (*e.g.*, x:-373$''$, y:-75$''$), in addition to the case of broadening that coincides with both blue and red-shifted velocities at (-366$''$, -72$''$).

According to Kaneko and Yokoyama (2018), the RTI-like plasma packets within their simulation were initially cool and remained as such during their

$\approx$ 8 km s^{-1} descent *i.e.*, there was no apparent heating nor cooling involved. In the simulation of Keppens et al. (2015), a similar result was presented although they noted that there was significant mixing of plasma that may make it difficult to establish temperature variations along the LOS from above. Not to mention, the authors also reported that the dense fingers in their simulation fell with velocities of the order 60 km s^{-1}, a value that is far in excess of those measured here. In any case, according to these works the RTI *should* appear in these BCM model maps with a distinct signature in the LOS velocity but an absence of associated heating. The combination of signatures previously pointed out at (-373″, -75″) are therefore, if we continue to associate the line broadening with heating, most consistent with the results of the previous studies.

As initially stated, the plasma parameters for six positions within the prominence have previously been inverted by Schwartz et al. (2019) using a fully NLTE 2.5D model. The (NLTE) inverted values for the velocity and optical thickness within these six positions are reproduced here in Table 6.2 alongside the values returned in the identical locations as found using the BCM. Following the analysis presented by Mein et al. (1996) the BCM method is expected to overestimate the true velocity values by up to 20%, however the comparison between the NLTE and BCM methods show significantly differing results. In particular, two of the positions have completely contradicting directionality in their inverted velocities.

The magnitude of the inverted plasma parameters may vary between the two methods according to the errors associated with each. Conversely, the explanation for the dependence of the inverted directionality on the method used is not immediately obvious. However, to address this apparent inconsistency, recall that the measurement for the velocity is derived as a shift in the line profile and not a direct quantity (in reality we only ever measure intensity). Ignoring for a moment that the zero LOS velocity is defined from a profile that is *assumed* to represent the rest profile, the errors on any measurements associated with these inversions are dependent on the sparsity of the initial spectral scans. Based on the spectral sampling shown in

Area	Velocity (km s^{-1})		Optical Depth τ		Line Width $\Delta\lambda_{th}$ (Å)	
	NLTE	BCM[a]	NLTE	BCM	NLTE	BCM
f1	6.02±7%	3.22±57%	2.54±16%	1.85	0.35±46%	0.31
f2	6.87±5%	N/A	2.02±5%	N/A	0.28±94%	N/A
f3	7.35±10%	N/A	1.05±35%	N/A	0.27±26%	N/A
f4	1.31±83%	-0.69±265%	3.88±17%	1.90	0.34±82%	0.39
f5	2.53±37%	-1.58±116%	3.01±12%	3.0[b]	0.31±88%	0.29
f6	0.1±502%	0.70±261%	3.89±13%	2.68	0.35±44%	0.38

[a] The errors presented here are subject to an additional <20% error, as a function of τ, according to Mein et al. (1996).
[b] BCM saturated suggesting the true optical thickness for this position is actually larger than this.

Table 6.2: Comparison between velocities and optical thicknesses inverted using the NLTE and BCM methods. N/A represents positions within the BCM model where the fitting failed and therefore no comparable value exists.

Figure 6.3, the sensitivity of the observations have a maximum[4] of $\approx$ 1.83 km s^{-1}. As such, the change in directionality lies within the errors of the model but the resulting interpretation can only be that the material within such pixels was close to being at rest.

Unfortunately, it is not possible to compare the interesting and strongly redshifted velocities around (-355″, -80″) within the BCM maps with that inverted using the fully NLTE model as no comparable measurements exist. As outlined by Schwartz et al. (2019), it was believed that the top-right of the FOV contained the prominence's footpoint. This was suggested as this section of the prominence was located at the end of a much longer absorption signature as seen in H-α by the GONG instruments; see panel a of Figure 6.2. The author's NLTE model requires that the magnetic field penetrating the 2D slab be largely horizontal to the surface whereas if the footpoint was located here then the associated field would be more vertical (see also Heinzel and Anzer, 2001). This is further evidenced by the work of Wang et al. (2020) in which their HAZEL inversion shows that the magnetic field strength increases by several orders of magnitude in this region indicating highly

[4]Schwartz et al. (2019) took a more practical approach in the calculation of their errors, by varying the inputs of their model around their best fit values they could directly measure at what point their assumed model would lie outside the error bars on the intensity. Hence, the authors achieved a higher sensitivity than permitted from direct inversions such as the BCM.

concentrated field as would be expected in a footpoint; this is explored in more detail in the next section. Therefore the NLTE modelling was not attempted in this region nor indeed anywhere that included strong and likely field-aligned flows.

In conclusion, according to the BCM's 2D maps of plasma parameters there were regions within the prominence that harboured velocity and (assumed-) heating profiles consistent with both the conclusions of previous works and the theoretical signature of the RTI. Nevertheless, as these measurements are subject to large uncertainties that can be interpreted as either confirmatory or contradictory to the occurrence of the RTI, these results are insufficient evidence on their own. Furthermore, the properties presented in the maps of Figure 6.6 are LOS-integrated and provide no information about the stratification of these properties in height. The focus of the following section is to therefore reconstruct such height-stratifications and explore what the parameters are inside any resulting structures potentially associated with the prominence of interest.

6.3.3 NLTE Inversion of Plasma Temperature in the Low Solar Atmosphere

As discussed at the start of this chapter, it is unclear whether the material associated with the RTI in prominences is capable of completely leaving the prominence. It has been theorised that some form of interchange reconnection may occur at the pinch point of the falling fingers and the material may successfully fall out of the prominence as a result (*e.g.*, Liu et al., 2012). For the prominence observed here the analysis thus far has been inconclusive as to whether an RTI-like process was occurring within. Indeed, the model of Schwartz et al. (2019) and the HAZEL inversion of Wang et al. (2020) extracted thermodynamic and magnetic properties for the prominence that can be considered consistent with the RTI. However, and as indicated in these works, spectral lines that are sensitive to flows within prominences are complex and can have optical thicknesses above one. For prominences that contain material with such an optical thickness, the ability to *accurately* invert the associated plasma properties depends heavily on the assumed geometry (see, *e.g.*, Heinzel and Anzer, 2001). Although a prominence-like geometry was

assumed in both Schwartz et al. (2019) and Wang et al. (2020), neither of these 1 – 2.5D geometries contained small-scale structures representative of the RTI and so the LOS-integrated parameters inverted in this way cannot hope to contain *clear* indicators of an ongoing RTI process.

In the best case scenario, the observations presented here would be inverted using a method capable of assuming a general geometry in full 3D. Unfortunately such an approach does not yet exist and its development lies outside of the scope of this thesis. Instead, if it were possible to directly detect packets of material leaving the prominence from its underside this would provide additional evidence towards answering both questions simultaneously, namely, was the RTI occurring here and did it completely remove mass from the prominence?

The NLTE inversion methods outlined thus far in this chapter are built with the primary assumption that the plasma exists within a 'cloud' suspended above the solar surface and with a general geometry believed to be indicative of a prominence. In each case the RTE is then solved along the LOS, taking into account this geometry and an assumed plasma species, with the resulting spectral profiles synthesised for comparison with observed profiles. Although this approach has been explicitly applied to what are, in a sense, prominence 'atmospheres', the method may be applied more generally to any such atmosphere that emits and/or absorbs a significant amount of light corresponding to a specific species of plasma. Specifically, the solar atmosphere itself may be modelled in much the same way (for more details, see the detailed review by de la Cruz Rodríguez and van Noort, 2017).

Radiation within the solar atmosphere, as in prominences, behaves in such a way that a full 3D representation is required to fully capture the NLTE effects and this is especially important when considering regions above the solar photosphere. The low density in the chromosphere and corona means LTE cannot be assumed as the time taken for material at such heights to average their energies across all degrees of freedom (cf. mean-free path) is longer than the time it takes for the radiation field to alter the properties of the material (*e.g.*, Beck et al., 2013b). As such, due to the lack of collisions the energy of the system cannot be evenly distributed

across all degrees of freedom. This significantly complicates attempts to model the solar atmosphere in a completely self-consistent way (recall, for example, that the state-of-the-art NLTE model of Schwartz et al. (2019) has a 2.5D geometry).

With the advent of many new space-borne instruments capable of observing the solar continuum at many wavelengths, a number of empirical 1D models of the solar atmosphere have been constructed (see the review by Gingerich and de Jager, 1968, that led to the formation of the BCA model). Building on the BCA, the now standard Harvard Smithsonian Reference Atmosphere (HSRA; Gingerich et al., 1971) claims to accurately (*i.e.*, including NLTE effects) represent the average evolution of atmospheric parameters through an 'idealised plane-parallel homogeneous atmosphere in hydrostatic equilibrium'. Although the model makes no claims that it accurately models the Sun specifically, such a model is believed to be representative of the solar atmosphere and indeed the HSRA model was initially constructed for this purpose. Hence, the HSRA models the τ-stratification of solar parameters such as temperature, plasma density, and electron pressure & density from $-8 < \log(\tau_{5000}) < 1.4$ with their NLTE properties intrinsically included (the subscript 5000 refers to the optical depth as observed at 5000 Å[5]).

With an average atmospheric model chosen it is then possible to, as before, pass these parameters through the RTE and synthesise the average shape of spectral lines present within such an average solar atmosphere. If a property of the average atmosphere is perturbed (*e.g.*, temperature) and re-synthesised as was the case in the prominence model by Schwartz et al. (2019), then the resulting spectral profiles will be a different shape to that of the average profile and will have such perturbations encoded in its new shape. This combination of the HSRA and RTE to synthesise spectral lines in the lower atmosphere is the basis of the LTE and NLTE methods of inverting Ca II observations presented in Beck et al. (2013a) and Beck et al. (2019), respectively, with the comparison between the LTE[6] and NLTE (LTE plus an

[5]The choice for this scale to be the reference is arbitrary and was historically set in Gingerich and de Jager (1968) as continuum measurements above this wavelength were not well constrained at the time of their study.

[6]Ca II synthesised in LTE using the Stokes Inversion based on Response functions (SIR; Ruiz Cobo and del Toro Iniesta, 1992) inversion code in forward synthesis mode

empirical temperature offset) approaches described in Beck et al. (2015). Although the LTE method (CAlcium Inversion using a Spectral ARchive; CAISAR) has been applied with great success in multiple studies of low-altitude structures (such as Beck et al., 2013b, 2014; Grant et al., 2018; Beck and Choudhary, 2019), Beck et al. (2015) showed how the upper altitude thermal structure of a sunspot light bridge is better modelled using the NLTE-like formulation (note, however, that the method used here is not the same as formal NLTE). Therefore, in order to isolate high-altitude structures, such as material leaving the underside of the prominence, it is necessary to use the formal NLTE[7] approach as in Beck et al. (2019).

The NLTE archive of Ca II spectral profiles is generated in Beck et al. (2019) by first perturbing the temperature stratification of the HSRA model using two separate methods. The first applies a general temperature offset of between $-1000-+200$ K in increments of $20-40$ K to all optical depths equally. The second applies localised temperature perturbations in the form of a Gaussian with amplitudes A between $10-100$ K in increments of 10 K, and widths σ between $0.2-3.1$ $\log(\tau)$ in increments of 0.1, to positions in $\log(\tau)$ in increments of 0.1. As the heating of Ca II is related to the passing of shocks, the amplitude of the Gaussian perturbation is scaled with electron pressure ($\propto$ electron density) in τ as $P_{\rm e}^{-\frac{1}{2}}(P_{\rm e} \propto \rho_{\rm e})$ to ensure that the signature of these shocks is preserved in height (in order to conserve the energy of shocks, the temperature has to increase as the atmospheric density decreases with height *e.g.*, Solanki et al., 1991; Vecchio et al., 2009; Beck et al., 2013a). The NLTE method then has the added improvement over the LTE formulation in that these temperature perturbations are realised as possible decreases from the HSRA average, not just increases. The resulting archive contains $\approx$ 2,000,000 unique temperature stratifications.

The archive of temperature stratifications is then input into the NICOLE code, hydrostatic equilibrium is forced (see Beck and Choudhary, 2019), and the RTE solved in NLTE to convert these $\approx$ 2,000,000 temperature stratifications into their corresponding Ca II spectral profiles. Although the LOS velocity contributions to

[7]Ca II synthesised in NLTE using the Non-LTE Inversion COde using the Lorien Engine (NICOLE; Socas-Navarro et al., 2015) inversion code in forward synthesis mode

the spectral profiles are neglected due to the resulting size of the archive, Beck et al. (2019) have previously shown that the lack of velocities within the archive appears to have only a negligible effect on the inversion. Specifically, provided there are no significant velocity gradients along the LOS, the shape of the Ca II line does not deform but instead shifts its position in its entirety, an effect that can be taken into account post synthesis and inversion albeit forfeiting the stratified information. This does, however, result in the least-squares procedure minimising to similar profiles from one pixel to the next in regions containing similar thermal structure but varying slightly in velocity, see Figures 6, 7, and 9 of Beck et al. (2019). Nevertheless, the authors showed that this effect is most noticeable in the LTE formulation (where the limited degrees of freedom lead to coupling between atmospheric parameters) and not so much in the NLTE.

The result of applying the Ca II inversion method developed by Beck et al. (2019) to the Ca II observation shown in Figure 6.2 is a $1000 \times 1000 \times 95$ datacube containing temperature values arbitrarily saturated between 4000 and 8000 K and stratified between $-8 < \log(\tau_{5000}) < 1.4$. In geometrical terms this equates to a range of heights of approximately $1800 > h > -83$ km, with respect to the solar photosphere (Gingerich et al., 1971). However, Ca II emission is only sensitive to the temperature of its surrounding radiation field between $-5.5 < \log(\tau_{5000}) < 0$ (see the response function of Ca II presented in Figure 6 of Quintero Noda et al., 2016). Neglecting the values within the datacube that correspond to $\log(\tau_{5000}) < -5.5$ sets the top boundary of the inversion at a lower approximate height of 1.2 Mm.

At the limb observed with SDO/AIA, 1.2 Mm corresponds to a projected height of almost three (2.8) pixels. Prominences are frequently observed at heights far in excess of this, for example Wang et al. (2020) assumed this prominence was located at a height of 14.5 Mm in their HAZEL inversion using observations from SDO/AIA. Therefore, it is unlikely that the inversion of the Ca II observation presented in Figure 6.2 would be able to reconstruct the plasma residing in the underside/belly of the quiescent prominence. Indeed, unlike in the study by Díaz Baso

et al. (2019), there is no clear absorption signature of the prominence present within the Ca II FOV. Nevertheless, and as these authors effectively demonstrate, the exact signature of the presence of a prominence within Ca II observations has not been exhaustively explored. Therefore, if a portion of the prominence does extend to lower altitudes within the FOV *e.g.*, the footpoint speculated to be rooted within the FOV by Schwartz et al. (2019) or any RTI-related packets of plasma, a corresponding signature may be present within the temperature inversion.

To minimise the effect of sporadic solutions that vary on the scale of a single pixel, the cube is smoothed in the horizontal direction by five pixels (cf. Díaz Baso et al., 2019). This approach also reduces the signature of structures less than 350 km in diameter and increases those above this threshold. This specific width was chosen as it suppresses the signatures of small scale structures such as spicules whilst enhancing those of any larger and potentially global structure present (Pereira et al., 2012).

To first address the more trivial question of the two posed, whether the footpoint of the prominence is present within the FOV, recall that Wang et al. (2020) reported on particularly high values of the magnetic field strength at one end of the absorption structure. Indeed, this is the same end of the absorption structure that was speculated to have contained the footpoint by Schwartz et al. (2019), and contained the strongly red-shifted flows as derived here using the BCM in Section 6.3.2. Qualitatively, if the strong LOS flows are field-aligned then their coincidence with increased field strength is consistent with the interpretation of higher-density magnetic field that is also aligned with the LOS and rooted in the co-located surface flux concentrations *i.e.*, a footpoint.

The high values of field strength above 400 G in this area of the prominence are far in excess of those typically measured within prominences (cf. Casini et al., 2003; Labrosse et al., 2010). Assuming for a moment that the magnetic field measured within this portion of the prominence did connect to the surface polarities then it would have to pass through the formation height of Ca II. In addition, although the response functions of Quintero Noda et al. (2016) note that the response of the

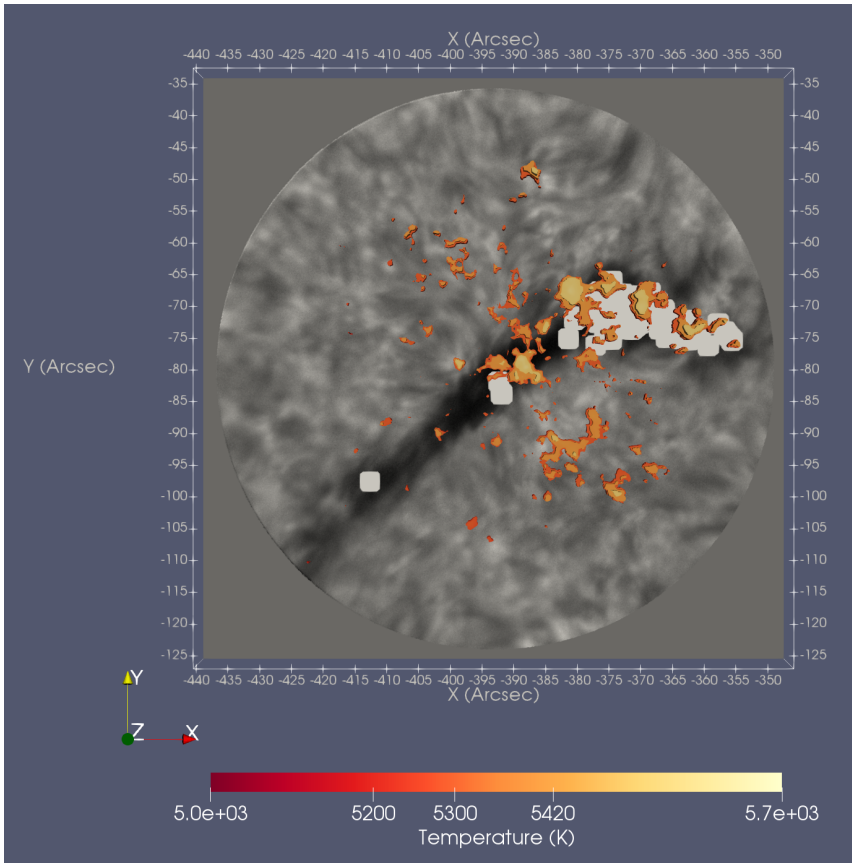

Figure 6.8: Comparison between Ca II thermal ($T = 5200$, 5300, 5420 K at $-\log(\tau_{5000}) =$ 5.8, 5.9, 6), H-α absorption structure, and He I 10830 strong magnetic field locations. A significant portion of the thermal profile appears to trace the shape of the prominence in the region believed to be a footpoint wherein the offset can be attributed to viewing angle and associated projection effects. In addition, highest temperatures are co-located with strong field concentrations (> 400 G) as derived by Wang et al. (2020), indicated by the white squares that have been enlarged for visualisation purposes.

line-core intensity to temperature perturbations drops to zero at $\log(\tau) = -5.5$, perturbations along magnetic field with strengths of $\approx$ 500 G may produce small signatures within the line-core intensity of Ca II up to $\log(\tau) = -6$. Notwithstanding that the model atmosphere did not contain magnetic field and was primarily varied in temperature, the existence of any reconstructed thermal structure above the temperature sensitivity cut-off cannot be related directy to acoustic (thermal) shocks, but may instead be related to the magnetic field.

To explore this, Figure 6.8 shows the inversion cube as viewed along the z axis with the temperatures $T = 5200$, 5300, and 5420 K contoured at $-\log(\tau) =$

5.8, 5.9, and 6.0, respectively. The H-α observation is inserted manually at a height of $-\log(\tau) = 5.7$ wherein the white contours represent the portions of the FOV that contained magnetic field in excess of 400 G according to the He I 10830 HAZEL inversion of Wang et al. (2020). It is important to emphasise again that the insertion of the H-α and FIRS observation at $-\log(\tau_{5000}) = 5.7$ has been done for comparison purposes alone as the H-α signature is believed to be sourced much higher in the solar atmosphere. As can be seen in this figure, there is a spatial coincidence (both location and shape) between the thermal structure below the prominence and the larger-than-usual field strengths within the prominence. Considering a correlation existed between these two independent observations, it is a strong indication of an existing relationship between the two; this is explored in more detail in Section 6.4.

As it has been established that this inversion method is capable of reconstructing thermal structures that are seemingly prominence related at the upper boundary of the Ca II inversion volume ($-\log(\tau_{5000}) = 6$), it is reasonable to continue to explore whether additional prominence signatures are present at yet-lower altitudes than this. Figure 6.9 shows the complete cube viewed along its x-y plane from four perspectives with the size of the z-dimension scaled by a factor of 20 to aid in interpretation. The viewing angles are pointing north, east, south, and west in the top-left, top-right, bottom-left, and bottom-right panels, respectively. The temperature thresholds applied to the cube are indicated in the colourbar (4400 – 5200 K in 100 K steps).

Contouring the cube at a specific temperature isolates vertically aligned structures such as those that are shown in Figure 6.9, in addition to a noisy horizontal structure that has been removed from the top half of the visualisation. This horizontal structure is caused by a non-negligible number of thermal stratifications that are similar and interpreted as weakly perturbed from some average profile. As the focus of this work is to study the perturbed structure within these inversions whereas the horizontal contour traces only this average thermal stratification, it has been ignored here. This approach is responsible for the resulting coarse structure in $-\log(\tau_{5000})$ and the discretely-coloured temperature contours. It was found that the lower por-

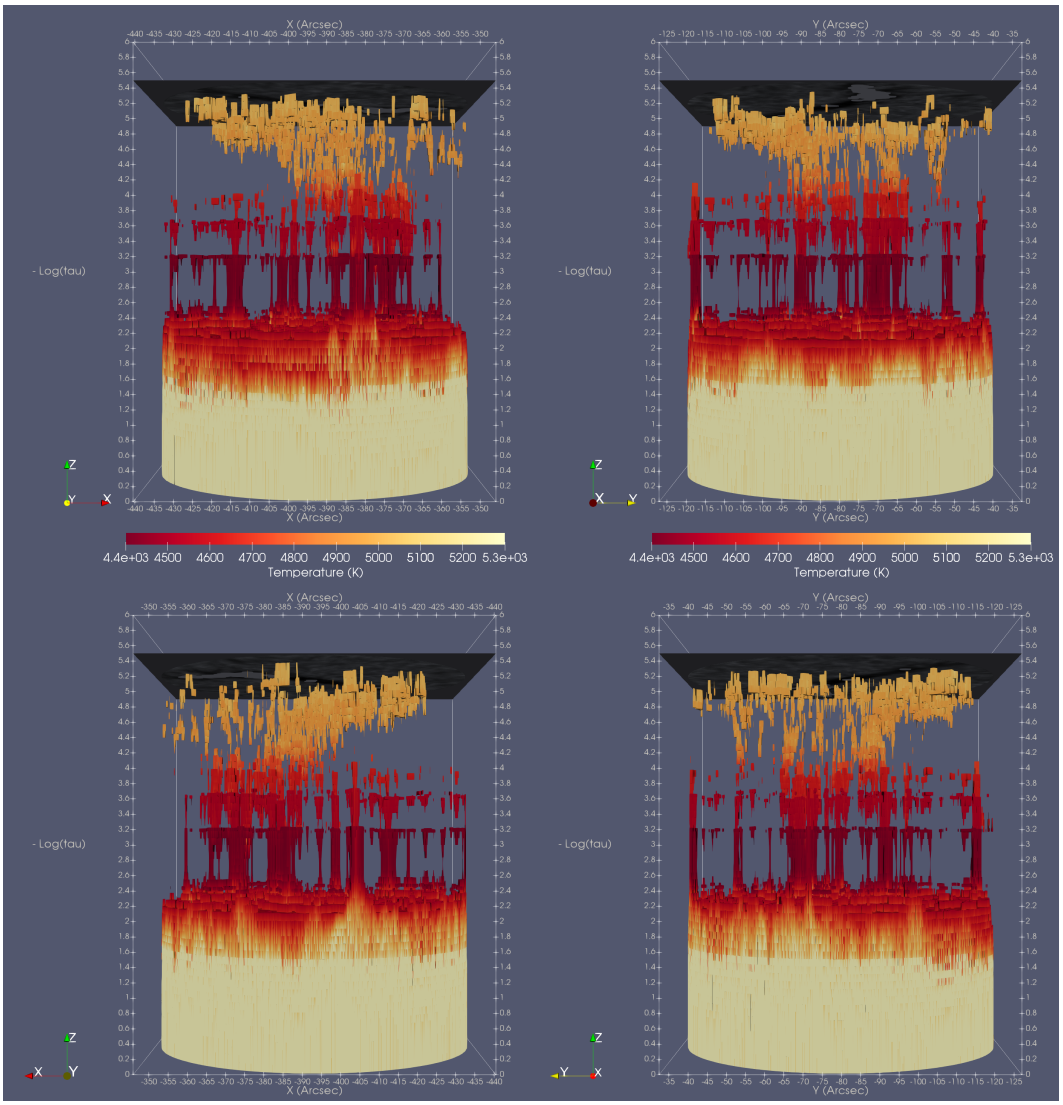

Figure 6.9: The temperature stratification of the Ca II inversions, rendered across the full FOV and viewed in the north, east, south, and west direction (a rotation counter-clockwise). The dimension of the z axis has been scaled up to aid in interpretation. The temperature thresholds are indicated within the colourbar. The coarse nature of the $-\log(\tau_{5000})$ stratification is due to the removal of the horizontal structure, at each temperature, that contours the entire x-y plane. Relatively cool monolithic , and a hot funnel, shapes can be clearly identified within the FOV.

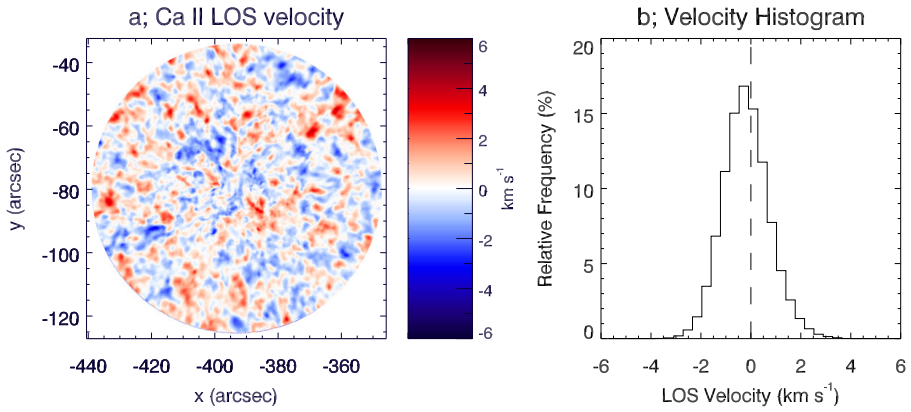

Figure 6.10: The LOS velocity of Ca II within the FOV. *Panel a*; the LOS measurement of the Ca II velocity as derived from the NLTE inversion, saturated to $\pm$ 6 km s^{-1}. *Panel b*; the corresponding histogram of the LOS velocities of (a). It is, therefore, unlikely that plasma shocks are responsible for the monolithic structures present in Figure 6.9.

tion of the cube ($-\log(\tau_{5000}) < 2$) contained a significant amount of noise that was difficult to interpret and as such these contours were not removed.

From each viewing angle within Figure 6.9 it is clear that the inversion volume contains a significant amount of fine structure detail. Most notably the volume contains a number of monolithic structures in addition to an angled temperature structure that appears to constrict with decreasing $-\log(\tau_{5000})$, appearing as a funnel-like structure. Beginning with the monolithic structures, they appear to vary in their dimensions and are seemingly present across the whole FOV. The intensity of Ca II (and therefore the temperature structure inverted here) is known to be strongly coupled to both the passing of shocks and the grouping of magnetic field such as is the case within the inter-granular network (*e.g.*, Grant et al., 2018; Beck and Choudhary, 2019).

The sound speed C_s of a medium can be defined as,

$$C_s = \sqrt{\frac{\gamma K_B T}{m}}, \tag{6.5}$$

where γ is the adiabatic index assumed equal to 5/3 for an ideal gas, and m is the mass of a particle of the material in which the sound wave is propagating (often assumed as hydrogen (m_H) for the solar atmosphere). Setting $T \gtrsim 4 \times 10^3$ and as-

suming $m > m_{\mathrm{H}}$, $C_{\mathrm{s}} \gtrsim 6$ km s^{-1}. Hence, the perturbations induced by either plasma flows or magnetic field must be greater than 6 km s^{-1} in order to shock the Ca II material and increase its emission (Beck and Choudhary, 2019). Unfortunately, unlike in the study of Grant et al. (2018), the observations presented here do not have corresponding magnetic field measurements as the field strength in the quiet-Sun chromosphere is far too low to produce a non-negligible S/N ratio within such measurements. Nevertheless, the field configuration that these authors describe as having been responsible for the conversion of Alfvén waves to magneto-accoustic waves is not present within the quiet-Sun and so magnetically-induced shocks of this form (*i.e.*, that perturb the atmosphere in the direction of the LOS) are unlikely. Therefore, the measurements of the LOS plasma velocity are presented in Figure 6.10 on their own. Panel a of the figure shows the distribution of velocities across the FOV as measured using the NLTE method, saturated to $\pm$ 6 km s^{-1}. A histogram of the LOS velocities is presented in panel b of the same figure. According to this plot there were no velocities above the 6 km s^{-1} limit within the FOV and as such it is unlikely that these monolithic structures are a result of transient acoustic shocks. However, it is important to note that the method of extracting these velocities is incomplete as unlike with the temperature within the inversion there are no stratifications in this velocity *i.e.*, it is assumed no velocity gradients exist along the LOS. This is an example of a case that would be better explored using NICOLE in a more formal way as in Díaz Baso et al. (2019) and indeed these authors noted a significant portion of their FOV contained velocities above the 6 km s^{-1} threshold.

Considering, instead, the configuration of the magnetic field within the photosphere and its relation to these monolithic structures, Figure 6.11 presents the combination of a HMI observation with the Ca II inversion results. Panel a of the figure shows the photospheric field concentrations as seen by HMI that lie within the FOV of the IBIS observations. This snapshot has been manually inserted at the $-\log(\tau_{5000}) = 0$ position in the same way that the H-α observation was in several previous figures. Panel b of the same figure shows the 7975 – 8000 K contour overlaid on the HMI image. This high temperature contour isolates the temperature per-

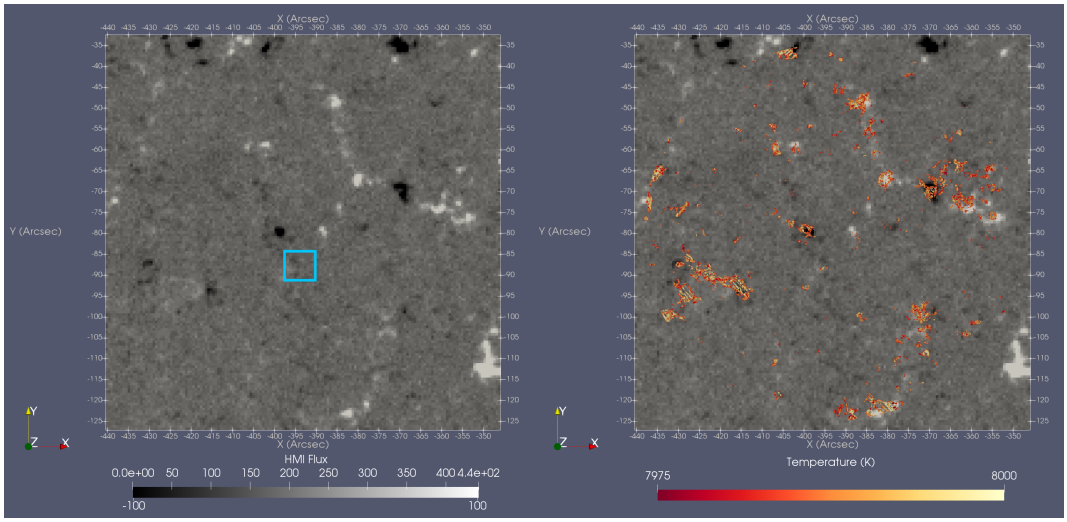

Figure 6.11: Comparison between the photospheric field structure of HMI and the Ca II monolithic structures. *Left*; the region of the HMI FOV restricted to the bounds of the IBIS observations, saturated at $\pm$ 100 G, and manually inserted at $-\log(\tau_{5000}) = 0$. The upper scale on the colourbar represents arbitrary pixel intensity. *Right*; the same as the left-hand panel but with the T=7975 – 8000 K threshold applied to the inversion cube and the results overlaid. There is a clear correlation in location between the bottom of the monolithic structures and the photospheric field concentrations of both polarities. The cyan box indicates the location of the monolithic structure underneath the belly of the prominence that does not have a corresponding photospheric signature.

turbations present at the bottom of the inversion cube ($-\log(\tau) \approx 0$), interestingly the contours lie directly underneath the previously identified monolithic structures of Figure 6.9. Indeed, the contours of Figure 6.11 are in fact connected to the aforementioned monolithic structures (This is explicitly shown in the later Figures 6.14 & 6.15). Therefore, the co-incidence between the locations of these hot contours (*i.e.*, the bottom of the monolithic structures shown in Figure 6.9) and the photospheric polarity concentrations indicate that a clear correlation exists between the two phenomena. This is discussed in more detail in Section 6.4.

Returning to the second fine-structure isolated within the Ca II inversions, the top panels of Figure 6.12 are oriented such that the LOS lies along the funnel-like structure. Here it appears that a complete connection existed between the top of the volume and the lower levels in the region directly underneath the prominence's body. Additional structures that traverse a range of $\log(\tau_{5000})$ values were present within the volume although none of these trace a continuous path from the upper to

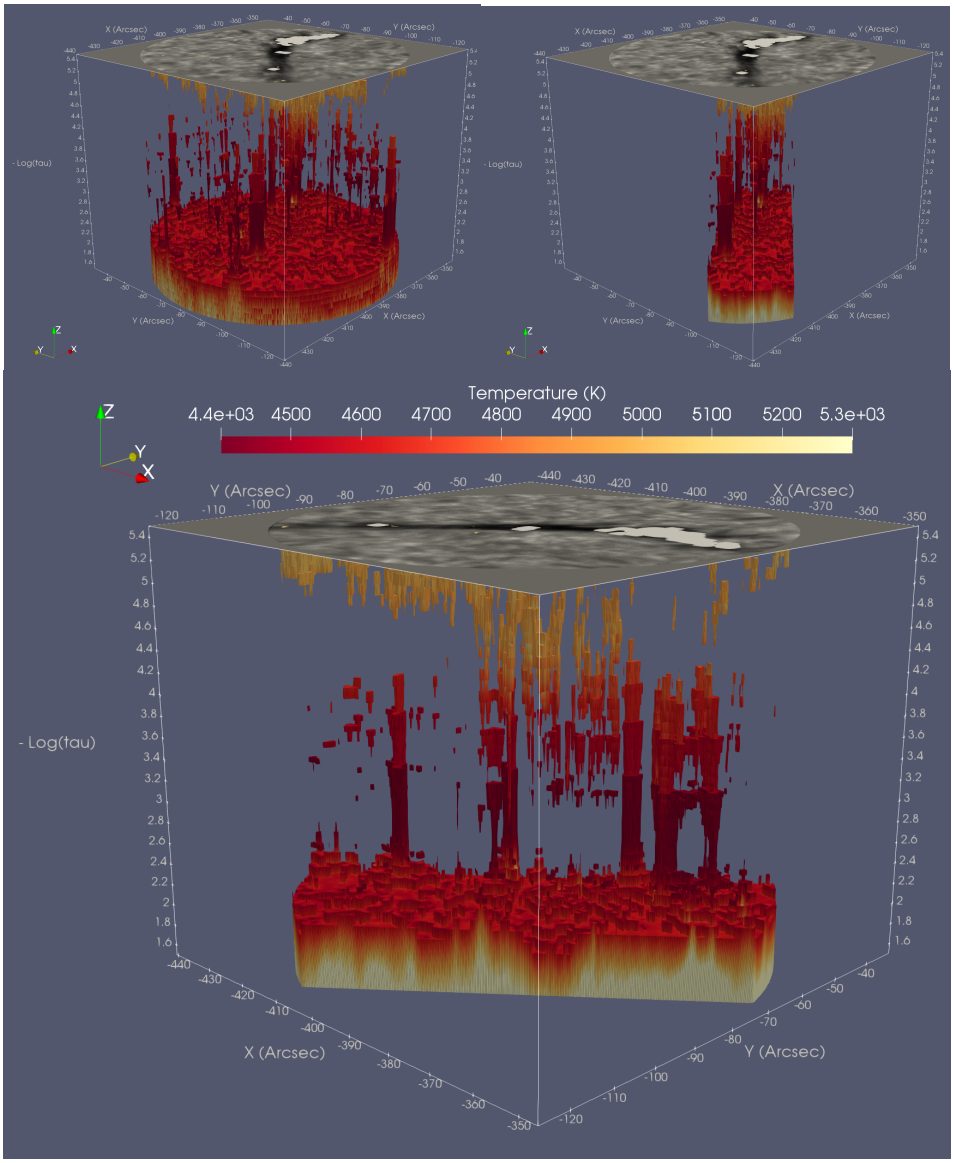

Figure 6.12: The temperature stratification of the Ca II inversions underneath the prominence. *Top left*; The complete inversion cube viewed along the funnel-like structure. *Top right*; The portion of the inversion cube that isolates only the funnel-like structure. *Bottom*; The same cut-down inversion cube presented in the top-right panel but viewed from the side. The IBIS H-α + FIRS He I 10830 observation has been inserted at the top of the cube as before. Here it appears as though the funnel is associated with the prominence structure and angled towards the region believed to host the prominence's footpoint.

lower levels and are therefore believed to not have been a part of the funnel structure of interest. The top-right panel of the figure is a subset of the full volume in which the funnel structure was located. The bottom panel of Figure 6.12 is the same as the panel in the top-right that has been rotated to show the sub-volume from the side-on. Interestingly, the rendered temperature structure appears to have been angled from the body of the prominence towards the suggested footpoint region.

The lower end of this inclined temperature structure then appears to be related to a series of the previously identified monolithic structures, grouped here on the right-hand side of the volume shown in the bottom panel of Figure 6.12. As we have already established that these monolithic structures are above concentrations of surface magnetic field, if the inclined temperature structure is related to these pillars then this would suggest the magnetic field of these monolithic structures is not only vertical in this region of the solar atmosphere. This is discussed in more detail in the next section.

For the prominence observed here, the majority of the low $-\log(\tau_{5000})$ structures that are oriented vertically and traverse a large τ range appear to have been related to the monolithic structures associated with photospheric polarity concentrations. However, a single vertically-aligned structure present underneath the prominence at (-396,-87) does not appear to have a corresponding photospheric signature, and is indicated by the cyan box of Figure 6.11.

In Figure 6.13 the structure in question has been isolated from the rest of the structures within the full inversion volume. The small figure embedded within shows the position of the vertical structure to have been at the very edge of the prominence's absorption signature observed in H-α with IBIS. The rest of the figure displays the monolith as a function of $-\log(\tau_{5000})$. The structure has been successfully contoured between $1.5 < -\log(\tau_{5000}) < 5.5$, the expansion of the monolith below $-\log(\tau_{5000}) = 1.5$ is suggestive of a vertical coincidence with some form of warm, low-chromospheric structure. Of particular interest is the apparent bulged shape with a diameter of 2.8 Mm present between $2.6 < -\log(\tau_{5000}) < 4.2$ that is reminiscent of the plasma 'blob' structure observed in the corona and drawn in the

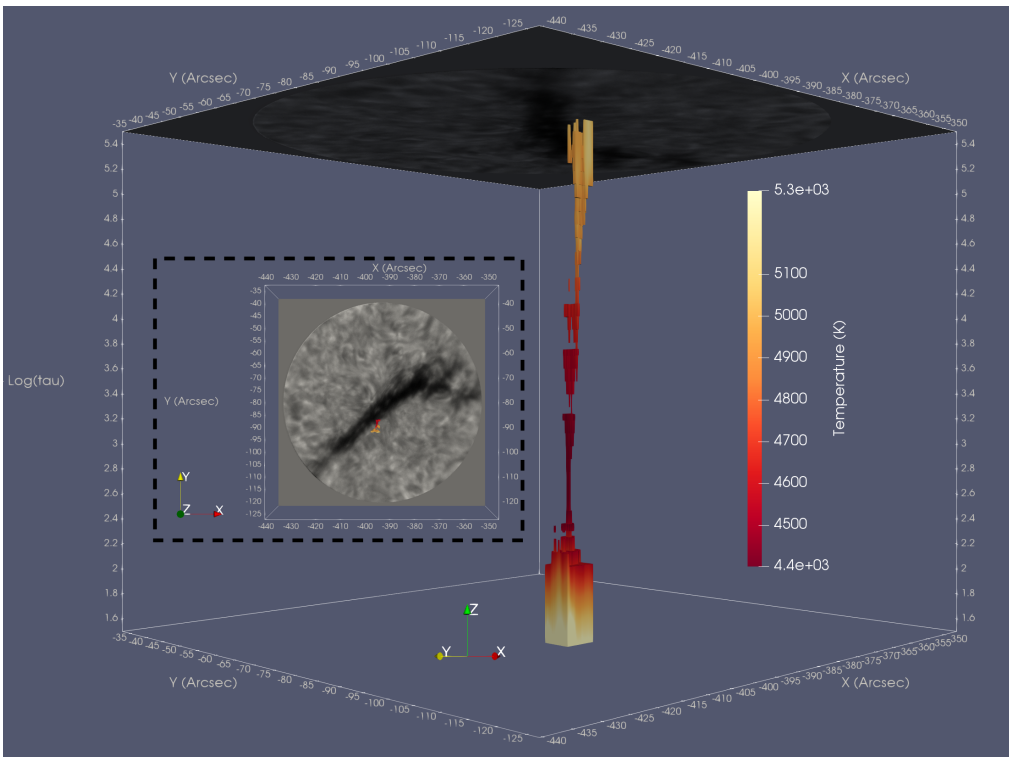

Figure 6.13: The possible detection of an RTI-like structure isolated within the Ca II NLTE inversion. *Embedded figure*; The location of the monolith overlaid on top of the IBIS/H-α FOV. The structure of the monolith as a function of $-\log(\tau_{5000})$ between 1.5 and 5.5. Note the bulged shape between $2.6 < -\log(\tau_{5000}) < 4.2$ with a diameter of ≈ 2.8 Mm.

cartoon in Figure 2 of Liu et al. (2012). This is explored in more detail at the end of the next section.

6.4 Discussion

In this chapter the results of multiple inversion methods have been used to correlate the structure and dynamics of the plasma and magnetic field within an on-disk prominence observed at the DST on 29 May 2017. Within this analysis, specific emphasis was first placed on whether any RTI-like signatures could be identified along the LOS, given the frequent observations of these dynamics in prominences at the solar limb where such motions are projected in the plane of the sky. The chapter then focused on whether such RTI-like dynamics were capable of completely liberating material from the underside of the prominence's structure.

To begin, the combination of the NLTE H-α prominence model of Schwartz et al. (2019) and the more recent HAZEL He I 10830 inversion of Wang et al. (2020) enabled measurements of plasma β at six positions within the spine of the prominence. Of course, the plasma populations used to infer the plasma and magnetic pressures within the prominence differ according to the observations used. In order to meaningfully combine these measurements of H-α and He I 10830, it has been assumed that the volume sampled by each observation is similar with regards to the magnetic field that permeated it. It is found that the β values extracted for the prominence observed here varied between $0.02 - 0.23$ and are thus consistent with previous studies of the RTI, both observations and simulations (*e.g.*, Hillier et al., 2012a; Keppens et al., 2015). However, the close proximity of these β values to the boundary of those previously established indicates these results are inconclusive on their own.

Although the NLTE H-α model includes measurements of the LOS velocity, the sparseness of these measurements, as a result of the involved nature of the method, renders the approach unfeasible in determining whether an RTI-like process was occurring within the prominence. Therefore, it was deemed that the simpler Becker's cloud model (BCM) was more suited to the process of directly inverting the full FOV and extracting the optical thickness, LOS velocity, and line width plasma parameters from the prominence absorption profiles.

Despite the large errors on the derived magnitude of these parameters as indicated in Table 6.2, clear correlations existed between them in the 2D maps of Figure 6.6. For example, the more optically thick portions of the prominence coincided with reduced LOS velocity and smaller line widths. The spine of a prominence is considered the collection of prominence material within the central dips of the associated flux rope and it is here that the majority of material associated with a prominence would lie (Zuccarello et al., 2016; Gunár et al., 2018). The magnetic field in such a region is assumed largely horizontal and in the absence of large-scale oscillations perpendicular to this field's axis any motions must be largely line tied. In the case of the prominence here, the viewing angle was such that the majority of the

LOS was projected perpendicular to the axis with a significantly smaller component aligned with the assumed-horizontal field *i.e.*, the prominence was close to but not exactly at disk centre. Hence, the smaller velocities noted in this region, as shown in Figure 6.6, would be consistent with the interpretation of this region having been the body/spine of the prominence. Similarly, the less optically thick regions, previously speculated by Schwartz et al. (2019) to have contained the prominence's footpoint, harboured strong LOS velocities of order 10 km s^{-1} in addition to heating as indicated by the much larger line widths; this is explored in more detail later on.

Across the spine of the prominence the optical thickness was measured to have been in excess of one, although in many cases it was significantly greater and reached up to values of four according to Schwartz et al. (2019). Large optical thickness values indicate there was sufficient material along the LOS to have attenuated the absorption profile in a non-linear fashion (*e.g.*, absorption and re-emission processes). Specifically, an optically thin absorption profile (in which optical thickness is less than one) is somewhat trivially characterised as an exponential decrease imposed on an initial intensity assumed to illuminate the underside of the absorbing 'cloud' *e.g.*, Eq. (6.2). In the case with optical thickness greater than one, the incident light is completely processed by the cloud.

The problem of extracting the properties of the plasma within such a cloud can be equally split between the internal, non-linear radiative transfer and the assumed geometry *i.e.*, the combination of the non-linear attenuation processes and how *much* the light is being attenuated in this way. Therefore, by definition, if the geometry is assumed to have been that which does not accurately describe the *actual* topology, the inverted parameters of the cloud will be incorrectly constrained. The NLTE model of Schwartz et al. (2019) fully models the internal processes ocurring within the prominence plasma, unlike the BCM. However, the magnetic field within the 2.5D NLTE model is assumed infinitely horizontal in the direction expected to contain the curvature of the RTI, and may therein misinterpret the true nature of the observable profiles of such a structure (Keppens et al., 2015; Kaneko

and Yokoyama, 2018). On the other hand, the BCM assumes no geometry but suffers from being an overly-simplistic and ill-constrained tool applied to a highly complex reality (Tziotziou, 2007). Therefore, it is assumed that although the BCM lacks the formalism available with the NLTE model, the approach remains both sufficient and more practical at extracting and studying the 2D motions of large-FOV observations whilst adopting minimal assumptions on the geometry involved.

In Section 6.3.3, the assumption of a prominence-specific geometry was removed altogether and the solar atmosphere was instead inverted assuming a plane-parallel stratification in the related plasma parameters. It was believed that this approach stood a better chance of probing the nature of the underside of the observed prominence given the shortcomings of the models that assumed a geometry, whilst maintaining the physical accuracy of handling the RTE in full NLTE. The temperature of the HSRA model atmosphere was perturbed using τ-scaled Gaussians to produce $\approx$ 2,000,000 unique stratifications between $-1.4 < -\log(\tau) < 8$ that were in turn synthesised using NLTE into Ca II spectral profiles via the NICOLE code. The comparison between this database of profiles and those observed below the prominence enabled the reconstruction of the 3D (2D group of 1D stratifications) solar Ca II atmosphere within the FOV.

According to the model of Quintero Noda et al. (2016), the temperature response function of Ca II has an upper limit of $-\log(\tau) = 5.5$, $\approx$ 1.2 Mm. However, the response of the recorded line intensity was also shown to be sensitive to perturbations in a photospheric magnetic field of order 500 G up to $-\log(\tau) = 6$, albeit weakly. As such, it was speculated that such an intensity increase induced by these magnetic perturbations, a property neglected from the model approach, would be reconstructed using this model as a weak temperature signal at heights up to $-\log(\tau) = 6$. Therefore, as the coherent temperature structures contoured at $-\log(\tau) = 5.8$, 5.9, and 6 in Figure 6.8 *cannot* have been induced by temperature perturbations, they have instead been interpreted as the perturbations in magnetic field present at these locations. This is additionally consistent with the measurements of the magnetic field strength measured within the prominence by

Wang et al. (2020) at altitudes believed to have been far above the inversion volume. Alternatively, if the temperature structures are not related to the presence of perturbed magnetic field, they must be the result of the ill-constrained nature of the model at such heights (recall that the model is perturbed up to a height of $-\log(\tau) = 8$). However, such signatures would have presumably been identified as noise rather than the spatially coherent structures shown here, although this may explain the other, rather less spatially-coherent structures within the FOV.

The compact temperature enhancements isolated above $-\log(\tau) = 5.5$ were then seen to have been related to the monolithic structures contoured and viewed side-on in Figure 6.9. The additional co-incidence of these structures with the photospheric polarity concentrations observed with HMI (Figure 6.11) suggested these monolithic structures were related to the magnetic field of the solar atmosphere within the inverted volume. Solar flux tubes that penetrate the solar surface, expand through the chromosphere and into the corona have frequently been invoked to explain thermal signatures observed using Ca II (cf. 'Umbral flashes' and their relation to expanding flux tubes *e.g.*, Solanki et al., 1991; Jess et al., 2010; Beck et al., 2013b; Grant et al., 2018).

Following Beck et al. (2013b), panel b (d) of Figure 6.14 shows the thermal structure of the solar atmosphere along the cut defined in panel a (c) of the same figure. This cut is then averaged across its width to enhance the larger temperature perturbations before the average profile within the cut is subtracted. The resulting figure details the locations, shape, and strengths of the temperature perturbations that both increased and decreased the local temperature within the inverted volume. The use of the improved NLTE method developed by Beck et al. (2019) over that of the LTE appears to have resulted in additional thermal structure inverted at all heights. Similarly, the ability of the NLTE approach to resolve negative temperature perturbations explains the large decreases in temperature present within panels b and d (cf. Figure 16 of Beck et al., 2013b).

Comparing with panel d of Figure 6.14, two distinct flux tubes can be identified in panel b at 30 and 45 Mm, each extending from the photosphere to the top of the

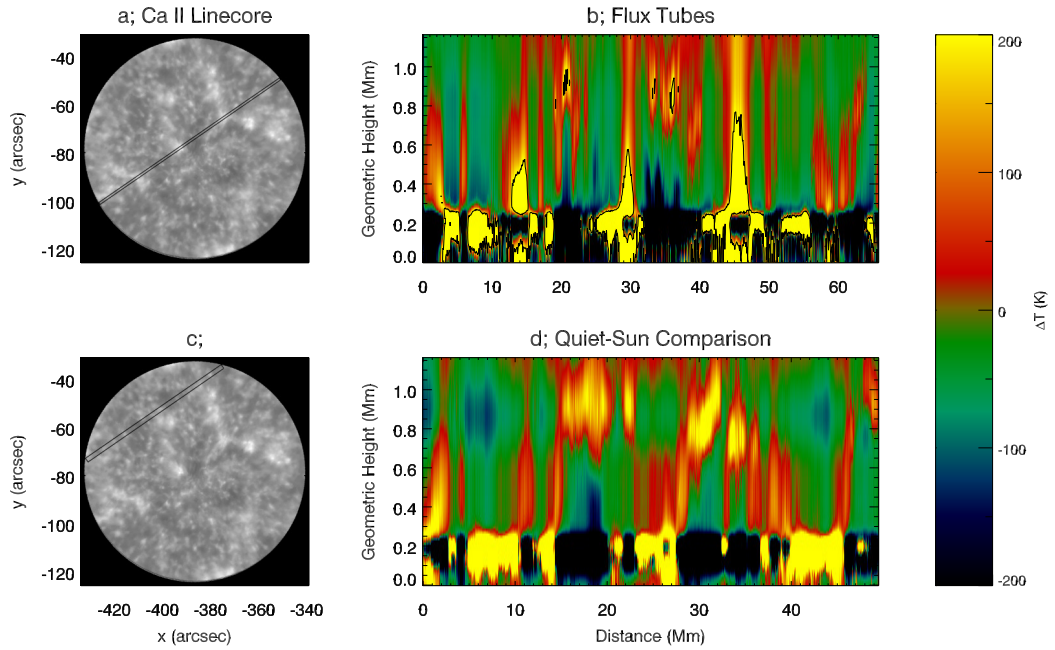

Figure 6.14: The thermal perturbation structure of inverted flux tubes compared with the quiet-Sun. *Panels b* and *d* The average thermal perturbation structure inverted across the widths of the cuts shown in (a) and (c) respectively, saturated between $\pm$ 200 K. The solid-black line in panel b contours regions of +200 K. The conversion between τ and geometrical height is only approximate and in accordance with the initial model of Gingerich et al. (1971).

inversion volume at $\approx$ 1.2 Mm (the approximate conversion between optical depth and geometric height was applied as in Gingerich et al., 1971). Note these structures are not ubiquitous as demonstrated by their absence from the cut taken in a region assumed to represent the quiet-Sun. Assuming, therefore, that the temperature enhancements here are related to the co-located surface magnetic field polarities, this would explain the lack of a velocity signature in these areas. Specifically, magneto-acoustic waves that propagate up the invoked flux tubes may travel much faster in their propagation direction than the 6 km s^{-1} required to shock the atmosphere, however the energy deposition and associated perturbation is applied to the wave's surroundings in a perpendicular direction to this guide field (*e.g.*, Grant et al., 2018). Hence, as the LOS of this observation is presumably oriented along the magnetic field permeating this environment *i.e.*, the magnetic field at this altitude may be as-

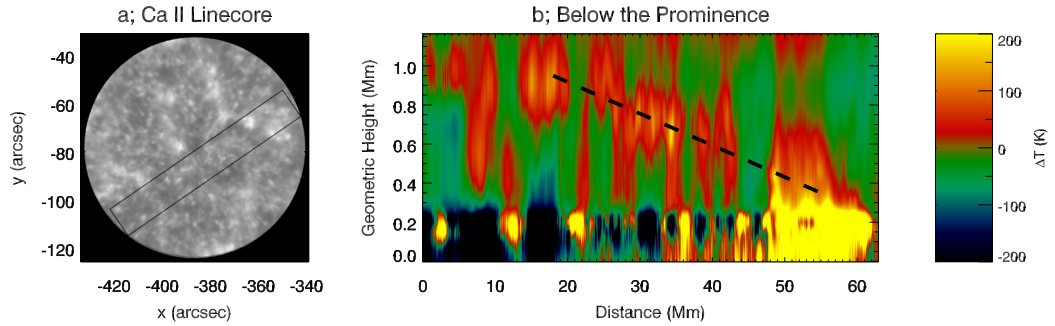

Figure 6.15: *Panel b*; The thermal perturbation structure of the region directly below the prominence's absorption signature, averaged across the width of the cut overlaid on the Ca II observation in (a), saturated between $\pm$ 200 K. The angled feature has been highlighted by the dashed-black line. As in Figure 6.14 the geometrical height is only approximate.

sumed radial, any velocity variations would be in the plane of sky and therefore not detected.

Curiously, the thermal profiles in these tubes appear to have decreased in magnitude with height, contrary to the conclusions of previous works that focused on perturbations to flux tubes (*e.g.*, Solanki et al., 1991; Beck et al., 2013b). The energy responsible for heating the Ca II material so as to appear in emission in such structures is believed to be supplied by the photospheric granulation buffeting the footpoints of the associated network field. According to these previous studies, such perturbations should propagate up the tube and increase in temperature and a $+$200 K contour outlined in solid-black has been included in panel b of Figure 6.14 to further emphasise this seemingly-contradictory behaviour. However, the authors also noted that the energy source responsible for the heating along the entire tube remains acoustic, yet somehow facilitated by the presence of the magnetic field - the exact physical process occuring in such locations remains an outstanding question (see also Rezaei et al., 2007; Beck et al., 2012). Therefore, as the cause of the heating in the region of the photospheric polarities lies outside the scope of this study, these monolithic structures are simply interpreted inline with these previous studies *i.e.*, the heating in the presence of near-vertical field associated with the footpoints of magnetic network elements by a currently-unknown source.

The second structure easily identified within the inversion cube was that of the angled funnel-like feature positioned underneath the prominence's absorption sig-

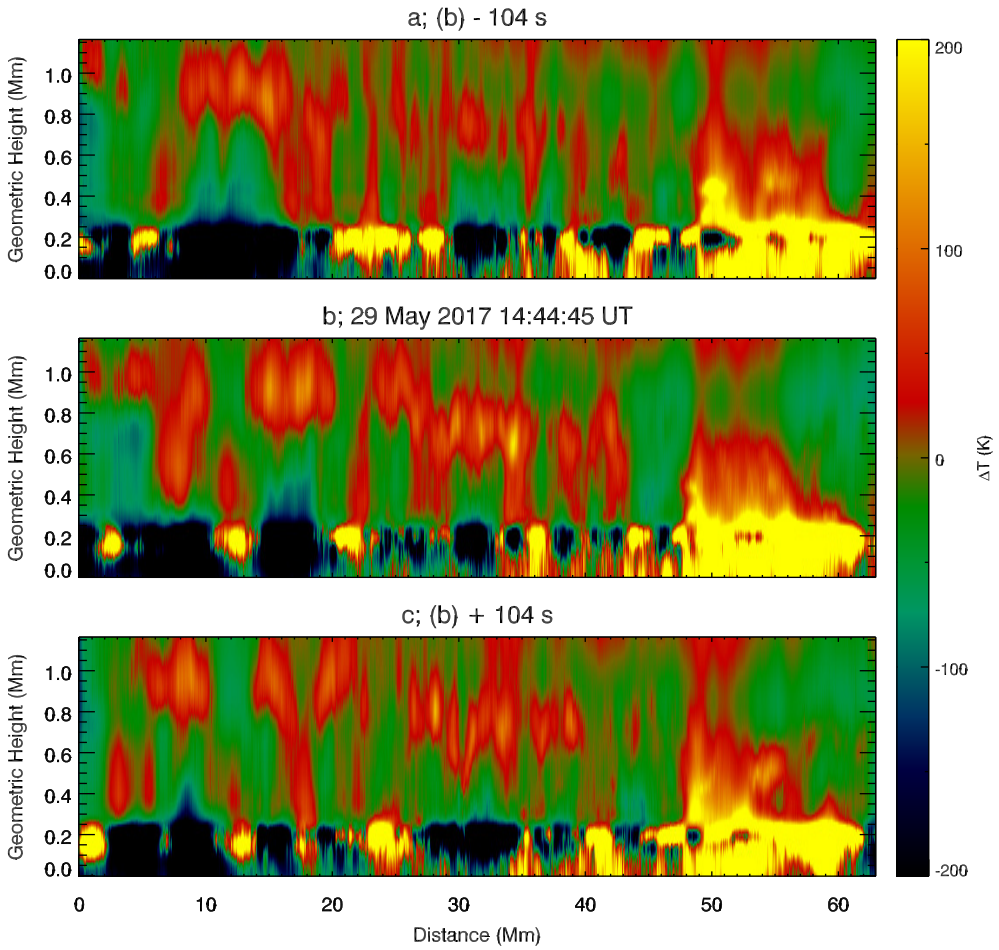

Figure 6.16: The temporal evolution of the inclined structure present within the Ca II inversion volume. *Panel b*; The thermal profile underneath the body of the prominence as observed at 14:44:55 UT. *Panels a* and *c*; The same as (b) but $\pm$ 104 s, showing that the inclined structure was persistent in time and inconsistent with the interpretation of random acoustic shocks.

nature according to Figure 6.12. Strikingly, the constriction of the funnel appears to have been oriented in the direction of the prominence's proposed footpoint. This is further evidenced by the average thermal perturbation profile taken in a cut directly underneath the prominence and presented in Figure 6.15, created using the same method as Figure 6.14. A dashed line has been included to highlight the inclined structure, although the angle of this line is not intended to represent the actual inclination of the structure it is tracing.

In order to interpret such signatures, first recall that the thermal signatures within Ca II observations are known to be caused by shocks. Then, in locations co-

incident with photospheric polarity concentrations, flux tubes have been invoked to explain the enhanced heating events that occur at $\approx$ 1 Mm and appear constrained by the associated magnetic topology. In such cases, the expansive nature of these flux tubes has been shown to facilitate the increased signature of these shocks (simply, decreased density with height causes an increased temperature with height, a guiding principle adopted within the perturbations initially applied to the HSRA atmospheric model, Solanki et al., 1991; Beck et al., 2013b).

One possible interpretation of these heating signatures in Figure 6.15 at altitudes below 1 Mm is that these flux tubes are expanding and forming the magnetic canopy at lower heights than would be the case in an unstructured atmosphere (*e.g.*, Solanki et al., 1991; Solanki, 1993; MacTaggart et al., 2016). The height that this occurs at, referred to as the merging height h_{m}, is a function of the pressure internal and external to the flux tube. By extension, the decreased merging height inferred by the thermal signatures within Figure 6.15 would have therefore been caused by a larger-than-typical pressure internal to the flux tubes (cf. Beck et al., 2013b).

Alternatively, the apparent grouping of the thermal signatures that have indicated an inclined structure could have been the result of chance. It is possible that a series of acoustic shocks may have aligned in this snapshot to produce a false positive (*e.g.*, Cauzzi et al., 2007). As such, this inclination would be a short-lived signature that dispersed with time. Figure 6.16 presents two more snapshots taken at both 104 seconds prior to and after the one presented in Figure 6.15 (reproduced here in panel b). These additional maps indicate that the location and shape of the inclined structure persisted, albeit with some anticipated variation therein *i.e.*, the magneto-acoustic waves travelling along these tubes are not stationary but the guiding structure is. The time series obtained at the DST began at 13:59 UT, however the AO of the telescope was unable to hold a consistent lock on the photospheric granulation pattern until approximately 14:43 UT. Hence, we cannot study further back in time than this point. The inclined signature appeared coherent for over 200 s and so it is suggested that a consistent structure was present at these altitudes that

facilitated the inclined heating signature present in Figure 6.16. Such a structure is most consistent with the previous description of flux tubes.

At this point, it is worthwhile consolidating the structural information extracted by the inversions thus far. The HAZEL inversion carried out by Wang et al. (2020) on the He I 10830 observation indicated that the field within the prominence was horizontal in the region previously suggested to have contained its footpoint by Schwartz et al. (2019). The LOS velocity derived by the BCM indicates strong and correlated flows towards the surface, co-incident with heating, in this 'footpoint' region. Assuming that flows within the solar atmosphere are line tied as described in Section 1.5.1, such agreement between the LOS velocity and line width is therefore consistent with the interpretation of plasma travelling away from the observer and to lower altitudes along less-inclined magnetic field. Finally, the Ca II inversion appears to indicate that some form of structure related to flux tubes was present at low altitude, with an inclination towards the region speculated to contain the prominence's footpoint.

The HAZEL and NLTE H-α inversion results appear inconsistent on the question of whether the prominence's footpoint was within the FOV, however the response functions of H-α and He I 10830 indicate that the spectral lines responsible for these inverted parameters are formed at different heights and therefore correspond to different volumes (Socas-Navarro and Uitenbroek, 2004; Leenaarts et al., 2012; de la Cruz Rodríguez and van Noort, 2017). For H-α, the average formation height appears to be in the region of $1-1.5$ Mm, whereas He I 10830 is formed higher up at an average height of 2 Mm. As such, it is perfectly reasonable to suggest that the H-α material existed on field lines closer to the surface with less-inclined (to the radial) field whereas the He I material existed higher up and on more horizontal field.

In addition, recall that the initial fitting of the BCM to the H-α observations indicated that a large number of positions existed within the FOV wherein the fitting failed; see Figure 6.4. Panels b and c of Figure 6.5 show two profiles representative of the large χ^2 band on the left-hand side of panel a in Figure 6.4. Curiously, these

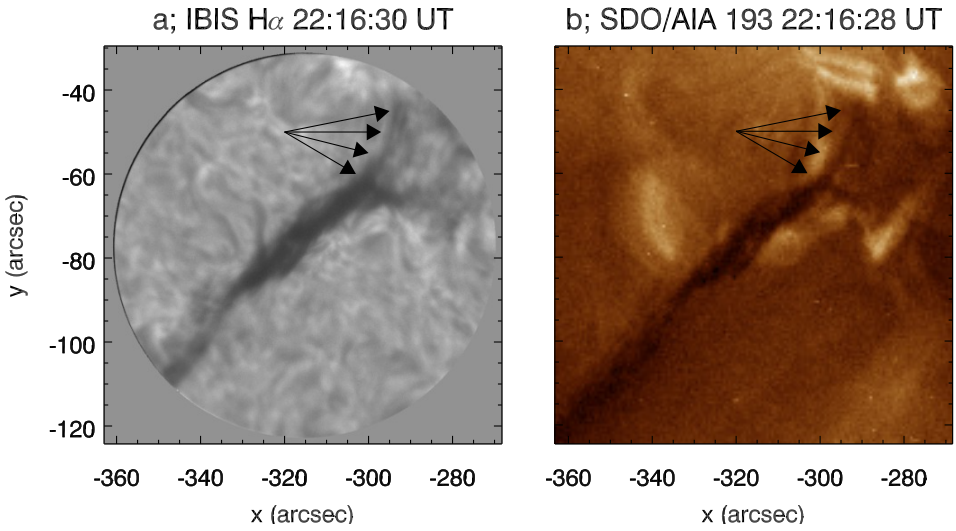

Figure 6.17: IBIS and SDO/AIA snapshots showing plasma illuminating a possible second plasma cloud along the LOS. *Panel a*; IBIS H-α observation of the prominence at 22:16:30 UT on 29 May 2017 wherein a plasma structure has highlighted an extension towards northern latitudes. *Panel b*; SDO/AIA 193 Å observation of the prominence at 22:16:28 UT on 29 May 2017 showing the same as (a). Arrows have been used in each panel to indicate the location of the extension being referred to.

two profiles indicate an additional absorption signature along the LOS that could not be fitted using the BCM, hence the large values of χ^2 here. The BCM inherently assumes a single cloud along the LOS, whereas these profiles suggest there may have been more than one. Furthermore, and as indicated by Wang et al. (2020), the prominence observed here was a portion of a much larger structure that continued up into the northern hemisphere. The absorption signature of this portion of the prominence was absent from the H-α observations, as in Kuckein et al. (2016), but was quasi-periodically illuminated by flows as observed in the 193 Å passband of SDO/AIA. One of the most obvious flows occurred at $\approx$ 22:16 UT and has been isolated and shown in Figure 6.17. If the second absorption profile within the H-α spectra is indicating that the corresponding plasma resided at a height different to that of the footpoint, it could have been associated with the more horizontal field present within the He I plasma *i.e.*, higher up within the prominence.

Based on these results and the associated response functions, a possible arrangement of these observations, in height, is presented within Figure 6.18. Here, the pressure (magnetic + plasma) of the prominence's footpoint is suggested to

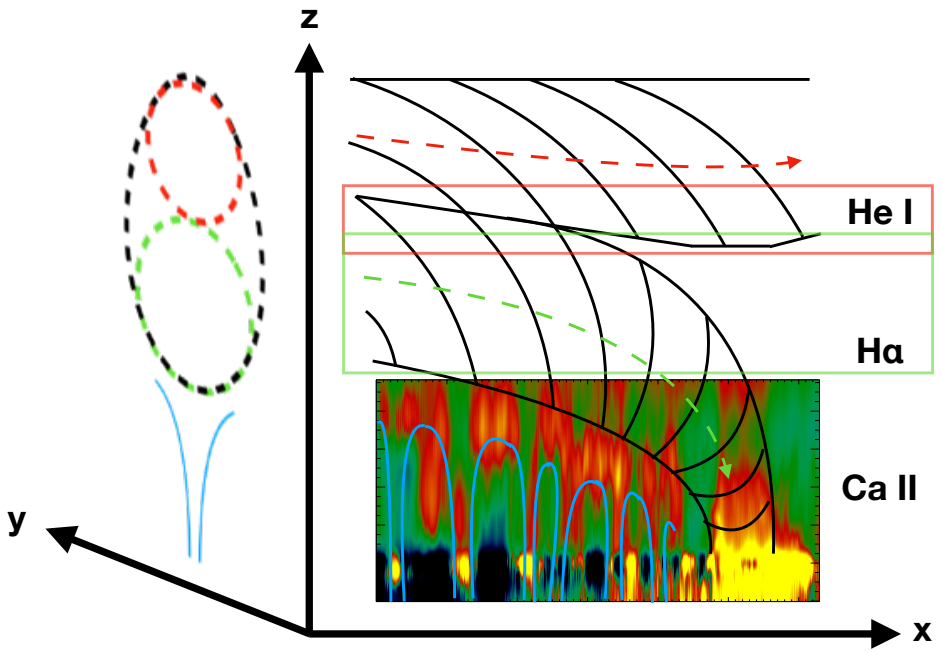

Figure 6.18: A cartoon representation of a possible structural relationship held between the individual observations presented within this chapter. The structure associated with the He I inversion is depicted with a dashed-red arrow and oval. The structure associated with the H-α BCM inversion is depicted with a dashed-green arrow and oval. The flux tubes responsible for the heating signature present within the Ca II inversion are indicated with solid-blue lines. The x-z plane represents the view from side on, whereas the y-z plane is a cut through the associated magnetic field structure that indicates the prominence domains within which each different observation lies.

have been responsible for the apparent decrease in the merging height of the underlying flux tubes. Likening it to a person sitting on a chair, a study of the cushion does not resolve the person but rather the response of the cushion to the presence of the person. Interestingly, this cartoon is somewhat reminiscent of the structure animated in Martínez González et al. (2015), albeit at a far lower altitude; see their Figure 3.

The independent yet correlated analysis between the location of the increased magnetic field strength as measured using the HAZEL inversion code by Wang et al. (2020), the increased LOS velocity in this region as measured with the BCM in Section 6.3.2, and the correlation between the location of the photospheric polarities and the reconstructed thermal profile of Section 6.3.3 at $-\log(\tau_{5000}) = 6$ in combination with the angled thermal structure within the inversion volume, provides a

confluence of evidence that the footpoint of the prominence was rooted within the FOV of the ground-based instrumentation.

The final part of this chapter focused on a structure underneath the prominence that appeared to not have a corresponding photospheric polarity underneath. It was suggested that such a signature would be consistent with the understanding of the RTI within prominences as established by studies carried out over the last decade (*e.g.*, Berger et al., 2008, 2010, 2011; Hillier et al., 2012b,a; Keppens et al., 2015; Kaneko and Yokoyama, 2018).

However, the density models of the low solar atmosphere (*e.g.*, Gingerich et al., 1971; Fontenla et al., 1993) are clear in that the prominence observed here, with a density measured by Schwartz et al. (2019), cannot exist at the altitudes probed using the Ca II inversion method *i.e.*, sub-1 Mm. For example, according to the FAL-C model of Fontenla et al. (1993) the ambient atmospheric plasma density would equal that of the prominence studied here at a height of 2 Mm. Indeed, this likely explains the absence and rarity of prominence absorption signatures within Ca II observations, as is the case here.

Yet, and as demonstrated by Díaz Baso et al. (2019), neither the atmospheric models, nor the associated response functions that have been derived therein, are completely infallible. To clarify, the authors showed that by not imposing hydrostatic equilibrium within their model atmosphere they could produce an absorption signature within a Ca II spectral profile from a synthetic prominence suspended at > 10 Mm. Of course, for the low solar atmosphere a lack of hydrostatic equilibrium is physically inaccurate (the low solar corona is not infinitely thin nor in the process of completely diffusing into space) but it is important to highlight that the model atmospheres are incomplete *i.e.*, they're not solved in magneto-hydrostatic equilibrium, a distinction that may alter the response functions in a similarly dramatic way (According to Spruit (1976), magnetic field aligned with the LOS can make the atmosphere more transparent). In any case, the clear lack of an absorption signature within the Ca II observation of Figure 6.2 indicates that the associated inversions

will not include the same signatures of cool dense material as was observed in He I or H-α, or the study by Díaz Baso et al. (2019).

Furthermore, it has just been assumed that flux tubes were responsible for the heating observed underneath the prominence. Such structures can have diameters as small as $0.2''$ in the photosphere, so at a third of the pixel size of HMI it is possible that HMI observations simply could not resolve the polarity signature of such small structures (cf. G-Band bright points, Puschmann and Wiehr, 2006). Therefore, the monolith that has been resolved within Figure 6.13 may simply be the heating of the atmosphere due to a wave having propagated up a flux tube located here.

If this heating signature is related to the presence of flux tubes, as was inferred for the inclined structure underneath the prominence, then the signature of this heating should travel at, or around, the sound speed of the environment and in the direction away from the surface. To explore this, the evolution of the LOS velocities derived for the H-α and Ca II observations within the bounds of the monolith are compared to the temporal evolution of this thermal structure in Figure 6.19, where the $t = 0$ s timestep refers to the observation at time 14:43:11 UT. The temporal evolution of the thermal structure presented in panel c has been constructed as a base difference wherein timestep 0 has been subtracted from the following timesteps 1 – 16.

Immediately contrary to this hypothesis, panel c shows that the thermal signature detected within the Ca II inversion propagated from the top of the inversion volume to the bottom (from $-\log(\tau_{5000}) = 5.5-1$). Isolating just the region that contained this monolith, the average Ca II LOS velocity measured within this region of the inversion is seen to have peaked in panel b with a value of 0.83 ± 0.04 km s^{-1} at $t = 65$ s, immediately before the thermal signature appeared within the inversion volume in the panel below. Recall that the $\Delta\lambda$ of the line core is solely taken into account in the measurement of the Ca II LOS velocities. This, by definition, corresponds to the velocity of the upper-most region of the Ca II atmosphere, strongly indicating that these measurements are related (Quintero Noda et al., 2016; Beck et al., 2019). Interestingly, the evolution in the LOS velocity inverted from the H-α

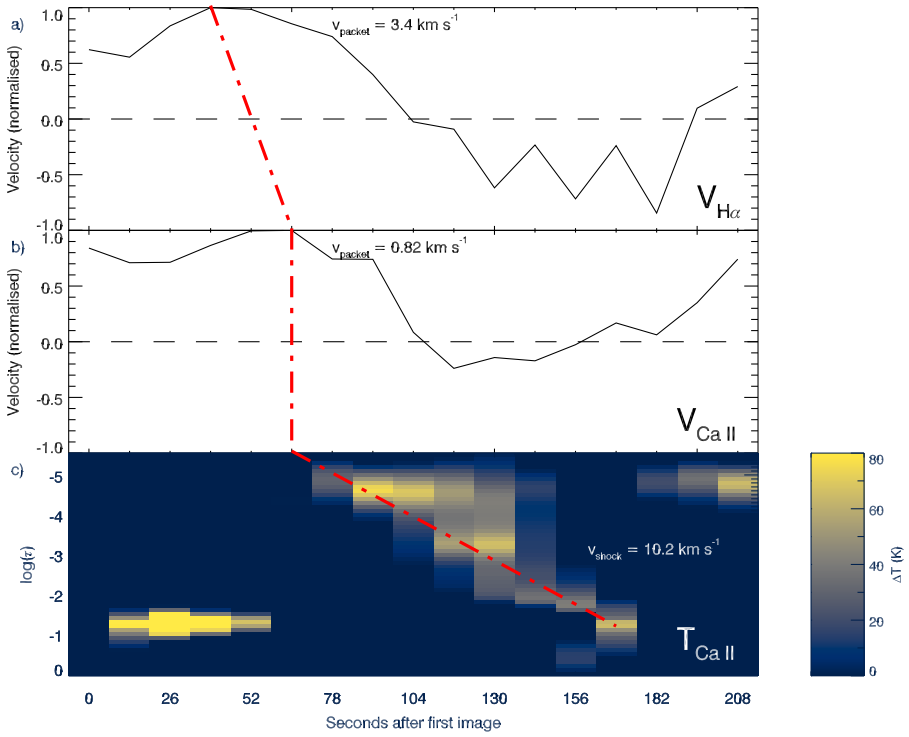

Figure 6.19: Possible detection of an RTI-like structure using the H-α LOS velocities and the Ca II NLTE inversion of both LOS velocity and temperature. *Panels a* and *b*; The evolution of the mean H-α and Ca II LOS velocity, respectively, measured within the same bounds as (c). *Panel c*; The evolution of base-difference Ca II temperature perturbations, saturated between 0 and +80 K, within a cube surrounding the monolithic structure of interest; see Figure 6.13. The dash-dotted-red line indicates the path of the 'Plasmoid' from the H-α – Ca II heights. $t = 0$ s refers to time index 14:43:11 UT.

observations within the same region appears to mimic that of the Ca II; see panel a of the same figure. Furthermore, this velocity enhancement is seen to have peaked slightly earlier at $t = 39$ s and with a larger velocity of $+3.4 \pm 0.1$ km s^{-1}.

Although the striking similarity in the evolution of the velocity profiles shown in panels a and b of Figure 6.19 could be coincidental, it more likely suggests a shared property between the two perturbations. If the perturbations were caused by the same phenomena then this complicates the suggestion of a single wave having been responsible. Specifically, any perturbation due to a magneto-acoustic wave passing along the vertically-aligned magnetic field of the low solar atmosphere would have been perpendicular to the LOS. If the wave was passing instead along horizontal field then the small recorded velocity signature of ≈ 3 km s^{-1} could not

have been caused by a wave with sufficient amplitude to perturb both H-α and Ca II, simultaneously or otherwise.

If these two velocity profiles refer to the same object then this is suggestive of it having travelled in the direction of the lower atmosphere. Assuming the height difference between the two layers to have been 500 km (cf. Leenaarts et al., 2012; de la Cruz Rodríguez and van Noort, 2017) then the object had a velocity of 20 km s^{-1}, a value much larger than 3.4 km s^{-1} as measured in the H-α velocity inversion. However, the Ca II velocity estimate is dependent on $\Delta\lambda$ in the line core, whereas the H-α velocity is more sensitive in the wings of the profile. According to Socas-Navarro and Uitenbroek (2004), the absorption at such positions within the H-α spectral line is somewhat unconstrained but is most certainly sourced at a much lower altitude than its core. Therefore, the velocity of the packet need not have necessarily been significantly higher than as inverted using the BCM, especially when also taking into account the errors on such measurements.

Relating these independent measurements taken at different altitudes within the solar atmosphere (the dashed-red line) tentatively suggests that the signature was that of a single physical structure of some form, rather than a wave as previously suggested in relation to the presence of flux tubes. Assuming the stratification of structures as set-out in Figure 6.18, this 'plasmoid' may have been associated with the underside of the prominence, albeit at a far low altitude than initially speculated. The assumption of a lower initiation height simultaneously addresses the unlikely aforementioned scenario whereby a RTI packet from the underside of the prominence had travelled from a height of some 10+ Mm down to sub-1 Mm. Instead, by invoking a prominence wherein the associated magnetic field penetrated the chromosphere, akin to a bald patch separatrix surface (BPSS; Bungey et al., 1996) but in the chromosphere, it may finally be speculated that overdensities of this chromospheric plasma formed an RTI-like packet that fell with a velocity of 10.2 km s^{-1} from this already low-lying prominence field (consistent with $v_{\mathrm{RTI}} =$ 10-15, 60, and 12 km s^{-1} as found by Berger et al., 2008; Hillier et al., 2012b; Keppens et al., 2015; Kaneko and Yokoyama, 2018, respectively). It is similarly

reasonable to speculate that should this signature have been related to the RTI, this detection would not be an isolated case but instead suggestive of the likelihood of detecting similar cases. However, to achieve this a more detailed study of the temporal evolution of all parameters measured or inverted within this chapter would be required.

6.5 Summary and Conclusion

The structure of a prominence observed on disk on 29 May 2017 has been studied using a variety of inversion techniques. The combination of the NLTE H-α model of Schwartz et al. (2019) and the HAZEL inversion study of Wang et al. (2020) enabled the first inversion measurements of plasma β along the spine of a prominence. The estimated values ranging between $0.02-0.23$ were in line with the previous studies of the RTI within prominences, suggesting the plasma parameters of material present within this prominence may have harboured signatures of motions along the LOS also consistent with the RTI.

Due to the involved nature of the NLTE H-α model of Schwartz et al. (2019), the BCM was shown to be a sufficient method of inverting the H-α spectral profiles so as to measure the evolution of the LOS velocity and line width across the entire FOV. A second absorption signature within the prominence resulted in the BCM being unable to invert a significant number of the spectral profiles within the prominence. Those positions that could be inverted using this method suggested that the spine of the prominence harboured plasma with small, near-rest velocities whereas the end of the absorption signature was host to plasma with significantly larger receding velocities of up to 10 km s^{-1}. These fast flows were also shown to have coincided with large line widths, in addition to an increase in the magnitude of the field strength within the prominence material, suggesting that these flows were along, and heated by, constricting field inclined towards lower altitudes (Wang et al., 2020). However, the inclination of the field in this region was measured to have been largely horizontal, an inconsistency interpreted to have been related to the spectral line's optically thin nature, and a second absorption signature present within the

H-α spectral lines. Consequently, the prominence is interpreted to have had at least two distinct layers, with the upper of the two having field aligned largely with the horizontal and the lower containing field more inclined towards the surface.

The Ca II observation of the chromosphere below the prominence was then inverted using the novel NLTE inversion technique of Beck et al. (2019) to study the structure therein. The spatial and geometrical coincidence between: increased field strength within the He I 10830 HAZEL inversion, a thermal Ca II structure present above $-\log(\tau_{5000}) = 5.5$ interpreted as magnetically induced, the presence of Ca II monolithic structures connecting this thermal structure to the bottom of the inversion volume, and the presence of photospheric polarity concentrations at the footpoints of these monolithic structures, is used to conclude that a portion of the prominence's host magnetic field was rooted within this region. The persistent structure present within the inversion volume with a shallow inclination from the prominence's body and towards the proposed footpoint was then interpreted as the response of the chromosphere to the pressure of the field hosting the prominence.

Finally, the monolithic structure that was present within the 14:44:55 UT snapshot and not coincident with a photospheric polarity was studied with interest in its relation to RTI-like phenomena. Studying the evolution of the temperature stratification and the H-α and Ca II LOS velocities in time revealed that this structure was indeed travelling towards the surface over time. Maintaining the structural assumptions outlined thus far, it is speculated that this 'plasmoid' may have been sourced from the underside of the prominence as with the RTI. However, if the prominence's magnetic field was as low-lying as suggested, the exact signature cannot be directly compared to the RTI previously observed.

In conclusion, this chapter has reported on the study of an on disk prominence observed on 29 May 2017 using instrumentation at the DST. The wealth of information available within the plethora of observations taken has enabled a comprehensive study of the prominence's small-scale properties to be undertaken. Based on the evidence, and interpretations therein, it has been possible to claim a tentative

detection of an RTI-like process having occurred underneath the prominence. However, this study would benefit greatly from the ability to more-consistently relate the low-altitude Ca II inversion to additional spectral lines found within prominences *e.g.*, Mg II h & k, H-α, and He I 10830. It is the hope of the author that such tools will be developed within the future that will allow the continued study of such magnificent and stunning structures within the solar atmosphere, the importance of which we are only just beginning to understand.

Chapter 7

Conclusions and Future Work

The solar prominence phenomena have been known to solar physicists for well over a century (Secchi, 1875). For the concluding decades of the last century their role in solar eruptions were studied in great detail. However, with the advent of comprehensive simulations and a shift in focus to the largest eruptions and their influence of the near-Earth environment, dedicated prominence studies have seemingly been left behind. Of course, prominences have received a significant amount of study within the last two decades, but after it was established that they played a negligible role within highly energetic eruptions it seems the wider solar physics community has implicitly assumed this to be true for eruptions at every scale.

The primary focus of this thesis was to address that assumption and discuss the role of mass within solar eruptions initiated under quieter-Sun conditions. This has been carried out using a combination of state-of-the-art observations, theory, models, and RTE inversions. The remainder of this thesis will highlight the advances in our understanding of solar prominences as a result of the research carried out in this thesis, before detailing the additional questions raised alongside those that remain to be understood.

7.1 General Conclusions

§— Mass-Induced Prominence Stability

Prominences are understood to be suspensions of chromospheric plasma maintained at coronal heights due to a delicate equilibrium between the magnetic and gravitational forces. At some point this equilibrium gets destabilised and the associated magnetic field and plasma are ejected out of the solar atmosphere and into the heliosphere, forming the CMEs that solar physicists aim to one day predict. On average, solar eruptions take on the order of three days to reach near-Earth space once ejected. By considering this delicate equilibrium in a simple but comprehensive model, the results presented in Chapter 5, in addition to the timescales derived by van Driel-Gesztelyi et al. (2003), showed that the eruption of a heavy quiescent prominence could be delayed by up to two days (see also the conclusions drawn from Fan (2018), wherein the authors adopted a similar but fully-MHD approach). Of course, there exist a variety of conditions (active, intermediate, quiescent) in which the role of mass within the prominence evolution and eruption can be considered important or not, and this was explored in the same chapter. But a key conclusion here is that by considering magnetic field and mass values measured within quiescent prominences, the error on the assumed eruption time can be off, in time, by as much as 66% of the time it takes for these structures to travel from the Sun to the Earth.

In conclusion, although these quiescent prominence eruptions may not be the most energetic and therefore may not create the *largest* geomagnetic disturbances, the inclusion of mass within the understanding of their equilibrium criteria is critical for accurate predictions.

§— Mass-Induced Prominence Destabilisation

The evolution of mass within quiescent prominences has previously been suggested to have the ability to perturb the delicate balance between the gravitational and magnetic forces of a prominence's host flux rope (*e.g.*, Bi et al., 2014). Chapter 4 of this

thesis provided additional observational evidence to this effect whilst expanding on the analysis to include a quantified estimate to this perturbation. This dimensionless ratio approach was developed further in Chapter 5 wherein it was shown that the removal of mass from the modelled flux rope caused it to increase in height by up to $\approx 40\%$ (much like the reversed effect noted in both Petrie et al. (2007) and Hillier and van Ballegooijen (2013)). Most crucially, this increase in height was shown to have the potential of leading the prominence's host flux rope into a torus unstable region and in turn triggering its eruption.

In conclusion, the evolution of mass within a prominence has been shown to be of critical importance when considering the stability of the global structure. Indeed, the end-state of a prominence with evolving total mass depends foremost on the strength of the surrounding magnetic field, after which serious consideration must then be given to when and how much mass is drained from the structure.

§— Large- and Small-Scale Structure

In the first two science chapters of this thesis (Chapters 4 & 5), it has been assumed that the flux rope – prominence system could be largely regarded as a single entity. Of course, structure and dynamics exist on much smaller scales than this global picture and Chapter 6 focused on how simultaneous observations in multiple spectral lines enables the study of such structures on both global and local scales. It was shown that the use of the multiple variations on the Beckers' Cloud Model (Schwartz et al., 2019; Asensio Ramos et al., 2008) enabled the mapping of plasma parameters (both magnetic and thermodynamic) along a large portion of a prominence, leading to the first measurement of the associated plasma β with minimal assumptions. Observations of the Ca II line were then inverted using the novel approach devised in Beck et al. (2019) and based on the stratified NICOLE code developed by Socas-Navarro et al. (2015). The reconstructions of the low chromospheric atmosphere enabled the connection between the structures inferred to have existed at a large range of altitudes, and facilitated the identification of the observed prominence's footpoint; such an achievement would not have been possible using the cloud models alone. Furthermore, this global picture of the prominence's foot-

point allowed the reconciliation of supposedly inconsistent results, the existence of multiple layers within the prominence, and the speculation of the small-scale RTI-like structure having been involved with extremely low-lying, chromosphere-penetrating prominence magnetic field.

In conclusion, solar physics is approaching a state wherein the wealth of information available in simultaneous, spectroscopic observations can be used to compare, contrast, and combine multiple layers of the solar atmosphere. Without such observations, in combination with the stratified inversions, the self-consistent connection between the upper and lower portions of the prominence presented in Chapter 6 would not have been possible.

7.2 Future Work

Prominences exist as structures that appear in both optically-thick and optically-thin spectral lines. Furthermore, they straddle the chromospheric region of the solar atmosphere wherein its thermodynamic and magnetic properties scale by up to five orders of magnitude with height. One cannot forget that they are also relatively cool structures suspended within the much hotter corona by a complex and ever-changing magnetic field topology. In conclusion, prominences are marvelous phenomena that enable solar physicists to explore and test many plasma physics and magneto-hydrodynamic theories, in addition to those of general radiative transfer and atomic physics. Consequently, the outstanding studies to be done are extensive and almost innumerable. Nevertheless, I would like to take a moment to outline a number of those that I find particularly interesting and which may benefit from the research that I have carried out in this thesis.

7.2.1 Measuring the Mass of Solar Prominences

The method of measuring the density and mass of solar prominences described in Chapter 4 (from Williams et al., 2013; Carlyle et al., 2014) uses the opacity of material along the LOS in comparison with a snapshot that is assumed to represent the unattenuated background. By definition, this assumes material along the LOS is responsible for the removal of intensity via photoionisation, and attributes

all deductions of the intensity, therein, to the existence of suitable material. Although this sounds like a cyclical argument, the key distinction lies in that there has to be material along the LOS capable of removing photons from the light beam through photoionisation. By extension, there may be material along the LOS that is not being sampled as it has already been ionised and cannot, therefore, absorb the incident photons that then pass through. In such a case, no marker of this material's existence is imprinted on any detector, incorrectly indicating an absence of material. This ratio of ionised hydrogen or helium to its non-ionised counterpart is heavily dependent on the temperature of the respective species. If the temperature changes then so would the ratio of ionisation, complicating the interpretation of any absorption signature measured within the multiple passbands of SDO/AIA. This is of particular importance for studies focused on observations that include erupting prominences, as was the case in Chapter 4. It would be interesting to use simulations of prominences to both benchmark the associated density measurement method, but also explore how the temperature of the included plasma affects these measurements.

7.2.2 The Global & Local Structure of Solar Prominences

Prominences are typically modelled or simulated as largely horizontal plasma structures embedded within the dips of a magnetic topology widely believed to resemble a magnetic flux rope. However, such models struggle somewhat at representing the nature of the plasma that resides within the lower-altitude portions of the magnetic topology, whether footpoints or barbs (although one such example by Xia and Keppens (2016) does show significant promise). In the case of Chapter 6, the interpretation as to the shape of the thermal structure remains speculative, albeit consistent with the structure inverted using the additional observations. Understanding the nature of these regions of a prominence will aid in both the understanding of the plasma within these regions *i.e.*, mass flows into and out of the prominence, and the topology of the magnetic field common to prominences and prominence-less flux ropes alike (Martínez González et al., 2015). As such, additional development of the NICOLE code (or equivalent) that forms the basis of the NLTE inversion ap-

proach used in Chapter 6 will advance the study of such low-altitude portions of a prominence. Specifically, the inclusion of inversion approaches for Mg II h&k, H-α, and He I 10830 are required.

7.2.3 The Global Stability of Solar Prominences

Chapters 4 & 5 present compelling evidence that the mass of solar prominences must be taken into account when studying the stability criteria of their host magnetic flux ropes. In particular, the formulation of the problem adopted in Chapter 5 reduces the problem to one comparable to the classic set-up between bar magnets and current wires that can be easily demonstrated in a classroom. Applying it to the solar environment was achieved by making the extension to flux evolution rather than explicitly that of the current within the wire, a property dependent on the surrounding magnetic environment. Reducing the complex magnetic field of the surrounding solar corona to the 2D representation used within this model is non-trivial and could be done in a variety of ways depending on the complexity of this surrounding field. Considering the importance of the background magnetic field concentration on the equilibrium, the possible modifications to the methods of handling this background field must be explored in more detail.

7.2.4 The Predictability of Solar Eruptions

A goal at the forefront of solar physics and the study of solar eruptions lies in the ability to predict their occurrence. Currently, the state-of-the-art models and tools used to do this on an operational basis track and measure only the evolution of the solar magnetic field at the solar surface (as explained in Murray et al., 2018). It was stated at the start of this thesis, and again many times throughout, that the wider solar physics community has thus far operated under the assumption that mass provides a negligible force in the triggering of solar eruptions. Naturally, this explains why such a metric is yet to exist as a part of the operational monitoring systems. However, as has been clearly indicated by both the simple model of Chapter 5 and the more involved model of Fan (2018), such a statement on the role of mass does not hold across all scales. Furthermore, although the MHD model of Fan (2018)

may be ideally suited to exploring the finer details of the force balance involved within prominences, the computational expense required to complete a simulation run is extreme. Instead, with the additional development outlined in Section 7.2.3, it would be interesting to see whether the model of Chapter 5 and Jenkins et al. (2019) could be included within the aforementioned operational forecasting. Specifically, the current forecasting tools (such as that by Pagano et al., 2019) provide a predicted time t of an eruption, the model of Jenkins et al. (2019) then provides a Δt value that *should* improve the accuracy of the original forecast. Presumably, such an extension would be trivial given the computational power required to carry out the Δt calculation in comparison with the initial t prediction. This is something that I expect I would be able to persue as a part of a collaboration and with the assistance of a summer student or equivalent.

References

Kwangsu Ahn, Jongchul Chae, Wenda Cao, and Philip R. Goode. Patterns of Flows in an Intermediate Prominence Observed by Hinode. *Astrophys. J.*, 721(1):74–79, Sep 2010. doi: 10.1088/0004-637X/721/1/74.

H. Alfvén. Existence of Electromagnetic-Hydrodynamic Waves. *Nature*, 150 (3805):405–406, Oct 1942. doi: 10.1038/150405d0.

C. E. Alissandrakis, G. Tsiropoula, and P. Mein. Physical parameters of solar H-alpha absorption features derived with the cloud model. *Astron. Astrophys.*, 230 (1):200–212, Apr 1990.

T. Amari, J. F. Luciani, J. J. Aly, Z. Mikic, and J. Linker. Coronal Mass Ejection: Initiation, Magnetic Helicity, and Flux Ropes. I. Boundary Motion-driven Evolution. *Astrophys. J.*, 585:1073–1086, March 2003. doi: 10.1086/345501.

Tahar Amari, Aurélien Canou, Jean-Jacques Aly, Francois Delyon, and Fréderic Alauzet. Magnetic cage and rope as the key for solar eruptions. *Nature*, 554 (7691):211–215, Feb 2018. doi: 10.1038/nature24671.

S. K. Antiochos and J. A. Klimchuk. A model for the formation of solar prominences. *Astrophys. J.*, 378:372–377, September 1991. doi: 10.1086/170437.

U. Anzer. Stability Analysis of the Kippenhahn-Schlüter Model of Solar Filaments. *Solar Phys.*, 8(1):37–52, Jul 1969. doi: 10.1007/BF00150656.

U. Anzer and P. Heinzel. Prominence Parameters Derived from Magnetic-Field Measurements and NLTE Diagnostics. *Solar Phys.*, 179(1):75–87, Jan 1998. doi: 10.1023/A:1005000616138.

Markus J. Aschwanden. *Physics of the Solar Corona. An Introduction with Problems and Solutions (2nd edition)*. Praxis Publishing Ltd., Chichester, UK; Springer, New York, Berlin, 2005., 2005.

A. Asensio Ramos, J. Trujillo Bueno, and E. Landi Degl'Innocenti. Advanced Forward Modeling and Inversion of Stokes Profiles Resulting from the Joint Action of the Hanle and Zeeman Effects. *Astrophys. J.*, 683:542–565, August 2008. doi: 10.1086/589433.

G. Aulanier and P. Démoulin. 3-D magnetic configurations supporting prominences. I. The natural presence of lateral feet. *Astron. Astrophys.*, 329:1125–1137, January 1998.

G. Aulanier, P. Démoulin, L. van Driel-Gesztelyi, P. Mein, and C. Deforest. 3-D magnetic configurations supporting prominences. II. The lateral feet as a perturbation of a twisted flux-tube. *Astron. Astrophys.*, 335:309–322, July 1998.

G. Aulanier, T. Török, P. Démoulin, and E. E. DeLuca. Formation of Torus-Unstable Flux Ropes and Electric Currents in Erupting Sigmoids. *Astrophys. J.*, 708:314–333, January 2010. doi: 10.1088/0004-637X/708/1/314.

Horace W. Babcock and Harold D. Babcock. The Sun's Magnetic Field, 1952-1954. *Astrophys. J.*, 121:349, Mar 1955. doi: 10.1086/145994.

G. Bateman. *MHD instabilities*. Cambridge, Mass., MIT Press, 1978. 270 p., 1978.

C. Beck and D. P. Choudhary. Magnetic Properties and Flow Angle of the Inverse Evershed Flow at Its Downflow Points. *Astrophys. J.*, 874(1):6, Mar 2019. doi: 10.3847/1538-4357/ab06f9.

C Beck, R Rezaei, and KG Puschmann. The energy of waves in the photosphere and lower chromosphere-ii. intensity statistics. *Astronomy & Astrophysics*, 544: A46, 2012.

C. Beck, R. Rezaei, and K. G. Puschmann. The energy of waves in the photosphere and lower chromosphere. III. Inversion setup for Ca II H spectra in local thermal

equilibrium. *Astron. Astrophys.*, 549:A24, Jan 2013a. doi: 10.1051/0004-6361/201220048.

C. Beck, R. Rezaei, and K. G. Puschmann. The energy of waves in the photosphere and lower chromosphere. IV. Inversion results of Ca II H spectra. *Astron. Astrophys.*, 553:A73, May 2013b. doi: 10.1051/0004-6361/201220463.

C. Beck, D. P. Choudhary, and R. Rezaei. A Three-dimensional View of the Thermal Structure in a Super-penumbral Canopy. *Astrophys. J.*, 788(2):183, Jun 2014. doi: 10.1088/0004-637X/788/2/183.

C. Beck, D. P. Choudhary, R. Rezaei, and R. E. Louis. Fast Inversion of Solar Ca II Spectra. *Astrophys. J.*, 798(2):100, Jan 2015. doi: 10.1088/0004-637X/798/2/100.

C. Beck, S. Gosain, and C. Kiessner. Fast Inversion of Solar Ca II Spectra in Non-local Thermodynamic Equilibrium. *Astrophys. J.*, 878(1):60, Jun 2019. doi: 10.3847/1538-4357/ab1d4c.

J. M. Beckers. *A Study of the Fine Structures in the Solar Chromosphere*. PhD thesis, Sacramento Peak Observatory, Air Force Cambridge Research Laboratories, Mass., USA, September 1964.

T. E. Berger, R. A. Shine, G. L. Slater, T. D. Tarbell, A. M. Title, T. J. Okamoto, K. Ichimoto, Y. Katsukawa, Y. Suematsu, S. Tsuneta, B. W. Lites, and T. Shimizu. Hinode SOT Observations of Solar Quiescent Prominence Dynamics. *Astrophys. J. Lett.*, 676:L89, March 2008. doi: 10.1086/587171.

Thomas Berger, Paola Testa, Andrew Hillier, Paul Boerner, Boon Chye Low, Kazunari Shibata, Carolus Schrijver, Ted Tarbell, and Alan Title. Magneto-thermal convection in solar prominences. *Nature*, 472(7342):197–200, Apr 2011. doi: 10.1038/nature09925.

Thomas Berger, Andrew Hillier, and Wei Liu. Quiescent Prominence Dynamics Observed with the Hinode Solar Optical Telescope. II. Prominence Bubble

Boundary Layer Characteristics and the Onset of a Coupled Kelvin-Helmholtz Rayleigh-Taylor Instability. *Astrophys. J.*, 850(1):60, November 2017. doi: 10.3847/1538-4357/aa95b6.

Thomas E. Berger, Gregory Slater, Neal Hurlburt, Richard Shine, Theodore Tarbell, Alan Title, Bruce W. Lites, Takenori J. Okamoto, Kiyoshi Ichimoto, and Yukio Katsukawa. Quiescent Prominence Dynamics Observed with the Hinode Solar Optical Telescope. I. Turbulent Upflow Plumes. *Astrophys. J.*, 716(2):1288–1307, Jun 2010. doi: 10.1088/0004-637X/716/2/1288.

Y. Bi, Y. Jiang, J. Yang, J. Hong, H. Li, D. Yang, and B. Yang. Solar Filament Material Oscillations and Drainage before Eruption. *Astrophys. J.*, 790:100, August 2014. doi: 10.1088/0004-637X/790/2/100.

J. W. S. Blokland and R. Keppens. Toward detailed prominence seismology. I. Computing accurate 2.5D magnetohydrodynamic equilibria. *Astron. Astrophys.*, 532:A93, August 2011. doi: 10.1051/0004-6361/201117013.

P. Boerner, C. Edwards, J. Lemen, A. Rausch, C. Schrijver, R. Shine, L. Shing, R. Stern, T. Tarbell, A. Title, C. J. Wolfson, R. Soufli, E. Spiller, E. Gullikson, D. McKenzie, D. Windt, L. Golub, W. Podgorski, P. Testa, and M. Weber. Initial Calibration of the Atmospheric Imaging Assembly (AIA) on the Solar Dynamics Observatory (SDO). *Solar Phys.*, 275:41–66, January 2012. doi: 10.1007/s11207-011-9804-8.

R. J. Bray. High-Resolution Photography of the Solar Chromosphere. X: Physical Parameters of Hα Mottles. *Solar Phys.*, 29(2):317–325, Apr 1973. doi: 10.1007/BF00150809.

D. S. Brown, R. W. Nightingale, D. Alexander, C. J. Schrijver, T. R. Metcalf, R. A. Shine, A. M. Title, and C. J. Wolfson. Observations of Rotating Sunspots from TRACE. *Solar Phys.*, 216(1):79–108, Sep 2003. doi: 10.1023/A:1026138413791.

T. N. Bungey, V. S. Titov, and E. R. Priest. Basic topological elements of coronal magnetic fields. *Astron. Astrophys.*, 308:233–247, Apr 1996.

J. Carlyle, D. R. Williams, L. van Driel-Gesztelyi, D. Innes, A. Hillier, and S. Matthews. Investigating the Dynamics and Density Evolution of Returning Plasma Blobs from the 2011 June 7 Eruption. *Astrophys. J.*, 782:87, February 2014. doi: 10.1088/0004-637X/782/2/87.

R. Casini, A. López Ariste, S. Tomczyk, and B. W. Lites. Magnetic Maps of Prominences from Full Stokes Analysis of the He I D3 Line. *Astrophys. J.*, 598(1): L67–L70, Nov 2003. doi: 10.1086/380496.

Fausto Cattaneo, Thierry Emonet, and Nigel Weiss. On the Interaction between Convection and Magnetic Fields. *Astrophys. J.*, 588(2):1183–1198, May 2003. doi: 10.1086/374313.

G. Cauzzi, K. P. Reardon, A. Vecchio, K. Janssen, and T. Rimmele. *Acoustic Shocks in the Quiet Solar Chromosphere*, volume 368 of *Astronomical Society of the Pacific Conference Series*, page 127. 2007.

F. Cavallini. IBIS: A New Post-Focus Instrument for Solar Imaging Spectroscopy. *Solar Phys.*, 236:415–439, July 2006. doi: 10.1007/s11207-006-0103-8.

Jongchul Chae. The Formation of a Prominence in NOAA Active Region 8668. II. Trace Observations of Jets and Eruptions Associated with Canceling Magnetic Features. *Astrophys. J.*, 584(2):1084–1094, Feb 2003. doi: 10.1086/345739.

Jongchul Chae, Young-Deuk Park, and Hyung-Min Park. Imaging Spectroscopy of a Solar Filament Using a Tunable Hα Filter. *Solar Phys.*, 234(1):115–134, Mar 2006. doi: 10.1007/s11207-006-0047-z.

P. F. Chen and K. Shibata. An Emerging Flux Trigger Mechanism for Coronal Mass Ejections. *Astrophys. J.*, 545:524–531, December 2000. doi: 10.1086/317803.

Xin Cheng, Yang Guo, and MingDe Ding. Origin and Structures of Solar Eruptions I: Magnetic Flux Rope. *Science in China Earth Sciences*, 60:1383–1407, August 2017. doi: 10.1007/s11430-017-9074-6.

M. C. M. Cheung and H. Isobe. Flux Emergence (Theory). *Living Reviews in Solar Physics*, 11:3, December 2014. doi: 10.12942/lrsp-2014-3.

C. Chiuderi and M. Velli. *Basics of Plasma Astrophysics*. 2015.

E. Clementi, D. L. Raimondi, and W. P. Reinhardt. Atomic Screening Constants from SCF Functions. II. Atoms with 37 to 86 Electrons. *J. Chem. Phys*, 47(4): 1300–1307, Aug 1967. doi: 10.1063/1.1712084.

Arthur N. Cox. *Allen's astrophysical quantities*. 2000.

L. E. Cram. Interpretation of Hα contrast profiles of chromospheric fine structures. *Solar Phys.*, 42(1):53–66, May 1975. doi: 10.1007/BF00153284.

Steven R. Cranmer. Coronal Holes. *Living Reviews in Solar Physics*, 6(1):3, Sep 2009. doi: 10.12942/lrsp-2009-3.

J. L. Culhane, L. K. Harra, A. M. James, K. Al-Janabi, L. J. Bradley, R. A. Chaudry, K. Rees, J. A. Tandy, P. Thomas, M. C. R. Whillock, B. Winter, G. A. Doschek, C. M. Korendyke, C. M. Brown, S. Myers, J. Mariska, J. Seely, J. Lang, B. J. Kent, B. M. Shaughnessy, P. R. Young, G. M. Simnett, C. M. Castelli, S. Mahmoud, H. Mapson-Menard, B. J. Probyn, R. J. Thomas, J. Davila, K. Dere, D. Windt, J. Shea, R. Hagood, R. Moye, H. Hara, T. Watanabe, K. Matsuzaki, T. Kosugi, V. Hansteen, and Ø. Wikstol. The EUV Imaging Spectrometer for Hinode. *Solar Phys.*, 243(1):19–61, Jun 2007. doi: 10.1007/s01007-007-0293-1.

S. Dacie, P. Démoulin, L. van Driel-Gesztelyi, D. M. Long, D. Baker, M. Janvier, S. L. Yardley, and D. Pérez-Suárez. Evolution of the magnetic field distribution of active regions. *Astron. Astrophys.*, 596:A69, Dec 2016. doi: 10.1051/0004-6361/201628948.

S. Dacie, T. Török, P. Démoulin, M. G. Linton, C. Downs, L. van Driel-Gesztelyi, D. M. Long, and J. E. Leake. Sequential Eruptions Triggered by Flux Emergence: Observations and Modeling. *Astrophys. J.*, 862(2):117, Aug 2018. doi: 10.3847/1538-4357/aacce3.

K. H. David. Die Mitte-Rand Variation der Balmerlinien Hα-Hδ auf der Sonnenscheibe. Mit 9 Textabbildungen. *Zeitschrift fuer Astrophysik*, 53:37, Jan 1961.

J. de la Cruz Rodríguez and M. van Noort. Radiative Diagnostics in the Solar Photosphere and Chromosphere. *Space Sci. Rev.*, 210(1-4):109–143, Sep 2017. doi: 10.1007/s11214-016-0294-8.

Ineke De Moortel and Philippa Browning. Recent advances in coronal heating. *Philosophical Transactions of the Royal Society of London Series A*, 373(2042): 20140269–20140269, Apr 2015. doi: 10.1098/rsta.2014.0269.

Bart de Pontieu, Scott McIntosh, Viggo H. Hansteen, Mats Carlsson, Carolus J. Schrijver, Theodore D. Tarbell, Alan M. Title, Richard A. Shine, Yoshinori Suematsu, Saku Tsuneta, Yukio Katsukawa, Kiyoshi Ichimoto, Toshifumi Shimizu, and Shin'ichi Nagata. A Tale of Two Spicules: The Impact of Spicules on the Magnetic Chromosphere. *Pub. Astron. Soc. Japan*, 59:S655, Nov 2007. doi: 10.1093/pasj/59.sp3.S655.

J.-P. Delaboudinière, G. E. Artzner, J. Brunaud, A. H. Gabriel, J. F. Hochedez, F. Millier, X. Y. Song, B. Au, K. P. Dere, R. A. Howard, R. Kreplin, D. J. Michels, J. D. Moses, J. M. Defise, C. Jamar, P. Rochus, J. P. Chauvineau, J. P. Marioge, R. C. Catura, J. R. Lemen, L. Shing, R. A. Stern, J. B. Gurman, W. M. Neupert, A. Maucherat, F. Clette, P. Cugnon, and E. L. van Dessel. EIT: Extreme-Ultraviolet Imaging Telescope for the SOHO Mission. *Solar Phys.*, 162:291–312, December 1995. doi: 10.1007/BF00733432.

P. Démoulin. Magnetic Fields in Filaments (Review). In D. F. Webb, B. Schmieder, and D. M. Rust, editors, *IAU Colloq. 167: New Perspectives on Solar Promi-*

nences, volume 150 of *Astronomical Society of the Pacific Conference Series*, page 78, 1998.

P. Démoulin and G. Aulanier. Criteria for Flux Rope Eruption: Non-equilibrium Versus Torus Instability. *Astrophys. J.*, 718:1388–1399, August 2010. doi: 10.1088/0004-637X/718/2/1388.

P. Démoulin and E. R. Priest. Instability of a prominence supported in a linear force-free field. *Astron. Astrophys.*, 206:336–347, November 1988.

P. Démoulin, J. Ferreira, and E. R. Priest. Instability of a prominence supported in a linear force-free field. II - Effect of twist or flux conservation. *Astron. Astrophys.*, 245:289–298, May 1991.

Yuanyong Deng, Yong Lin, Brigitte Schmieder, and Oddbjørn Engvold. Filament activation and magnetic reconnection. *Solar Phys.*, 209(1):153–170, Sep 2002. doi: 10.1023/A:1020924406991.

C. J. Díaz Baso, M. J. Martínez González, A. Asensio Ramos, and J. de la Cruz Rodríguez. Diagnostic potential of the Ca II 8542 Å line for solar filaments. *Astron. Astrophys.*, 623:A178, Mar 2019. doi: 10.1051/0004-6361/201834793.

A. Diercke, C. Kuckein, M. Verma, and C. Denker. Counter-streaming flows in a giant quiet-Sun filament observed in the extreme ultraviolet. *Astron. Astrophys.*, 611:A64, Mar 2018. doi: 10.1051/0004-6361/201730536.

V. Domingo, B. Fleck, and A. I. Poland. The SOHO Mission: an Overview. *Solar Phys.*, 162:1–37, December 1995. doi: 10.1007/BF00733425.

Tobin A Driscoll, Nicholas Hale, and Lloyd N Trefethen. Chebfun guide, 2014.

M. Druckmüller. Phase Correlation Method for the Alignment of Total Solar Eclipse Images. *Astrophys. J.*, 706(2):1605–1608, Dec 2009. doi: 10.1088/0004-637X/706/2/1605.

John A. Eddy and Rein Ise. *A new sun : the solar results from SKYLAB*. 1979.

A. G. Emslie, H. Kucharek, B. R. Dennis, N. Gopalswamy, G. D. Holman, G. H. Share, A. Vourlidas, T. G. Forbes, P. T. Gallagher, G. M. Mason, T. R. Metcalf, R. A. Mewaldt, R. J. Murphy, R. A. Schwartz, and T. H. Zurbuchen. Energy partition in two solar flare/CME events. *J. Geophys. Res.(Space Physics)*, 109 (A18):A10104, October 2004. doi: 10.1029/2004JA010571.

Oddbjørn Engvold, Tadashi Hirayama, Jean Louis Leroy, Eric R. Priest, and Einar Tandberg-Hanssen. *Hvar Reference Atmosphere of Quiescent Prominences*, volume 363, page 294. Springer-Verlag, New York, 1990. doi: 10.1007/BFb0025709.

Y. Fan. MHD Simulations of the Eruption of Coronal Flux Ropes under Coronal Streamers. *Astrophys. J.*, 844:26, July 2017. doi: 10.3847/1538-4357/aa7a56.

Y. Fan and S. E. Gibson. Onset of Coronal Mass Ejections Due to Loss of Confinement of Coronal Flux Ropes. *Astrophys. J.*, 668:1232–1245, October 2007. doi: 10.1086/521335.

Yuhong Fan. MHD Simulation of Prominence Eruption. *Astrophys. J.*, 862:54, July 2018. doi: 10.3847/1538-4357/aaccee.

Yuhong Fan and Tie Liu. MHD simulation of prominence-cavity system. *arXiv e-prints*, art. arXiv:1905.08226, May 2019.

J. Feynman and S. F. Martin. The initiation of coronal mass ejections by newly emerging magnetic flux. *J. Geophys. Res.*, 100:3355–3367, March 1995. doi: 10.1029/94JA02591.

R. A. S. Fiedler and A. W. Hood. Numerical models of quiescent normal polarity prominences. *Solar Phys.*, 141:75–90, September 1992. doi: 10.1007/BF00155905.

R. A. S. Fiedler and A. W. Hood. The effect of shear on numerical models of quiescent normal-polarity prominences. *Solar Phys.*, 146:297–311, August 1993. doi: 10.1007/BF00662015.

G. B. Field. Thermal Instability. *Astrophys. J.*, 142:531, August 1965. doi: 10.1086/148317.

B. Filippov. Two-step solar filament eruptions. *Mon. Not. Roy. Astron. Soc.*, 475:1646–1652, April 2018. doi: 10.1093/mnras/stx3277.

B. P. Filippov. Method for the determination of the height of a solar filament. *Geomagnetism and Aeronomy*, 56:1–7, January 2016. doi: 10.1134/S0016793216010059.

B. P. Filippov and O. G. Den. A critical height of quiescent prominences before eruption. *J. Geophys. Res.*, 106:25177–25184, November 2001. doi: 10.1029/2000JA004002.

J. M. Fontenla, E. H. Avrett, and R. Loeser. Energy Balance in the Solar Transition Region. III. Helium Emission in Hydrostatic, Constant-Abundance Models with Diffusion. *Astrophys. J.*, 406:319, Mar 1993. doi: 10.1086/172443.

T. G. Forbes. A review on the genesis of coronal mass ejections. *J. Geophys. Res.*, 105:23153–23166, October 2000. doi: 10.1029/2000JA000005.

T. G. Forbes and P. A. Isenberg. A Catastrophe Mechanism for Coronal Mass Ejections. *Astrophys. J.*, 373:294, May 1991. doi: 10.1086/170051.

B. C. Forland, S. E. Gibson, J. B. Dove, L. A. Rachmeler, and Y. Fan. Coronal Cavity Survey: Morphological Clues to Eruptive Magnetic Topologies. *Solar Phys.*, 288:603–615, December 2013. doi: 10.1007/s11207-013-0361-1.

S. L. Freeland and B. N. Handy. Data Analysis with the SolarSoft System. *Solar Phys.*, 182(2):497–500, Oct 1998. doi: 10.1023/A:1005038224881.

A. H. Gabriel and H. E. Mason. Solar physics. In H. S. W. Massey and D. R. Bates, editors, *Applied Atomic Collision Physics, Volume 1: Atmospheric Physics and Chemistry*, volume 1, pages 345–397, 1982.

G. Allen Gary. Plasma Beta above a Solar Active Region: Rethinking the Paradigm. *Solar Phys.*, 203(1):71–86, Oct 2001. doi: 10.1023/A:1012722021820.

S. E. Gibson and Y. Fan. Coronal prominence structure and dynamics: A magnetic flux rope interpretation. *J. Geophys. Res.(Space Physics)*, 111(A10):A12103, December 2006. doi: 10.1029/2006JA011871.

S. E. Gibson, D. Foster, J. Burkepile, G. de Toma, and A. Stanger. The Calm before the Storm: The Link between Quiescent Cavities and Coronal Mass Ejections. *Astrophys. J.*, 641:590–605, April 2006. doi: 10.1086/500446.

Sarah E. Gibson. Solar prominences: theory and models. Fleshing out the magnetic skeleton. *Living Reviews in Solar Physics*, 15(1):7, Oct 2018. doi: 10.1007/s41116-018-0016-2.

H. R. Gilbert, T. E. Holzer, and J. T. Burkepile. Observational Interpretation of an Active Prominence on 1999 May 1. *Astrophys. J.*, 549:1221–1230, March 2001. doi: 10.1086/319444.

H. R. Gilbert, T. E. Holzer, and R. M. MacQueen. A New Technique for Deriving Prominence Mass from SOHO/EIT Fe XII (19.5 Nanometers) Absorption Features. *Astrophys. J.*, 618:524–536, January 2005. doi: 10.1086/425975.

H. R. Gilbert, L. E. Falco, T. E. Holzer, and R. M. MacQueen. Application of a New Technique for Deriving Prominence Mass from SOHO EIT Fe XII (19.5 nm) Absorption Features. *Astrophys. J.*, 641:606–610, April 2006. doi: 10.1086/500354.

O. Gingerich and C. de Jager. The Bilderberg Model of the Photosphere and Low Chromosphere. *Solar Phys.*, 3(1):5–25, Jan 1968. doi: 10.1007/BF00154238.

O. Gingerich, R. W. Noyes, W. Kalkofen, and Y. Cuny. The Harvard-Smithsonian reference atmosphere. *Solar Phys.*, 18(3):347–365, Jul 1971. doi: 10.1007/BF00149057.

Philip R Goode and Wenda Cao. The 1.6 m off-axis new solar telescope (nst) in big bear. In *Ground-based and Airborne Telescopes IV*, volume 8444, page 844403. International Society for Optics and Photonics, 2012.

Samuel D. T. Grant, David B. Jess, Teimuraz V. Zaqarashvili, Christian Beck, Hector Socas-Navarro, Markus J. Aschwanden, Peter H. Keys, Damian J. Christian, Scott J. Houston, and Rebecca L. Hewitt. Alfvén wave dissipation in the solar chromosphere. *Nature Physics*, 14(5):480–483, Mar 2018. doi: 10.1038/s41567-018-0058-3.

L. M. Green, B. Kliem, T. Török, L. van Driel-Gesztelyi, and G. D. R. Attrill. Transient Coronal Sigmoids and Rotating Erupting Flux Ropes. *Solar Phys.*, 246:365–391, December 2007. doi: 10.1007/s11207-007-9061-z.

Lucie M. Green, Tibor Török, Bojan Vršnak, Ward Manchester, and Astrid Veronig. The Origin, Early Evolution and Predictability of Solar Eruptions. *Space Sci. Rev.*, 214(1):46, Feb 2018. doi: 10.1007/s11214-017-0462-5.

N. Grevesse, M. Asplund, and A. J. Sauval. The Solar Chemical Composition. *Space Sci. Rev.*, 130:105–114, June 2007. doi: 10.1007/s11214-007-9173-7.

Ulrich Grossmann-Doerth and Marina von Uexküll. Spectral Investigation of Chromospheric Fine Structure. *Solar Phys.*, 20(1):31–46, Oct 1971. doi: 10.1007/BF00146092.

W. Grotrian. Zur Frage der Deutung der Linien im Spektrum der Sonnenkorona. *Naturwissenschaften*, 27(13):214–214, Mar 1939. doi: 10.1007/BF01488890.

S. Gunár and D. H. Mackay. 3D Whole-Prominence Fine Structure Modeling. *Astrophys. J.*, 803:64, April 2015. doi: 10.1088/0004-637X/803/2/64.

S. Gunár, P. Heinzel, B. Schmieder, P. Schwartz, and U. Anzer. Properties of prominence fine-structure threads derived from SOHO/SUMER hydrogen Lyman lines. *Astron. Astrophys.*, 472(3):929–936, Sep 2007. doi: 10.1051/0004-6361:20077785.

S. Gunár, P. Heinzel, U. Anzer, and B. Schmieder. On Lyman-line asymmetries in quiescent prominences. *Astron. Astrophys.*, 490(1):307–313, Oct 2008. doi: 10.1051/0004-6361:200810127.

S. Gunár, D. H. Mackay, U. Anzer, and P. Heinzel. Non-linear force-free magnetic dip models of quiescent prominence fine structures. *Astron. Astrophys.*, 551:A3, March 2013. doi: 10.1051/0004-6361/201220597.

S. Gunár, P. Schwartz, J. Dudík, B. Schmieder, P. Heinzel, and J. Jurčák. Magnetic field and radiative transfer modelling of a quiescent prominence. *Astron. Astrophys.*, 567:A123, Jul 2014. doi: 10.1051/0004-6361/201322777.

Stanislav Gunár, Jaroslav Dudík, Guillaume Aulanier, Brigitte Schmieder, and Petr Heinzel. Importance of the Hα Visibility and Projection Effects for the Interpretation of Prominence Fine-structure Observations. *Astrophys. J.*, 867(2):115, Nov 2018. doi: 10.3847/1538-4357/aae4e1.

Y. Guo, E. Pariat, G. Valori, S. Anfinogentov, F. Chen, M. K. Georgoulis, Y. Liu, K. Moraitis, J. K. Thalmann, and S. Yang. Magnetic Helicity Estimations in Models and Observations of the Solar Magnetic Field. III. Twist Number Method. *Astrophys. J.*, 840:40, May 2017. doi: 10.3847/1538-4357/aa6aa8.

George E. Hale, Ferdinand Ellerman, S. B. Nicholson, and A. H. Joy. The Magnetic Polarity of Sun-Spots. *Astrophys. J.*, 49:153, Apr 1919. doi: 10.1086/142452.

V. H. Hansteen, B. De Pontieu, L. Rouppe van der Voort, M. van Noort, and M. Carlsson. Dynamic Fibrils Are Driven by Magnetoacoustic Shocks. *Astrophys. J.*, 647(1):L73–L76, Aug 2006. doi: 10.1086/507452.

J. W. Harvey, J. Bolding, R. Clark, D. Hauth, F. Hill, R. Kroll, G. Luis, N. Mills, T. Purdy, C. Henney, D. Holland, and J. Winter. Full-disk Solar H-alpha Images From GONG. In *AAS/Solar Physics Division Abstracts #42*, AAS/Solar Physics Division Meeting, page 17.45, May 2011.

P. Heinzel. The Fine Structure of Solar Prominences. In P. Heinzel, I. Dorotovič, and R. J. Rutten, editors, *The Physics of Chromospheric Plasmas*, volume 368 of *Astronomical Society of the Pacific Conference Series*, page 271, May 2007.

P. Heinzel and U. Anzer. Magnetic Dips in Prominences. *Solar Phys.*, 184(1): 103–111, Jan 1999. doi: 10.1023/A:1005098704665.

P. Heinzel and U. Anzer. Prominence fine structures in a magnetic equilibrium: Two-dimensional models with multilevel radiative transfer. *Astron. Astrophys.*, 375:1082–1090, Sep 2001. doi: 10.1051/0004-6361:20010926.

P. Heinzel, N. Mein, and P. Mein. Cloud model with variable source function for solar Hα structures. II. Dynamical models. *Astron. Astrophys.*, 346:322–328, Jun 1999.

P. Heinzel, U. Anzer, and S. Gunár. Prominence fine structures in a magnetic equilibrium. II. A grid of two-dimensional models. *Astron. Astrophys.*, 442(1):331–343, Oct 2005. doi: 10.1051/0004-6361:20053360.

P. Heinzel, B. Schmieder, F. Fárník, P. Schwartz, N. Labrosse, P. Kotrč, U. Anzer, G. Molodij, A. Berlicki, E. E. DeLuca, L. Golub, T. Watanabe, and T. Berger. Hinode, TRACE, SOHO, and Ground-based Observations of a Quiescent Prominence. *Astrophys. J.*, 686:1383-1396, October 2008. doi: 10.1086/591018.

P. Heinzel, S. Gunár, and U. Anzer. Fast approximate radiative transfer method for visualizing the fine structure of prominences in the hydrogen Hα line. *Astron. Astrophys.*, 579:A16, Jul 2015. doi: 10.1051/0004-6361/201525716.

A. Hillier and A. van Ballegooijen. On the Support of Solar Prominence Material by the Dips of a Coronal Flux Tube. *Astrophys. J.*, 766:126, April 2013. doi: 10.1088/0004-637X/766/2/126.

Andrew Hillier. The magnetic Rayleigh-Taylor instability in solar prominences. *Reviews of Modern Plasma Physics*, 2(1):1, Dec 2018. doi: 10.1007/s41614-017-0013-2.

Andrew Hillier, Richard Hillier, and Durgesh Tripathi. Determination of Prominence Plasma β from the Dynamics of Rising Plumes. *Astrophys. J.*, 761(2):106, Dec 2012a. doi: 10.1088/0004-637X/761/2/106.

Andrew Hillier, Hiroaki Isobe, Kazunari Shibata, and Thomas Berger. Numerical Simulations of the Magnetic Rayleigh-Taylor Instability in the Kippenhahn-Schlüter Prominence Model. II. Reconnection-triggered Downflows. *Astrophys. J.*, 756(2):110, Sep 2012b. doi: 10.1088/0004-637X/756/2/110.

T. Hirayama. On the Model of the Solar Quiescent Prominence and the Effect of the Solar UV Radiation on the Prominence. *Pub. Astron. Soc. Japan*, 15:122, Jan 1963.

J. T. Hoeksema, Y. Liu, K. Hayashi, X. Sun, J. Schou, S. Couvidat, A. Norton, M. Bobra, R. Centeno, K. D. Leka, G. Barnes, and M. Turmon. The Helioseismic and Magnetic Imager (HMI) Vector Magnetic Field Pipeline: Overview and Performance. *Solar Phys.*, 289:3483–3530, September 2014. doi: 10.1007/s11207-014-0516-8.

R. A. Howard, J. D. Moses, A. Vourlidas, J. S. Newmark, D. G. Socker, S. P. Plunkett, C. M. Korendyke, J. W. Cook, A. Hurley, J. M. Davila, W. T. Thompson, O. C. St Cyr, E. Mentzell, K. Mehalick, J. R. Lemen, J. P. Wuelser, D. W. Duncan, T. D. Tarbell, C. J. Wolfson, A. Moore, R. A. Harrison, N. R. Waltham, J. Lang, C. J. Davis, C. J. Eyles, H. Mapson-Menard, G. M. Simnett, J. P. Halain, J. M. Defise, E. Mazy, P. Rochus, R. Mercier, M. F. Ravet, F. Delmotte, F. Auchere, J. P. Delaboudiniere, V. Bothmer, W. Deutsch, D. Wang, N. Rich, S. Cooper, V. Stephens, G. Maahs, R. Baugh, D. McMullin, and T. Carter. Sun Earth Connection Coronal and Heliospheric Investigation (SECCHI). *Space Sci. Rev.*, 136:67–115, April 2008. doi: 10.1007/s11214-008-9341-4.

Rachel Howe. Solar Interior Rotation and its Variation. *Living Reviews in Solar Physics*, 6(1):1, Feb 2009. doi: 10.12942/lrsp-2009-1.

Charles L. Hyder. A Phenomenological Model for Disparitions Brusques followed by Flarelike Chromospheric Brightenings, I: The Model, its Consequences, and Observations in Quiet Solar Regions. *Solar Physics*, 2(1):49–74, Jul 1967. doi: 10.1007/BF00155892.

Sarah A. Jaeggli. *An observational study of the formation and evolution of sunspots*. PhD thesis, University of Hawai'i at Manoa, January 2011.

A. W. James, L. M. Green, E. Palmerio, G. Valori, H. A. S. Reid, D. Baker, D. H. Brooks, L. van Driel-Gesztelyi, and E. K. J. Kilpua. On-Disc Observations of Flux Rope Formation Prior to Its Eruption. *Solar Phys.*, 292:71, May 2017. doi: 10.1007/s11207-017-1093-4.

J. M. Jenkins, D. M. Long, L. van Driel-Gesztelyi, and J. Carlyle. Understanding the Role of Mass-Unloading in a Filament Eruption. *Solar Phys.*, 293:7, January 2018. doi: 10.1007/s11207-017-1224-y.

Jack M. Jenkins, Matthew Hopwood, Pascal Démoulin, Gherardo Valori, Guillaume Aulanier, David M. Long, and Lidia van Driel-Gesztelyi. Modeling the Effect of Mass-draining on Prominence Eruptions. *Astrophys. J.*, 873(1):49, March 2019. doi: 10.3847/1538-4357/ab037a.

D. B. Jess, M. Mathioudakis, D. J. Christian, F. P. Keenan, R. S. I. Ryans, and P. J. Crockett. ROSA: A High-cadence, Synchronized Multi-camera Solar Imaging System. *Solar Phys.*, 261(2):363–373, Feb 2010. doi: 10.1007/s11207-009-9500-0.

C. Jiang, S. T. Wu, X. Feng, and Q. Hu. Nonlinear Force-free Field Extrapolation of a Coronal Magnetic Flux Rope Supporting a Large-scale Solar Filament from a Photospheric Vector Magnetogram. *Astrophys. J. Lett.*, 786:L16, May 2014. doi: 10.1088/2041-8205/786/2/L16.

Ju Jing, Jeongwoo Lee, Thomas J. Spirock, Yan Xu, Haimin Wang, and G. S. Choe. Periodic Motion along a Solar Filament Initiated by a Subflare. *Astrophys. J.*, 584(2):L103–L106, Feb 2003. doi: 10.1086/373886.

M. L. Kaiser, T. A. Kucera, J. M. Davila, O. C. St. Cyr, M. Guhathakurta, and E. Christian. The STEREO Mission: An Introduction. *Space Sci. Rev.*, 136: 5–16, April 2008. doi: 10.1007/s11214-007-9277-0.

Takafumi Kaneko and Takaaki Yokoyama. Impact of Dynamic State on the Mass Condensation Rate of Solar Prominences. *Astrophys. J.*, 869:136, December 2018. doi: 10.3847/1538-4357/aaee6f.

R. Keppens, C. Xia, and O. Porth. Solar Prominences: "Double, Double... Boil and Bubble". *Astrophys. J. Lett.*, 806(1):L13, Jun 2015. doi: 10.1088/2041-8205/806/1/L13.

I. W. Kienreich, M. Temmer, and A. M. Veronig. STEREO Quadrature Observations of the Three-Dimensional Structure and Driver of a Global Coronal Wave. *Astrophys. J. Lett.*, 703:L118–L122, October 2009. doi: 10.1088/0004-637X/703/2/L118.

R. Kippenhahn and A. Schlüter. Eine Theorie der solaren Filamente. Mit 7 Textabbildungen. *Zeitschrift fuer Astrophysik*, 43:36, 1957.

B. Kliem and T. Török. Torus Instability. *Physical Review Letters*, 96(25):255002, June 2006. doi: 10.1103/PhysRevLett.96.255002.

B. Kliem, J. Lin, T. G. Forbes, E. R. Priest, and T. Török. Catastrophe versus Instability for the Eruption of a Toroidal Solar Magnetic Flux Rope. *Astrophys. J.*, 789(1):46, Jul 2014. doi: 10.1088/0004-637X/789/1/46.

J. A. Klimchuk. Theory of Coronal Mass Ejections. *Washington DC American Geophysical Union Geophysical Monograph Series*, 125:143, January 2001. doi: 10.1029/GM125p0143.

J. A. Klimchuk, S. K. Antiochos, and J. T. Mariska. A numerical study of the nonlinear thermal stability of solar loops. *Astrophys. J.*, 320:409–417, September 1987. doi: 10.1086/165554.

James A. Klimchuk. On Solving the Coronal Heating Problem. *Solar Phys.*, 234 (1):41–77, Mar 2006. doi: 10.1007/s11207-006-0055-z.

James A. Klimchuk. The Distinction Between Thermal Nonequilibrium and Thermal Instability. *arXiv e-prints*, art. arXiv:1911.11849, Nov 2019.

E. P. Kontar, I. G. Hannah, and A. L. MacKinnon. Chromospheric magnetic field and density structure measurements using hard X-rays in a flaring coronal loop. *Astron. Astrophys.*, 489(3):L57–L60, October 2008. doi: 10.1051/0004-6361:200810719.

C. Kuckein, M. Verma, and C. Denker. Giant quiescent solar filament observed with high-resolution spectroscopy. *Astron. Astrophys.*, 589:A84, May 2016. doi: 10.1051/0004-6361/201526636.

M. Kuperus and M. A. Raadu. The Support of Prominences Formed in Neutral Sheets. *Astron. Astrophys.*, 31:189, March 1974.

Robert L. Kurucz, Ingemar Furenlid, James Brault, and Larry Testerman. *Solar flux atlas from 296 to 1300 nm*. 1984.

K. Kusano, Y. Bamba, T. T. Yamamoto, Y. Iida, S. Toriumi, and A. Asai. Magnetic Field Structures Triggering Solar Flares and Coronal Mass Ejections. *Astrophys. J.*, 760(1):31, Nov 2012. doi: 10.1088/0004-637X/760/1/31.

N. Labrosse, P. Heinzel, J. C. Vial, T. Kucera, S. Parenti, S. Gunár, B. Schmieder, and G. Kilper. Physics of Solar Prominences: I—Spectral Diagnostics and Non-LTE Modelling. *Space Sci. Rev.*, 151:243–332, April 2010. doi: 10.1007/s11214-010-9630-6.

E. Landi and F. Reale. Prominence Plasma Diagnostics through Extreme-ultraviolet Absorption. *Astrophys. J.*, 772:71, July 2013. doi: 10.1088/0004-637X/772/1/71.

James E. Leake, Mark G. Linton, and Tibor Török. Simulations of Emerging Magnetic Flux. I. The Formation of Stable Coronal Flux Ropes. *Astrophys. J.*, 778 (2):99, Dec 2013. doi: 10.1088/0004-637X/778/2/99.

J. Leenaarts, M. Carlsson, and L. Rouppe van der Voort. The Formation of the Hα Line in the Solar Chromosphere. *Astrophys. J.*, 749(2):136, Apr 2012. doi: 10.1088/0004-637X/749/2/136.

K. D. Leka, R. C. Canfield, A. N. McClymont, and L. van Driel-Gesztelyi. Evidence for Current-carrying Emerging Flux. *Astrophys. J.*, 462:547, May 1996. doi: 10.1086/177171.

J. R. Lemen, A. M. Title, D. J. Akin, P. F. Boerner, C. Chou, and J. F. Drake. The Atmospheric Imaging Assembly (AIA) on the Solar Dynamics Observatory (SDO). *Solar Phys.*, 275:17–40, January 2012. doi: 10.1007/s11207-011-9776-8.

JL Leroy and ER Priest. Dynamics and structure of quiescent solar prominences. *Kluwer Acad. Pub*, page 77, 1989.

P. J. Levens, N. Labrosse, L. Fletcher, and B. Schmieder. A solar tornado observed by EIS. Plasma diagnostics. *Astron. Astrophys.*, 582:A27, October 2015. doi: 10.1051/0004-6361/201425586.

P. J. Levens, B. Schmieder, N. Labrosse, and A. López Ariste. Structure of Prominence Legs: Plasma and Magnetic Field. *Astrophys. J.*, 818(1):31, Feb 2016a. doi: 10.3847/0004-637X/818/1/31.

P. J. Levens, B. Schmieder, A. López Ariste, N. Labrosse, K. Dalmasse, and B. Gelly. Magnetic Field in Atypical Prominence Structures: Bubble, Tornado, and Eruption. *Astrophys. J.*, 826(2):164, Aug 2016b. doi: 10.3847/0004-637X/826/2/164.

P. J. Levens, N. Labrosse, B. Schmieder, A. López Ariste, and L. Fletcher. Comparing UV/EUV line parameters and magnetic field in a quiescent prominence with

tornadoes. *Astron. Astrophys.*, 607:A16, Oct 2017. doi: 10.1051/0004-6361/201730808.

J. Lin, A. A. van Ballegooijen, and T. G. Forbes. Evolution of a semicircular flux rope with two ends anchored in the photosphere. *J. Geophys. Res.(Space Physics)*, 107:1438, December 2002. doi: 10.1029/2002JA009486.

Y. Lin, O. R. Engvold, and J. E. Wiik. Counterstreaming in a Large Polar Crown Filament. *Solar Phys.*, 216:109–120, September 2003. doi: 10.1023/A:1026150809598.

Y. Lin, O. Engvold, L. Rouppe van der Voort, J. E. Wiik, and T. E. Berger. Thin Threads of Solar Filaments. *Solar Phys.*, 226:239–254, February 2005. doi: 10.1007/s11207-005-6876-3.

Y. Lin, O. Engvold, L. H. M. Rouppe van der Voort, and M. van Noort. Evidence of Traveling Waves in Filament Threads. *Solar Phys.*, 246:65–72, November 2007. doi: 10.1007/s11207-007-0402-8.

Yuri E. Litvinenko and Sara F. Martin. Magnetic reconnection as the cause of a photospheric canceling feature and mass flows in a filament. *Solar Phys.*, 190:45–58, Dec 1999. doi: 10.1023/A:1005284116353.

Yuri E. Litvinenko and M. S. Wheatland. A Simple Dynamical Model for Filament Formation in the Solar Corona. *Astrophys. J.*, 630(1):587–595, Sep 2005. doi: 10.1086/432116.

Wei Liu, Thomas E. Berger, and B. C. Low. First SDO/AIA Observation of Solar Prominence Formation Following an Eruption: Magnetic Dips and Sustained Condensation and Drainage. *Astrophys. J. Lett.*, 745(2):L21, Feb 2012. doi: 10.1088/2041-8205/745/2/L21.

I. P. Loboda and S. A. Bogachev. Quiescent and Eruptive Prominences at Solar Minimum: A Statistical Study via an Automated Tracking System. *Solar Phys.*, 290:1963–1980, July 2015. doi: 10.1007/s11207-015-0735-7.

David M. Long. Kinematic Properties of Globally-Propagating Waves in the Solar Corona. *arXiv e-prints*, art. arXiv:1202.4360, Feb 2012.

A. López Ariste and R. Casini. Magnetic Fields in Prominences: Inversion Techniques for Spectropolarimetric Data of the He I D_3 Line. *Astrophys. J.*, 575(1): 529–541, Aug 2002. doi: 10.1086/341260.

R. E. Loughhead. High-Resolution Photography of the Solar Chromosphere. XI: H&alpha Constrast Profiles of Mottles near the Limb. *Solar Phys.*, 29(2): 327–332, Apr 1973. doi: 10.1007/BF00150810.

B. C. Low. The field and plasma configuration of a filament overlying a solar bipolar magnetic region. *Astrophys. J.*, 246:538–548, June 1981. doi: 10.1086/158954.

B. C. Low. Solar Activity and the Corona. *Solar Phys.*, 167:217–265, August 1996. doi: 10.1007/BF00146338.

B. C. Low, B. Fong, and Y. Fan. The Mass of a Solar Quiescent Prominence. *Astrophys. J.*, 594:1060–1067, September 2003. doi: 10.1086/377042.

M. Luna and J. Karpen. Large-amplitude Longitudinal Oscillations in a Solar Filament. *Astrophys. J.*, 750(1):L1, May 2012. doi: 10.1088/2041-8205/750/1/L1.

D. H. Mackay, V. Gaizauskas, and A. R. Yeates. Where Do Solar Filaments Form?: Consequences for Theoretical Models. *Solar Phys.*, 248:51–65, March 2008. doi: 10.1007/s11207-008-9127-6.

D. H. Mackay, J. T. Karpen, J. L. Ballester, B. Schmieder, and G. Aulanier. Physics of Solar Prominences: II—Magnetic Structure and Dynamics. *Space Sci. Rev.*, 151:333–399, April 2010. doi: 10.1007/s11214-010-9628-0.

David MacTaggart, Salvo L. Guglielmino, and Francesca Zuccarello. The Prepenumbral Magnetic Canopy in the Solar Atmosphere. *Astrophys. J. Lett.*, 831 (1):L4, Nov 2016. doi: 10.3847/2041-8205/831/1/L4.

T. Magara. Dynamics of Emerging Flux Tubes in the Sun. *Astrophys. J.*, 549(1): 608–628, Mar 2001. doi: 10.1086/319073.

J. M. Malherbe. The formation of solar prominences. In Eric Ronald Priest, editor, *Dynamics and Structure of Quiescent Solar Prominences*, volume 150 of *Astrophysics and Space Science Library*, pages 115–141, Jan 1989. doi: 10.1007/978-94-009-3077-3_16.

P. C. H. Martens and N. P. M. Kuin. A Circuit Model for Filament Eruptions and Two-Ribbon Flares. *Solar Phys.*, 122:263–302, September 1989. doi: 10.1007/BF00912996.

M. J. Martínez González, R. Manso Sainz, A. Asensio Ramos, C. Beck, J. de la Cruz Rodríguez, and A. J. Díaz. Spectro-Polarimetric Imaging Reveals Helical Magnetic Fields in Solar Prominence Feet. *Astrophys. J.*, 802(1):3, Mar 2015. doi: 10.1088/0004-637X/802/1/3.

P. I. McCauley, Y. N. Su, N. Schanche, K. E. Evans, C. Su, S. McKillop, and K. K. Reeves. Prominence and Filament Eruptions Observed by the Solar Dynamics Observatory: Statistical Properties, Kinematics, and Online Catalog. *Solar Phys.*, 290:1703–1740, June 2015. doi: 10.1007/s11207-015-0699-7.

Z. X. Mei, R. Keppens, I. I. Roussev, and J. Lin. Magnetic reconnection during eruptive magnetic flux ropes. *Astron. Astrophys.*, 604:L7, August 2017. doi: 10.1051/0004-6361/201731146.

N. Mein, P. Mein, P. Heinzel, J. C. Vial, J. M. Malherbe, and J. Staiger. Cloud model with variable source function for solar Hα structures. *Astron. Astrophys.*, 309:275–283, May 1996.

R. Molowny-Horas, P. Heinzel, P. Mein, and N. Mein. A non-LTE inversion procedure for chromospheric cloud-like features. *Astron. Astrophys.*, 345:618–628, May 1999.

R. L. Moore, A. C. Sterling, H. S. Hudson, and J. R. Lemen. Onset of the Magnetic Explosion in Solar Flares and Coronal Mass Ejections. *Astrophys. J.*, 552:833–848, May 2001. doi: 10.1086/320559.

F. Moreno-Insertis, J. Martinez-Sykora, V. H. Hansteen, and D. Muñoz. Small-scale Magnetic Flux Emergence in the Quiet Sun. *Astrophys. J. Lett.*, 859(2):L26, Jun 2018. doi: 10.3847/2041-8213/aac648.

H. Morgan and M. Druckmüller. Multi-Scale Gaussian Normalization for Solar Image Processing. *Solar Phys.*, 289:2945–2955, August 2014. doi: 10.1007/s11207-014-0523-9.

Sophie A. Murray, Jordan A. Guerra, Pietro Zucca, Sung-Hong Park, Eoin P. Carley, Peter T. Gallagher, Nicole Vilmer, and Volker Bothmer. Connecting Coronal Mass Ejections to Their Solar Active Region Sources: Combining Results from the HELCATS and FLARECAST Projects. *Solar Phys.*, 293(4):60, Apr 2018. doi: 10.1007/s11207-018-1287-4.

Clayton E. Myers, Masaaki Yamada, Hantao Ji, Jongsoo Yoo, William Fox, Jonathan Jara-Almonte, Antonia Savcheva, and Edward E. Deluca. A dynamic magnetic tension force as the cause of failed solar eruptions. *Nature*, 528(7583):526–529, Dec 2015. doi: 10.1038/nature16188.

Takenori J. Okamoto, Wei Liu, and Saku Tsuneta. Helical Motions of Fine-structure Prominence Threads Observed by Hinode and IRIS. *Astrophys. J.*, 831(2):126, Nov 2016. doi: 10.3847/0004-637X/831/2/126.

G. Olivieri. Disparition Brusque d'un Grand Filament Solaire. *L'Astronomie*, 62:343–343, Jan 1948.

E. S. Oran, J. T. Mariska, and J. P. Boris. The condensational instability in the solar transition region and corona. *Astrophys. J.*, 254:349–360, March 1982. doi: 10.1086/159739.

Paolo Pagano, Duncan H. Mackay, and Stephanie L. Yardley. A New Space Weather Tool for Identifying Eruptive Active Regions. *Astrophys. J.*, 886(2):81, December 2019. doi: 10.3847/1538-4357/ab4cf1.

Olga Panasenco, Sara F. Martin, and Marco Velli. Apparent Solar Tornado-Like Prominences. *Solar Phys.*, 289(2):603–622, Feb 2014. doi: 10.1007/s11207-013-0337-1.

S. Parenti. Solar Prominences: Observations. *Living Reviews in Solar Physics*, 11: 1, December 2014. doi: 10.12942/lrsp-2014-1.

E. Pariat, G. Aulanier, B. Schmieder, M. K. Georgoulis, D. M. Rust, and P. N. Bernasconi. Resistive Emergence of Undulatory Flux Tubes. *Astrophys. J.*, 614 (2):1099–1112, Oct 2004. doi: 10.1086/423891.

E. N. Parker. The Dynamical State of the Interstellar Gas and Field. *Astrophys. J.*, 145:811, Sep 1966. doi: 10.1086/148828.

Tiago M. D. Pereira, Bart De Pontieu, and Mats Carlsson. Quantifying Spicules. *Astrophys. J.*, 759(1):18, Nov 2012. doi: 10.1088/0004-637X/759/1/18.

W. D. Pesnell, B. J. Thompson, and P. C. Chamberlin. The Solar Dynamics Observatory (SDO). *Solar Phys.*, 275:3–15, January 2012. doi: 10.1007/s11207-011-9841-3.

G. J. D. Petrie, J. W. S. Blokland, and R. Keppens. Magnetohydrostatic Solar Prominences in Near-Potential Coronal Magnetic Fields. *Astrophys. J.*, 665:830–845, August 2007. doi: 10.1086/519276.

Edison Pettit. The Properties of Solar, Prominences as Related to Type. *Astrophys. J.*, 98:6, Jul 1943. doi: 10.1086/144539.

V. Polito, G. Del Zanna, G. Valori, E. Pariat, H. E. Mason, J. Dudík, and M. Janvier. Analysis and modelling of recurrent solar flares observed with Hinode/EIS on March 9, 2012. *Astron. Astrophys.*, 601:A39, May 2017. doi: 10.1051/0004-6361/201629703.

K. G. Puschmann and E. Wiehr. The flux-gap between bright and dark solar magnetic structures. *Astron. Astrophys.*, 445(1):337–340, Jan 2006. doi: 10.1051/0004-6361:20054049.

C. Quintero Noda, T. Shimizu, J. de la Cruz Rodríguez, Y. Katsukawa, K. Ichimoto, T. Anan, and Y. Suematsu. Spectropolarimetric capabilities of Ca II 8542 Å line. *Mon. Not. Roy. Astron. Soc.*, 459(3):3363–3376, Jul 2016. doi: 10.1093/mnras/stw867.

Harry E. Ramsey and Sara F. Smith. Flare-initiated filamei it oscillations. *Astron. J.*, 71:197, Apr 1966. doi: 10.1086/109903.

Fabio Reale. Coronal Loops: Observations and Modeling of Confined Plasma. *Living Reviews in Solar Physics*, 11(1):4, Jul 2014. doi: 10.12942/lrsp-2014-4.

Katharine K. Reeves and Terry G. Forbes. The Effects of Gravity of an Loss-of-Equilibrium CME Initiation Model. In *Coronal and Stellar Mass Ejections, IAU Symposium Proceedings of the International Astronomical Union 226, Held 13-17 September, Beijing, edited by K. Dere, J. Wang, and Y. Yan. Cambridge: Cambridge University Press, 2005., pp.250-255*, volume 226, pages 250–255, January 2005. doi: 10.1017/S1743921305000657.

S. Régnier, R. W. Walsh, and C. E. Alexander. A new look at a polar crown cavity as observed by SDO/AIA. Structure and dynamics. *Astron. Astrophys.*, 533:L1, September 2011. doi: 10.1051/0004-6361/201117381.

M. Rempel, M. Schüssler, R. H. Cameron, and M. Knölker. Penumbral Structure and Outflows in Simulated Sunspots. *Science*, 325(5937):171, Jul 2009a. doi: 10.1126/science.1173798.

M. Rempel, M. Schüssler, and M. Knölker. Radiative Magnetohydrodynamic Simulation of Sunspot Structure. *Astrophys. J.*, 691(1):640–649, Jan 2009b. doi: 10.1088/0004-637X/691/1/640.

A. A. Reva, A. S. Kirichenko, A. S. Ulyanov, and S. V. Kuzin. Observations of the Coronal Mass Ejection with a Complex Acceleration Profile. *Astrophys. J.*, 851: 108, December 2017. doi: 10.3847/1538-4357/aa9986.

R. Rezaei, R. Schlichenmaier, C. A. R. Beck, J. H. M. J. Bruls, and W. Schmidt. Relation between photospheric magnetic field and chromospheric emission. *A&A*, 466(3):1131–1144, 2007. doi: 10.1051/0004-6361:20067017. URL https://doi.org/10.1051/0004-6361:20067017.

Thomas R. Rimmele. Plasma Flows Observed in Magnetic Flux Concentrations and Sunspot Fine Structure Using Adaptive Optics. *Astrophys. J.*, 604(2):906–923, April 2004. doi: 10.1086/382069.

B. Rompolt. Small Scale Structure and Dynamics of Prominences. *Hvar Observatory Bulletin*, 14:37, January 1990.

I. I. Roussev, T. G. Forbes, T. I. Gombosi, I. V. Sokolov, D. L. DeZeeuw, and J. Birn. A Three-dimensional Flux Rope Model for Coronal Mass Ejections Based on a Loss of Equilibrium. *Astrophys. J. Lett.*, 588:L45–L48, May 2003. doi: 10.1086/375442.

P. Ruan, T. Wiegelmann, B. Inhester, T. Neukirch, S. K. Solanki, and L. Feng. A first step in reconstructing the solar corona self-consistently with a magnetohydrostatic model during solar activity minimum. *Astron. Astrophys.*, 481(3): 827–834, Apr 2008. doi: 10.1051/0004-6361:20078834.

B. Ruiz Cobo and J. C. del Toro Iniesta. Inversion of Stokes Profiles. *Astrophys. J.*, 398:375, Oct 1992. doi: 10.1086/171862.

R. J. Rutten, R. H. Hammerschlag, and F. M. Bettonvil. The Dutch Open Telescope. In F. P. Pijpers, J. Christensen-Dalsgaard, and C. S. Rosenthal, editors, *SCORe'96 : Solar Convection and Oscillations and their Relationship*, volume 225 of *Astrophysics and Space Science Library*, pages 289–292, Dec 1997. doi: 10.1007/978-94-011-5167-2_31.

Kuniji Saito and E. Tandberg-Hanssen. The Arch Systems, Cavities, and Prominences in the Helmet Streamer Observed at the Solar Eclipse, November 12, 1966. *Solar Phys.*, 31(1):105–121, July 1973. doi: 10.1007/BF00156076.

K. Sankarasubramanian, Craig Gullixson, Stephen Hegwer, Thomas R. Rimmele, Scott Gregory, Tony Spence, Stephen Fletcher, Kit Richards, Emilie Rousset, Bruce Lites, David Elmore, Kim Streander, and Michael Sigwarth. The Diffraction Limited Spectro-Polarimeter: a new instrument for high-resolution solar polarimetry. volume 5171, February 2004. doi: 10.1117/12.508790.

G Scharmer, Klas Bjelksj, Tapio K. Korhonen, Bo Lindberg, Bertil Petterson, Stockholms Digitalmekanik Ab, Opteon Oy, and Lenstech Ab. The 1-meter swedish solar telescope. *Proceedings of SPIE - The International Society for Optical Engineering*, 09 2002. doi: 10.1117/12.460377.

Martin W. Scheeler, Wim M. van Rees, Hridesh Kedia, Dustin Kleckner, and William T. M. Irvine. Complete measurement of helicity and its dynamics in vortex tubes. *Science*, 357(6350):487–491, Aug 2017. doi: 10.1126/science.aam6897.

P. H. Scherrer, R. S. Bogart, R. I. Bush, J. T. Hoeksema, A. G. Kosovichev, J. Schou, W. Rosenberg, L. Springer, T. D. Tarbell, A. Title, C. J. Wolfson, I. Zayer, and MDI Engineering Team. The Solar Oscillations Investigation - Michelson Doppler Imager. *Solar Phys.*, 162:129–188, December 1995. doi: 10.1007/BF00733429.

P. H. Scherrer, J. Schou, R. I. Bush, A. G. Kosovichev, R. S. Bogart, and J. T. Hoeksema. The Helioseismic and Magnetic Imager (HMI) Investigation for the Solar Dynamics Observatory (SDO). *Solar Phys.*, 275:207–227, January 2012. doi: 10.1007/s11207-011-9834-2.

B. Schmieder, J. M. Malherbe, P. Mein, and E. Tand berg-Hanssen. Dynamics of solar filaments. III - Analysis of steady flows in H-alpha and C IV lines. *Astron. Astrophys.*, 136(1):81–88, Jul 1984.

J. Schou, P. H. Scherrer, R. I. Bush, R. Wachter, S. Couvidat, M. C. Rabello-Soares, R. S. Bogart, J. T. Hoeksema, Y. Liu, T. L. Duvall, D. J. Akin, B. A. Allard, J. W. Miles, R. Rairden, R. A. Shine, T. D. Tarbell, A. M. Title, C. J. Wolfson, D. F. Elmore, A. A. Norton, and S. Tomczyk. Design and Ground Calibration of the Helioseismic and Magnetic Imager (HMI) Instrument on the Solar Dynamics Observatory (SDO). *Solar Phys.*, 275:229–259, January 2012. doi: 10.1007/s11207-011-9842-2.

C. J. Schrijver and M. L. De Rosa. Photospheric and heliospheric magnetic fields. *Solar Phys.*, 212:165–200, January 2003. doi: 10.1023/A:1022908504100.

C. J. Schrijver, C. Elmore, B. Kliem, T. Török, and A. M. Title. Observations and Modeling of the Early Acceleration Phase of Erupting Filaments Involved in Coronal Mass Ejections. *Astrophys. J.*, 674:586-595, February 2008. doi: 10.1086/524294.

N. A. J. Schutgens and G. Tóth. Numerical simulation of prominence oscillations. *Astron. Astrophys.*, 345:1038–1048, May 1999.

P. Schwartz, S. Gunár, J. M. Jenkins, D. M. Long, P. Heinzel, and D. P. Choudhary. 2D non-LTE modelling of a filament observed in the Hα line with the DST/IBIS spectropolarimeter. *Astron. Astrophys.*, 631:A146, Nov 2019. doi: 10.1051/0004-6361/201935358.

D. B. Seaton, M. Mierla, D. Berghmans, A. N. Zhukov, and L. Dolla. SWAP-SECCHI Observations of a Mass-loading Type Solar Eruption. *Astrophys. J. Lett.*, 727:L10, January 2011. doi: 10.1088/2041-8205/727/1/L10.

Angelo Secchi. *Le soleil*, volume 1. , 1875.

V. D. Shafranov. On Magnetohydrodynamical Equilibrium Configurations. *Soviet Journal of Experimental and Theoretical Physics*, 6:545, Jan 1958.

H. Socas-Navarro and H. Uitenbroek. On the Diagnostic Potential of Hα for Chromospheric Magnetism. *Astrophys. J. Lett.*, 603(2):L129–L132, Mar 2004. doi: 10.1086/383147.

H. Socas-Navarro, J. de la Cruz Rodríguez, A. Asensio Ramos, J. Trujillo Bueno, and B. Ruiz Cobo. An open-source, massively parallel code for non-LTE synthesis and inversion of spectral lines and Zeeman-induced Stokes profiles. *Astron. Astrophys.*, 577:A7, May 2015. doi: 10.1051/0004-6361/201424860.

Hector Socas-Navarro, David Elmore, Anna Pietarila, Anthony Darnell, Bruce W. Lites, Steven Tomczyk, and Steven Hegwer. Spinor: Visible and Infrared Spectro-Polarimetry at the National Solar Observatory. *Solar Phys.*, 235(1-2): 55–73, May 2006. doi: 10.1007/s11207-006-0020-x.

S. K. Solanki, O. Steiner, and H. Uitenbroeck. Two-dimensional models of the solar chromosphere. I - The CA II K line as a diagnostic: 1.5-D radiative transfer. *Astron. Astrophys.*, 250(1):220–234, Oct 1991.

Sami K. Solanki. Smallscale Solar Magnetic Fields - an Overview. *Space Sci. Rev.*, 63(1-2):1–188, Mar 1993. doi: 10.1007/BF00749277.

H. C. Spruit. Pressure equilibrium and energy balance of small photospheric fluxtubes. *Solar Phys.*, 50(2):269–295, Dec 1976. doi: 10.1007/BF00155292.

G. Stellmacher and E. Wiehr. Non-thermal line-broadening in solar prominences. *Astron. Astrophys.*, 581:A141, September 2015. doi: 10.1051/0004-6361/201322781.

Y. Su, V. Surges, A. van Ballegooijen, E. DeLuca, and L. Golub. Observations and Magnetic Field Modeling of the Flare/coronal Mass Ejection Event on 2010 April 8. *Astrophys. J.*, 734:53, June 2011. doi: 10.1088/0004-637X/734/1/53.

E. Tandberg-Hanssen. Books-Received - the Nature of Solar Prominences. *Science*, 269:111, Jul 1995.

B. J. Thompson, E. W. Cliver, N. Nitta, C. Delannée, and J.-P. Delaboudinière. Coronal dimmings and energetic CMEs in April-May 1998. *Geophys. Res. Lett.*, 27:1431–1434, May 2000. doi: 10.1029/1999GL003668.

V. S. Titov and P. Démoulin. Basic topology of twisted magnetic configurations in solar flares. *Astron. Astrophys.*, 351:707–720, November 1999.

T. Török and B. Kliem. The evolution of twisting coronal magnetic flux tubes. *Astron. Astrophys.*, 406:1043–1059, Aug 2003. doi: 10.1051/0004-6361:20030692.

T. Török and B. Kliem. Confined and Ejective Eruptions of Kink-unstable Flux Ropes. *Astrophys. J. Lett.*, 630:L97–L100, September 2005. doi: 10.1086/462412.

T. Török, M. A. Berger, and B. Kliem. The writhe of helical structures in the solar corona. *Astron. Astrophys.*, 516:A49, June 2010. doi: 10.1051/0004-6361/200913578.

R. A. Treumann and C. H. Jaroschek. The Heliospheric Termination Shock. *arXiv e-prints*, art. arXiv:0807.4170, Jul 2008.

K. Tziotziou. Chromospheric Cloud-Model Inversion Techniques. In P. Heinzel, I. Dorotovič, and R. J. Rutten, editors, *The Physics of Chromospheric Plasmas*, volume 368 of *Astronomical Society of the Pacific Conference Series*, page 217, May 2007.

Thomas A. Underwood, David Voelz, François-Xavier Schmider, Jason Jackiewicz, Julien Dejonghe, Yves Bresson, Robert Hull, Ivan Goncalves, Patrick Gualme, Frédéric Morand, and Olivier Preis. Adaptation of Dunn Solar Telescope for Jovian Doppler spectro imaging. volume 10401, September 2017. doi: 10.1117/12.2275909.

A. A. van Ballegooijen and P. C. H. Martens. Formation and eruption of solar prominences. *Astrophys. J.*, 343:971–984, August 1989. doi: 10.1086/167766.

L. van Driel-Gesztelyi, P. Démoulin, C. H. Mandrini, L. Harra, and J. A. Klimchuk. The Long-Term Evolution of AR 7978: The Scalings of the Coronal Plasma Parameters with the Mean Photospheric Magnetic Field. *Astrophys. J.*, 586: 579–591, March 2003. doi: 10.1086/367633.

Lidia van Driel-Gesztelyi and Lucie May Green. Evolution of Active Regions. *Living Reviews in Solar Physics*, 12(1):1, Sep 2015. doi: 10.1007/lrsp-2015-1.

W. van Tend and M. Kuperus. The development of coronal electric current systems in active regions and their relation to filaments and flares. *Solar Phys.*, 59:115–127, September 1978. doi: 10.1007/BF00154935.

A. Vecchio, G. Cauzzi, and K. P. Reardon. The solar chromosphere at high resolution with IBIS. II. Acoustic shocks in the quiet internetwork and the role of magnetic fields. *Astron. Astrophys.*, 494(1):269–286, Jan 2009. doi: 10.1051/0004-6361:200810694.

J. C. Vial, K. Olivier, A. A. Philippon, A. Vourlidas, and V. Yurchyshyn. High spatial resolution VAULT H-Lyα observations and multiwavelength analysis of an active region filament. *Astron. Astrophys.*, 541:A108, May 2012. doi: 10.1051/0004-6361/201118275.

Jean-Claude Vial and Oddbjørn Engvold. *Solar Prominences*. Springer, 2015.

A. N. Vyssotsky. Astronomical records in the Russian chronicles from 1000 to 1600 A.D. (as collected by D.O. Sviatsky). *Meddelanden fran Lunds Astronomiska Observatorium Serie II*, 126:3–52, Jan 1949.

Shuo Wang, Jack M. Jenkins, Valentin Martinez Pillet, Christian Beck, David M. Long, Debi Prasad Choudhary, Karin Muglach, and James McAteer. Magnetic Structure of an Erupting Filament. *arXiv e-prints*, art. arXiv:2002.02104, February 2020.

Y. M. Wang. The Jetlike Nature of He II λ304 Prominences. *Astrophys. J.*, 520(1): L71–L74, Jul 1999. doi: 10.1086/312149.

Y.-M. Wang and N. R. Sheeley, Jr. Filament Eruptions near Emerging Bipoles. *Astrophys. J. Lett.*, 510:L157–L160, January 1999. doi: 10.1086/311815.

J. E. Wiik, K. Dere, and B. Schmieder. UV prominences observed with the HRTS: structure and physical properties. *Astron. Astrophys.*, 273:267, Jun 1993.

J. E. Wiik, I. E. Dammasch, B. Schmieder, and K. Wilhelm. Multiple-Thread Model of a Prominence Observed by SUMER and EIT on SOHO. *Solar Phys.*, 187(2): 405–426, Jul 1999. doi: 10.1023/A:1005151015043.

D. R. Williams, T. Török, P. Démoulin, L. van Driel-Gesztelyi, and B. Kliem. Eruption of a Kink-unstable Filament in NOAA Active Region 10696. *Astrophys. J. Lett.*, 628:L163–L166, August 2005. doi: 10.1086/432910.

D. R. Williams, D. Baker, and L. van Driel-Gesztelyi. Mass Estimates of Rapidly Moving Prominence Material from High-cadence EUV Images. *Astrophys. J.*, 764:165, February 2013. doi: 10.1088/0004-637X/764/2/165.

T. N. Woods, F. G. Eparvier, R. Hock, A. R. Jones, D. Woodraska, D. Judge, L. Didkovsky, J. Lean, J. Mariska, H. Warren, D. McMullin, P. Chamberlin, G. Berthiaume, S. Bailey, T. Fuller-Rowell, J. Sojka, W. K. Tobiska, and R. Viereck. Extreme Ultraviolet Variability Experiment (EVE) on the Solar Dynamics Observatory (SDO): Overview of Science Objectives, Instrument Design, Data Products, and Model Developments. *Solar Phys.*, 275:115–143, January 2012. doi: 10.1007/s11207-009-9487-6.

J.-P. Wuelser, J. R. Lemen, T. D. Tarbell, C. J. Wolfson, J. C. Cannon, and B. A. Carpenter. EUVI: the STEREO-SECCHI extreme ultraviolet imager. In S. Fineschi and M. A. Gummin, editors, *Telescopes and Instrumentation for Solar Astrophysics*, volume 5171 of *Proc. SPIE*, pages 111–122, February 2004. doi: 10.1117/12.506877.

C. Xia and R. Keppens. Formation and Plasma Circulation of Solar Prominences. *Astrophys. J.*, 823:22, May 2016. doi: 10.3847/0004-637X/823/1/22.

C. Xia, P. F. Chen, and R. Keppens. Simulations of Prominence Formation in the Magnetized Solar Corona by Chromospheric Heating. *Astrophys. J.*, 748:L26, April 2012. doi: 10.1088/2041-8205/748/2/L26.

S. L. Yardley, L. M. Green, D. R. Williams, L. van Driel-Gesztelyi, G. Valori, and S. Dacie. Flux Cancellation and the Evolution of the Eruptive Filament of 2011 June 7. *Astrophys. J.*, 827(2):151, Aug 2016. doi: 10.3847/0004-637X/827/2/151.

Anthony R. Yeates, Tahar Amari, Ioannis Contopoulos, Xueshang Feng, Duncan H. Mackay, Zoran Mikić, Thomas Wiegelmann, Joseph Hutton, Christopher A. Lowder, Huw Morgan, Gordon Petrie, Laurel A. Rachmeler, Lisa A. Upton, Aurelien Canou, Pierre Chopin, Cooper Downs, Miloslav Druckmüller, Jon A. Linker, Daniel B. Seaton, and Tibor Török. Global Non-Potential Magnetic Models of the Solar Corona During the March 2015 Eclipse. *Space Sci. Rev.*, 214(5):99, Aug 2018. doi: 10.1007/s11214-018-0534-1.

Jun Zhang, Jingxiu Wang, Yuanyong Deng, and Dejin Wu. Magnetic Flux Cancellation Associated with the Major Solar Event on 2000 July 14. *Astrophys. J.*, 548 (1):L99–L102, Feb 2001. doi: 10.1086/318934.

Yu-Hao Zhou, C. Xia, R. Keppens, C. Fang, and P. F. Chen. Three-dimensional MHD Simulations of Solar Prominence Oscillations in a Magnetic Flux Rope. *Astrophys. J.*, 856:179, April 2018. doi: 10.3847/1538-4357/aab614.

Zhenjun Zhou, Xin Cheng, Jie Zhang, Yuming Wang, Dong Wang, Lijuan Liu, Bin Zhuang, and Jun Cui. Why Do Torus-unstable Solar Filaments Experience Failed Eruptions? *Astrophys. J. Lett.*, 877(2):L28, Jun 2019. doi: 10.3847/2041-8213/ab21cb.

J. B. Zirker, O. Engvold, and S. F. Martin. Counter-streaming gas flows in solar prominences as evidence for vertical magnetic fields. *Nature*, 396(6710):440–441, Dec 1998. doi: 10.1038/24798.

F. P. Zuccarello, G. Aulanier, and S. A. Gilchrist. The Apparent Critical Decay Index at the Onset of Solar Prominence Eruptions. *Astrophys. J. Lett.*, 821:L23, April 2016. doi: 10.3847/2041-8205/821/2/L23.